



HAL
open science

Modèles microscopiques et propriétés des phases désordonnées des réseaux métallo-organiques pour la séparation de CO₂

Nicolas Castel

► **To cite this version:**

Nicolas Castel. Modèles microscopiques et propriétés des phases désordonnées des réseaux métallo-organiques pour la séparation de CO₂. Chimie analytique. Université Paris sciences et lettres, 2023. Français. NNT : 2023UPSLC004 . tel-04835678

HAL Id: tel-04835678

<https://pastel.hal.science/tel-04835678v1>

Submitted on 13 Dec 2024

HAL is a multi-disciplinary open access archive for the deposit and dissemination of scientific research documents, whether they are published or not. The documents may come from teaching and research institutions in France or abroad, or from public or private research centers.

L'archive ouverte pluridisciplinaire **HAL**, est destinée au dépôt et à la diffusion de documents scientifiques de niveau recherche, publiés ou non, émanant des établissements d'enseignement et de recherche français ou étrangers, des laboratoires publics ou privés.

THÈSE DE DOCTORAT
DE L'UNIVERSITÉ PSL

Préparée à Chimie ParisTech

Modèles microscopiques et propriétés des phases désordonnées des réseaux métallo-organiques pour la séparation de CO₂

Atomistic models and properties of amorphous metal-organic frameworks for CO₂ separation

Soutenue par

Nicolas CASTEL

Le 18 juillet 2023

École doctorale n°388

**Chimie Physique et
Chimie Analytique de
Paris Centre**

Spécialité

Chimie Physique

Composition du jury :

Benjamin ROTENBERG Directeur de Recherche, Sorbonne Université	<i>Président</i>
Kim JELFS Full Professor, Imperial College London	<i>Rapportrice</i>
Céline CHIZALLET Ingénieur-chercheur IFPEN	<i>Rapportrice</i>
François-Xavier COUDERT Directeur de Recherche, Chimie ParisTech	<i>Directeur de thèse</i>

REMERCIEMENTS

En premier lieu, je voudrais adresser ici mes plus vifs remerciements à Kim Jelfs et Céline Chizallet pour avoir accepté d'être les rapportrices de ce manuscrit, et pour leurs remarques constructives exprimées dans leur rapport. Je remercie aussi Benjamin Rotenberg d'avoir fait partie de mon jury de thèse, et pour l'intérêt non moindre qu'il a porté à ce travail.

Même s'il n'arrive que second dans l'ordre protocolaire, mes principaux remerciements vont à François-Xavier Coudert pour avoir dirigé ma thèse pendant ces trois années. En montant mon dossier de thèse, on m'avait recommandé sa bienveillance et sa disponibilité, et trois ans après je peux dire que je n'ai pas été déçu. Il a toujours pris le temps d'échanger dès que j'en avais besoin (être dans le même bureau aidant), mais a su aussi me laisser évoluer à mon rythme. Je ne compte plus les amis doctorants qui se sont montrés envieux d'une telle qualité d'encadrement. En plus de ses conseils précieux sur les aspects scientifiques et techniques de cette thèse, je souhaite lui exprimer ma gratitude pour tout ce que j'ai pu apprendre à son contact sur le monde de la recherche ainsi que mon admiration devant son engagement pour une recherche plus ouverte et intègre.

Je tiens ensuite à remercier tous ceux avec qui j'ai eu la chance de travailler pendant cette thèse. Je tiens en particulier à remercier Jack Evans pour la collaboration très fructueuse que nous avons entretenue cette dernière année et Tom Bennett pour les discussions inspirantes que nous avons au début de mes aventures dans le monde des aMOF. Je remercie également toute l'équipe du GHGT-16, et plus particulièrement Florence Delprat-Jannaud, Tim Dixon, Sophia Chorazewicz et Suzanne Killick, pour m'avoir permis de prendre part à l'organisation de ce beau congrès qui a su me tenir occupé entre deux dynamiques moléculaires.

Venons-en maintenant aux remerciements moins directement liés au travail. Merci aux doctorants et postdocs de notre petite équipe pour tous ces moments passés ensemble, qu'ils aient quitté le laboratoire avant ma soutenance ou non. Merci surtout aux doctorants actuels, à commencer par Emmanuel, mon co-bureau de toujours, qui aura fait toute sa thèse en décalé d'un ou deux mois. Je le remercie de m'avoir servi de consultant en chimie théorique, à défaut de vouloir s'occuper de mes table of content pictures, et surtout d'avoir égayé mes heures au labo et en dehors. Ces deux derniers remerciements s'étendent à Dune, la dernière arrivée du bureau, même si au début elle a largement complexifié mon lexique en m'empêchant désormais de désigner Emmanuel par "mon co-bureau". Merci d'apporter un regard neuf sur les MOF amorphes en étudiant enfin autre chose que ZIF-4, et merci également de progressivement prendre le relais sur les MLP. Je remercie enfin Lionel, le 3e larron de notre télétravail intensif au bord de la mer, pour essayer d'augmenter les standards de code de l'équipe comme pour servir de guide aux randonnées que j'étais en théorie censé organiser.

Mais je n'ai pas fait que passer ma vie au travail et j'ai aussi puisé de l'inspiration auprès de mes amis. Je remercie tous ceux qui sont venus à ma soutenance malgré les sirènes de toutes les destinations de vacances envisageables au milieu de l'été. Ils ont formé un bel échantillon des personnes rencontrées ces 16 dernières années, entre ceux croisés au collège ou lycée, en prépa, en école ou pendant ma thèse. Mention spéciale à Elliot qui, en plus de compter parmi ces trois derniers groupes, a affronté ses trois années de thèse en même temps que les miennes en qualité de colloc. Je les remercie tous pour tous ces moments passés ensemble pendant ces trois ans sur Paris, en vacances ou en télétravail (une composante importante de cette thèse).

Je remercie également ma famille, à commencer par mon frère Sébastien qui est venu d'aussi loin que Marcoule pour assister à ma soutenance au prix de 2 jours de congés. Je remercie tout particulièrement mes parents à qui je dois beaucoup : sans leur soutien, leurs encouragements constants, et la haute image de l'éducation qu'ils m'ont transmise, je ne serais pas là aujourd'hui.

Pour rester sur le thème de l'éducation, je vais clôturer ces remerciements par un hommage à la longue lignée de professeurs qui se sont succédé en démarrant au collège et dont FX est en un sens le dernier. Je leur suis reconnaissant de m'avoir transmis le goût des sciences, une certaine curiosité intellectuelle, un grand nombre d'outils ainsi que, pour une partie d'entre eux, une forte sensibilisation aux enjeux environnementaux. Ensemble, ils m'ont permis de vivre une (très) longue formation initiale, sincèrement passionnante, qui se conclut par cette thèse.

Bonne lecture!

TABLE OF CONTENTS

General introduction	1
1 Amorphous metal–organic frameworks for CO₂ separation	5
1.1 CO ₂ separation and climate change mitigation	6
1.1.1 Climate targets and negative emissions	6
1.1.2 Carbon capture, utilization and storage	7
1.1.3 Porous materials for CO ₂ separation	12
1.2 Metal–organic frameworks	16
1.2.1 A versatile class of porous materials.	16
1.2.2 Novel materials for CO ₂ separation	19
1.2.3 Zeolitic imidazolate frameworks	20
1.2.4 Amorphous metal–organic frameworks	22
1.3 Atomistic models of amorphous MOFs.	26
1.3.1 Reverse Monte Carlo models	26
1.3.2 Continuous random networks	27
1.3.3 Relying on crystalline models	29
1.3.4 <i>Ab initio</i> molecular dynamics	30
1.3.5 Reactive force fields.	32
1.3.6 Polymerization algorithms	33
Conclusions and perspectives	35
2 Molecular simulation methods	37
2.1 Molecular dynamics simulations	39
2.1.1 Space and time scales	39
2.1.2 Principles of molecular dynamics.	40
2.1.3 Thermodynamic ensembles	41
2.2 <i>Ab initio</i> molecular dynamics	44
2.2.1 Unifying MD and quantum calculations	44
2.2.2 Density functional theory	45
2.3 Force fields	48
2.3.1 Motivations and principles	48
2.3.2 Classical force fields	49
2.3.3 Reactive force fields.	50
2.4 Machine-learned potentials	53
2.4.1 Principles and construction	53
2.4.2 Neural network potentials	55
2.4.3 Equivariant message passing neural networks	58
2.5 Characterizing structural properties of amorphous models	62
2.5.1 Local order	62
2.5.2 Bulk properties	64
2.5.3 Topology	65
2.5.4 Characterizing liquids	67
2.5.5 <i>aMOF</i> , a Python library	69

3	Challenges in molecular dynamics of <i>a</i>ZIFs using reactive force fields	71
3.1	Producing glass models with <i>in silico</i> melt-quenching	73
3.1.1	System and methods	73
3.1.2	Preparation of the crystal	74
3.1.3	Melt-quenching	75
3.1.4	Choice of the melting temperature	76
3.1.5	Equilibration	79
3.2	Properties of the glass models	80
3.2.1	Local order: interatomic distances and bond angles	80
3.2.2	Bulk properties: density and porosity	83
3.2.3	Topological properties of the coordination network	83
3.3	Challenges in using ReaxFF	85
3.3.1	(<i>N, P, T</i>) ensemble and densification.	85
3.3.2	Description of the crystal.	86
	Conclusions and perspectives	91
4	Generation of <i>a</i>ZIF models with machine-learned potentials	93
4.1	MLPs for MOFs and amorphous systems	95
4.1.1	MLPs for MOFs	95
4.1.2	Generation of glass models with MLPs.	96
4.2	Construction of MLPs for ZIF-4	97
4.2.1	<i>Ab initio</i> reference data	97
4.2.2	Training	97
4.2.3	Reproducing structural properties	99
4.3	Generating <i>a</i> ZIF-4 glass models	103
4.3.1	Producing glass models by melt-quenching	103
4.3.2	Properties of the glass models	104
4.4	Towards a universal MLP for ZIFs	108
4.4.1	Multiple ZIF structures	108
4.4.2	Multiple volumes.	108
4.4.3	Simulation of liquid systems	109
	Preliminary conclusions and perspectives	112
5	Finite temperature mechanical properties of <i>a</i>ZIFs	115
5.1	Computation of mechanical properties with molecular dynamics	117
5.1.1	Extracting mechanical properties from simulations	117
5.1.2	Finite difference methods.	117
5.1.3	Strain-fluctuation method	118
5.1.4	Mechanical properties of ZIFs	119
5.2	<i>Ab initio</i> molecular dynamics	121
5.2.1	Systems and methods	121
5.2.2	Finite strain difference method.	121
5.2.3	Reference values	123
5.3	Reactive force fields	125
5.3.1	Finite strain difference method.	125
5.3.2	Finite stress difference method.	126
5.3.3	Strain-fluctuation method	128

5.4	Classical force fields	131
5.4.1	Adaptation of the force fields	131
5.4.2	Validation with AIMD results	133
5.4.3	Exploring other methods	134
5.5	Machine-learned potentials	138
5.5.1	Finite strain difference method with NequIP	138
5.5.2	Accurately training for stress	139
5.5.3	Reproduction of <i>a</i> ZIF-4 mechanical properties	140
5.5.4	Exploratory use of the (N, P, T) ensemble	141
	Conclusions and perspectives	143

General conclusions **145**



List of Publications **149**

Published	149
In Press	149

Bibliography **151**

Résumé en français **173**

1	Des MOF amorphes pour la séparation de CO ₂	174
2	Étude des <i>a</i> MOF par simulation moléculaire.	177
3	Défis de la simulation d' <i>a</i> ZIF par champs de force réactifs	178
4	Potentiels ML pour la production de modèles d' <i>a</i> ZIF.	180
5	Propriétés mécaniques à température finie des <i>a</i> ZIF	181
	Conclusions	183

GENERAL INTRODUCTION

Metal–organic frameworks (MOFs) are hybrid materials composed of inorganic nodes (clusters or metal ions) bridged by organic linkers to form three-dimensional architectures, often porous. They have been the subject of an intensive research effort for over 20 years and, taking advantage of their porosity and structural and chemical tunability, have been proposed for applications in various industrial-scale processes, such as gas storage and separation or catalysis. Among these numerous applications, MOFs are widely investigated as next-generation materials for CO₂ separation in carbon capture, utilization and storage (CCUS) technologies. This suite of technologies are present in multiple pathways to achieve our collective climate goals, notably as negative emissions technologies and solutions to decarbonize hard-to-abate emissions from heavy industries. Significant research effort goes into reducing their costs, by looking for new materials such as MOFs, which could be used in less energy-intensive processes than current industrial standards.

Of the rapidly increasing number of studies of MOFs in the research literature, most are focused on perfectly ordered, crystalline structures, because of ease of experimental identification and characterization with common laboratory equipment. However, the dynamic nature of MOFs is a key characteristic of these relatively weakly bonded frameworks – compared to more traditional porous solids like zeolites – and accounts in a large part for their appeal, and some of their extraordinary chemical and physical properties. Additionally, the definition of MOF does not restrict this term to crystalline phases, and recently the number of amorphous MOF (*a*MOF) states reported has seen a rapid expansion. These include the recently discovered MOF liquids, MOF gels, and a large variety of glassy states and amorphous solids, which can be produced by pressure-induced amorphization, temperature-induced amorphization, melt-quenching, ball milling, irradiation, etc. These non-crystalline states possess useful physical and chemical properties distinct from those achievable in the crystalline phases, such as isotropy, the absence of grain boundaries, high transparency, and mechanical robustness, while retaining most of the intrinsic advantages of crystals and powders. They also allow for a greater ease of processing when used in industrial applications.

However, in balance with their promising properties, amorphous states are particularly challenging to characterize and their framework structures at the microscopic scale are hard to determine. Indirect structural information can be available from diffraction experiments, but unlike for crystals, it cannot be solved into a nice periodic atomic structure as a matter of routine analysis. Moreover, the computational description of disordered materials is also more complex than that of crystals: computational methods to model these disordered materials are complex, and relatively few atomistic models of amorphous MOFs are present in the literature. Efforts towards a better numerical description of *a*MOFs are crucial as a complement to experimental works and to provide tools to predict novel architectures, yielding the potential to significantly accelerate the rational development of materials.

During my PhD, I explored one possible strategy which consists in simulating the phase transition from a crystalline MOF to the amorphous state, using molecular dynamics (MD) to mimic *in silico* the experimental formation routes. I used a large number of simulation methods with different scopes, time and length scales and computational costs – *ab initio* molecular dynamics, classical and reactive

force fields, and machine-learned potentials – to generate atomistic models of *a*MOFs and study their properties. I studied zeolitic imidazolate frameworks (ZIFs), a subclass of MOFs closely related to zeolites and home to a number of prototypical *a*MOF structures. I reviewed and compared the existing methodologies available for the determination of microscopic models of amorphous MOFs, as well as the structure they generated, assessing their strengths and weaknesses. I also proposed a new methodology, with the development of machine-learned potentials which led to an excellent reproduction of the structural properties of a number of different systems. As a demonstration of the interest of performing such molecular simulations, I have focused on the characterization of finite temperature mechanical properties, which are essential for MOFs to fully achieve their potential in industrial-scale processes, but difficult to determine experimentally.



This thesis is composed of five chapters. I start by presenting the broader context of CCUS and climate change mitigation, to put into context the research on next-generation materials for CO₂ separation. I then introduce MOFs, both crystalline and amorphous, before reviewing the different atomistic models of *a*MOFs published to this date in the literature. In a second chapter, I present the different methods of molecular simulations employed during my PhD, first introducing molecular dynamics in general and then four of its flavors: *ab initio*, with classical and reactive force fields, and with machine learned potentials. The third chapter probes the accuracy and reliability of modeling the formation and structure of amorphous ZIFs using reactive force fields, which have been proposed as a tractable alternative to the successful but computationally expensive *ab initio* simulations. The significant challenges evidenced called for the development of new interatomic potentials, and led to the work presented in chapter 4, where I propose the first machine-learned potentials to generate *a*MOF models and evaluate their applicability. The last chapter describes the computation of finite temperature mechanical properties of both crystal and glass models by critically assessing multiple computational methodologies and molecular dynamics schemes.



AMORPHOUS METAL–ORGANIC FRAMEWORKS FOR CO₂ SEPARATION

1.1	CO ₂ separation and climate change mitigation	6
1.1.1	Climate targets and negative emissions	6
1.1.2	Carbon capture, utilization and storage	7
1.1.3	Porous materials for CO ₂ separation	12
1.2	Metal–organic frameworks	16
1.2.1	A versatile class of porous materials.	16
1.2.2	Novel materials for CO ₂ separation	19
1.2.3	Zeolitic imidazolate frameworks	20
1.2.4	Amorphous metal–organic frameworks	22
1.3	Atomistic models of amorphous MOFs.	26
1.3.1	Reverse Monte Carlo models	26
1.3.2	Continuous random networks	27
1.3.3	Relying on crystalline models	29
1.3.4	<i>Ab initio</i> molecular dynamics	30
1.3.5	Reactive force fields.	32
1.3.6	Polymerization algorithms	33
	Conclusions and perspectives	35



The recent and still largely uncharted family of amorphous metal–organic frameworks provides an opportunity to look for next generation materials for CO₂ separation. After putting carbon capture, utilization and storage in the larger context of climate change mitigation, and briefly introducing the different technologies available for CO₂ separation in section 1.1, I will give an overview of metal–organic frameworks in general with a particular focus on their amorphous phases in section 1.2. I will finally review in section 1.3 the different atomistic models of these amorphous metal–organic frameworks published to this date in the literature.

1.1 CO₂ SEPARATION AND CLIMATE CHANGE MITIGATION

1.1.1 Climate targets and negative emissions

THE NEED FOR NEGATIVE EMISSIONS TO STAY BELOW 2°C

The 2015 Paris Agreement aims to strengthen the global response to the threat of climate change by “holding the increase in the global average temperature to well below 2°C above pre-industrial levels and pursuing efforts to limit the temperature increase to 1.5°C above pre-industrial levels, recognizing that this would significantly reduce the risks and impacts of climate change”.¹

As the rise in temperature is primarily caused by the increase in the concentration of greenhouse gases (GHG) in the atmosphere [1], limiting this rise implies at least stabilizing this concentration. To the first order, this means that the flow of anthropogenic GHGs into the atmosphere must be canceled out (or even become negative), which is often referred to as zero (or negative) net emissions or *carbon neutrality* [2].

If we assume that there will always be residual positive emissions caused by various human activities (e.g. long-distance transport, agriculture, etc.), then a certain amount of GHGs will have to be removed from the atmosphere to compensate. Figure 1.1 exemplifies, with different illustrative pathways from the latest assessment report by the Intergovernmental Panel on Climate Change (IPCC), the need for significant negative emissions in the medium term along with very ambitious reduction in absolute emissions [3].

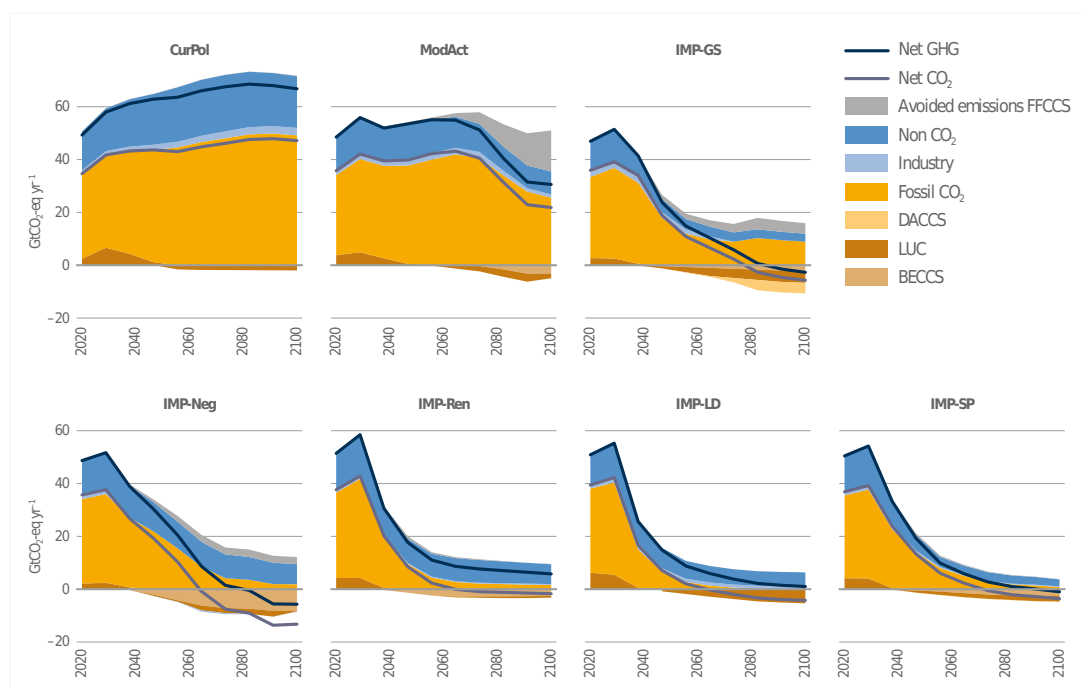


Figure 1.1: Negative emissions (LUC, DACCS, BECCS) and residual emissions for each of the seven illustrative pathways (IPs). CurPol and ModAct are illustrative of higher emissions, while five are illustrative mitigation pathways (IMP) exploring various mitigation strategies. Reproduced from Ref. [3].

CO₂ CAPTURE AS A MAJOR SOURCE OF NEGATIVE EMISSIONS

Several categories of negative emissions exist with highly heterogeneous levels of maturity and potential, most of them focusing on carbon dioxide (CO₂), which represents 75% of anthropogenic GHG emissions in tons of CO₂ equivalent (tCO₂eq) [4] and whose atmospheric concentration is the highest among GHGs (excluding water vapor).

¹Paris Agreement to the United Nations Framework Convention on Climate Change, Dec. 12, 2015.

These sources of negative emissions, illustrated on figure 1.2, range from the increase of the natural sink linked to land-use change (LUC), to carbon capture and storage (CCS) [5]. In the latter option, the CO₂ can be directly captured from the atmosphere (*direct air capture* or DACCS), or from the combustion of biomass (*bioenergy with CCS* - BECCS) [6]. The five illustrative mitigation pathways of the IPCC report shown on figure 1.1 are based on various combinations on three of these sources: LUC, BECCS and DACCS. It is worth noting that while technologies for capturing the two other major GHGs, methane (CH₄) [7] and nitrous oxide (N₂O) [8], have been proposed in the academic literature, they are far from industrialization.

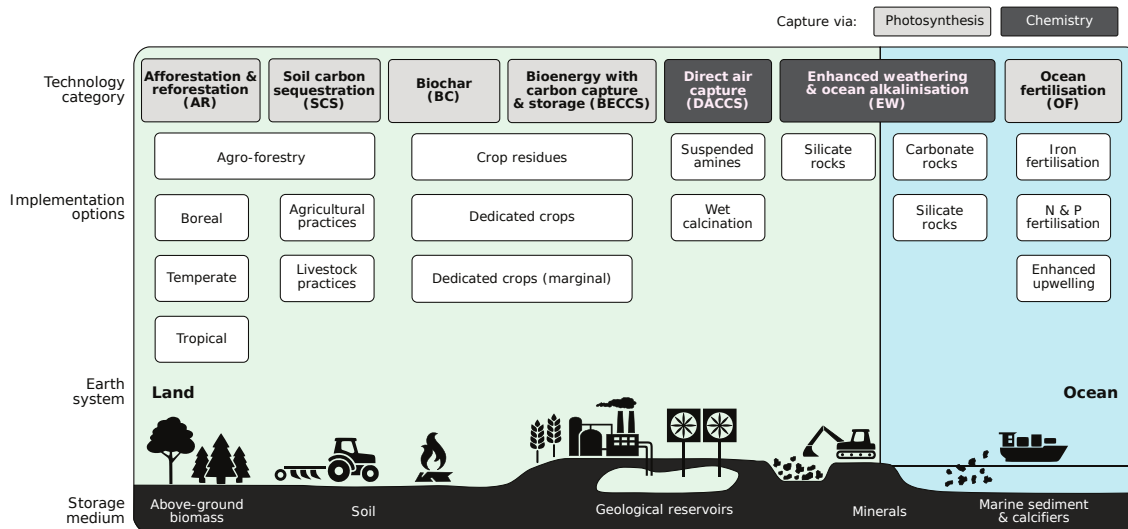


Figure 1.2: An overview of negative emissions technologies. Reproduced from Ref. [5].

TARGETS IN FRANCE AND THE EUROPEAN UNION

While the priority is a drastic reduction in GHG emissions, a simultaneous effort towards increasing negative emissions, in particular relying on CCS, are present in multiple national long-term transition strategies, including that of France and the European Union. It should be emphasized that negative emissions and CCUS are not a substitute for reducing emissions through more sustainable practices, improved energy efficiency, or conventional decarbonization.

In the latest revision exercise of the national low-carbon strategy (SNBC - *Stratégie Nationale Bas-Carbone*), France aims to reach carbon neutrality in 2050 [9], a target which has been enshrined into law in 2019.² In the scenario underlying it (AMS - *Avec Mesures Supplémentaires*) 20% of the GHG sink in 2050 is made by CCS technologies.

Similar ambitions are shared at the European level, with the European Commission's strategic long-term vision depending in part on CO₂ removal techniques based on CCS [10]. In this strategy, CCS represents between 10 and 45% of the negative emissions, corresponding to various scenarios. The European Climate Law passed in 2021 enshrined the 2050 climate-neutrality target into law.³

1.1.2 Carbon capture, utilization and storage

Carbon capture, utilization and storage (CCUS) refers to a suite of technologies that involves the capture of CO₂ from a variety of sources, and its subsequent transport, utilization or storage. The CCUS value chain is represented on figure 1.3.

²Loi n° 2019-1147 du 8 novembre 2019 relative à l'énergie et au climat, JORF n°0261 du 9 novembre 2019, texte n° 1

³Regulation (EU) 2021/1119 of the European Parliament and of the Council of 30 June 2021 establishing the framework for achieving climate neutrality and amending Regulations (EC) No 401/2009 and (EU) 2018/1999 ('European Climate Law')

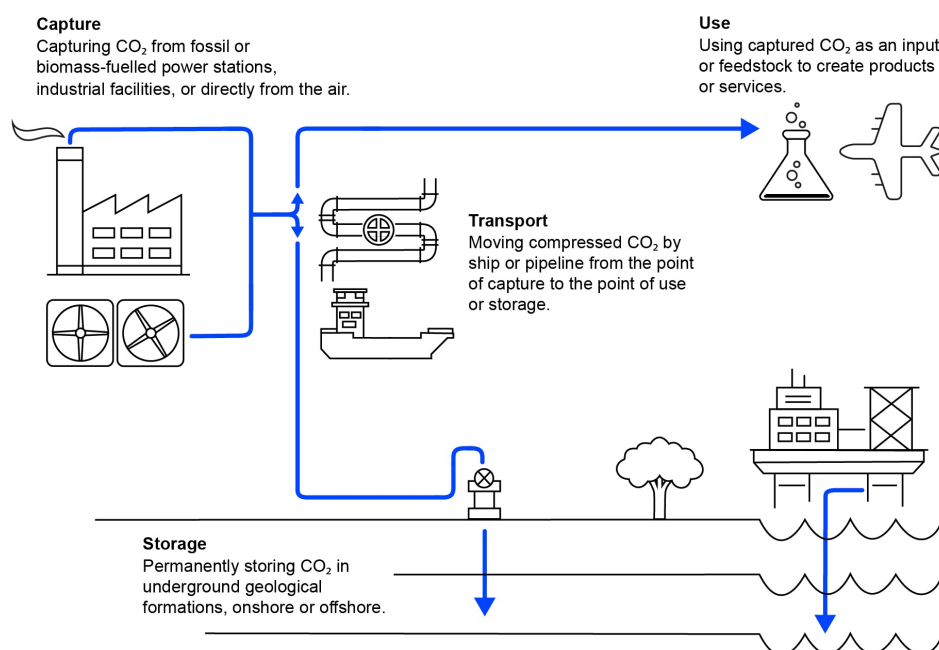


Figure 1.3: Schematic of carbon capture utilization and storage (CCUS). Reproduced from Ref. [11].

CO₂ CAPTURE

CO₂ can be captured from large point sources such as power generation or industrial facilities that use either fossil fuels or biomass for fuel, or directly from the air. The goal of CO₂ capture is thus to separate the CO₂ from the other gases (e.g. N₂, H₂O), by providing the thermodynamic minimum work required for separation [12].

Due to the low density of CO₂ in air (around 400 ppm), it is technologically easier, energetically more efficient, and economically more profitable to capture CO₂ in gases where it is present in high density, than directly from the atmosphere (with DACCS) [12, 13]. As a consequence, national and international prospective strategies often consider its deployment when less expensive alternatives (e.g. BECCS) are no longer possible, notably when the world energy system is already close to net zero [4, 11]. Although still in its infancy, DACCS is nonetheless the subject of active research efforts and significant technical developments, and its place in the energy system and climate change mitigation efforts still remains to be clearly defined [14, 15].

Among the technologies that could be applied to large point sources, there are three configurations of capture processes, illustrated on figure 1.4, differing by the moment at which the CO₂ is captured: pre-combustion (before combustion), post-combustion (after combustion with air) and oxy-combustion (after combustion with pure oxygen). The major advantage of post-combustion, which explains why it is the most widely deployed technology today, is its ability to retrofit an existing installation by adding a unit that treats its flue gases [17].

The product of all capture processes is high-purity CO₂ gas, which can then be compressed and transported by technically mature technologies similar to those developed for natural gas (pipelines, ships after liquefaction, etc.) [11].

INDUSTRIAL SECTORS AND POTENTIALS

A first use of CCUS consists in capturing CO₂ from fuel-powered power plants, which has been proposed as a solution for decarbonizing the electricity sector in countries with recent assets which considerable investment costs are not amortized yet [11]. In bioenergy with CCS (BECCS), *i.e.* when biomass is the source of energy, it allows achieving negative emissions by sequestering the CO₂ captured by the

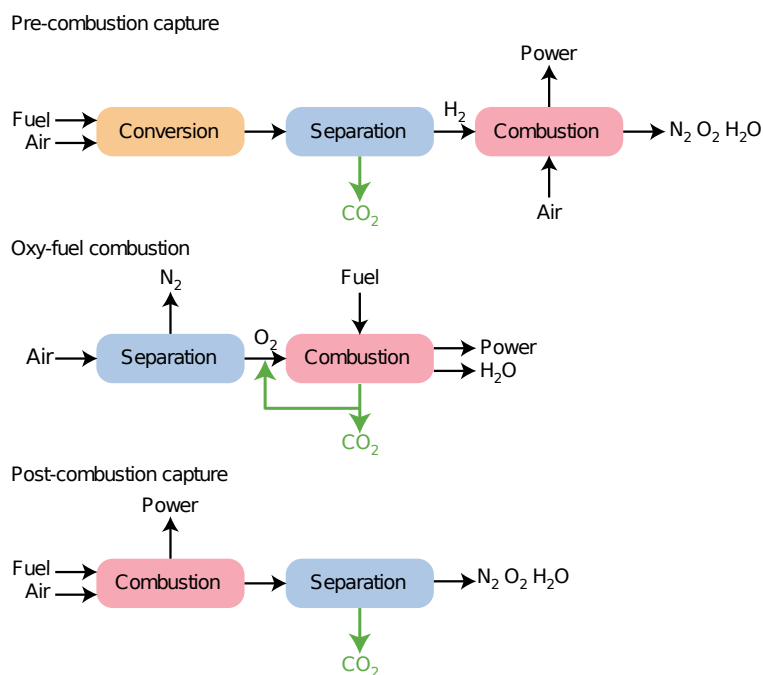


Figure 1.4: Carbon capture configurations. Adapted from Ref. [16].

biomass during its growth. Estimates of the potential for BECCS at the world scale vary between 3 and 20 gigatonnes of CO₂ (GtCO₂) per year [18], which are significant with respect to the 35 GtCO₂ emitted worldwide in 2021 [19]. In the underlying scenario of the SNBC, it is assumed that about 10 MtCO₂ yr⁻¹ would be captured with BECCS in France in 2050, compared to total territorial emissions of 80 MtCO₂eq the same year [9].

Heavy industry is another major field of application where CCUS represents part of the solution to decarbonize hard-to-abate emissions. CO₂ can be captured either from process emissions – inherent to the chemical reactions involved in producing certain bulk materials (e.g. cement kiln) or chemicals [20] – or from the flue gases following fuel combustion for industrial heat production. Direct emissions from the industrial sector (excluding emissions related to energy production) represent a quarter of global emissions (8 GtCO₂eq yr⁻¹), including 2.2 GtCO₂eq yr⁻¹ for cement production, 2.1 GtCO₂eq yr⁻¹ for iron and steel production and 1.1 GtCO₂eq yr⁻¹ from the chemical industry. The potential for decarbonization through CCUS is significant, as exemplified by the “Clean Technology Scenario” proposed by the International Energy Agency (IEA) in which a quarter of the industry’s emission reductions come from CCUS (the remainder being obtained from technical progress, efficiency gains and energy decarbonization) [21]. This industrial capture potential for the French industry in the SNBC is of 5 MtCO₂ yr⁻¹ avoided in 2050 [9], a volume that can be compared to an estimated maximal threshold of 24 MtCO₂eq yr⁻¹ based on the current state of the industry [22].

Finally, CCUS can play a role in facilitating the production of low-carbon hydrogen for use across the energy system and the industry. Although present in many decarbonization pathways, the demand for hydrogen is still today met almost entirely by unabated fossil fuels with only 0.7% produced from low-emission routes in 2021 [23]. CCUS could contribute to reducing emissions from existing hydrogen plants and provide a least-cost pathway to scale up new hydrogen production in a number of regions (compared to renewable energy for water electrolysis) [11].

Overall, as a result of both negative emissions and emission reductions, the contribution of CCUS technologies to the reduction of global emissions could be significant. It is illustrated by the different decarbonization scenarios of the IEA in which CCUS represents between 10 and 20% of the total

decarbonization effort [11]. Figure 1.5 shows the relative impact of CCUS (in orange) compared to other decarbonization options that need to be deployed simultaneously. It should be emphasized at this stage that CCUS is not a silver bullet that would allow to offset on its own the GHG emissions of a business as usual scenario.

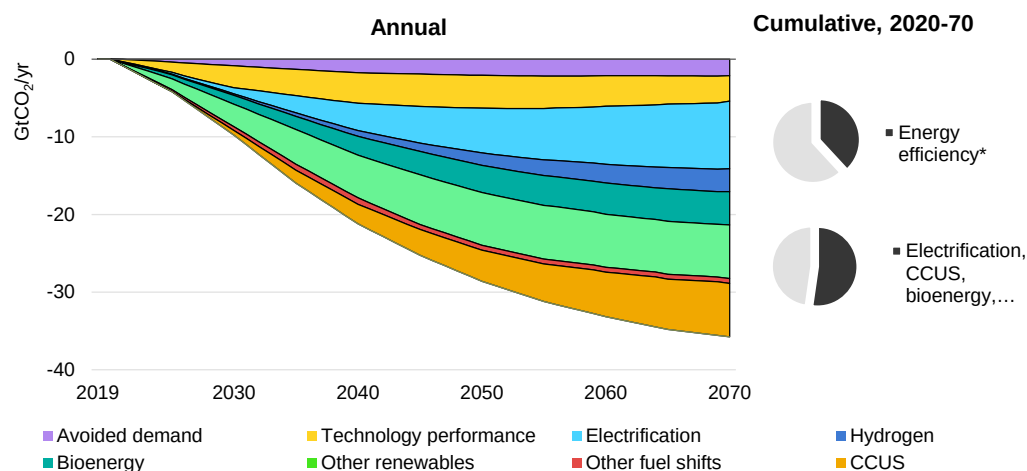


Figure 1.5: Global energy sector CO₂ emissions reductions by measure in the IEA “Sustainable Development Scenario” relative to the “Stated Policies Scenario”. Reproduced from Ref. [11].

CO₂ UTILIZATION: MARKETS AND POTENTIAL

Today, 230 MtCO₂ are used each year, mainly for the manufacture of urea as a source of fertilizer (130 MtCO₂) and as a solvent for enhanced oil recovery (EOR - 80 MtCO₂) [24]. As illustrated in figure 1.6, a number of CO₂-derived products and services can be envisaged, which could represent a significant part of the potentially captured CO₂ volumes.

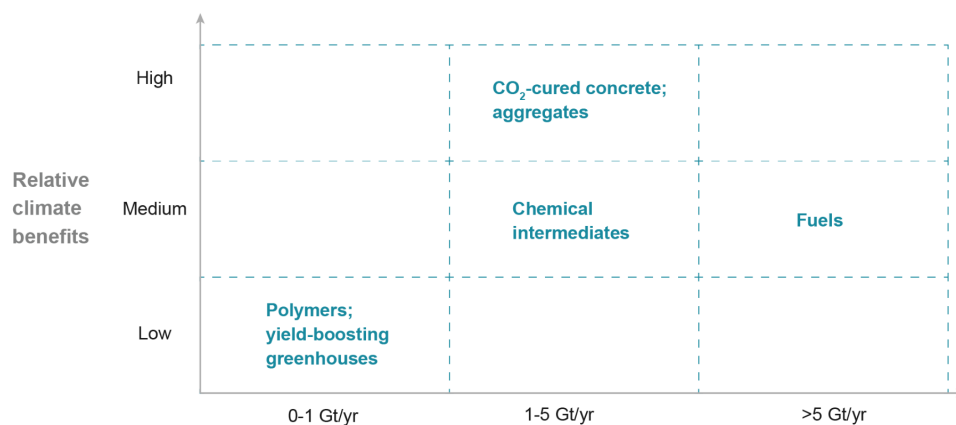


Figure 1.6: Theoretical potential and climate benefits of CO₂-derived products and services. Reproduced from Ref. [24].

However CO₂ utilization cannot cover all global emissions, and the climate benefits differ greatly between different products (e.g. synthetic fuels in turn emit GHGs during their use). In addition, the costs are generally higher than current production methods, making the deployment of all these products uncertain [24]. It is particularly the case, when the final product requires at least the amount of energy released by burning a fuel (e.g. synthetic fuels) [17]. Thus, despite its significant potential, CO₂ utilization can only represent a fraction of the contribution of CCUS technologies to the decarbonization of the world economy.

PERMANENT STORAGE

The objective of storage is to permanently immobilize the captured CO₂ in order to avoid its return to the atmosphere. Numerous methods have been considered (ocean storage, mineral carbonation), but as of today only geological sequestration has reached a sufficient level of maturity [6]. It consists in the injection of CO₂ into a deep underground geological reservoir of porous rock overlaid by an impermeable layer. The gaseous CO₂ is usually compressed before injection to transition to its superfluid phase with an increased density, which is retained if the reservoir depth is greater than 800 meters [17]. The main geological sites considered for CO₂ storage are deep saline aquifers and depleted oil and gas reservoirs [11].

The storage potential is still not fully known, but is estimated to be at least 2000 GtCO₂ in the world [25] and 1 GtCO₂ in France [26], which would be sufficient in view of the volumes that could be captured by 2100 in most decarbonization scenarios [25].

CURRENT STATE OF CCUS

Today, there are 30 operational CCUS facilities around the world with a combined capacity to capture up to 42.5 MtCO₂ each year [27], and with the first industrial facilities having been operated since the 1980s. Early CCUS projects focused on industrial applications where CO₂ could be captured at relatively low additional cost, and virtually all the CO₂ captured came from gas processing plants until the 2000s as shown on figure 1.7. The captured CO₂ was at first exclusively used for enhanced oil recovery (EOR), and is still today mainly dedicated to this use with only one quarter stored in depleted reservoirs or deep saline formations. While EOR has the potential to deliver some climate benefits on its own [6, 11], it is not one of the key applications of CCUS to get towards a net zero economy that were listed above.

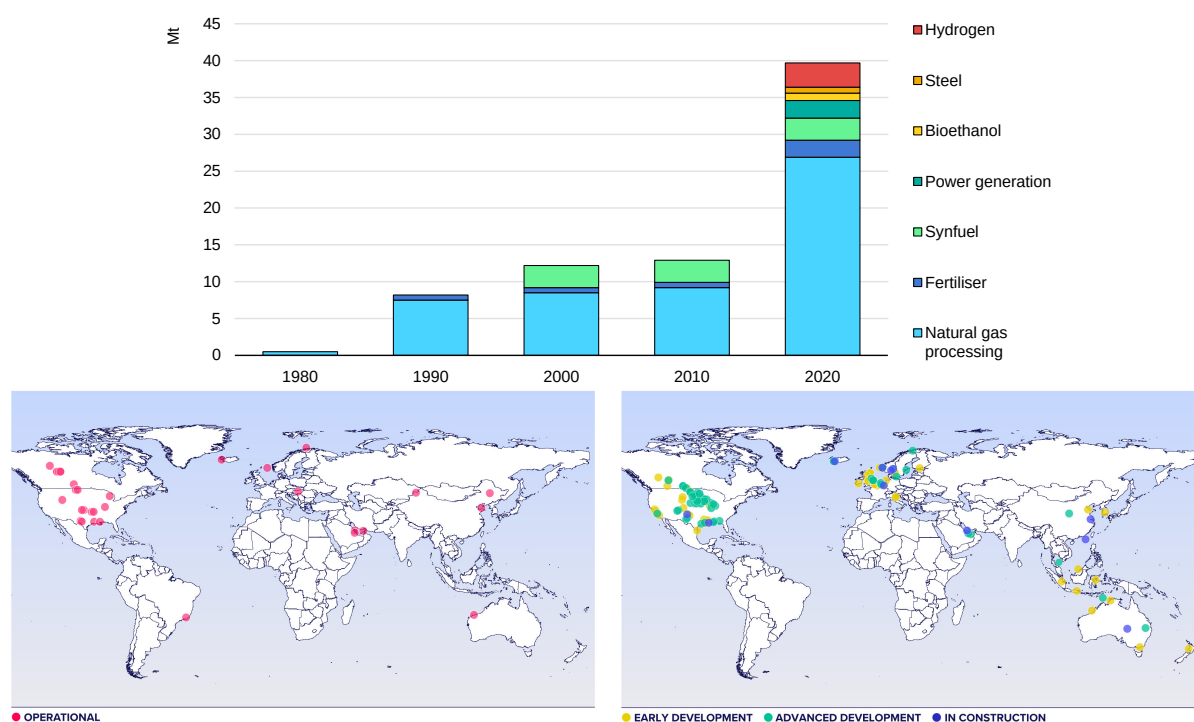


Figure 1.7: (above) Global CO₂ capture capacity by source and (below) world map of CCUS facilities at various stage of development. Reproduced from Ref. [11, 27].

As shown on figure 1.7, the deployment of carbon capture has been concentrated in the United States, with almost half of all operating facilities, due in large part to the availability of a CO₂ pipeline network (combined length of more than 8000 km), demand for CO₂ for EOR, and public funding programs [11]. The first European facility was commissioned in 1996, and the last decade saw CCUS facilities commissioned in other regions (e.g. China, Australia, and the Middle East).

CCUS has been the subject of renewed global interest and attention in recent years, with 10 MtCO₂ of facilities in construction and 100 MtCO₂ in advanced development [27]. Although the current CCUS capacity shows that a number of its technologies are mature and have already been deployed at an industrial scale, there is a gap between how many CCUS facilities are operating or planned, and what is needed in transition scenarios to provide a significant contribution to meet the Paris temperature goal [28]. In France, while a large number of laboratories and companies have been working on all aspects of the CCUS value chain – at the laboratory scale, in pilot projects and in demonstrators [29] – reaching the SNBC targets would require the development of concrete CCUS projects at the industrial scale.

COSTS AND BARRIERS TO THE DEVELOPMENT OF CCUS

The cost of capturing and storing one ton of CO₂ varies greatly depending on the capture technology, source quality, mobilized transportation infrastructure, storage infrastructure and scale of the project. According to a review on the state of the art of current installations [13], the cost of capture is typically comprised between 20 and 110 \$/tCO₂ for large point sources, with considerable variation depending on the CO₂ source as indicated on figure 1.8. Costs of the remainder of the CCS value chain also vary significantly, comprised between 1 and 15 \$/tCO₂ for transport and 1 and 30 \$/tCO₂ for storage.

Because of these significant costs, CCUS may simply not make any commercial sense in the absence of incentives or emissions penalties, especially when the CO₂ has no significant value as an industrial input [11]. Still, multiple sources are already economically viable in some regions, with respect to current trading schemes prices and existing or planned carbon taxes [30].

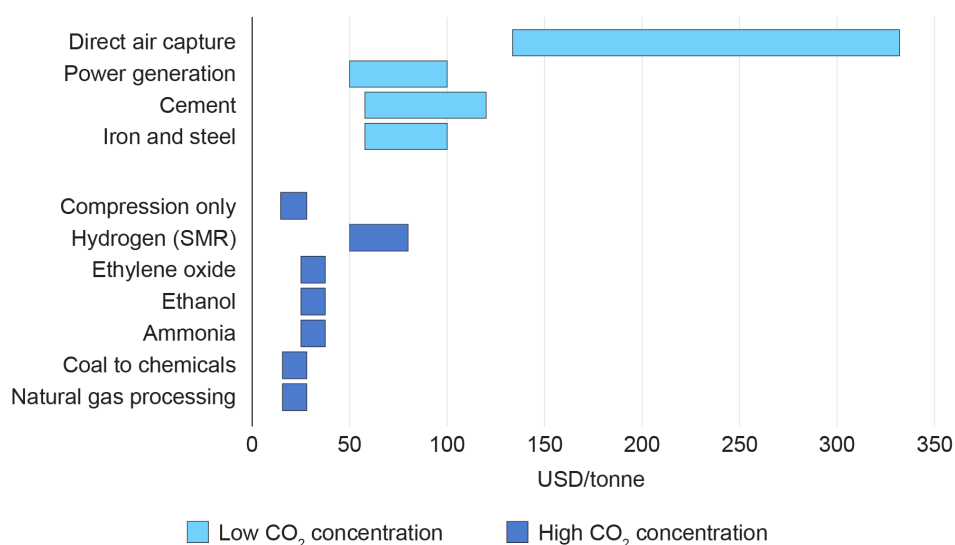


Figure 1.8: Levelized cost of CO₂ capture by sector and initial CO₂ concentration in 2019. Reproduced from Ref. [11].

The challenges to CCUS development are, however, not only technical and economic, with a number of other barriers to be overcome. We can cite the difficulty in securing investments, the lack of supportive policies offering long-term visibility, a legal and normative framework still under construction [6], and limited stakeholder engagement [31]. For governments which include CCUS in their decarbonization strategies, accelerating deployment requires a massive increase in government support, with a range of policy instruments being available [11].

1.1.3 Porous materials for CO₂ separation

Among the numerous challenges that would need to be overcome to scale up the development of CCUS, academic research in material science is mostly relevant for its contribution to cost reduction efforts.

Focusing on CO₂ capture, the most expensive part of the CCS value chain, I will now compare different technologies and introduce porous materials, encompassing the materials studied in this work.

ABSORPTION PROCESSES, MATURE YET COSTLY

Patented in 1930, the amine scrubbing process which is based on absorption is still today the most common CO₂ capture process. It relies on using a solvent with a high affinity for CO₂. Schematically, the capture is done in two steps shown on figure 1.9: the flue gas is first brought into contact with the solvent, which absorbs the CO₂, and then the solvent is regenerated in another compartment (the stripper) by raising its temperature to release the absorbed CO₂ [17]. Aqueous amine solvents (e.g. monoethanolamine or MEA) are the most widely used and deployed at an industrial scale on multiple large-scale facilities [6].

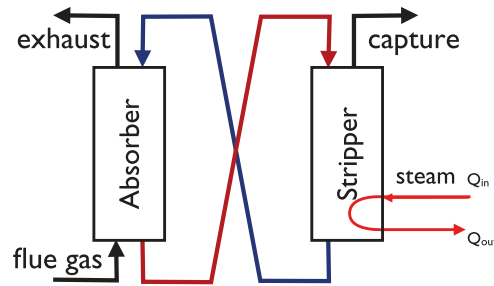


Figure 1.9: Schematic of a simple absorption process. Reproduced from Ref. [17].

Several limitations point to the need for better processes: the solvents are relatively unstable at high temperatures which restricts the quality of regeneration, their lifetime is limited by the amine decomposition and, most importantly, the large heat capacity of these solvents (related to that of water) is the primary cause of the energy penalty paid during regeneration [32].

This significant energy penalty is the main factor impacting the financial cost of capturing a ton of CO₂. It varies greatly depending on the nature of the flue gas to be treated and the specific installation, and is typically comprised between 200 and 400 kWh per tCO₂ captured. It corresponds to having to dedicate about 10-25% of the energy that a gas power plant produces to capture its own emissions [33].

POROUS MATERIALS

As only incremental improvements in overall process efficiency are anticipated for solvent-based processes [16], several capture technologies have been proposed to overcome these limitations. A number of promising approaches rely on porous materials, presenting within their structure voids or cavities called *pores*. A key property of these materials is their large specific surface area (*i.e.* the total surface area of a material per unit of mass) which is exploited in a number of important industrial applications such as gas adsorption or catalysis [34].

The pores can be of various shapes, sizes and constitute different networks. As it affects their properties, the porous materials are categorized based on their pore size in three groups by the International Union for Pure and Applied Chemistry (IUPAC) [35]. There are *microporous* solids with pores smaller than 2 nm in diameter, *mesoporous* solids with pore diameter between 2 and 50 nm, and *macroporous* solids with pores larger than 50 nm. Microporous and mesoporous solids are often grouped together as *nanoporous* solids. Some examples highlighting the diversity of this family of materials are shown on figure 1.10.

The majority of porous materials produced on a large scale today are based on purely inorganic or purely organic architectures. Some inorganic materials, such as zeolites, are particularly adapted to post-combustion, while some organic materials, activated carbons in particular, ideally operate in pre-combustion [36]. However, the characteristics sought are numerous in terms of performance, stability or operability in an industrial process, and no material is perfect in every respect [32].

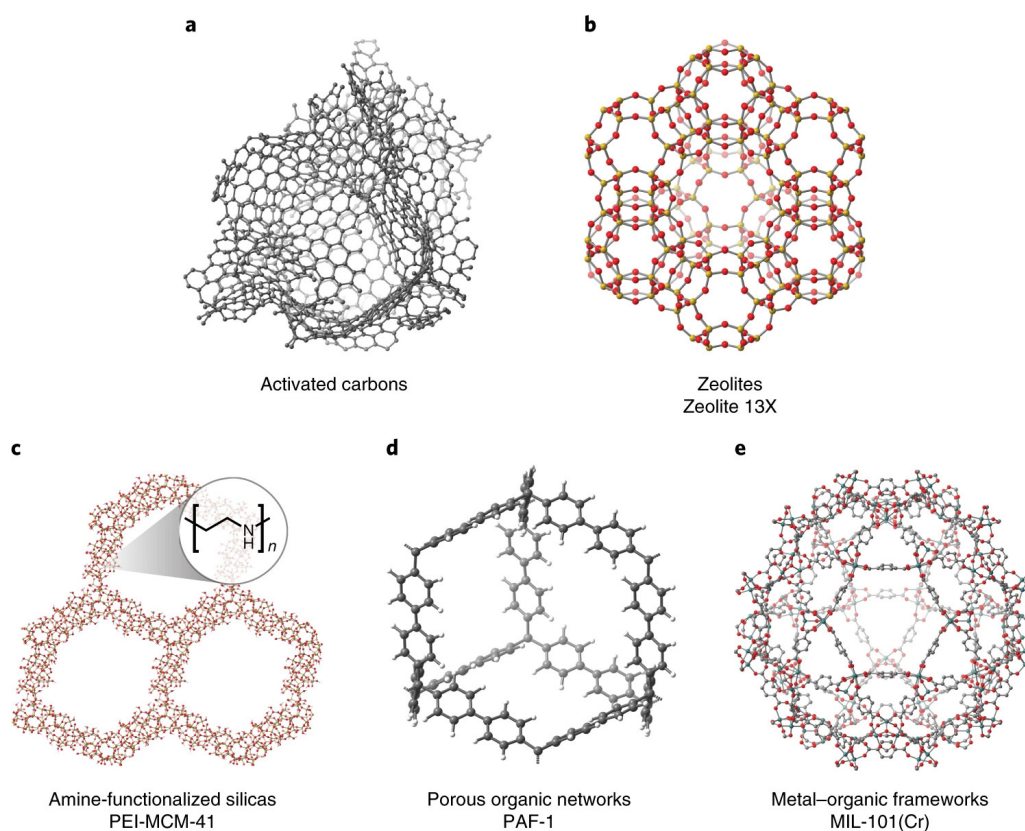


Figure 1.10: Illustrative examples of porous materials relevant for CO₂ adsorption. Reproduced from Ref. [16].

ADSORPTION

Adsorption processes relying on porous materials have received a growing attention for CCUS due to their potential to reduce the energy penalty of the capture process, in particular thanks to the lower calorific capacity of porous materials compared to aqueous solvents [16, 32]. A solvent-free process also enables a reduction in water consumption and may limit the environmental risks posed by the toxic compounds contained in most commercial solvents [17].

Different industrial processes exist, but schematically the gas to be treated passes through a column in which there is a “bed” (i.e. a coating of the walls) made of porous adsorbent. The bed can be fixed, as in figure 1.11, in which case the loading of the adsorbent and regeneration phases must be alternated cyclically, or mobile to allow for a continuous process [37]. Regeneration can typically be induced by heating the adsorbent to its optimum desorption (i.e. opposite of adsorption) temperature (*Temperature Swing Adsorption* - TSA) or by decreasing the pressure until the captured gas desorbs (*Pressure Swing Adsorption* - PSA) [32]. At the end of the cycle, the purified CO₂ is recovered while the porous materials, still attached to the walls of the adsorption column, remains in place.

Adsorption technologies have now successfully passed the scale of the demonstrator for large point sources [38]. Additionally, they are considered as a particularly promising option for DACCS, both technically and economically [39].

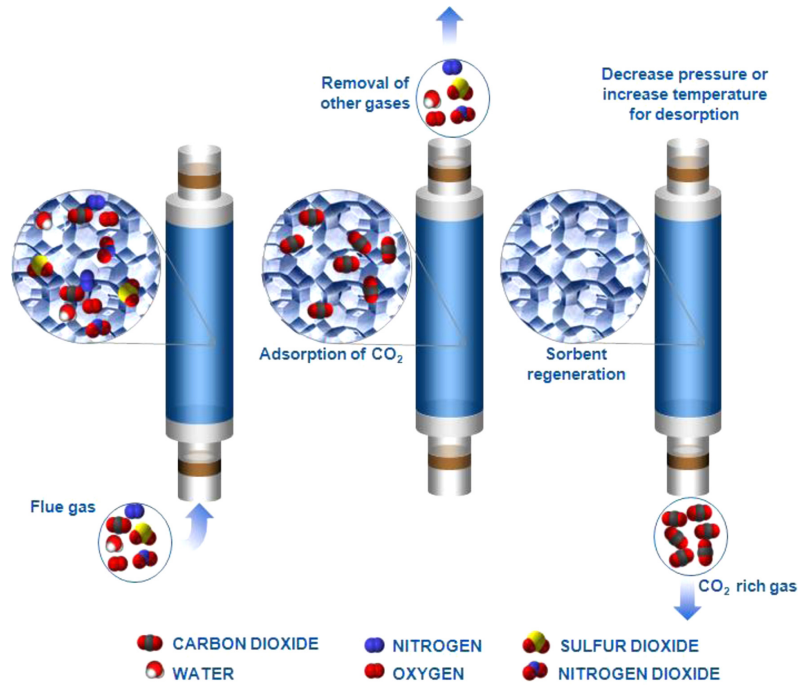


Figure 1.11: Schematic of a simple adsorption process with a fixed bed for CO₂ removal from flue gas. Reproduced from Ref. [40].

MEMBRANES

Other promising technologies for CO₂ capture in which porous materials are particularly relevant are based on membrane gas separation. Schematically this approach consists in separating different gases based on their difference in permeability in a membrane, as illustrated on figure 1.12 [17]. Compared to sorption processes, membrane-based separations represent an attractive option for energy-efficient operations as they do not require thermally driven regeneration of the liquid or solid sorbent [41]. The membrane can be made of porous materials similar to those used for adsorption processes, with inorganic membranes and mixed matrix membranes having received a lot of attention [42].

These technologies have initially been developed for natural gas processing and CO₂/CH₄ separation, and is deployed today in a number of operating industrial-scale gas separation membrane plants [43]. They are, however, not yet available commercially for CO₂ removal from flue gas, for which they are still at the research and development stage [6].

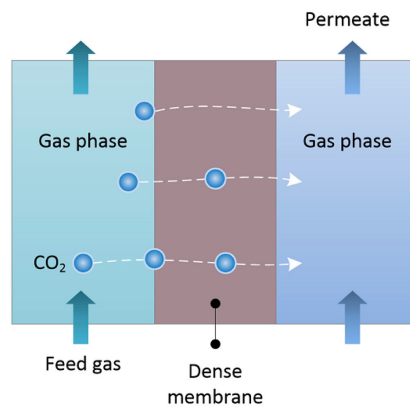


Figure 1.12: Schematic of membrane gas separation. Adapted from Ref. [43].

1.2 METAL-ORGANIC FRAMEWORKS

Now that we have seen how porous materials can be applied to CO₂ separation, I will introduce in this section the materials studied in this work, namely amorphous metal-organic frameworks. I will start with presenting metal-organic frameworks in general and their promises for CCUS, before introducing the specific materials studied (zeolitic imidazolate frameworks) and their phases of interest for this work (amorphous).

1.2.1 A versatile class of porous materials

Metal-organic frameworks (MOFs) are hybrid materials composed of inorganic nodes (clusters or metal ions) bridged by organic linkers to form three-dimensional architectures, often porous. First studied in 1989 by Richard Robson and coauthors [44], the term *MOF* was coined ten years later by Omar Yaghi's team to name these materials, along with the synthesis of a new framework called MOF-5 [45]. With its large permanent porosity and chemical tunability, the discovery of MOF-5 sparked interest in the community and led MOFs to be the subject of an intensive research effort for over 20 years. Figure 1.13 shows both the stellar increase in reported MOF structures and the extremely large specific surface area accessible through these materials, compared to alternative porous materials.

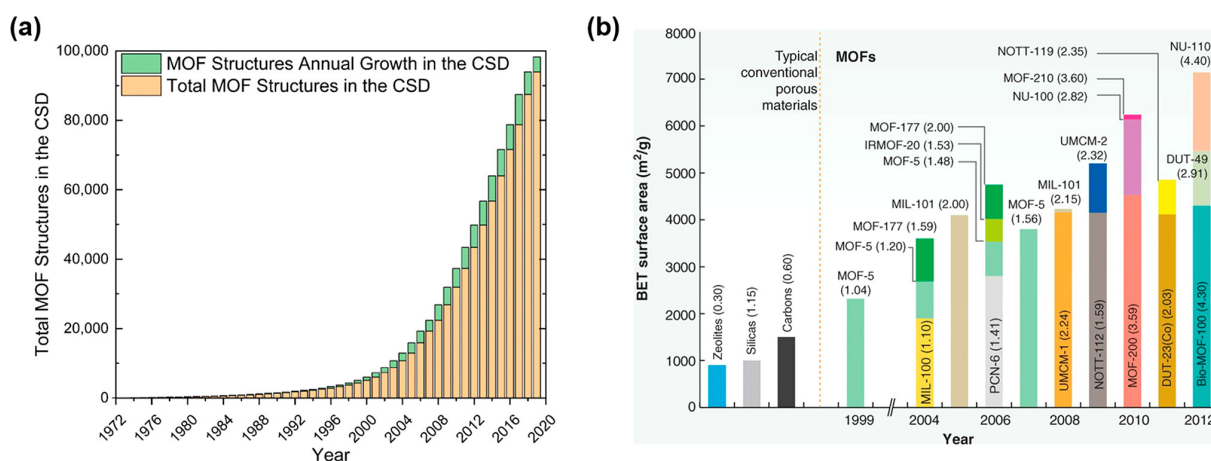


Figure 1.13: (a) Exponential growth in the number of structures reported in the Cambridge Structural Database (CSD) [46] and (b) progress in the synthesis of ultrahigh-porosity MOFs. Reproduced from Ref. [41, 47].

DIVERSITY AND TUNABILITY

The success of MOFs is largely due to the remarkable diversity of structures that can be built from the combination of numerous inorganic clusters and organic linkers, grouped together under the term *secondary building units*, and of which a small subset is shown in figure 1.14.

With the versatility provided by the coordination and organic chemistry, the number of potential structure is only limited by the thermodynamic and chemical stability of each combination, and also by the existence of a synthetic route to generate the porous phase of interest [48]. Figure 1.15 shows a few of the thousands of synthesized MOFs structures reported to date in the literature.

A MULTIPLICITY OF APPLICATIONS

This diversity of structures makes it *a priori* possible to synthesize “tailor-made” materials, aiming for sets of characteristics that traditional nanoporous materials (purely inorganic or organic) cannot achieve. In this “design to applications” approach, one aims at producing the best structure for a given functionality, which can be the optimization of a single metric (e.g. highest uptake of a specific gas [49]) or a combination of metrics [50].

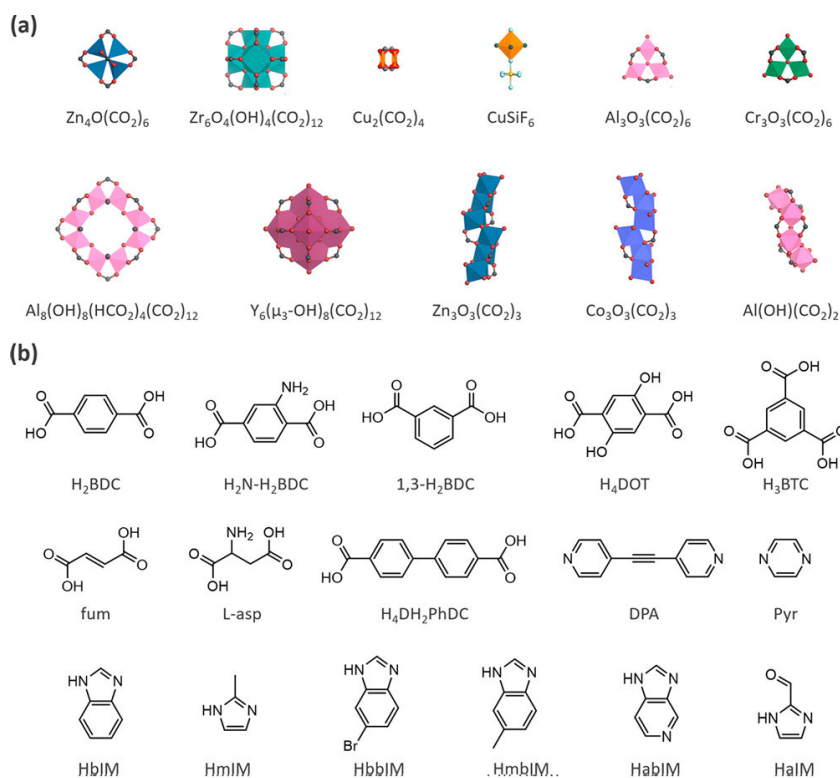


Figure 1.14: Examples of (a) inorganic clusters and (b) organic linkers. Adapted from Ref. [41].

MOFs have thus been proposed for applications in various industrial-scale processes [47] such as gas separation [51, 52] or catalysis [53]. Among these multiple applications, a number could contribute to the climate targets mentioned in section 1.1.1 outside of the CCUS realm. They have notably been proposed for gas storage of hydrogen and methane as an alternative to compression or liquefaction [54]. There has also been an increased interest in the use of MOFs in other energy-related applications, such as fuel cells, batteries, and supercapacitors [55]. They have also been proposed for other environmental applications, demonstrating potential toward their utility in air-pollution control [56], remediation of water pollution [57] and treatment of nuclear waste [58].

Although some MOFs have been produced at the ton scale by industrial companies, it is still a challenge to transition from laboratory preparation to industrial production and their development for practical applications is still ongoing [59].

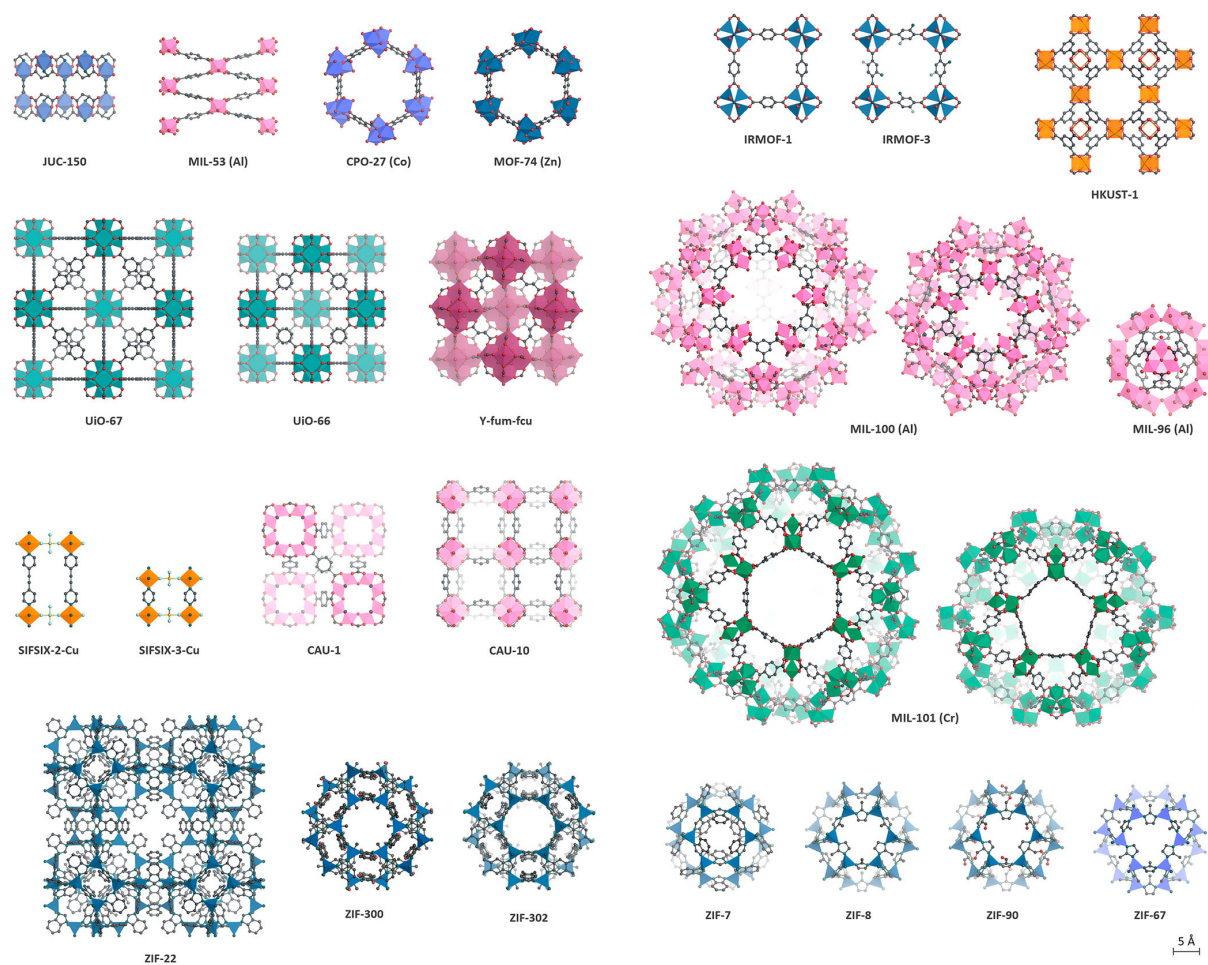


Figure 1.15: Examples of MOF structures scaled to accurately show relative size. Adapted from Ref. [41].

1.2.2 Novel materials for CO₂ separation

CO₂ ADSORPTION

Among their many applications, MOFs received a lot of attention for their application in CCUS. Their performances can be directly compared to other porous materials, as illustrated on figure 1.16. MOFs are particularly promising for CO₂ capture by adsorption due to their large surface area per unit volume, and their highly customizable pore sizes and chemical affinities [32]. This allows a level of control in a manner that is unfeasible for other classes of adsorbents, offering the ability to fine-tune the thermodynamics and kinetics of the CO₂ adsorption/desorption processes [60, 61].

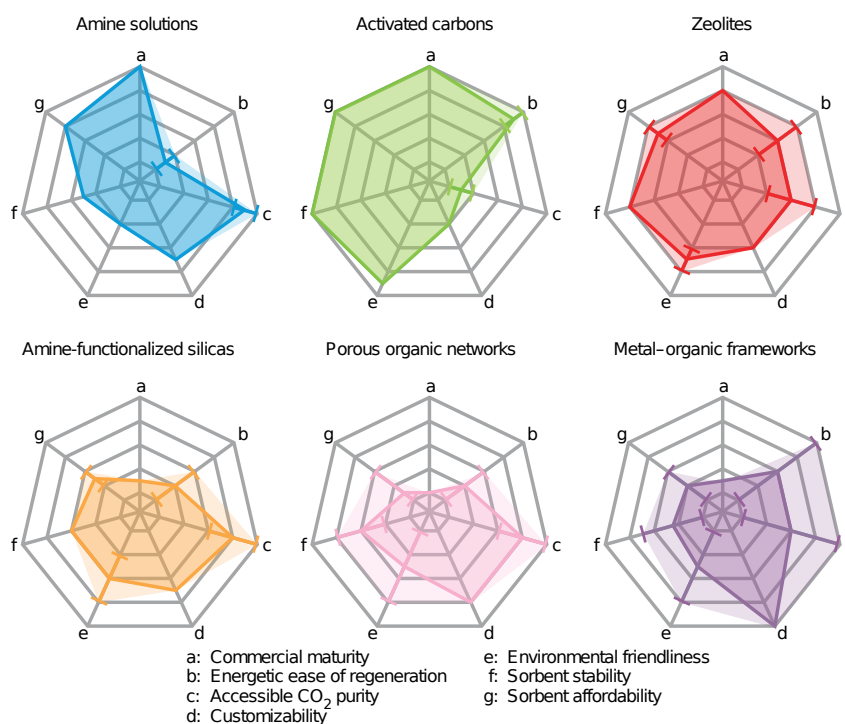


Figure 1.16: Radar charts for key sorbent selection criteria showing a qualitative assessment of key metrics for material selection in carbon capture applications. Bold lines indicate average, with error bars indicating typical variability. Reproduced from Ref. [16].

Additionally, the large choice of possible compositions makes it possible to customize MOFs depending on their use case, such as post-combustion or pre-combustion processes. It is also possible to optimize them for direct air capture, an application neither zeolites nor activated carbons can achieve effectively [36]. As it is highly unlikely that there will be a “one size fits all” adsorbent that could work in every application and process condition (pressure, temperature, gas mixture composition, CO₂ levels, etc.), the customizability of the MOF family makes them promising candidates [61].

DESIRED PROPERTIES FOR CO₂ ADSORPTION

A first research and development challenge is to keep searching for more efficient materials designed for specific uses, in particular through a better understanding of structure-property relationships. It will also be necessary to better take into account the operating constraints of capture processes [62]. The work performed during this PhD contributes to this research effort to discover and characterize new materials.

The quantities to be evaluated and improved for this are multiple. First, the working capacity, CO₂ selectivity and strength of the adsorbate–adsorbent interaction (i.e. heat of adsorption) greatly determine the performance of an adsorbent with respect to CO₂ capture, the amount of material needed and the

energy penalty [32]. Additionally, mechanical, thermal and chemical stability (especially resistance to hydrolysis) are crucial for extending the life of the material, especially because of the harsh conditions during regeneration. The study of mechanical properties constitutes an essential part of this thesis (see chapter 5).

In order to reach industrial scale, a number of challenges still need to be overcome in the optimization of the regeneration, recycling, and production processes (synthesis strategy, costs, availability of resources, feasibility of scale-up, etc.) [36]. Regarding the latter, an inspiring work has been conducted on a zinc-based framework (CALF-20) [63] which was used on a pilot plant simulating cement flue gases (1 ton of CO₂ captured per day) [64]. It required the production of one tonne of CALF-20, a large value compared to typical laboratory quantities, but still short of the what would be required for a typical cement flue gas capture plant (~ 200 tons).

MEMBRANES

Apart from adsorption processes, MOFs also have a role to play as new materials for membrane technologies with their well-defined pore sizes [62], either as pure MOF films or as fillers in a polymer matrix to create mixed-matrix membranes [41].

The use of MOFs to form membranes is particularly interesting for industrial processes carried out at high pressure (typically 20-30 bar) [36]. Exceptional gas separation performances were achieved for certain gas mixtures [41]. However, membrane technologies relying on MOFs require a similar, yet even larger, research effort before industrialization than adsorption technologies. To be applied at an industrial level, a membrane must, among other things, be mechanically robust and stable at operating conditions.

1.2.3 Zeolitic imidazolate frameworks

A SUBCLASS OF MOFs

Zeolitic imidazolate frameworks (ZIFs) are a subclass of MOFs and were first synthesized in 2006 [65]. ZIFs are built around tetrahedral single transition metal nodes such as Fe, Co, Zn, Cd or Cu, linked together by imidazolate (denoted Im) or functionalized imidazolate linkers, favoring the formation of tetrahedral topologies [66]. As the name suggests, the structures of ZIFs are closely related to those of zeolites, a class of porous crystalline aluminosilicates, with a structure built around a regular arrangement of SiO₄ or AlO₄ tetrahedra. In ZIFs, the angle M-Im-M between two metal centers (M) bridged by an imidazolate is typically 145°, a value similar to that found for the Si-O-Si angle in zeolites as illustrated on figure 1.17.

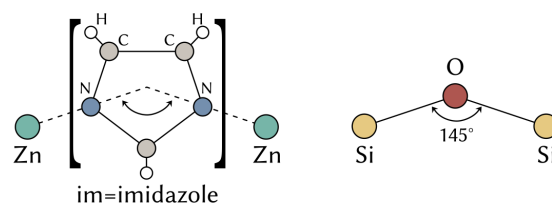


Figure 1.17: Illustration of the analogy between ZIFs and zeolite coordination. Reproduced from Ref. [67].

Out of the theoretically infinite number of topologies, ZIFs with more than 100 different topologies have been synthesized and structurally characterized, with some illustrated on figure 1.18. The topologies can be analogous to those found in the zeolite chemistry (which counts several hundred), but are not limited to them [66]. They are often denoted by a lower case three-letter code following the recommendations of the Reticular Chemistry Structure Resource (RCSR) Database [68] (e.g. **rho**) or with the uppercase three-letter code of the International Zeolite Association (IZA) [69] if applicable

(e.g. RHO). Like zeolites, the ZIF family displays rich polymorphism, *i.e.* different topologies for the same chemical composition, with more than 18 polymorphs reported for the $\text{Zn}(\text{Im})_4$ composition alone [70].

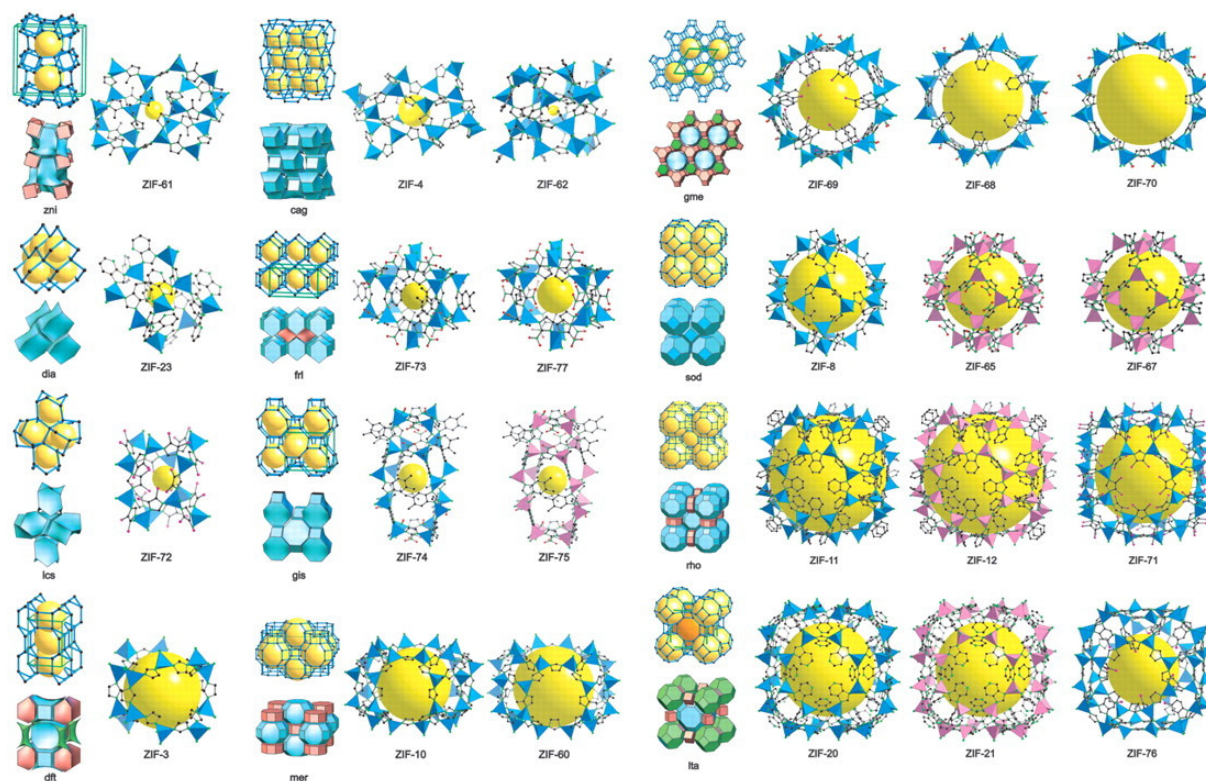


Figure 1.18: Examples of ZIF structures possessing different topologies and linkers. From left to right are represented the topologies and the crystal structures (space in the cage indicated by a yellow ball). Adapted from Ref. [71].

The strong interaction between the charged imidazolate linkers and the metal ions, along with the hydrophobic nature of the aromatic linkers, give rise to high chemical and thermal stability. Additionally, their tetrahedral structures lead to high mechanical and architectural stabilities [65].

The high robustness of these porous materials, in combination with the chemical tunability inherent to MOFs, make them particularly interesting industrial candidates in the context of gas adsorption or gas separation. In particular, they have been largely studied for CO_2 adsorption with some choices of functionalized linkers and pore shapes demonstrating good performances [32, 71]. They were also investigated in mixed matrix membranes for CO_2 separation, owing to their adjustable pore channels, unsaturated sites, and facile functionalization [42, 72].

SYSTEMS STUDIED IN THIS WORK

One of the key systems throughout most of this PhD will be ZIF-4, which is built up from Zn^{2+} metal nodes and imidazolate (Im) organic linkers and has a **cag** topology. As illustrated on figure 1.19, its building units are organized as $\text{Zn}(\text{Im})_4$ tetrahedra linked by Zn–N coordinative bonds.

I also studied other ZIF systems with different ligands and topologies, but always with Zn^{2+} metal nodes. Whenever it is the case, such as in chapter 4, I further describe the structures before commenting the results.

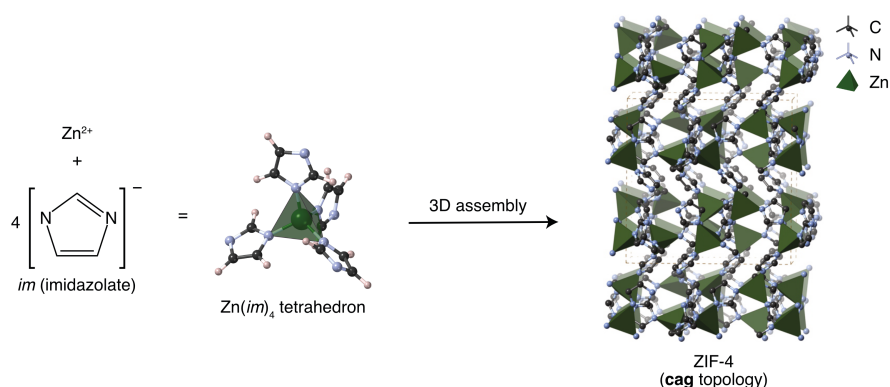


Figure 1.19: Representation of the assembly of ZIF-4 as a three-dimensional network of Zn(Im)₄ tetrahedra.

1.2.4 Amorphous metal–organic frameworks

BEYOND CRYSTALLINITY

Of the rapidly increasing number of studies of MOFs in the research literature, most are focused on perfectly ordered, crystalline structures, because of ease of experimental identification and characterization with common laboratory equipment. However, the dynamic nature of MOFs is a key characteristic of these relatively weakly bonded frameworks, compared to more traditional porous solids like zeolites — and accounts in a large part for their appeal, and some of their extraordinary chemical and physical properties. Throughout this family of materials, many authors have noted the common occurrence of large-scale flexibility under stimulation, the presence of crystallographic defects, and the possibility of correlated disorder [73].

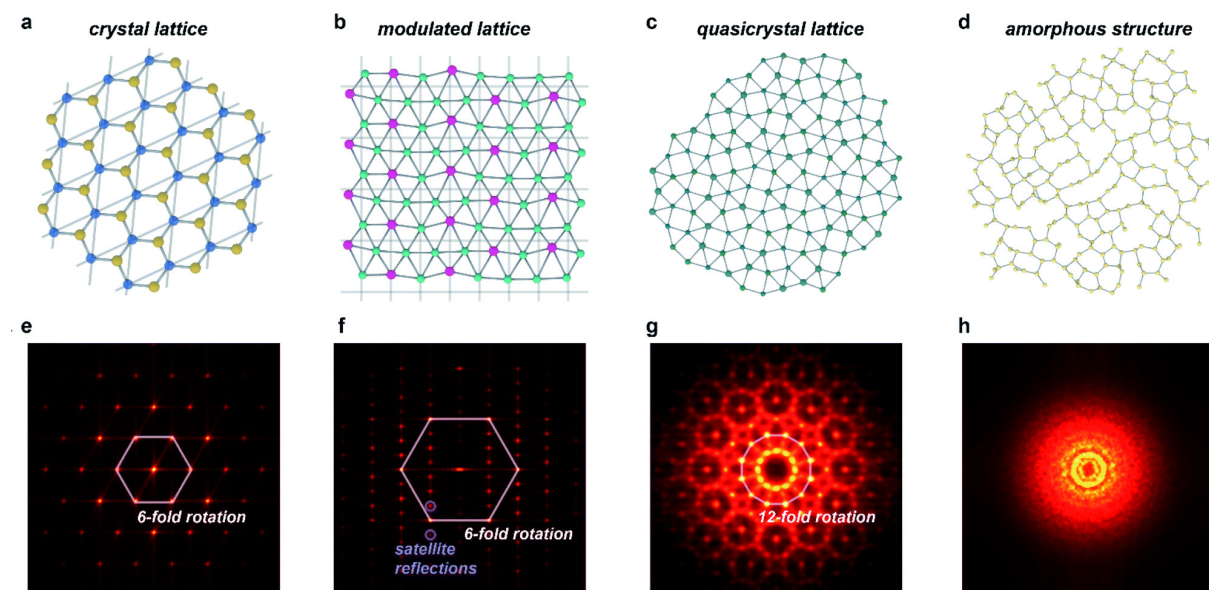


Figure 1.20: (a–d) Structures of periodic and aperiodic crystallography along with (e–h) their simulated diffraction patterns. Adapted from Ref. [74].

While the definition of MOFs does not restrict this term to crystalline phases [75], the reliance on crystalline databases in counting the “number of known MOF materials” offers a clear example of bias towards crystals [76]. Even among crystals, defined by the International Union of Crystallography (IUC) as “any solid having an essentially discrete diffraction diagram” [77], most reported structures are perfectly ordered systems with translational periodicity and which can be described by a unit cell. Aperiodic structures, i.e. lacking translational periodicity in at least one of the three Cartesian

dimensions, are only in the single digits in the Cambridge Structural Database (CSD) [46] among over 90 000 published MOF structures [74]. Figure 1.20 illustrates these different structures along with representative diffraction diagrams.

Although aperiodicity in MOFs is still a nascent field, in part because of the time-consuming structural characterization required and general lack of awareness of aperiodic structures in the community, it is an active and promising one. An illustration of this interest is the recent synthesis of TRUMOF-1, a topologically aperiodic MOF which consists of a periodically arranged assembly of identical metal clusters, connected uniformly in a well-defined but disordered fashion [78].

EMERGENCE OF AMORPHOUS MOFs

Recently, the number of non-crystalline MOF states (and porous coordination polymers) reported have seen a rapid expansion [79] as illustrated on figure 1.21. These include the recently discovered MOF liquids, MOF gels, and a large variety of glassy states and amorphous solids, defined as possessing no long-range order [80] and which therefore lack any translational symmetry.

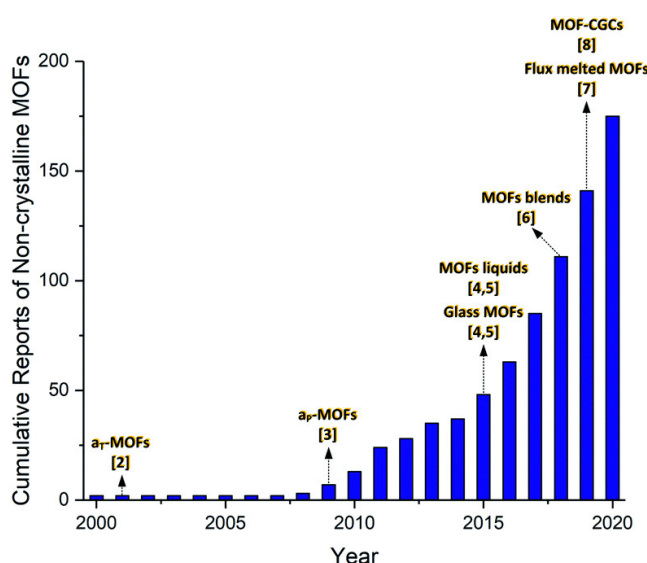


Figure 1.21: Reports in the field of non-crystalline MOFs. Reproduced from Ref. [81].

These amorphous MOFs (*a*MOFs) can be produced by a variety of physical or chemical routes [79]. The majority of studies were focused on the ZIF family (introduced in section 1.2.3) owing to their remarkable thermal stability [82], with a first work in 2009 on the amorphization of ZIF-8 under the application of pressure [83]. It was followed in 2010 by a work by Bennett et al. which led to the first “well characterized” structure of an amorphous MOF, obtained from the amorphization of ZIF-4 upon heating [84]. Amorphous ZIF-4 then became the prototypical example, later obtained by alternative formation routes [85–87], and is the only MOF-based entry included in a recently curated database of porous rigid amorphous materials out of 205 models of carbons, polymers, kerogens, and other material classes [76].

Even if only a few MOFs have been observed to be able to melt upon elevation of temperature without oxidizing or decomposing, there are multiple reported *a*MOF structures outside of the ZIF family such as UiO-66 [88, 89] or Fe-BTC [82].

AMORPHIZATION STRATEGIES

There are several ways to amorphize a MOF structure, as illustrated on figure 1.22. A number of routes are physical, with a first option consisting in submitting a MOF crystal to pressures in the MPa to GPa range with a diamond anvil cell (*pressure-induced amorphization* - PIA) [83, 85]. Another mechanical option is *ball-milling*, which is the process of milling a material inside a shaker mill with steel balls to create

amorphous structures from crystalline systems [87, 90]. *Thermal-induced amorphization* (TIA), is another option in which amorphization is caused by heating a MOF crystal in a furnace to temperatures between 300 and 700 °C [84, 91]. If heated further, some systems can undergo a phase transition to a liquid state [92] which can then be quenched to form a glass [86] by a procedure called *melt-quenching*. For some frameworks the phase transitions were found to happen at lower temperatures under a combined application of temperature and pressure, whether under static stress [93] or using *in situ* mechanical vibrations [94].

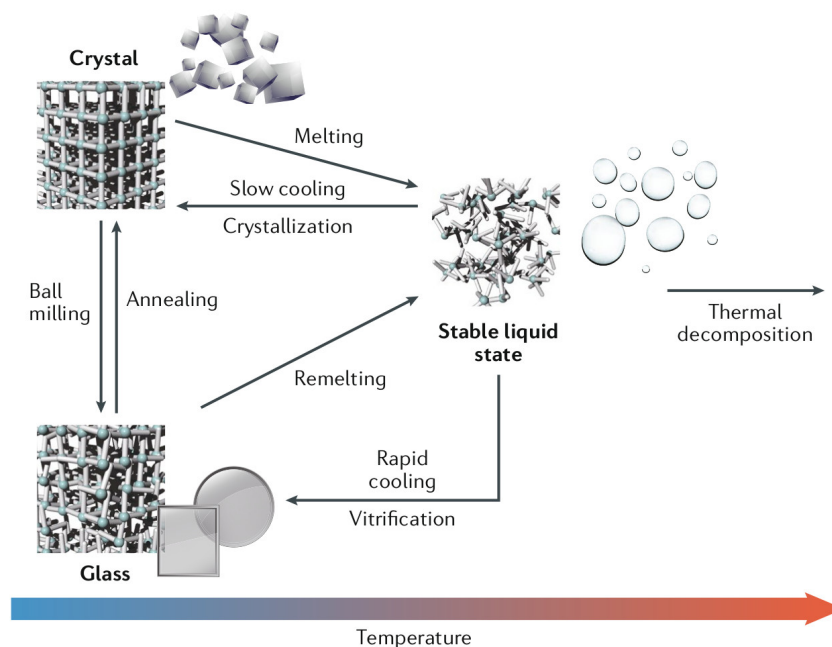


Figure 1.22: Different routes to the fabrication of MOF glasses. Reproduced from Ref. [79].

In addition to these physical routes, it is also possible to obtain *a*MOFs by *chemical treatment-induced amorphization*, via removing coordinated solvent, atmospheric water-induced amorphization, amorphization by ligand competition, and loading induced amorphization [81]. Direct synthesis of an *a*MOF has also been reported for certain frameworks [95]. It is also worth mentioning that MOFs can undergo *irradiation-induced amorphization*, e.g. under a scanning electron beam [96], even if this approach rather aims at proving the applicability of some MOFs in radiation environments (e.g. nuclear plants or aerospace) than at producing them [97].

Polyamorphism is frequently observed, as different productions routes may lead to distinct amorphous phases, identical in composition but with different physical properties (e.g. density or entropy) [98]. It is analogous to the polymorphism of crystalline materials discussed in section 1.2.3.

In addition, variation or alternative methodologies to melt-quenching can achieve different glassy states, such as MOF blends which are created by melting and quenching a mixture of two glass-forming MOFs [99]. It is also possible to combine crystalline and amorphous states, starting with flux melted MOFs which are glasses made from a glass-forming MOF and a non-glass forming MOF [100]. MOF crystal-glass composites (MOF-CGCs) constitute another possible structure in which a crystalline MOF is embedded within a glass MOF matrix [101]. It is also possible to combine MOF glasses with inorganic glasses to produce composite materials [102], such as MOF glass membranes [103]. Finally, the MOF gel state is another non-crystalline state of particular interest as it is the precursor to sol-gel MOF monoliths [104].

PROPERTIES AND APPLICATIONS

Non-crystalline states of MOFs possess useful physical and chemical properties distinct from those achievable in the crystalline phases, such as isotropy, the absence of grain boundaries, high transparency, and mechanical robustness. They can do so while retaining intrinsic advantages of crystalline MOFs mentioned in section 1.2.1 including high surface areas, tunable pore sizes, shapes and chemical functions [81].

These amorphous states could allow for greater ease of processing, notably by circumventing the performance drop due to the necessary densification of the MOF powders [105, 106]. By exploring novel material space, these disordered phases may provide new opportunities to attain chemical and physical properties that simply cannot be reached with porous crystalline frameworks [73]. In the domain of gas separation, an ordered crystalline state is not a requirement for gas uptake [107], and *a*MOFs provide opportunities for more robust materials that could operate under realistic process conditions, in particular for CO₂ separation [16, 108]. It is therefore possible to fabricate grain-boundary-free membranes from MOF glasses [109, 110], such as a mixed matrix membrane obtained by amorphization of ZIF-8 for CO₂/CH₄ separation [111], or a polycrystalline ZIF-62 membrane on a porous ceramic alumina support that underwent a melt-quenching treatment and which was evaluated for CO₂/CH₄ and CO₂/N₂ separation [103].

In addition to enlarging the material space, studying disorder in MOFs can be useful in better understanding the crystalline phases (e.g. the mechanism of crystallization [112]) and in creating alternative properties in porous materials with multiple studies focusing on “defect engineering” [113, 114] or “defective by design” strategies [115]. Thus, several *a*MOFs, including ZIFs [116], have been proposed as candidates for drug delivery using the amorphization of the framework for the controlled release of the drug [88]. Exploiting the phase transition between different amorphous and crystalline states has also been proposed for reversible long-term harmful substance storage [117], thermal energy storage and conversion [118] or even phase-transition memory units [119] exploiting changes in conductive properties [120].

1.3 ATOMISTIC MODELS OF AMORPHOUS MOFs

In balance with their promising properties, amorphous states are particularly challenging to characterize and their framework structures at the microscopic scale hard to determine. Indirect structural information can be available from diffraction experiments, but unlike for crystals, it cannot be solved into a nice periodic atomic structure as a matter of routine analysis. Moreover, the computational description of disordered materials is also more complex than that of crystals, firstly due to their lack of periodicity and symmetry [74]. As it is inherently impossible to reduce an amorphous material to a small finite set of atomic coordinates, each atomic structure should best be seen as representative of a plausible local configuration [121]. To complicate matters further, the structure and properties of many amorphous systems – including most glasses – depend on their formation route, calling for specific methodological developments of plausible numerical analogues to experimental production processes [122]. It is all the more difficult when the formation of the amorphous phase involves changes in coordination which severely limits the use of every method relying on a classical description of the interactions [123].

For these reasons, there are only very few atomistic models of amorphous MOFs – mostly glasses – available in the literature, whether from experimental or computational studies. It is unfortunate as the possession of atomistic models has the potential to significantly accelerate the rational development of materials [124], both to complement experimental techniques [125] and to predict novel architectures [126]. In this section, I review and compare the existing methodologies available for the determination of microscopic models of amorphous MOFs, as well as the structure they generated, assessing their strengths and weaknesses. This review has been published in *The Journal of Physical Chemistry C* (2022) [127], and is updated in the present section with the works published since.

1.3.1 Reverse Monte Carlo models

The determination of material structures from limited, indirect experimental data, is a classic example of an inverse problem. Reverse Monte Carlo (RMC) modeling is a general method for the resolution of such inverse problems, which in condensed matter aims to produce atomistic models based on available experimental data, in particular from X-ray or neutron-scattering experiments [128]. Starting from an initial configuration provided by the user, atomic positions are iteratively adjusted using a Monte Carlo algorithm to minimize the difference between calculated and experimental total structure factors. The minimization can be performed under a set of constraints (density, coordination, bond lengths or angles, etc.) which are added to the structure factor difference with customizable weights. No knowledge of the physics or chemistry of the system is required; for example, no interatomic potential is used in the conventional sense [129]. This makes RMC modeling applicable to any system, a very appealing property for new classes of materials [130]. The downside is that the thermodynamical consistence of the model is not guaranteed, as the optimized configuration could be physically unrealistic. The problem is also typically underconstrained, as a large number of different configurations could equally fit the experimental data.

For these reasons, RMC modeling was used to generate the first published model of an amorphous MOF, an amorphous ZIF-4 (*a*ZIF-4) obtained by temperature-induced amorphization [84, 131] – and is still, to date, the only technique that has been used to construct an amorphous MOF model from experimental data. This *a*ZIF-4 model was constructed from neutron and X-ray total scattering data collected at a synchrotron facility. In addition to this experimental data, it used density, connectivity and molecular geometry constraints to preserve the network topology of the initial configuration. Three initial configurations were tested: two crystalline polymorphs (ZIF-4 and ZIF-zni), and a continuous random network (CRN) model of *a*-SiO₂ adapted by substituting atom groups (see next section and figure 1.24c for details). As shown on figure 1.23, only the latter configuration allowed RMC refinements to capture the experimental data and resolve its structure, which was therefore confirmed to be highly

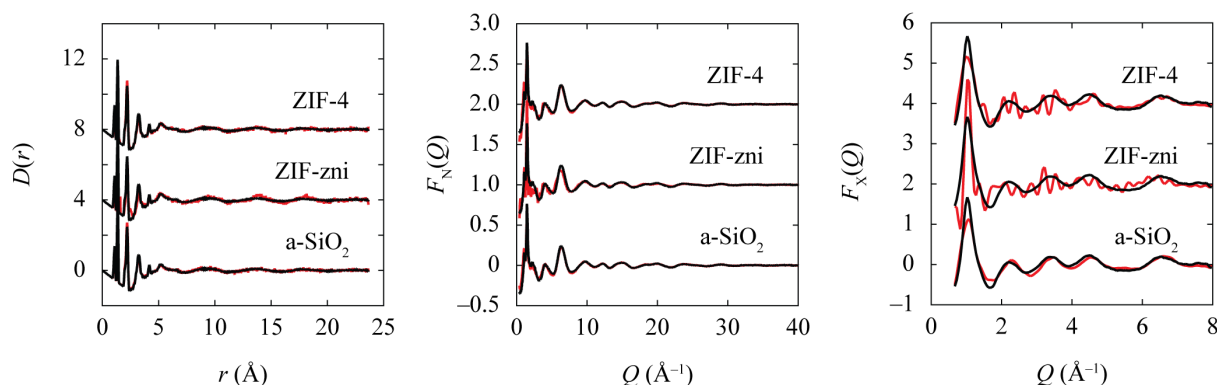


Figure 1.23: RMC fits (red) to experimental data (black) of the differential pair correlation function $D(r)$, neutron and X-ray total scattering functions $F_N(Q)$ and $F_X(Q)$. Calculated with three initial configurations: ZIF-4 (top), ZIF-zni (middle) and an $a\text{-SiO}_2$ CRN (bottom). Reproduced from Ref. [84].

disordered and not crystal-like. Additionally, the very process of RMC modeling with different initial configurations showed that the system undergoes a reconstructive (i.e. involving bond breaking and forming events) phase transition during amorphization, and hints that the framework topology is markedly different from the crystal phases.

Later works by Keen and Bennett on different ZIF systems have adopted the same method and improved it by inputting experimental values of the density, as obtained from pycnometric density measurements. It was first extended to produce a model of ZIF-8 (featuring 2-methylimidazolate ligands instead of imidazolate) amorphized by ball milling [132], starting from the same CRN model with a change of organic ligand. A reconstructive phase transition was also demonstrated. Then it was applied to amorphous phases of ZIF-4 produced by two other routes, which were modeled and compared to temperature induced amorphization: melt-quenching [92] and ball milling [87]. The atomistic models were found to be near-identical, with indistinguishable short-range order. To have more insight into the structural changes during the melt-quenching procedure, an intermediate model of the liquid state was also fitted to X-ray data, although the accuracy of RMC for such complex liquids is not firmly established and might depend strongly on the constraints used.

1.3.2 Continuous random networks

Even though MOFs are chemically more complex than inorganic phases, the microscopic modeling of amorphous MOFs can draw inspiration from models of long-studied disordered materials, such as silica. The structure of amorphous silica has been consensually modeled as a continuous random network (CRN), and there is a large body of work on this topic [133]. Random networks possess a significant degree of local order, while allowing sufficient bond distortions to have some freedom in the medium-range order, and (as desired) exhibit no long-range order [80]. If they have no broken bonds in reference to their ideal connectivity, they are said to be continuous. CRNs can be generated with a variety of approaches and possess different structures which can be validated by looking at the agreement of computed properties with experimental data: the most commonly available data is the total pair distribution function, or radial distribution functions (RDF). Just like perfect crystals, CRNs should be considered as idealized, yet particularly insightful, structures of the real-world materials they represent [134].

The first CRN model of an amorphous MOF was constructed for ZIF-4, on the basis of the structural similarities between ZIF-4 – $\text{Zn}(\text{Im})_2$ – and amorphous silica $a\text{-SiO}_2$ [84]. They both share a similar short-range order with the tetrahedral coordination of the metal ion and a node–ligand–node angle of 145° . They also display corresponding features in their RDFs, while their numerous crystalline polymorphs exhibit several shared topologies. Therefore, a CRN model of $a\text{-SiO}_2$ was adapted by substituting Si and

O to Zn and Im (Im = imidazolate), respectively, as represented in figure 1.24c. This experimentally consistent [133] *a*-SiO₂ CRN had been obtained by expanding an *a*-Si model (adding O atoms between each Si as illustrated on figure 1.24b), which was itself produced following the Wooten–Winer–Weaire (WWW) method. This widely used procedure for tetrahedrally bonded single-component networks starts from a crystal and proceeds to minimize an energy function using a simulated annealing algorithm that performs successive steps of bond rearrangements shown on figure 1.24a [135, 136].

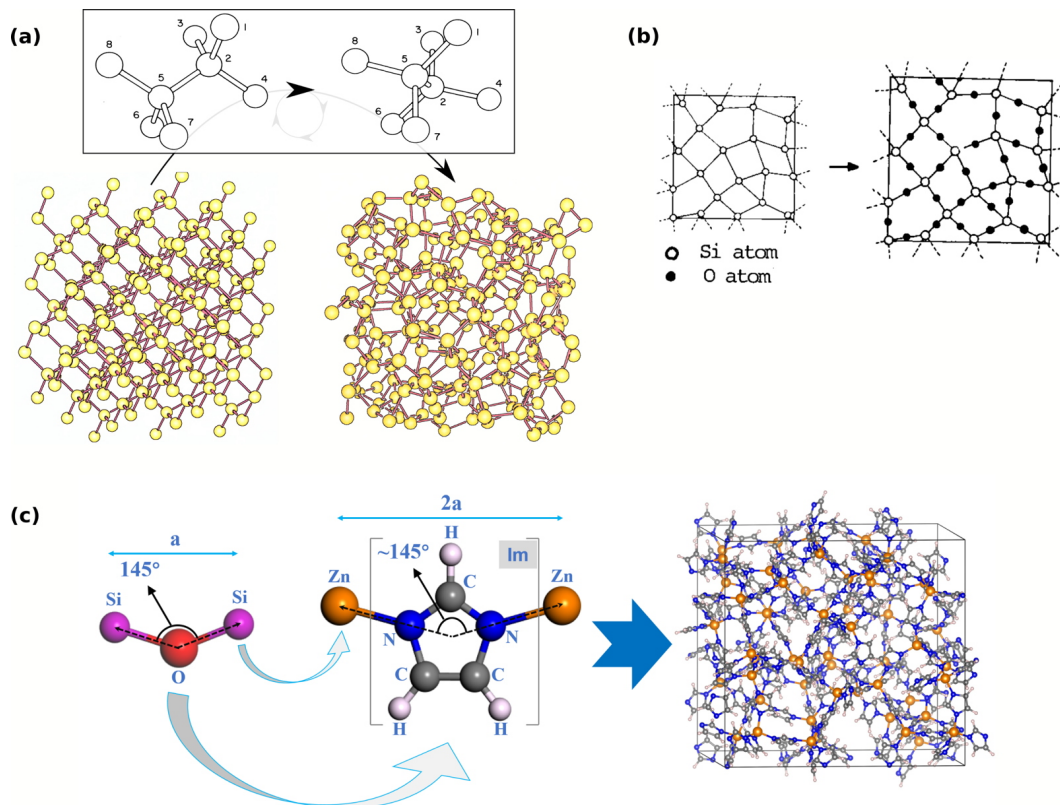


Figure 1.24: (a) Creation of an *a*-Si continuous random network (right) following the WWW procedure, starting from a crystal (left) and performing successive bond rearrangements (inset) [136]. (b) Expansion of the *a*-Si CRN into an *a*-SiO₂ model [137]. (c) Expansion of the *a*-SiO₂ model into a model of *a*-ZIF, where the Si–O–Si linkage is replaced by Zn–Im–Zn [138]. Adapted from ref. [136–138].

Used as an initial configuration for the RMC refinements mentioned in the previous section [84], this first CRN paved the way for CRNs to be considered as representative of *a*ZIFs atomic structure. A similar construction procedure starting from a different *a*-Si CRN was used for the creation of an *a*ZIF-4 model, which was studied after a density functional theory (DFT)-based geometry optimization [139]. The *a*-Si model was constructed following a method predating WWW that starts from an initial centered cubic system with quasirandom coordination before also minimizing the energy, albeit with alternative bond rearrangement and minimization procedures [140]. Although this method was eclipsed by WWW which was more successful at generating large systems of arbitrary size [135], it has the virtue of generating fully coordinated CRNs which possess no memory of the initial crystalline phase. The resulting *a*ZIF model was validated by comparing its RDF with experimental data, and was sufficiently large (918 atoms) to realistically calculate the electronic structure, interatomic bonding and optical properties. Unlike other amorphous ZIF models, it is fully coordinated by design and is of lower density than the crystal. This surprisingly low density is caused by the enlargement of the *a*-Si cell before the substitution procedure as displayed on figure 1.24c, where an arbitrary – and seemingly excessive – factor of 2 was applied. The elastic behavior of this model was studied in a later work by successive steps of isotropic deformation of the cell and geometry optimization. The mechanical properties were

computed, as well as the evolution of the electronic and optical properties under compression [141]. An insulator-to-metal transition leading to a novel phase is claimed to be observed under extreme compression, but the apparent breaking down of the organic ligands questions the physical validity of these simulations.

This *a*ZIF CRN model can easily be expanded to other materials of the ZIF family, by substituting the organic ligands and metal nodes to investigate their influence on derived physical properties. In particular the change in electronic and optical properties were studied for ZIF-4 and MAF-7 (featuring 1,2,4-triazole ligands) with alternating Li/B metal nodes [138], ZIF-62 (imidazolate and benzimidazolate ligands) for various ligand ratios [142], and ZIF-4 with halogenated imidazolates (H atoms substituted with Cl or Br) [143]. When available (i.e. only for one ZIF-62 system with a given ratio), the system was validated by comparing the RDF with experimental data, but this could not systematically be performed. The physical realism of the CRN models obtained is therefore not systematically demonstrated.

1.3.3 Relying on crystalline models

Because of the difficulties of directly modeling amorphous phases, some research groups have tried to address this issue by *ad hoc* adaptation of modeling strategies designed for crystalline states. One such example is the creation of disordered models of UiO-66, MIL-140B and MIL-140C, three zirconium-based MOFs, by incorporating defects into the crystalline model through several possible pathways [89]. Those pathways, initially devised based on chemical intuition, were selected to display a small enough energy penalty to be thermodynamically accessible and lead to an experimentally plausible change of lattice constants. NMR (Nuclear magnetic resonance) chemical shift calculations of the defective structures derived from each pathway were performed based on DFT, and the NMR spectra were compared to experimental data. As several pathways led to a better agreement than the perfect crystalline model, it was inferred that some of these defects are present in the amorphous structure.

Another possible strategy, which aims not only at highlighting the presence of defects but rather at generating amorphous models, consists in simulating the phase transition from a crystalline MOF using classical molecular dynamics. Molecular dynamics (MD), further detailed in section 2.1, reproduces the time evolution of molecules and materials by numerically integrating Newton's equations of motion, based on the knowledge of atomic interactions at a given level of theory, and can be performed at varying conditions of temperature and mechanical constraints. It is therefore a way to mimic *in silico* the experimental formation routes, such as melt-quenching, by imposing adequate thermodynamic variables such as pressure or temperature. Not only does this approach generate amorphous systems, it also provides detailed knowledge of the underlying microscopic mechanism causing amorphization.

The most commonly used type of MD simulations for crystalline MOF phases is classical MD, where the interatomic potential is evaluated as an analytical function of the atomic positions, called the force field. That force field is optimized to reproduce the structure and dynamics of the framework, based on experimental data or quantum chemistry calculations (more details in section 2.3.2). Although classical MD simulations are routinely used for crystalline MOFs [144, 145], they cannot describe changes in the electronic state of the atoms. In particular, they are unable to simulate bond breaking or reformation and thus cannot simulate reconstructive phase transitions (i.e. crystal-to-crystal or crystal-to-amorphous processes in which the coordination changes).

However, some authors have attempted to use such classical MD models to study the amorphization of MOFs. For example, Ortiz et al. showed that while the classical force field could not be relied upon to describe the nature of the amorphous phase, it could still be useful to study the mechanical stability of the crystal before amorphization, and determine the onset of the phase transition [146]. Ortiz performed the first computational study on the pressure-induced amorphization (PIA) of ZIF-8, by simulating the crystal at various pressures in a constant-stress ensemble (N, σ, T), which allowed to estimate

the amorphization pressure by identifying the point at which the phase transition occurs, illustrated on figure 1.25. Increasing the pressure above this threshold numerically leads to a new phase, the physical reality of which is not clear: it can be seen as a hypothetical amorphous ZIF-8 system under the constraint that no bond breaking takes place during amorphization. The same approach was also used in two separate studies, in one for illustrative purposes only [98] and in the other as a validation experiment of a newly developed force field [147]. In the latter, the final amorphous system was validated by comparing the structure factor to experimental data. However, the underlying assumption of the non-reconstructive nature of this pressure-induced amorphization has yet to be directly confirmed, e.g. by *in situ* measurements. It is in stark contrast with other studies that found ZIF-8 amorphization by ball milling and melt-quenching to be reconstructive [123, 132].

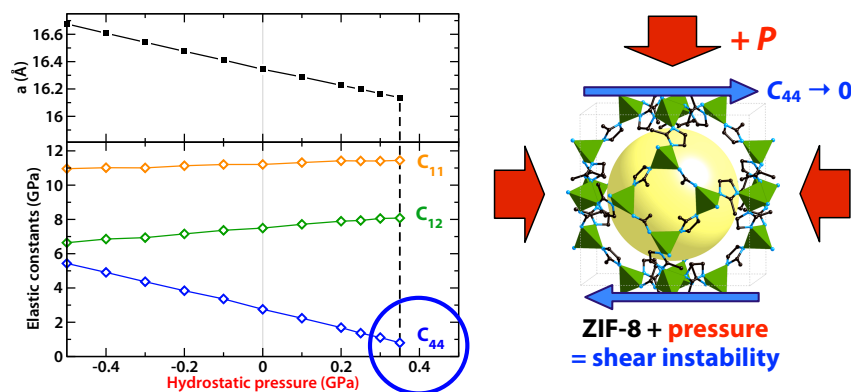


Figure 1.25: Evolution of the unit cell edge length and elastic constants of ZIF-8 under hydrostatic pressure, from classical molecular dynamics simulations, showing the onset of amorphization at $P = 0.35$ GPa, where the shear modulus C_{44} goes to zero. Adapted from Ref. [146].

Finally, Bhogra et al. developed another approach to gain insight into the amorphization process by studying the instability of the crystalline phase [148]. They combined geometry optimization calculations based on DFT and phonon-spectral analysis to investigate the amorphization pathways of MOF-5, a MOF comprised of ZnO_4 tetrahedra bonded with benzene dicarboxylate ligands. Starting with a strained crystal, they proceed by finding its unstable phonon modes (if any) to distort the structure in order to have the atomic displacements forming linear combinations of these modes, before performing a final energy minimization at fixed cell shape and volume. At sufficient strain, this last step leads to amorphization which manifests itself as an internal structural rearrangement. Although unique in the study of amorphous MOFs and performed in the zero-Kelvin limit, this approach has the benefit of hinting at the microscopic mechanism for pressure-induced amorphization – even though pressure and temperature are not explicitly present.

1.3.4 *Ab initio* molecular dynamics

Unlike classical MD, *ab initio* molecular dynamics (AIMD) is a method that allows a full description of the electronic state of the system at the quantum chemical level and can describe the formation and breaking of chemical bonds. It is therefore highly suited for the modeling of reconstructive phase transitions. AIMD, of which there are several “flavors”, combines the modeling of the equations of motion of the nuclei and the quantum nature of the electrons and is further described in section 2.2. More computationally demanding than classical MD, AIMD can only simulate phenomena at smaller time and length scales. However, using modern high-performance computing resources, it is tractable for MOFs with a few hundred atoms in the unit cell, such as most ZIFs, for times ranging from tens to hundreds of picoseconds.

The first AIMD simulations in the field of amorphous MOFs studied the melting and subsequent amorphization of ZIF-4 by quenching [92]. Starting from a single unit cell of the ZIF-4 crystal, several

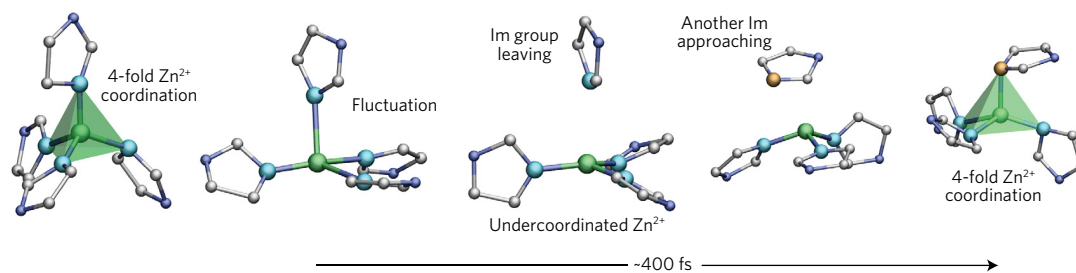


Figure 1.26: Visualization of a representative imidazolate (Im) exchange event in the microscopic mechanism of ZIF-4 melting, as observed by *ab initio* molecular dynamics. Reproduced from Ref. [92].

distinct simulations were performed in the constant-volume (N, V, T) ensemble with temperatures ranging from 300 to 2250 K, and adequate volume to reproduce the experimentally measured densities. This procedure did not aim at generating a glass model, but rather at identifying the melting transition and studying the microscopic mechanism involved. By presenting a representative imidazolate exchange event at the origin of bond rearrangements, figure 1.26 exemplifies the atomistic insight permitted by AIMD, looking at structural and dynamical details. Additionally, AIMD was used to investigate the thermodynamics of melting and characterize the generated liquid ZIF, in synergy (and good agreement) with *in situ* variable temperature X-ray and *ex situ* neutron pair distribution function experiments performed in the same study. The same procedure was subsequently performed on two other networks with different topologies: ZIF-zni, chemically identical, and ZIF-8, composed of different ligands [149]. As the details of the DFT methodology are largely independent from the topology, the chemical similarity of the frameworks ensured a smooth transferability. By computing the melting temperature of each framework and comparing it to its experimentally determined decomposition temperature, this second work helped explain why some frameworks are experimentally observed to melt while others collapse before melting.

While particularly insightful into the melting dynamics, these two studies did not explicitly generate atomistic models of ZIF glasses. This was later completed by a subsequent work simulating the entire glass formation procedure, through melting and quenching, which highlighted the distinct structural properties of the glasses compared to both the liquid and crystalline phases [123]. Three ZIFs crystals – ZIF-4, ZIF-8 and SALEM-2 (which features imidazolate ligands like ZIF-4, but has the same topology as ZIF-8) – were first melted at 1500 K, before being quenched to 300 K with a cooling rate of 50 K/ps. Because the high computational cost of AIMD puts strong limits on the system size, and makes it unfeasible in this case to study larger supercells, 10 quenching simulations were performed for each material to reduce the impact of finite size effects and get a statistically representative description of the glasses. We should note, however, that the computational cost also limits the total simulation time, and means that the cooling rates attained are several orders of magnitude higher than any achievable in the laboratory [80]. We note that although this is an inherent limitation of any molecular dynamics simulation, it is more pronounced for *ab initio*.

The use of the constant-pressure MD simulation in the (N, P, T) ensemble would prove a potential improvement of these works, as it would allow the joint study of both dynamical and thermal effects without having to input the system density. However, *ab initio* simulations of such systems are notoriously challenging to equilibrate, as these frameworks respond very sensitively to small external stimuli and thus to small deviations in the computation of the stress tensor [150]. As of today, no computational scheme has been demonstrated to accurately describe the equilibrium between the three phases involved (crystal, liquid and glass) and the respective values of their density.

However, AIMD was used to help study the effect of pressure on various types of amorphization processes, through the application of high pressure, high temperature, or both. Widmer et al. studied the

low-temperature melting of two ZIFs, ZIF-4 and ZIF-62, under the application of hydrostatic pressure [93]. Multiple simulations were performed in the constant-pressure (N, P, T) ensemble around the thermal amorphization temperature with various pressures in the 0.1 to 5 GPa range. Similarly to the aforementioned melting studies [92, 149] this work gave insight into the melting process under pressure, but did not aim at providing an atomistic model of the final, fully equilibrated molten frameworks.

Finally, two works tackled pressure-induced amorphization by running AIMD simulations with increasing pressure, going above the amorphization onset, with a different methodology. Erkartal et al. developed an *ad hoc* technique that proceeds by running successive short out-of-equilibrium isoenthalpic-isobaric (N, P, H) MD runs at various pressures. Neither the system enthalpy nor temperature are actually controlled in the process, making it somewhat akin to an energy minimization algorithm. The first work studied the MOF-5 amorphization under hydrostatic pressure by investigating the change in structural and electronic properties and provided the first amorphous MOF-5 atomistic model ever reported [151]. The second one investigated pressure-induced amorphization of ZIF-8 both under hydrostatic and uniaxial stress. The resulting amorphous ZIF-8 was obtained without bond-breaking, and the method was validated by comparing the RDF with experimental data [152].

1.3.5 Reactive force fields

Despite its chemical accuracy and ability to simulate reconstructive phase transitions, AIMD significant computational cost limits its use to small systems on rather short time scales (hundreds of ps) and all but prohibits its use for high-throughput screening. Reactive force fields are empirical force fields that possess connection-dependent terms, enabling the simulation of bond breaking and reformation. Compared to *ab initio* methods, they trade accuracy for lower computation cost [153]. They are further described in section 2.3.3.

Their use to study amorphous MOFs is so far primarily focused on melt-quenched ZIF glasses. The systems were simulated using ReaxFF, a flavor of reactive force fields which interatomic potentials are functions of bond order, itself calculated from interatomic distances. This was made possible by the development of a reactive force field conceived for the study of Zn-Imidazoles complexes in aqueous, validated for these systems with *ab initio* data [154]. This ReaxFF force field was then used to generate amorphous ZIFs, after a limited preliminary validation on crystalline structures [155]. We note that this force field was neither originally developed – nor subsequently shown – to accurately reproduce the geometry of the Zn(Im)₄ tetrahedra, key to the framework properties.

In a first work, three ZIF crystals, ZIF-4, ZIF-62 and ZIF-77 (2-nitroimidazolate ligands), were heated above melting temperature before being quenched in the constant-pressure (N, P, T) ensemble as illustrated on figure 1.27. The heating/cooling rates were of 96 K/ps, higher than the AIMD melt-quenching work [123]. The inexpensiveness of the method allowed to simulate a ($2 \times 2 \times 2$) supercell, limiting the finite size effects. The approach was validated for ZIF-4 by comparing the RDF to experimental data and several properties to the first *ab initio* work on *a*ZIF-4 [92]. Compared to AIMD, the ReaxFF simulation yielded the same heat capacity and reproduced the same relationship, albeit more pronounced, between temperature and the undercoordination of Zn nodes. However, unlike ZIF-4 glasses later obtained by an AIMD melt-quenching simulation [123] which preserved the density (1.2) and porosity of the crystal, the ReaxFF glass was of significantly higher density (1.6) and lost its porosity.

This melt-quenching procedure with ReaxFF was then replicated on various ZIFs in further works, albeit with a slower heating/cooling rate of 24 K/ps, to study properties that would otherwise be prohibitively expensive with AIMD. An amorphous ZIF-62 model was generated to study the fracture toughness of the glass by inducing a precrack in an enlarged ($2 \times 6 \times 4$) supercell before a stepwise elongation [156]. It was validated by comparing to experimental data the RDF and multiple mechanical properties, i.e. Young modulus, Poisson's ratio and fracture toughness. A subsequent study performed equivalent simulations

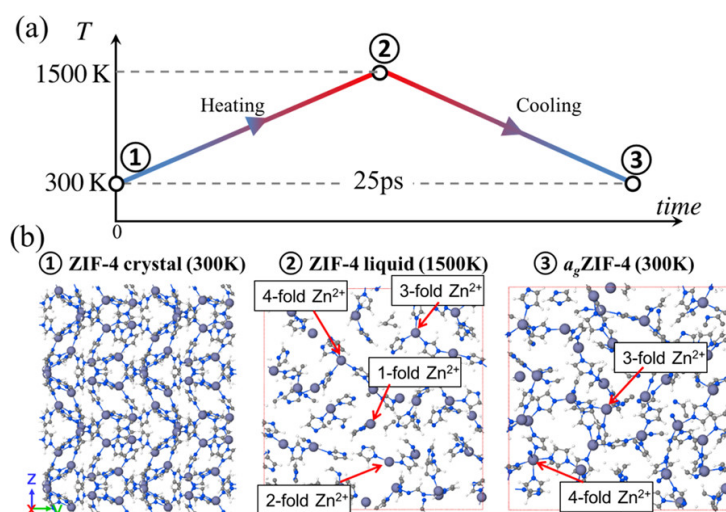


Figure 1.27: Representation of the melt-quenching process applied to ZIF-4 using the ReaxFF reactive force field. (a) Evolution of temperature over time. (b) Successive snapshots at three different times, in the crystal, liquid, then glass states. Reproduced from Ref. [155].

for ZIF-4 and ZIF-76 (mix of imidazolate and 5-methylbenzimidazolate ligands), before investigating the structural origin of the fracture behavior [157]. Yet another work computed the thermal conductivity of amorphous ZIF-4, ZIF-62 and ZIF-8, which were validated by comparison with experimental values [158]. The glass was shown to have a higher conductivity than the crystal, a very unusual relation, and the atomistic models were key to investigate the structural origin of this phenomenon. In another study, ReaxFF was used to simulate an irradiation process on both ZIF-4 crystal and glass models [159]. Finally, the obtained atomistic models were used, along with experimental data, to develop a topological constraint model which predicted the glass transition temperatures of any ZIF sharing the topology of ZIF-4 (cag) with an arbitrary mix of three ligands (imidazolate, benzimidazolate and 5-methylbenzimidazolate) [160].

In addition to this large body of work on melt-quenched ZIFs glasses, an earlier ReaxFF-based force field, initially developed for the interaction of glycine with a copper surface [161] and not validated for MOFs, was used to study the mechanical amorphization of three copper based MOFs [162]. These frameworks, chosen to contain non-accessible regions in their crystalline form, were subjected to shear or compressive deformations performed in the constant-pressure (N, P, T) ensemble. At moderate strain levels, they displayed an enhancement of their porosity, made possible by the breakage of metal-linker bonds which lead to partial amorphization.

1.3.6 Polymerization algorithms

Although classical MD cannot be used to simulate a reconstructive phase transition, it can still play a role in the generation of atomistic models using simulated assembly/polymerization-based modeling. Polymatic, a generalized simulated polymerization algorithm, was first developed for amorphous polymers and later used to generate amorphous MOFs following a well-defined procedure illustrated on figure 1.28. Starting from a low-density random packing of the building units of the amorphous material, i.e. the metal nodes and organic linkers for MOFs, successive steps of bond formation and structural rearrangement are performed. Bond formation is only allowed between predefined reactive sites and considered when two sites are within a defined cut-off distance. Structural rearrangement at turns involves energy minimizations and MD steps in the (N, V, T) or (N, P, T) ensemble. When no further bonds can be formed, the structure is annealed using a multistep MD protocol that applies for a limited time artificially high pressure to compress the system to a reasonable density [163]. As the

bonds are at all time well-defined, classical force fields can and are employed for energy minimizations and MD runs.

The first amorphous MOF generated with Polymatic is the well-studied ZIF-4, of which 5 atomistic models were generated to sample different regions of configuration space [164]. The validation of the approach was limited to the comparison of the density and pore volume fraction to experimental values.

A more comprehensive study by Sapnik et al. modeled for the first time two MOFs, Fe-BTC and Basolite F300, one of its commercial forms [82]. As illustrated on figure 1.28, they contain two sorts of nodes, trimer units (FeO₆ octahedra that cluster around a shared oxo-anion) and tetrahedral assemblies (4 assembled trimers via an organic linker), and 1,3,5-benzenetricarboxylate anions as linkers. Before this work, their atomic-scale structures were unknown, and they were previously being described as either disordered, amorphous or nanocrystalline. *Ab initio* methods are not an option due to the considerable number of atoms (more than 10,000) needed to describe such systems, and no reactive force fields are available for their chemical compositions. UFF4MOF, the extension of the Universal Force Field parametrized for the description of MOFs [144], was used in this study after validation on trimers and linkers with DFT. As the node ratio was unknown, three models were built: a short-range order model (SRO) containing 100% trimers, a mixed model (MIX) containing a 50/50% mixture of trimers and tetrahedra, and a medium-range order model (MRO) containing 100% tetrahedra. Each model was built 5 times and properties were averaged. Guided by RDF similarity and pore analysis, the authors concluded that two of these models could be considered representative of the atomic structure of Fe-BTC and Basolite F300. From this they deduced a structure–property relationship between the degree of tetrahedral assembly and porosity. A subsequent study explored the influence of defects on the structural properties by generating nine amorphous models with the composition of Fe-BTC using various node ratios (SRO, MIX, MRO) and levels of defects. [165] These two works on two carboxylate MOFs exemplify how the comparatively low computational cost of this approach, along with the versatility of classical force fields, make it viable for the generation and investigation of various disordered structures, including outside of the well-studied ZIF family.

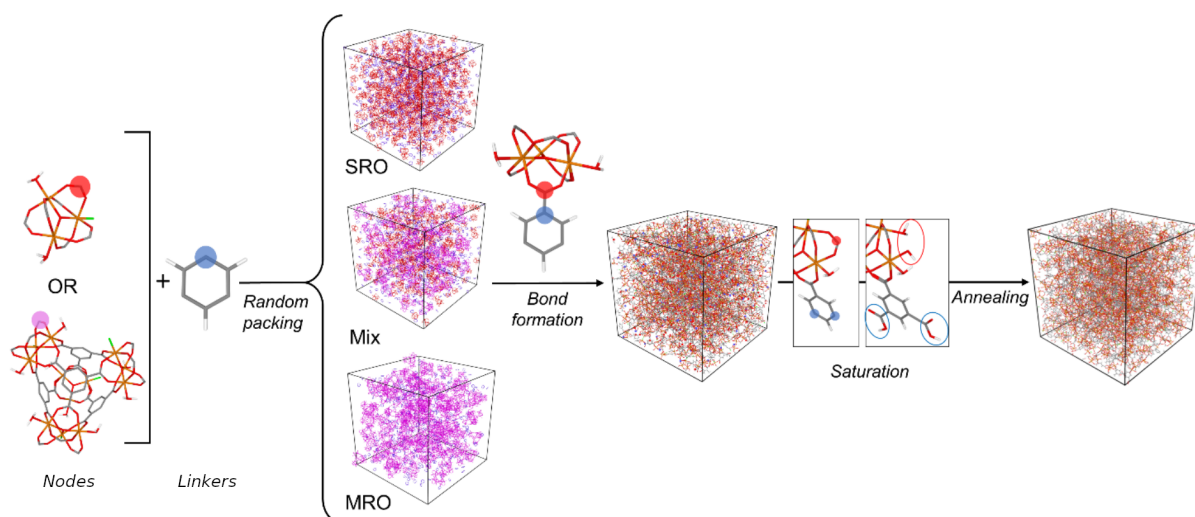


Figure 1.28: Representation of the procedure used to build three amorphous models (SRO, MIX and MRO, see text for details) of Fe-BTC with the Polymatic method. Adapted from Ref. [82].

CONCLUSIONS AND PERSPECTIVES

In this introductory chapter, I introduced the need for negative emissions to reach our climate targets, and how carbon capture, utilization and storage could be one out of multiple options that should simultaneously be applied to limit the increase in temperature. Among the multiple challenges to overcome, a significant research effort goes into reducing the energy penalty, in part by looking for new materials that could be used in less energy-intensive processes.

Metal–organic frameworks are a large family of porous materials which have been proposed for this task. There is an increasing interest in the amorphous states of MOFs, which notably yield the opportunity of increased robustness. Exploring the material space constituted by these amorphous states could lead to much desired new materials for CO₂ separation, and would benefit from having access to the atomistic models of numerous *a*MOFs.

However, the determination of the *a*MOFs framework structures at the microscopic scale is difficult. We reviewed and compared the existing methodologies available, based on both experimental data and numerical simulations, which are Reverse Monte Carlo methods, continuous random networks, classical and *ab initio* molecular dynamics, reactive force fields, and polymerization algorithms. From that review, it is clear that in most cases, the problem of modeling is mathematically underdetermined, and it is difficult to arbitrate between different possible models. This is due to the relative lack of available experimental data, with only indirect structural information obtained from diffraction measurements.

In order to improve the quality of amorphous models in the future, I think there is a clear need for wider studies, integrating many different experimental techniques, in order to provide *in situ* data, for example by spectroscopic methods: infrared and Raman, NMR, etc. [166] In addition to providing direct insight into the nature of the amorphous phases of MOFs, such data could be used as a benchmark to test the different types of microscopic models generated. Databases of amorphous porous materials could then be expanded, along the lines of what has been done for years for the crystalline phases, and help accelerate efforts to model these systems [76].

I also conclude that there is, in the existing literature, a lack of direct and in-depth comparison of the models. In particular, their geometrical, physical and chemical properties have not been systematically compared against each other. While the generating methods vary a lot (some are purely mathematical, some rely on physical or chemical insight, some perform direct molecular simulations), the models produced have very different characteristics that should be systematically computed and contrasted: density, porosity, framework coordination, topology, etc.

Finally, it appears to me that no single modeling method can currently yield an accurate microscopic representation of the MOF glasses, which suggests the development of multi-scale modeling strategies, combining the strength of the different methods already available. I have tested and commented some of these strategies during my PhD.

MOLECULAR SIMULATION METHODS

2.1	Molecular dynamics simulations	39
2.1.1	Space and time scales	39
2.1.2	Principles of molecular dynamics	40
2.1.3	Thermodynamic ensembles	41
2.2	Ab initio molecular dynamics	44
2.2.1	Unifying MD and quantum calculations	44
2.2.2	Density functional theory	45
2.3	Force fields	48
2.3.1	Motivations and principles	48
2.3.2	Classical force fields	49
2.3.3	Reactive force fields	50
2.4	Machine-learned potentials	53
2.4.1	Principles and construction	53
2.4.2	Neural network potentials	55
2.4.3	Equivariant message passing neural networks	58
2.5	Characterizing structural properties of amorphous models	62
2.5.1	Local order	62
2.5.2	Bulk properties	64
2.5.3	Topology	65
2.5.4	Characterizing liquids	67
2.5.5	<i>aMOF</i> , a Python library	69



Since its emergence in the 1950s, molecular simulation has seen an ever-growing use in the fields of physical, chemical, and materials sciences, to the point that today numerical simulations constitute a field of research in their own right and are sometimes referred to as *in silico* experiments [167]. Complementary to experimental techniques and pen-and-paper theoretical models, they can shed light on some microscopic mechanisms that experimental measurements cannot grasp, for example accessing very short space and time scales or studying experimentally inaccessible conditions. Computational tools offer a better understanding of multiple mechanisms which can assist experimental synthesis works [125], and have been massively used to study gas separation in MOFs [168], notably for CO₂ separation [169].

In addition, molecular simulations offer an opportunity to predict novel architectures, with considerable effort devoted to enumerate all the plausible MOF structures constructed by the assembly of a large diversity of inorganic and organic building blocks [126]. These hypothetical MOFs, along with the development of large databases of experimental MOF structures [170], make it possible to search for a MOF with a set of required properties by building on the study of structure-property relationships and the development of various high-throughput computational screening methods [126, 171]. The past decade has seen an increase in the use of data-driven techniques, with the application of artificial intelligence (AI), in particular, machine learning (ML) [124], notably for the selection and/or prediction of MOFs with good performance for CO₂ separation [172, 173]. This computation effort has the potential to significantly accelerate the rational development of materials, where the traditional experimental materials discovery process is slow [124, 174].

In this chapter I will present the different computational methods I used during my PhD. Among the many molecular simulation methods, I focused mostly on molecular dynamics which I first introduce in section 2.1. I used four different flavors of molecular dynamics which are presented in three separate sections: *ab initio*, (section 2.2), with classical and reactive force fields (presented jointly in section 2.3), and finally with machine learned potentials (section 2.4). Finally, section 2.5 aggregates multiple methods I used for the analysis of the molecular dynamics simulations.

2.1 MOLECULAR DYNAMICS SIMULATIONS

2.1.1 Space and time scales

DIVERSITY OF SIMULATION METHODS

To understand real materials through computation, one needs to consider a variety of effects from quantum interactions at very small length scales to macroscopic properties at very large length scales. Achieving this requires the use of a range of numerical methods tailored for different purposes, which are represented on figure 2.1. Based on multiple levels of theory, they provide access to different space and time scales with various accuracies, and are often highly interconnected [175].

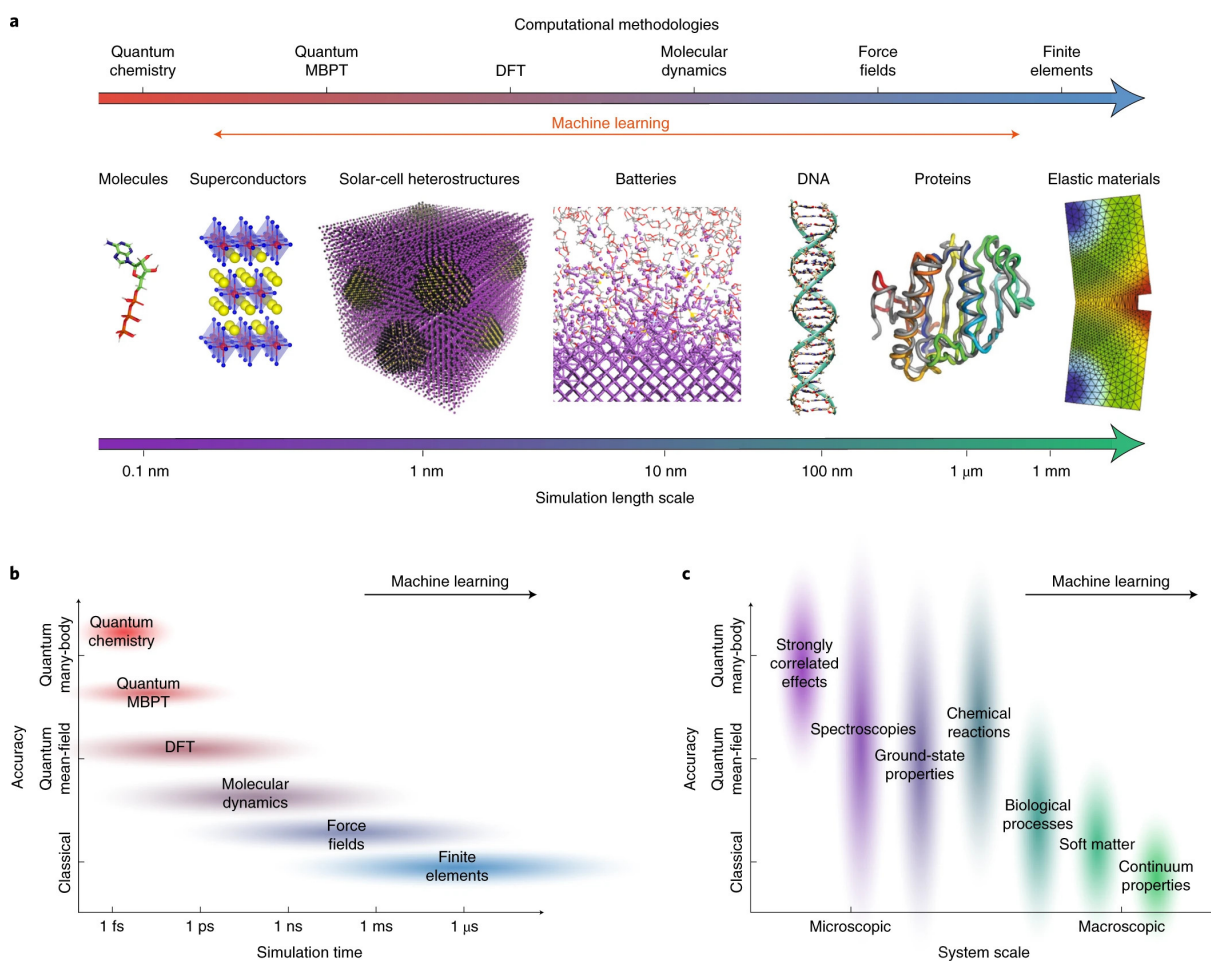


Figure 2.1: (a) Computational methodologies address systems spanning from microscopic to macroscopic length scales. Based on different levels of theory, these methods provide (b) different accuracies, achievable simulation times, and (c) access to different phenomena. Reproduced from Ref. [175].

SCALES IN THIS WORK

Among this multiplicity of methods, I have used in this work computational tools able to simulate systems typically comprised between $N = 200$ and 10,000 atoms (corresponding to ~ 10 -100 nm), with typical time scales found between 10 ps and 10 ns. On figure 2.1, they correspond to “DFT” (section 2.2), “Molecular Dynamics”, “Force fields” (section 2.3.2 and section 2.3.3) and “machine learning” (section 2.4).

PERIODIC BOUNDARY CONDITIONS

While these numerical methods are used to study atomistic models of a few hundreds atoms, the end goal is generally to study macroscopic materials and chemical systems composed of a number of atoms of the order of Avogadro’s number ($\sim 10^{23}$ atoms). A typical way to represent these materials is to use

periodic boundary conditions (PBC). The basic idea is the simulation of a small box containing N atoms, called the *unit cell*, which is replicated throughout space to form an infinite lattice, as illustrated on figure 2.2 [176]. The copies of the initial box are called *images* of this box.

The unit cell can be represented by three *unit cell vectors* – $\mathbf{a}, \mathbf{b}, \mathbf{c}$ – which define the primitive axes. For convenience, the *unit cell matrix* (also called *unit cell tensor*) $\mathbf{h} = [\mathbf{a}, \mathbf{b}, \mathbf{c}]$ can be introduced.

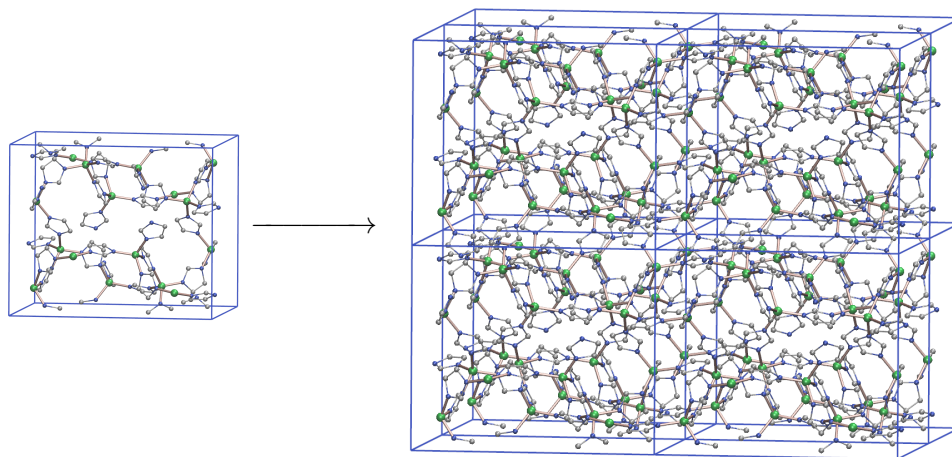


Figure 2.2: Example of ZIF-4 with periodic boundary conditions showing the replication of a unit cell (right) in all three directions to yield a $(2 \times 2 \times 2)$ supercell (left). Reproduced from Ref. [177].

The periodicity of the crystals makes it easy to simulate a single unit cell and virtually extend the size of the system by periodic boundary conditions. However, as the use of PBC introduces an artificial periodicity into the system, it is harder to study defects that are inherently replicated over all the images. Studying aperiodic (e.g. disordered) systems is even more complex, as they do not possess any translational periodicity. They can, however, be approximated by periodic structures with large unit cells [74].

2.1.2 Principles of molecular dynamics

Molecular dynamics (MD) is a family of numerical techniques which have in common to reproduce the time evolution of molecules and materials by numerically integrating Newton’s equations of motion, based on the knowledge of atomic interactions at a given level of theory. I will now briefly outlay the principles of MD, and recommend the following books for an in-depth description [176, 178].

EQUATIONS OF MOTION

In all the different flavors of MD used in this work, the nuclear motion of the constituent particles obeys the laws of classical mechanics.

Let us therefore consider an atomistic system containing N individual atoms with Cartesian coordinates \mathbf{r}_i , masses m_i and momentum \mathbf{p}_i . For convenience, let us denote \mathbf{r} and \mathbf{p} the set of all positions $\{\mathbf{r}_i\}$ and momentum $\{\mathbf{p}_i\}$. The interactions between the atoms are described by a potential energy $U(\mathbf{r})$, with no explicit dependence on time and \mathbf{p} , such that the classical Hamiltonian of the system is:

$$H(\mathbf{r}, \mathbf{p}) = \sum_i^N \frac{\mathbf{p}_i^2}{2m_i} + U(\mathbf{r}) \quad (2.1)$$

The equations of motion of the system are therefore:

$$\begin{aligned}\frac{\partial \mathbf{r}_i}{\partial t} &= \frac{\mathbf{v}_i}{m_i} \\ \frac{\partial \mathbf{p}_i}{\partial t} &= -\frac{\partial U(\mathbf{r})}{\partial \mathbf{r}_i}\end{aligned}\quad (2.2)$$

POTENTIAL ENERGY

A variety of approaches coexist to obtain the potential energy $U(\mathbf{r})$ from a configuration of atomic positions \mathbf{r} . I will detail in the next three sections the approaches used in this PhD: from quantum calculations (section 2.2), using classical and reactive force fields (section 2.3), and finally using machine-learned potentials (section 2.4). In this section we will consider that we know how to compute $U(\mathbf{r})$ from the knowledge of \mathbf{r} .

INTEGRATION SCHEME

The evolution of the atomic positions and velocities of the system are obtained by integrating the equations of motion using finite difference methods and by discretizing time. Starting from an initial configuration at time t , these equations allow computing the positions and velocities at the next time step $t + \delta t$.

A number of integration schemes suitable for MD simulations exist in the literature, which all possess a number of desirable qualities for this task (satisfy the conservation laws of the system, time-reversible, fast, accurate, etc.) [176, 178]. Most MD programs use a variant of the algorithm initially adopted by Verlet [179], that is described here as an illustrative example. The algorithm written in its velocity Verlet form is as follows:

$$\begin{aligned}\mathbf{v}(t + \delta t/2) &= \mathbf{v}(t) + \frac{1}{2} \mathbf{a}(t) \delta t, \\ \mathbf{r}(t + \delta t) &= \mathbf{r}(t) + \mathbf{v}(t + \delta t/2) \delta t, \\ \mathbf{a}(t + \delta t) &= \mathbf{m}^{-1} \mathbf{f}(t + \delta t), \\ \mathbf{v}(t + \delta t) &= \mathbf{v}(t + \delta t/2) + \frac{1}{2} \mathbf{a}(t + \delta t) \delta t,\end{aligned}\quad (2.3)$$

where $\mathbf{f}_i = -\partial U(\mathbf{r})/\partial \mathbf{r}_i$ is the force acting on atom i , $\mathbf{v} = \mathbf{m}^{-1} \mathbf{p}$ are the velocities, and \mathbf{m} the mass matrix.

For this discretization to be valid, the time step δt has to be small enough so that both the second and higher order terms in δt are negligible, and the forces acting on each atom can be considered constant between t and $t + \delta t$. For the systems in this work, δt was comprised between 0.25 fs and 1 fs. This is dictated by the fastest motion in the system.

2.1.3 Thermodynamic ensembles

By default, molecular dynamics sample the microcanonical, or (N, V, E) ensemble, which conserves the mechanical energy E , volume V and number of particles N , as total energy is conserved in the integration of Newton's equations of motion.

A great strength of MD, however, is the ability to perform simulations at varying conditions of temperature and mechanical constraints. An example use case in the study of amorphous MOFs is the possibility to mimic *in silico* experimental formation routes, such as melt-quenching or pressure-induced amorphization, by imposing adequate thermodynamic variables such as pressure P or temperature T . It can be achieved by sampling alternative thermodynamic ensembles such as the canonical (constant (N, V, T)) or isothermal-isobaric (constant (N, P, T)) ensembles, illustrated on figure 2.3.

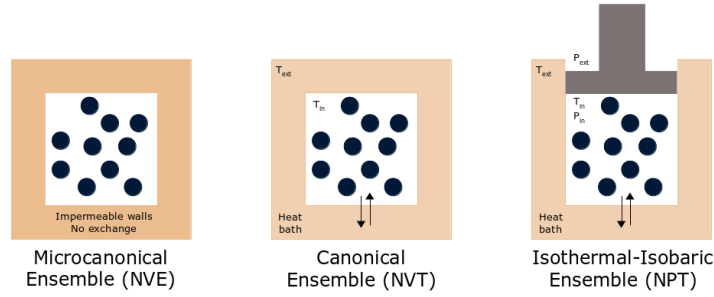


Figure 2.3: Schematic of the microcanonical, canonical and isothermal-isobaric ensembles. Reproduced from Ref. [180].

THERMOSTATS

The canonical (N, V, T) ensemble can be simulated by using *thermostats*, i.e. algorithms that control the temperature by changing the kinetic energy of the system, or more generally by changing the velocities of the atoms. A number of thermostats exist in the literature, with implications on the temperature response of the studied systems [181, 182], of which I will introduce those used in this work.

A widely used thermostat to probe the correct canonical ensemble is the Nosé-Hoover thermostat [183, 184]. In this approach, the Hamiltonian of equation (2.1) is extended to include an additional variable s representing an extra degree of freedom:

$$H(\mathbf{r}, \mathbf{p}, s, p_s) = \sum_i^N \frac{\mathbf{p}_i^2}{2m_i s^2} + U(\mathbf{r}) + \frac{p_s^2}{2Q} + g k_B T \ln(s) \quad (2.4)$$

where $(\mathbf{r}, \mathbf{p}, t)$ are virtual variables, related to the real variables $(\mathbf{r}', \mathbf{p}', t')$ by

$$\mathbf{r} = \mathbf{r}' \quad \mathbf{p} = s\mathbf{p}' \quad \delta t = s\delta t' \quad (2.5)$$

and where g is a parameter essentially equal to the number of degrees of freedom of the physical system, p_s is the conjugate momentum of s , k_B the Boltzmann constant and Q is a parameter that behaves as a mass and which can be tuned to change the intensity of the coupling. This thermostat supplements the physical phase space with the additional variable s which mimics the effect of a heat bath using a deterministic scheme [181].

Instead of using such extended Hamiltonian methods, another approach consists in using rescaling methods to sample the canonical ensemble. This is the basis of the Canonical Sampling through Velocity Rescaling (CSVR) [185] thermostat, also used during my PhD, in which the velocities of all the particles are rescaled by a properly chosen random factor. While the Nosé-Hoover thermostat can exhibit nonergodic behavior, this version of CSVR was found to be more ergodic while still probing the correct canonical ensemble [185].

BAROSTATS

Controlling the pressure can be done with the same approaches as the temperature to generate the isothermal-isobaric, or constant (N, P, T) ensemble. In this case, the *barostat* aims at converging the average value of the pressure $\langle P \rangle$ by dynamically changing the volume V . This change can be done by fixing the cell shape, represented by the normalized unit cell tensor $\hat{\mathbf{h}} = V^{-1/3} \mathbf{h}$, and applying a uniform dilation of the cell, or by allowing $\hat{\mathbf{h}}$ to change.

In this work, following the nomenclature of Ref. [182], I will refer to the first of these ensembles (fixed $\hat{\mathbf{h}}$) as $(N, P(\hat{\mathbf{h}}), T)$, or (N, P, T) with an isotropic cell. The (N, P, T) ensemble with varying $\hat{\mathbf{h}}$ will be referred to as $(N, P(\sigma_a), T)$, (N, P, T) with a flexible cell or as the constant-stress ensemble denoted (N, σ, T) .

To better spot the difference between these ensembles, let us decompose the stress tensor σ , into the hydrostatic pressure $P = \text{Tr}(\sigma)$ and a deviatoric stress σ_a :

$$\sigma = P\mathbf{1} + \sigma_a \quad (2.6)$$

While both ensembles ensure convergence of the average pressure $\langle P \rangle$ of the system, $(N, P(\hat{\mathbf{h}}), T)$ does it by keeping $\hat{\mathbf{h}}$ constant while $(N, P(\sigma_a), T)$ have $\langle \sigma_a \rangle$ converge, generally aiming for $\mathbf{0}$. Table 2.1 provides a summary of the ensembles used in this work with the precise quantities which are fixed.

Ensemble	N	V	E	$\langle T \rangle$	$\hat{\mathbf{h}}$	$\langle P \rangle$	$\langle \sigma_a \rangle$	Alternative names
(N, V, E)	×	×	×		×			
(N, V, T)	×	×		×	×			
$(N, P(\hat{\mathbf{h}}), T)$	×			×	×	×		(N, P, T) isotropic cell
$(N, P(\sigma_a), T)$	×			×		×	×	(N, P, T) flexible cell; (N, σ, T)

Table 2.1: Thermodynamic ensembles considered in this work, with comparison of the fixed quantities chosen among from $N, V, E, \langle T \rangle, \hat{\mathbf{h}}, \langle P \rangle, \langle \sigma_a \rangle$.

Similarly as for thermostats, there are a multiplicity of barostats in the literature [181]. The Nosé-Hoover barostat [183, 184], the only one used in this work, is based on a similar extension of the Hamiltonian to that of the (N, V, T) ensemble. In the case of a fixed cell shape, this extended Hamiltonian is:

$$H(\mathbf{r}, \mathbf{p}, s, p_s, V, p_V) = \sum_i^N \frac{\mathbf{p}_i^2}{2m_i V^{2/3} s^2} + U(V^{1/3} \mathbf{r}) + \frac{p_s^2}{2Q} + gk_B T \ln(s) + \frac{p_V^2}{2W} + P_{ex} V \quad (2.7)$$

Where p_V is the conjugate momentum of V , W a mass for the volume motion, P_{ex} is the externally set pressure, and with the virtual variables $(\mathbf{r}, \mathbf{p}, t)$ now related to the real variables $(\mathbf{r}', \mathbf{p}', t')$ by:

$$\mathbf{r} = V^{-1/3} \mathbf{r}' \quad \mathbf{p} = V^{1/3} s \mathbf{p}' \quad \delta t = s \delta t' \quad (2.8)$$

For the $(N, P(\sigma_a), T)$ ensemble, the equations are similar in spirit and can be found in ref. [186].

The level of coupling, quantified with Q and W in the Nose-Hoover formulation reported above, is often expressed with time constants in MD codes that we will call τ_T and τ_P here. Both thermostat and barostat should have sufficient time to react to changes. In particular it means that for every change of volume induced by the barostat, the thermostat must have time to change the velocities to adapt the kinetic energy to the new potential energy. It translates to a larger damping constant for the barostat than for the thermostat. In my simulations I used $\tau_P = 10 \tau_T$, with τ_T being typically equal to $100 \delta t$.

2.2 AB INITIO MOLECULAR DYNAMICS

Ab initio molecular dynamics (AIMD) simulations rely on the computation of the forces acting on the nuclei from electronic structure calculations. In this section I will give an overview of AIMD, and recommend the following books for an in-depth description [187, 188].

2.2.1 Unifying MD and quantum calculations

THE SCHRÖDINGER EQUATION

The starting point of combining MD and quantum calculations, in the framework of non-relativistic quantum mechanics, is formalized via the time-dependent Schrödinger equation:

$$i\hbar \frac{\partial}{\partial t} \Phi(\mathbf{r}, \mathbf{R}, t) = \hat{\mathcal{H}} \Phi(\mathbf{r}, \mathbf{R}, t) \quad (2.9)$$

with the wave function $\Phi(\mathbf{r}, \mathbf{R}, t)$ a function of both electrons and nuclei, and the Hamiltonian $\hat{\mathcal{H}}$ describing the electron-electron, electron-nuclear, and nuclear-nuclear Coulomb interactions:

$$\begin{aligned} \hat{\mathcal{H}} = & - \sum_I \frac{\hbar^2}{2M_I} \nabla_I^2 - \sum_i \frac{\hbar^2}{2m_e} \nabla_i^2 \\ & + \frac{1}{4\pi\epsilon_0} \sum_{i<j} \frac{e^2}{|\mathbf{r}_i - \mathbf{r}_j|} - \frac{1}{4\pi\epsilon_0} \sum_{I,i} \frac{e^2 Z_I}{|\mathbf{R}_I - \mathbf{r}_i|} + \frac{1}{4\pi\epsilon_0} \sum_{I<J} \frac{e^2 Z_I Z_J}{|\mathbf{R}_I - \mathbf{R}_J|} \end{aligned} \quad (2.10)$$

where \mathbf{r}_i and m_e describe the electrons positions and masses, \mathbf{R}_I , M_I and Z_I the positions, mass and atomic number of the nuclei, \hbar is the reduced Plank's constant, e the elementary charge and ϵ_0 the vacuum permittivity.

BORN-OPPENHEIMER DYNAMICS

Among the multiple AIMD schemes (e.g. Ehrenfest dynamics, Car-Parinello dynamics, etc.) I exclusively used Born-Oppenheimer AIMD during my PhD. It relies on the Born-Oppenheimer approximation, in which the dynamics of the electrons and the nuclei are decoupled, owing to the great difference of mass between the electrons and the nuclei. This approximation means that at a given point in time, the (quantum) electrons evolve in the constant electrostatic potential generated by the fixed (classical) nuclei. A Born-Oppenheimer dynamics therefore consist in successive time-independent quantum problems, requiring the resolution of the time-independent, stationary Schrödinger equation for the electrons, performed at each MD time step.

Denoting Ψ the wave function for the electrons, the Born-Oppenheimer MD method can be written down for the electronic ground state (Ψ_0, E_0) as:

$$\begin{aligned} \hat{\mathcal{H}}_e \Psi_0 &= E_0 \Psi_0 \\ M_I \frac{\partial \mathbf{R}_I}{\partial t} &= -\nabla_I \min_{\Psi_0} \{ \langle \Psi_0 | \hat{\mathcal{H}}_e | \Psi_0 \rangle \} \end{aligned} \quad (2.11)$$

where $\hat{\mathcal{H}}_e$ is the electronic Hamiltonian:

$$\hat{\mathcal{H}}_e = - \sum_i \frac{\hbar^2}{2m_e} \nabla_i^2 + \frac{1}{4\pi\epsilon_0} \sum_{i<j} \frac{e^2}{|\mathbf{r}_i - \mathbf{r}_j|} - \frac{1}{4\pi\epsilon_0} \sum_{I,i} \frac{e^2 Z_I}{|\mathbf{R}_I - \mathbf{r}_i|} \quad (2.12)$$

This method is therefore conceptually identical to the general description of MD of section 2.1, with quantum calculations only representing a way to compute the energy of the system, and therefore the forces. The complete electronic wave function is, however, a very complicated mathematical function with $\sim 3N$ variables, even for a simple molecule, as each atom has several electrons. Quantum chemistry offers a lot of methods to solve this problem, and we relied on density functional theory.

2.2.2 Density functional theory

THE DFT THEOREMS AND THE KOHN-SHAM PICTURE

Among the multiple *ab initio* methods for the computational study of materials' ground-state properties, density functional theory (DFT) has been arguably the most dominant and successful method over the past half century [175]. The central idea of DFT is to solve equation (2.12) in terms of the total electronic density $n(\mathbf{r})$, defined for a normalized Ψ as:

$$n(\mathbf{r}) = \left\langle \Psi \left| \sum_{i=1}^N \delta_{\mathbf{r}_i} \right| \Psi \right\rangle \quad (2.13)$$

where $\delta_{\mathbf{r}_i}$ is the Dirac delta function $\delta(\mathbf{r} - \mathbf{r}_i)$.

The foundations of DFT were laid down by Hohenberg and Kohn [189], which showed that the electronic ground-state total energy E_0 can be expressed as a functional of the ground-state charge density $n(\mathbf{r})$, and by Kohn and Sham [190], which showed that the ground-state charge density can be determined by a set of self-consistent one-body equations. These equations, called *Kohn-Sham equations*, can be expressed for the single electron wave functions $\psi_i(\mathbf{r})$, called the *Kohn-Sham orbitals*:

$$\left[-\frac{\hbar^2}{2m} \nabla^2 + V_{\text{ext}}(\mathbf{r}) + V_{\text{H}}(\mathbf{r}) + V_{\text{XC}}(\mathbf{r}) \right] \psi_i(\mathbf{r}) = \varepsilon_i \psi_i(\mathbf{r}) \quad (2.14)$$

where $V_{\text{ext}}(\mathbf{r})$ is the potential an electron feels due to the presence of the nuclei, and V_{H} , named the *Hartree potential*, describes the repulsion between the single-electron and the total electron density. Both can be computed directly from \mathbf{r} and $n(\mathbf{r})$ and are defined as:

$$V_{\text{ext}}(\mathbf{r}) = -\frac{e^2}{4\pi\epsilon_0} \sum_j \frac{Z_j}{|\mathbf{r} - \mathbf{R}_j|} \quad (2.15)$$

$$V_{\text{H}}(\mathbf{r}) = \frac{e^2}{4\pi\epsilon_0} \int \frac{n(\mathbf{r}')}{|\mathbf{r} - \mathbf{r}'|} d^3r' \quad (2.16)$$

The last term in equation (2.14) is the exchange-correlation contribution V_{XC} , which is not exactly known (except for a free electron gas) and requires the use of approximations.

Kohn-Sham equations are non-linear equations, as both V_{H} and V_{xc} depends on $\{\varphi_i\}$, and are usually solved by a self-consistent iterative algorithm called the *Self-Consistent Field* (SCF) method. Although the Kohn-Sham orbitals and their eigenvalues ε_i do not have physical significance as single particle wave functions, they have proven to give quite accurate descriptions of band structures and bonding characters [191].

In the end, the strength of DFT is simplifying a $3N$ -dimensional problem (many interacting electrons), into a 3-dimensional problem. The computational complexity is polynomial [192], which allows the

simulation of significantly larger systems compared to the exponential scaling of the original many-body problem.

EXCHANGE-CORRELATION

In principle, DFT is an exact theory for ground-state properties, but in practice, an approximation for the exchange correlation functional $E_{XC}[n]$ is needed to perform any actual calculation and obtain a numerical solution of the Kohn-Sham equations. The numerical solution involves multiple algorithmic choices which are translated into the diversity of widely used electronic-structure codes available nowadays [193].

The quest for approximations to $E_{XC}[n]$ is a fundamental one, and its choice has significant influence on how the energy depends on atomic positions, and thus on all calculated properties. There are many options available in the literature, and each choice of functional is a compromise between accuracy and computational cost [194]. In this work, I used generalized-gradient approximation (GGA) functionals which take into account the non-local exchange and correlation effects. The central idea is the assumption that $E_{XC}[n]$ can be expressed by the following form:

$$E_{XC}^{GGA}[n(\mathbf{r})] = \int n(\mathbf{r}) \varepsilon_{XC}(n(\mathbf{r}), \nabla n(\mathbf{r})) d\mathbf{r} \quad (2.17)$$

where $\varepsilon_{XC}(n(\mathbf{r}), \nabla n(\mathbf{r}))$ is the exchange-correlation energy per particle which is assumed to depend on both the density at each point $n(\mathbf{r})$ and the first order gradient term $\nabla n(\mathbf{r})$.

Among the multiple available GGA functionals, the PBE functional [274] was shown to produce consistent results in many porous systems [92] and was used in my work.

DISPERSION CORRECTIONS

A drawback of using information about the local density to construct the exchange-correlation functionals, is that DFT calculations often have trouble reproducing long-range correlation effects, such as dispersion interactions. This can be corrected by adding a dispersion correction term E_{disp} proposed by Grimme et al. [196, 197] to the energy obtained by DFT (E_{DFT}):

$$E_{\text{tot}} = E_{\text{DFT}} + E_{\text{disp}} \quad (2.18)$$

In this work, I used the DFT-D3 version of this correction [197], expressed as:

$$E_{\text{disp}} = - \sum_{J>I} \left[\frac{C_6^{IJ}}{R_{IJ}^6} f_6^{IJ}(R_{IJ}) + \frac{C_8^{IJ}}{R_{IJ}^8} f_8^{IJ}(R_{IJ}) \right] \quad (2.19)$$

where the sum is over all the pairs of atoms (I, J), $R_{IJ} = |\mathbf{R}_I - \mathbf{R}_J|$, C_6^{IJ} and C_8^{IJ} are parameters tabulated for each pair of elements, and f_n^{IJ} are damping functions defined as:

$$f_n^{IJ}(R) = \begin{cases} \frac{s_n}{1 + 6 \left(R / \sigma_n \sqrt{C_8^{IJ} / C_6^{IJ}} \right)^{-\alpha_n}} & \text{for } R < R_c \\ 0 & \text{for } R \geq R_c \end{cases} \quad (2.20)$$

In this expression, s_n , α_n and σ_n are parameters (with s_n and σ_n adapted to the particular E_{XC} used), and R_c is a cutoff radius.

BASIS SET

To solve the Kohn-Sham equations, there is a need for an accurate representation of the single-particle orbitals $\psi_i(\mathbf{r})$, which are usually described using a set of basis functions $\varphi_a(\mathbf{r})$:

$$\psi_i(\mathbf{r}) = \sum_a c_{ai} \varphi_a(\mathbf{r}) \quad (2.21)$$

Among the most popular basis sets, we find Gaussian basis sets (localized, or atom centered) and plane wave basis sets (delocalized). The Gaussian plane wave (GPW) method [198] used in this work, combines the two types of basis sets described above and is commonly found for simulations of materials [193]. I have mostly used the DZVP (double- ζ valence polarized) basis sets.

2.3 FORCE FIELDS

2.3.1 Motivations and principles

TOWARDS LARGER SCALES

Despite the accuracy and wealth of information obtainable by AIMD, this method is limited to relatively small scale studies. Classical MD simulations, however, are routinely used to explore longer time scales and larger systems, with simulations of several thousands of atoms over tens to hundreds of ns reasonably tractable. They enable molecular level insights into macroscopic material properties such as adsorption, diffusion and framework dynamics [199].

The basic idea behind classical MD is to evaluate the potential energy $U(\mathbf{r})$ as an analytical function of the atomic positions \mathbf{r} . This is done with *force fields* (FF), a term referring to the functional forms used to describe the intra- and inter-molecular potential energies of a collection of atoms, along with the corresponding parameters [176]. The knowledge of a force field therefore allows the integration of the equations of motion (equation (2.2)).

That force field is optimized to reproduce the structure, dynamics and other properties of a given material or set of materials, based on experimental data or quantum chemistry calculations. The choice and implementation of force fields is crucial to the accuracy obtained when resorting to this method.

ENERGY DECOMPOSITION

$U(\mathbf{r})$ is generally decomposed in several terms representing the contributions of different physical interactions. The specific decomposition depends on the force field, with a common form being:

$$U(\mathbf{r}) = \sum_{ij} U_{\text{pairs}}^{ij} + \sum_{\alpha} U_{\text{molecular}}^{\alpha} + U_{\text{Coulomb}} \quad (2.22)$$

where U_{Coulomb} is the Coulombic interaction between charged atoms, $U_{\text{molecular}}$ represent the internal molecular energy and U_{pairs} the interactions between non-bonded pairs (typically with the Lennard-Jones potential).

There are multiple functional forms to describe each contribution. For example the intra-molecular interactions $U_{\text{molecular}}$ (*i.e.* between atoms that are linked by covalent or metal-ligand bonds) are often further decomposed:

$$U_{\text{molecular}} = \sum_{\text{bonds}} U_{\text{bond}}(r) + \sum_{\text{angles}} U_{\text{angle}}(\theta) + \sum_{\text{dihedrals}} U_{\text{dihedral}}(\varphi) \quad (2.23)$$

Every energy term in this example only depends on the type of bonded atoms, and a single scalar variable. These scalars are the distance r between the two atoms for bonds contributions, the 3-body angle θ for angles contributions, and the 4-body dihedral angle φ or out of plane distance d for dihedral angles contributions. These variables are illustrated on figure 2.4.

FORCE FIELD PARAMETRIZATION

Force fields are parameterized to reproduce the molecular geometry or thermodynamic properties reported experimentally or obtained from higher level *ab initio* calculations. All the functional forms have one or more adjustable parameters. They are optimized to reproduce the expected energy and physical properties of the system, in a procedure called *parametrization* of the force field.

However the parametrization of a force field involves a trade-off between accuracy — *i.e.* how well a given force field can reproduce the system properties — and transferability — *i.e.* how well it fares on systems it was not trained for. A notable example of a generic force field that traded some accuracy

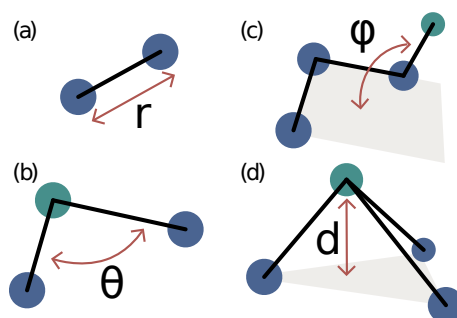


Figure 2.4: Parameters used to compute the energy of a molecular system with a classical force field for (a) bonds, (b) angles, (c) dihedral angles, and (d) improper dihedrals/out of plane distance. Adapted from Ref. [67].

for a better transferability is the Universal Force Field (UFF) [200], which was adapted to MOFs in 2016 [144].

2.3.2 Classical force fields

BONDED INTERACTIONS

The most commonly used type of MD simulations for crystalline MOF phases relies on classical force fields, for which the bonds between different atoms are defined only once over the entire course of the MD run, along with charges which are also fixed. They are therefore unable by design to simulate bond breaking or reformation, or changes in the electronic state of an atom.

This is typically achieved with functional forms adapted for the description of bonds and angles around equilibrium positions, only considering the vibration of the bond length or the angle. For example, the energy of bonds, angles and improper dihedrals can be represented as harmonic oscillators, and proper dihedrals as cosine potentials to reproduce the periodicity of the associated energy:

$$\begin{aligned}
 U_{\text{bond}}(r) &= \frac{1}{2}k_b (r - r_0)^2 \\
 U_{\text{angle}}(\theta) &= \frac{1}{2}k_a (\theta - \theta_0)^2 \\
 U_{\text{improper dihedral}}(\varphi) &= \frac{1}{2}k_i (\varphi - \varphi_0)^2 \\
 U_{\text{proper dihedral}}(\varphi) &= A [1 + \cos(n\varphi + \delta)]
 \end{aligned}
 \tag{2.24}$$

where (k_b, k_a, k_i) are spring constants, $(r_0, \theta_0, \varphi_0)$ equilibrium positions, A a multiplicative constant, n a positive integer indicating the periodicity and δ a phase shift [201].

MOF-FF FOR ZIFs

Unfortunately, generic force fields are not always optimal for simulating MOFs, in particular to predict their dynamic properties. One possible trade-off between accuracy and transferability lies in the systematic and consistent parametrization of force fields from first principles reference data. With this approach, the low transferability of each parameterized (and accurate) force field is compensated by the possession of a procedure to readily train new force fields on new materials. During the course of my PhD I used MOF-FF [145], a force field based on the MM3 functional form [202] which embodies such a parametrization strategy.

In 2019 Dürholt et al. used MOF-FF to generate new force fields for three ZIF-8 variants from *ab initio* input data [203]. They were able to reproduce well both geometric and dynamic properties, and the FF showed good transferability across a series of ZIF polymorphs. It also led to mechanical properties in line with earlier FFs [204].

MOF-FF has a specific parametrization for each atom type, defined as a combination of the atomic species X and its coordination environment (called *atypes*) and where it sits in the framework (called *fragments*). This nomenclature is the one used by *molsys*, the Python package behind MOF-FF for the parametrization of systems [205]. For example, a Zn atom connected to 4 N and sitting in its regular position (a fragment called *zn4tet* in *molsys*) in a ZIF-4 framework will be identified by these three characteristics, and noted *zn4_n4@zn4tet* in *molsys*.

ADAPTATION TO GLASSES

Even if a few studies used classical MD to study the amorphization of ZIFs [146, 147] as discussed in section 1.3.3, every classical FF for ZIFs published to this date has been developed with crystals in mind, and should thus first be adapted and validated before any study of ZIF glasses. While developing a new FF for glasses is beyond the scope of this study, the MOF-FF methodology for an automatic parametrization of FFs would make such a development achievable in future works.

Adapting the FF requires to add a parametrization for coordination environments which are not present in the crystalline framework. In the particular case of *a*ZIF-4, it requires the parametrization of the interaction between three-coordinated Zn atoms and their N neighbors (*zn3_n3zn3tet*, with a fragment *zn3tet* to be defined). In this work I created two FF adaptations of MOF-FF for ZIFs for the glasses: *Zn3tetra* and *Zn3trig*. In *Zn3tetra*, every three-coordinated Zn atom (denoted *zn3_n3* in *molsys* *atypes* format) was treated as a four-coordinated Zn (denoted *zn4_n4*). In *Zn3trig*, *zn3_n3* were treated as *zn4_n4* in all their interactions with other atoms, except for the N–Zn–N angle which was changed from the tetrahedral angle ($\arccos(-1/3) \approx 109.47^\circ$) to 120° , using the same spring constant. Their validation and use are further commented in section 5.4.1.

As the identification of the building units (Zn atoms and imidazoles) of the glass models could not be performed by *molsys*, due to large fluctuations in the bond angles and lengths as well as the presence of defects, it was carried out with an *ad hoc* identification algorithm presented in section 2.5.3, and interfaced with *molsys*.

2.3.3 Reactive force fields

DESCRIBING BOND REARRANGEMENT

Although classical force fields are well suited for nonreactive interactions, they are inadequate for modeling changes in atom connectivity. Modeling bonds breaking and reformation motivated the inclusion of connection-dependent terms in the force-field description, leading to the development of *reactive* force fields.

A number of different functional forms exist to represent these reactive potentials [206], for example by separating repulsive and attractive terms. A typical functional form of (early) reactive FF relies on exponential functions, illustrated on figure 2.5 for the following form [207]:

$$U_{\text{repulsive}}(r) = (1 + Q/r) A e^{-\alpha r} \quad (2.25)$$

$$U_{\text{attractive}}(r) = \sum_n b_n e^{-\beta_n r} \quad (2.26)$$

where $(Q, \alpha, b_n, \beta_n)$ are a set of parameters.

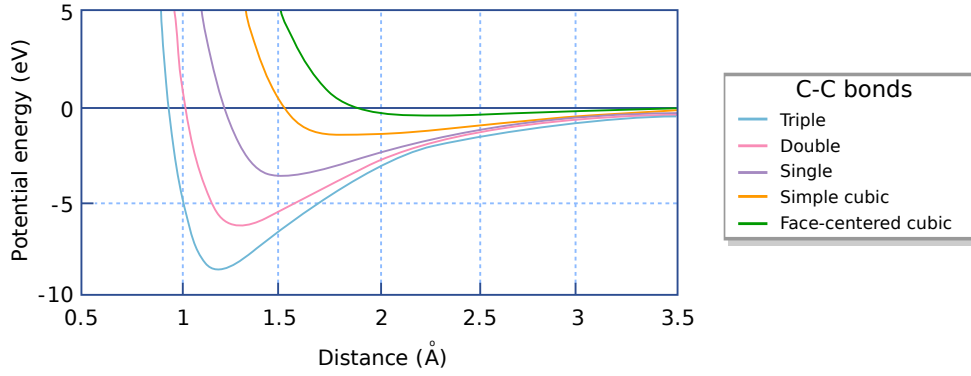


Figure 2.5: Representative reactive pair interactions for various carbon-carbon bond types. Adapted from Ref. [207, 208].

REAXFF

In the past decades, the sophistication of empirical potentials has been greatly improved by employing bond order concepts, dependent on the local chemical environment and exemplified by the widely used ReaxFF method [206]. Originally developed in 2001 by van Duin et al. for hydrocarbon description [209], ReaxFF considers each atomic interaction bond order dependent, without having to predefine reactive sites [210]. Bond order BO_{ij} is calculated directly from interatomic distances r_{ij} using empirical formulas, reproduced here for a carbon-carbon interaction:

$$\begin{aligned} BO'_{ij} &= BO_{ij}^{\sigma} + BO_{ij}^{\pi} + BO_{ij}^{\pi\pi} \\ &= \exp \left[p_{bo1} \cdot \left(\frac{r_{ij}}{r_0^{\sigma}} \right)^{p_{bo2}} \right] + \exp \left[p_{bo3} \cdot \left(\frac{r_{ij}}{r_0^{\pi}} \right)^{p_{bo4}} \right] + \exp \left[p_{bo5} \cdot \left(\frac{r_{ij}}{r_0^{\pi\pi}} \right)^{p_{bo6}} \right] \end{aligned} \quad (2.27)$$

where r_0 are equilibrium bond lengths and p_{bo} terms empirical parameters. A key feature of this definition as a sum of three exponentials representing single, double (π bond), and triple ($\pi\pi$ bond) bond order contributions, is that it involves no discontinuities through transitions between different bond characters.

The forces on each atom are derived from the system energy E_{system} described by the following many-body empirical potential terms:

$$E_{\text{system}} = E_{\text{bond}} + E_{\text{angle}} + E_{\text{tors}} + E_{\text{over}} + E_{\text{coulomb}} + E_{\text{vdWaals}} + E_{\text{specific}} \quad (2.28)$$

where ($E_{\text{bond}}, E_{\text{angle}}, E_{\text{tors}}$) respectively describe the energy associated with forming bonds between atoms, three-body valence angle strain and four-body torsional angle strain, E_{over} is an energy penalty preventing the over-coordination of atoms, E_{coulomb} and E_{vdWaals} are electrostatic and dispersive contributions, and E_{specific} represents system specific terms. The overall ReaxFF procedure to compute E_{system} from the atomic positions is outlaid in figure 2.6.

Multiple branches of ReaxFF have been developed over the years, the largest of which being the combustion and aqueous branches [153]. Within well-designed MD platform (e.g. LAMMPS [211]), the optimized ReaxFF potentials are capable of simulating systems larger than 10^6 atoms at the nanosecond time scale [206].

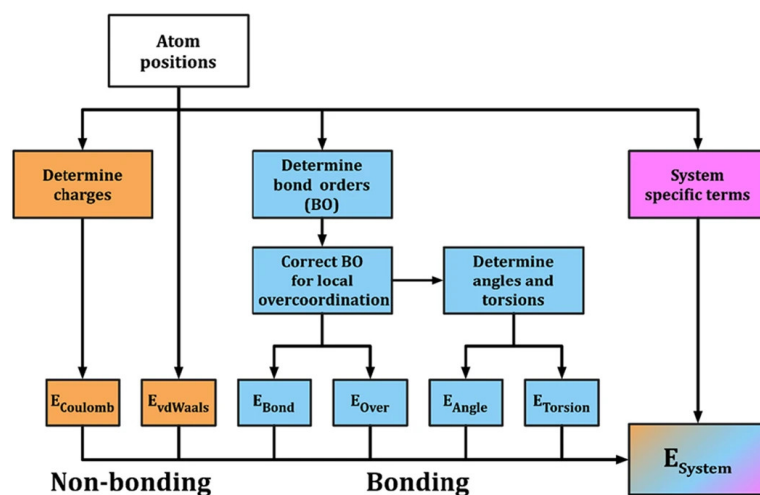


Figure 2.6: Overview of the ReaxFF total energy components. Adapted from Ref. [153].

PARAMETRIZATION FOR ZIFs

Among the multiple branches of ReaxFF, two have been used to study amorphous MOFs: one for copper based MOFs and one for ZIFs [155]. I detailed the different works in the literature that used them in section 1.3.5.

We should stress here that neither of these force fields were initially developed for nor thoroughly validated on MOFs. The force field used for copper based MOFs was initially developed for the interaction of glycine with a copper surface [161], while the ReaxFF force field for ZIFs was conceived for the study of Zn-Imidazolates complexes in aqueous [154]. In this PhD, I used the ReaxFF parametrization for ZIFs.

2.4 MACHINE-LEARNED POTENTIALS

The basic idea behind machine-learned potentials (MLP) is to use data obtained at a higher level of theory (such as *ab initio*) to fit interaction potentials, without relying on the analytic functional forms of classical force fields. In this section I will give an overview of MLPs, before further detailing neural network potentials (NNP), the family of MLPs used in this work. I will finish by presenting the precise architecture used, namely equivariant message passing neural networks, implemented as NequIP [212].

For further reference, I recommend Ref. [213, 214] for a general introduction of MLPs, Ref. [215] for their proposed applications, Ref. [216] for a general introduction to neural networks, and Ref. [217] for a recent review of the existing NNP architectures.

2.4.1 Principles and construction

SHIFTING THE COST-ACCURACY TRADE-OFF

The rapid growth of machine learning (ML) techniques in recent years has led to many applications in the computational materials science community. In addition to high-throughput techniques to predict new materials with targeted properties, supervised machine learning can be used to create next-generation force fields, called machine-learned potentials (MLP). Although many of the fundamental concepts can be dated back to 1995 with a seminal work by Blanck et al. [218], the recent progress in computational tools and power, data generation and analysis, and the availability of ML models in standard software toolkits, initiated the development of a large variety of promising methods to train and apply MLPs [175].

An MLP may be defined as an analytic expression for the potential energy $U(\mathbf{r})$ as a function of the atomic positions \mathbf{r} using an ML algorithm, which is constructed using a consistent set of reference electronic structure data, and which does not contain any *ad hoc* assumptions about the functional form [219].

This absence of a fixed functional form allows in principle to approximate multidimensional real-valued functions with arbitrary accuracy. In this regard, the construction of MLPs is a markedly different approach than the use of ML techniques to optimize force field parameters [220]. Because the computational cost is lower, especially when implemented through optimized frameworks leveraging GPU processing, MLPs enable large-space and long-time atomistic simulations beyond the reach of direct *ab initio* calculations, while retaining its level of accuracy as illustrated in figure 2.7. Furthermore, MLPs do not distinguish between bonded and non-bonded interactions and are therefore intrinsically reactive [215].

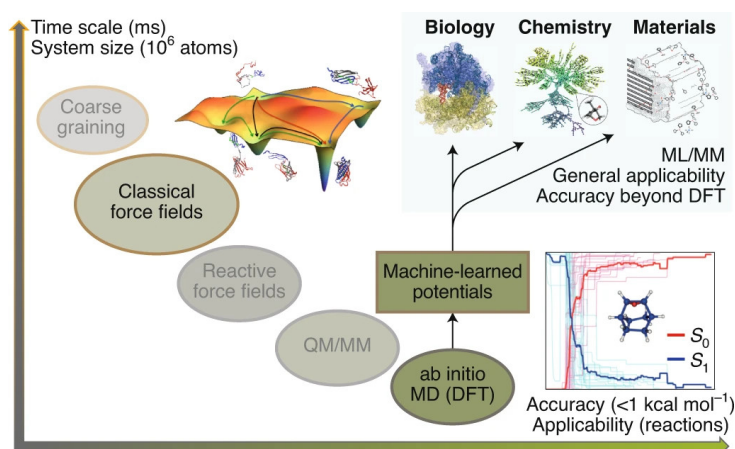


Figure 2.7: MLPs shown as a potential solution to the trade-off between cost and accuracy. Reproduced from Ref. [215].

The construction of any MLP consists of several individual steps illustrated on figure 2.8. First a reference data set is constructed, then the MLP is trained by a fitting process to accurately reproduce the reference data. Finally, a careful validation is required, before using the MLP in any simulation.

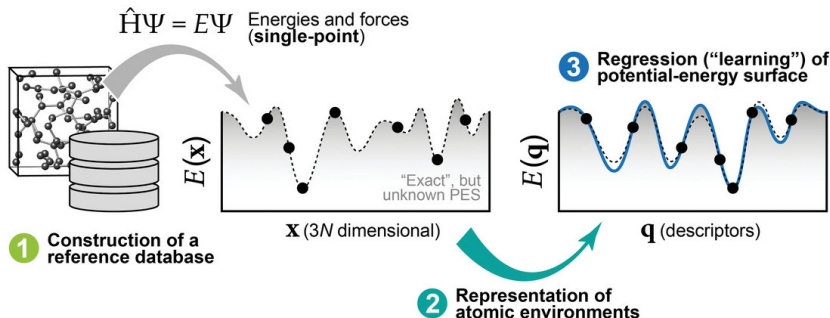


Figure 2.8: General overview of how MLPs are constructed. Adapted from Ref. [214].

DATA ACQUISITION

The reference data set, or training data, generally consists of the coordinates \mathbf{r} and elements $\{Z_i\}$ of all atoms in the system, as well as their corresponding energies E^{ref} and forces $\mathbf{F}_i^{\text{ref}}$. Diversity in the training data is key for good generalization of the MLP.

One of the most straightforward procedures to obtain reference data is to extract it from existing *ab initio* MD trajectories. It is, however, not necessarily the most efficient approach, because of the structural resemblance of consecutive time frames and long-time correlations. A solution to partially improve the procedure is to sample high temperature trajectories, which enhance coverage of off-equilibrium conformations which are of crucial importance when training MLPs [215]. Alternative and more efficient solutions exist such as active learning [219] or enhanced sampling. The latter has been demonstrated for the first time on MOFs in a recent work published in 2023 [221].

The data sets used to construct MLPs are often very large and contain tens of thousands of electronic structure calculations, making DFT (presented in section 2.2.2) the most frequently used electronic structure method for condensed systems.

TRAINING

For a given data set, the values of the parameters of the MLP have to be determined. This step, called *training*, is typically done by defining a loss function that needs to be minimized and by repeatedly cycling through the data with a gradient-based optimization algorithm. A full presentation of the dataset is called *epoch*, *i.e.* when every frame in the training dataset has had a chance to update the internal model parameters once.

The error of MLPs is typically measured by the mean absolute error (MAE) or the root mean squared error (RMSE), commonly normalized per atom:

$$\text{MAE} = \frac{1}{N} \sum_{i=1}^N |E_i^{\text{ref}} - E_i^{\text{MLP}}| \quad (2.29)$$

$$\text{RMSE} = \sqrt{\frac{1}{N} \sum_{i=1}^N (E_i^{\text{ref}} - E_i^{\text{MLP}})^2} \quad (2.30)$$

where E^{MLP} is the predicted potential energy.

A typical loss function for this task (e.g. NequIP default’s) is based on a weighted sum of energy and force loss terms:

$$\mathcal{L} = \lambda_E \mathcal{L}_E + \lambda_F \mathcal{L}_F \quad (2.31)$$

where λ_E and λ_F are the energy and force weightings, which relative weight depends on how the user wants to bias the learning procedure. Other quantities can be added to the loss function in a similar fashion, such as the stress.

VALIDATION

Assessing the accuracy of any interatomic potential is a question as old as atomistic simulations and not something specific to MLPs. However, while the approximations of classical FF might give rise to inaccuracies or failures, their physically meaningful functional forms may provide a physical understanding of their limitations. For MLPs the situation is different as the functional form is not based on physical interaction models. While it is an intrinsic strength of MLPs that allows to reach a much closer agreement with reference data, it makes it very difficult to determine the validity of an MLP outside of its training region [219].

Failures and inaccuracies can result from choices made at every step of the MLP construction shown on figure 2.8: the available data, the representation of atomic environments and interactions, and the optimization process (e.g. with the risk of getting trapped in local minimum).

Validating MLPs is therefore a crucial step before doing any production simulations, which relies both on a number of numerical validation tools commonly used in the ML literature, and on physically guided validation which relies on the practitioner’s domain knowledge. Ref. [222] provides a number of best-practice recommendations for the development of MLPs. Among them, a popular way to numerically validate an ML model is to use cross-validation. In its simplest form, this procedure involves the separation of the complete reference dataset into a training and a validation set. The performance of an ML model is then not judged by how well they predict the data they were trained on (which could lead to overfitting) but by how well the model is able to predict unseen data (from the validation set) [222, 223].

2.4.2 Neural network potentials

In recent years an increasing number of MLPs have been published, including a variety of neural network potentials (NNPs) or Gaussian approximation potentials (GAP) [219]. In this work I used a particular architecture of NNPs, which I will now introduce.

GENERALITIES ON NEURAL NETWORKS

Neural networks (NN) constitute a class of machine learning algorithms (very) loosely inspired by the human brain. Organized as a directed graph of trainable units (neurons), neural networks can learn highly nonlinear relations between input data and output data.

As illustrated on figure 2.9, a typical neuron is a scalar function that acts on a vector \mathbf{p} . The inputs $\{p_i\}$ are first multiplied by weights $\{w_{1,i}\}$ and are summed with a bias b . The sum n then goes into a *transfer function* (also called *activation function*) f , which produces the scalar output a . In summary the output is calculated as:

$$a = f \left(\sum_{i=1}^R w_{1,i} p_i + b \right) \quad (2.32)$$

$$= f(\mathbf{W}\mathbf{p} + \mathbf{b}) \quad (2.33)$$

With equation (2.33) written in a matrix form with the introduction of a $1 \times R$ weight matrix \mathbf{W} ,

The transfer function f may be a linear or a nonlinear function and is chosen to satisfy some specification of the problem that the NN is attempting to solve. Many types of activation functions can be used, such as the hyperbolic tangent, the sigmoid function, or Gaussian functions. An example used in part of NequIP architecture [212] is the sigmoid linear unit (SiLU) $f(x) = x/(1 + e^{-\beta x})$.

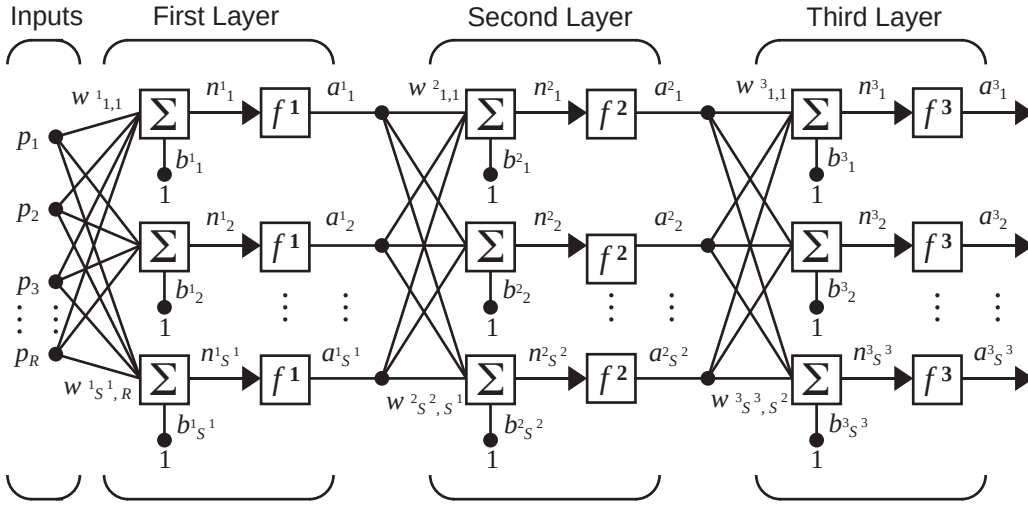


Figure 2.9: Example three-layer neural network. Adapted from Ref. [216].

The simplest neural network architecture, called *feed-forward* NN, consists of successive layers of neurons as shown on figure 2.9. Each layer i takes as input \mathbf{a}^{i-1} , the output of the previous layer, and therefore comes with its own weight matrix \mathbf{W}^i and bias vector \mathbf{b}^i . Its output is:

$$\mathbf{a}^i = f^i \left(\mathbf{W}^i \mathbf{a}^{i-1} + \mathbf{b}^i \right) \quad (2.34)$$

The final layer is called *output layer*, while the other ones are *hidden layers*. Both the weights \mathbf{W} and biases \mathbf{b} are adjustable parameters that will be determined according to a given learning rule so that the neuron network meets some specific goal. This is typically done by employing a gradient-based optimization algorithm to minimize a predefined loss function (see section 2.4.1). These gradients can be calculated very efficiently using a recursive scheme called backpropagation, in which the terms of the derivatives are computed step by step starting from the output layer and progressing through the network until the input layer is reached.

For further details on NN in general, Ref. [216] provides a thorough introduction.

NEURAL NETWORK POTENTIALS

Neural network potentials (NNP) are a subclass of MLPs that use neural networks to find a mapping between a three-dimensional configuration of an arbitrary number of atoms N and its corresponding energy E .

A prerequisite to achieve this is to find a suitable numerical representation of the material. Due to the nature of NNs, systems of an arbitrary size N should be represented by input vectors of fixed dimension which encode the complete information about the three-dimensional configuration and preserve the symmetries of the system [215]. A common way to proceed is to use a separate NN for each atom i in the system, which outputs its energy contribution $E_{i,atomic}$ [213]. The total energy E_{system} of the system is then obtained as the sum over all atoms in the system:

$$E_{system} = \sum_{i=1}^N E_{i,atomic} \quad (2.35)$$

This leads to a linear scaling of the computational cost with the system size [215]. It is frequent to constrain the atomic NNs to have the same architecture and weight parameters for each element.

Since the NNP has a well-defined functional form, the forces necessary to the integration of the equations of motion, can be calculated analytically as the negative gradients of the total potential energy with respect to the atomic positions:

$$F_i = -\nabla_i E_{system} \quad (2.36)$$

SYSTEM REPRESENTATION

The energy $E_{i,atomic}$ of each atom is typically obtained by considering its local chemical environment illustrated on figure 2.10 and defined by a cutoff radius R_c . To have a continuous and differentiable energy, necessary to enable the calculation of the forces, a cutoff function is generally used. A prototypical example is the monotonously decaying part of the cosine function [219]:

$$f_c(R_{ij}) = \begin{cases} 0.5 \left[\cos \left(\pi \frac{R_{ij}}{R_c} \right) \right] & \text{for } R_{ij} < R_c \\ 0 & \text{for } R_{ij} \geq R_c \end{cases} \quad (2.37)$$

where $R_{ij} = |\mathbf{r}_i - \mathbf{r}_j|$.

The input of each atomic NN, which has to be a fixed size vector, can be constructed using atom-centered symmetry functions that describe the local chemical environments and which should not change with the number of atoms in the cutoff sphere. It is desirable for these input coordinates to incorporate the

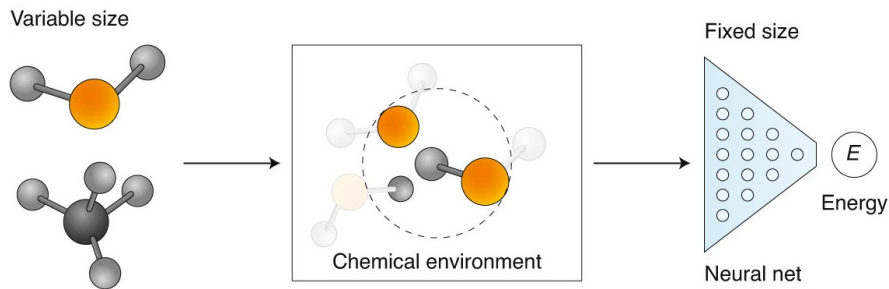


Figure 2.10: Representation of atom centered local chemical environments as a fixed-size representation of a system of arbitrary size. Adapted from Ref. [215].

translational, rotational, and permutational invariances of the system. A variety of different functional forms are available for these symmetry functions. Among the radial symmetry functions, the most commonly used consists of a sum of products of Gaussians and cutoff functions for all atoms j inside the cutoff sphere:

$$G_i^2 = \sum_j e^{-\eta(R_{ij}-R_s)^2} \cdot f_c(R_{ij}) \quad (2.38)$$

where η is a parameter that determines the effective spatial extension of the radial function and R_s an optional shift parameter.

An alternative to this use of static descriptors, where the symmetry functions are predefined, is to use dynamic descriptors, *i.e.* to optimize the input vectors in a data-driven way. This can be done *a priori*, or can be optimized during the training of the model. It is the strategy NequIP relies on to choose the functional form of its radial basis $R_\alpha(R_{ij})$, where α is a shorthand for a set of parameters corresponding to its architecture. It uses a multi-layer perceptron, *i.e.* a fully connected feed-forward NN, to implement a learnable radial basis [224]:

$$R_\alpha(R_{ij}) = \text{MLP}(R_n(r_{ij})f_c(r_{ij})) \quad (2.39)$$

where *MLP* is a multi-layer perceptron and R_n are a set of Bessel basis polynomials.

2.4.3 Equivariant message passing neural networks

One of the limiting factors in the development MLPs is the collection of large training sets of *ab initio* calculations, often including thousands or even millions of reference structures. In this work, we used the Neural Equivariant Interatomic Potential (NequIP) [212], an equivariant message passing NN, which has been proposed as a highly data-efficient approach (requiring in some cases fewer than 1,000 reference calculations) and has demonstrated high accuracy across a wide variety of systems, including in a recent study on MOF systems [221] (see section 4.1 for more details). I will now present this particular NN architecture, fully described in Ref. [212] and [224].

MESSAGE PASSING NEURAL NETWORKS

NequIP is a *message passing neural network* (MPNN) [217, 224], meaning that it belongs to a class of graph neural networks [225] that can parametrize a mapping from the space of labeled graphs to a vector space of features. In a typical graph NN architecture for NNPs, atoms correspond to the nodes of the graph, and an edge connects two nodes if their distance is less than a cutoff R_c . Figure 2.11a represents such a graph.

In MPNN methods, the descriptors are not predefined but automatically learned from the geometric structure. Each atom is described by a state $\sigma_i^{(t)}$ that we denote with the tuple:

$$\sigma_i^{(t)} = (r_i, \theta_i, h_i^{(t)}) \quad (2.40)$$

which contains the Cartesian position r_i , a set of its fixed attributes such as the chemical element θ_i and learnable features $h_i^{(t)}$, where t denotes the message passing iteration. They are illustrated on figure 2.11b.

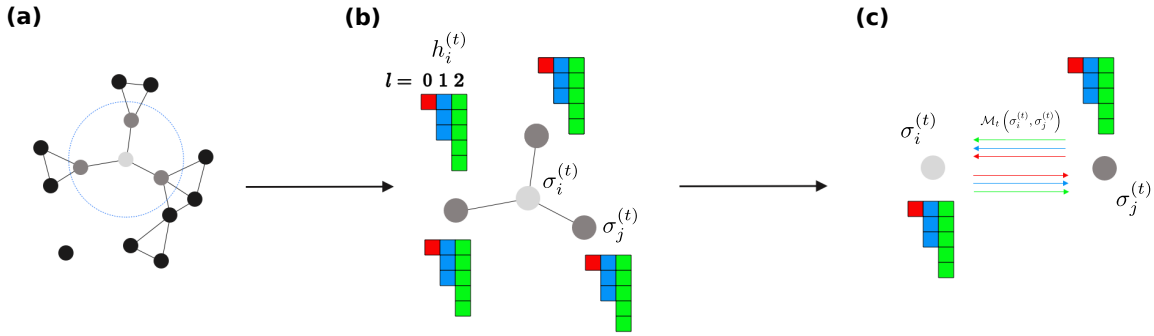


Figure 2.11: (a) The system is represented with an atomic graph. (b) Each atom is described by a state $\sigma_i^{(t)}$ which relies on scalar ($l = 0$, red), vector ($l = 1$, blue), and higher-order tensor ($l \geq 2$, green) features $h_i^{(t)}$, (c) updated using message functions \mathcal{M}_t . Adapted from Ref. [212].

In an MPNN, these learnable features are iteratively updated in a message passing phase using aggregated messages $m_i^{(t)}$ processing information about neighboring atoms $\mathcal{N}(i)$ as illustrated on figure 2.11c. These aggregated messages are obtained with learnable message functions \mathcal{M}_t , and will change the states $\sigma_i^{(t+1)}$ through learnable update functions U_t :

$$\begin{aligned} m_i^{(t)} &= \sum_{j \in \mathcal{N}(i)} \mathcal{M}_t(\sigma_i^{(t)}, \sigma_j^{(t)}) \\ h_i^{(t+1)} &= U_t(\sigma_i^{(t)}, m_i^{(t)}) \end{aligned} \quad (2.41)$$

This iterative process allows information to be propagated along the atomic graph through a series of convolutional layers (one per t). Message passing can therefore be understood as a convolution operation running over each node in a graph, and benefits from the broad adoption of convolution neural networks in the ML literature.

Once the message passing phase has been completed after a number of steps, the resulting atomic states are used in a readout phase to predict the atomic site energies with learnable functions \mathcal{R} :

$$E_i = \mathcal{R}(\sigma_i^{(t)}) \quad (2.42)$$

EQUIVARIANT NEURAL NETWORKS

Equivariant neural networks are a class of NN that are explicitly constructed from equivariant operations to guarantee the preservation of known transformation properties of physical systems under a change of coordinates corresponding to some symmetry operations. For example, if a molecule is rotated in space, the vectors of its forces also rotate accordingly, while its energy remains unchanged. The symmetry group of Euclidean symmetries in three-dimensional space, denoted $E(3)$ and which includes translations, rotations, and reflections is of special interest for atomistic modeling.

A function is said to be *equivariant* with respect to a group if we can act with the group on the inputs or the outputs of the function and are guaranteed to get the same answer. Formally, a function $f : X \rightarrow Y$ is equivariant with respect to a group G that acts on X and Y if:

$$D_Y[g]f(x) = f(D_X[g]x) \quad \forall g \in G, \forall x \in X \quad (2.43)$$

where $D_X[g]x$ and $D_Y[g]$ are the representations of the group element g in the vector spaces X and Y . NequIP uses an underlying NN architecture equivariant with respect to $E(3)$, called Euclidean neural networks (e3nn) [226].

A convenient way to ensure that the outputs of a NN model transform correctly to symmetry operations is to impose constraints on the internal representations of the model, namely the feature $h_i^{(t)}$ and messages $m_i^{(t)}$. In e3nn, the representations can be comprised of scalars, vectors, and higher-order tensors as represented on figure 2.11b.

The way they transform under rotations can be classified using representations of rotations, which are indexed by an integer l corresponding to the spherical harmonics. Scalars correspond to $l = 0$ (invariant under rotation), vectors to $l = 1$, and higher order quantities like for instance the d, f, g atomic orbitals transform with higher l . l is a hyperparameter in NequIP, as different values of l can be chosen to represent the feature vectors. The founding article found that the choice of $l \in \{1, 2, 3\}$ outperformed $l = 0$ in terms of sampling efficiency [212].

Complementing the invariant scalar features ($l = 0$) of more established MPNNs, such as SchNet [227] or DeePMD [228], with equivariant features is what makes equivariant MPNNs distinctive in their data efficiency [221].

NEQUIP ARCHITECTURE

The Neural Equivariant Interatomic Potential (NequIP) has been proposed in 2021 by Batzner et al. [212] as the first equivariant NNP architecture, shortly followed by other equivariant MPNNs. Its specific architecture is detailed in Ref. [212, 224] and is shown on figure 2.12.

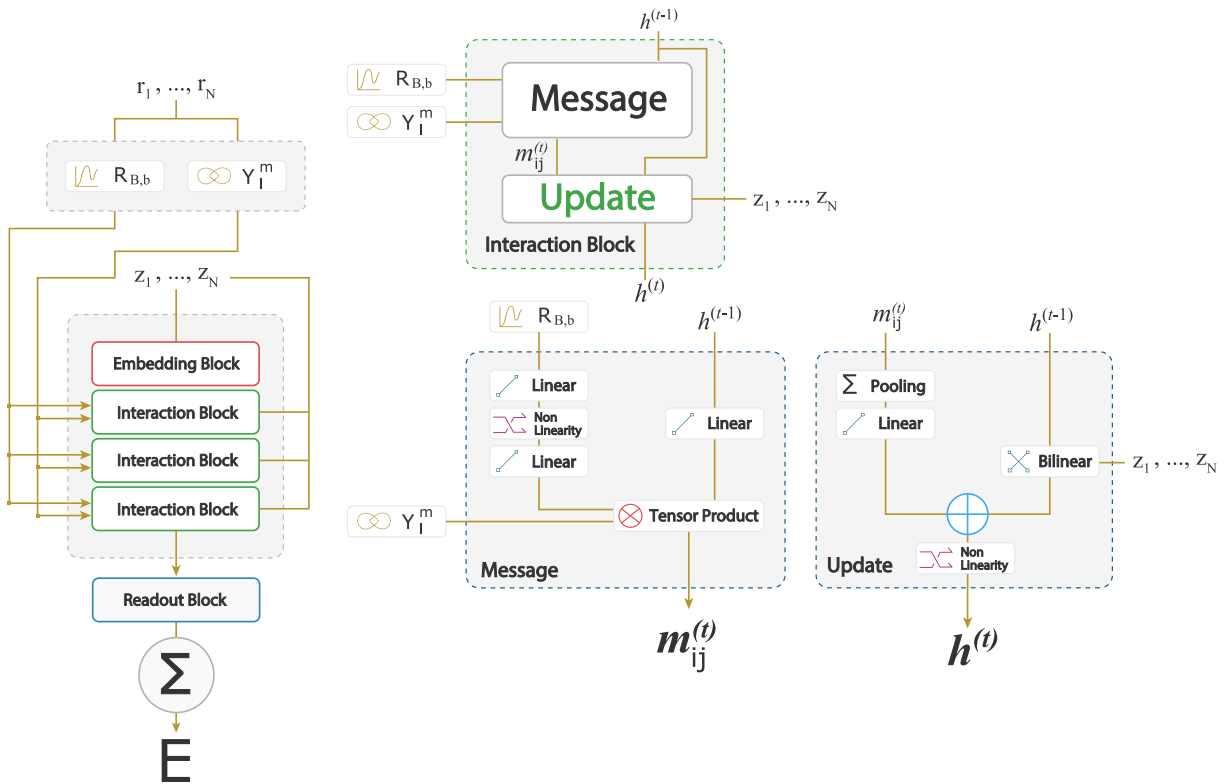


Figure 2.12: Schematic of the NequIP architecture. Adapted from Ref. [224].

The inputs of the NN are the positions \mathbf{r}_i and chemical species Z_i . Features and messages are expressed using spherical coordinates to achieve rotation equivariance. This is achieved by using, for the message passing phase, convolution filters $S_m^{(l)}(\mathbf{r}_{ij})$ which are products of learnable radial functions $R_\alpha(r_{ij})$ (introduced in equation (2.39)) and spherical harmonics $Y_m^{(l)}(\hat{\mathbf{r}}_{ij})$:

$$S_m^{(l)}(\mathbf{r}_{ij}) = R_\alpha(r_{ij}) Y_m^{(l)}(\hat{\mathbf{r}}_{ij}) \quad (2.44)$$

The NN architecture consists in a series of blocks, starting with an embedding block which generates initial features $h_i^{(0)}$ and therefore states $\sigma_i^{(0)}$. It is followed by a series of interaction blocks which encode interactions between neighboring atoms. It corresponds to the message passing phase described by equation (2.41), with each block having the $\sigma_i^{(t)}$ as input and $\sigma_i^{(t+1)}$ as output. The final output of the NN is obtained after a readout block (equation (2.42)) which gives the total potential energy of the system E as the sum of atomic potential energy (equation (2.35)), and therefore the forces by taking the gradients (equation (2.36)).

2.5 CHARACTERIZING STRUCTURAL PROPERTIES OF AMORPHOUS MODELS

A number of structural properties can be computed by analyzing the atomic structure of every frame of an MD trajectory. Those used in this PhD will be introduced in this section, along with the Python package *aMOF* that I developed for this task and published as open source (section 2.5.5). This section is primarily methodological, as the meaning and specific analysis of each property will be introduced where relevant in the subsequent chapters.

Unlike crystals that can be entirely described by their unit cell, it is inherently impossible to reduce an amorphous material to a small finite set of atomic coordinates. Each atomic structure should best be seen as statistically representative of a plausible local configuration, and averaging is therefore crucial. To complicate matters further, there is no unique amorphous phase per framework, as the structure and properties often depends on the formation route.

To illustrate the diversity of *aMOF* structures reported in the literature detailed in section 1.3, some properties will be computed on single frame models of *aZIF-4* obtained as a CRN [139], by RMC [92] and with ReaxFF [155]. These files were either extracted from the supporting information or communicated to us by the authors. They are compared to AIMD trajectories of a previous work in the group [123], which sampling is detailed in section 3.2. For further reference, ZIF-4 is described in section 1.2.3, and each of these models in section 1.3. Although it is merely illustrative, this direct comparison between models has never been published in the literature before.

2.5.1 Local order

Multiple properties can be constructed to investigate the local order, to get insight into the local chemical environment of each atom in the system.

RADIAL DISTRIBUTION FUNCTION

The radial distribution function (RDF) $g(r)$, also known as pairwise correlation function, represents the probability of finding an atom in a spherical shell of radius r and thickness Δr as illustrated on figure 2.13a.

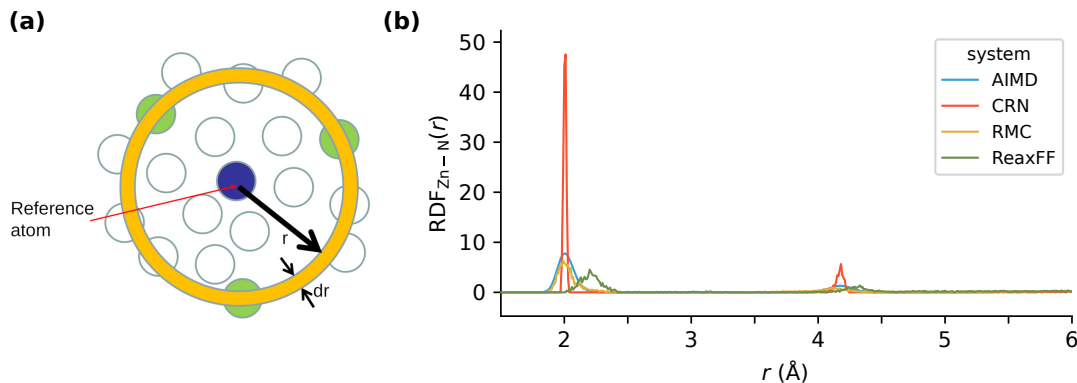


Figure 2.13: (a) Illustration of atoms of a species B (green) comprised in a spherical shell around the reference atom of species A (blue). (b) Radial distribution functions (RDF) for the Zn–N atom pairs of various *aZIF-4* models. (a) is adapted from Ref. [208].

The total RDF is defined as the sum of all pairwise RDF. For 2 atomic species A and B, the partial RDF for atoms A around B is the sum over A atoms of all pairwise RDFs with B atoms and can be computed from:

$$g_{AB}(r) = \frac{V_{cell}}{4\pi r^2 \Delta r N_A N_B} \sum_a^{N_A} n_{a,B}(r, \Delta r) \quad (2.45)$$

where V_{cell} is the volume of the cell, N_A (N_B) the number of A (B) atoms in the cell and $n_{a,B}(r, \Delta r)$ the number of B atoms in a shell of radius r and thickness Δr around atom a .

For unambiguous definitions of many commonly used correlation functions, and how they relate to scattering factors I recommend Ref. [229]. Example RDFs for the Zn–N pair in various *a*ZIF-4 are shown on figure 2.13b.

COORDINATION NUMBER

The coordination numbers CN_{AB} inside a given radius R_c , is the number of atoms of type B bonded to atoms to type A . It can formally be obtained by integrating $g(r)$:

$$CN_{AB}(r_c) = \int_0^{r_c} \frac{N_B}{V_{cell}} g_{AB}(r) 4\pi r^2 dr \quad (2.46)$$

Although in practice it is computed by simply counting the number of atoms in each coordination sphere of radius R_c . In this PhD, Zn–N coordination numbers are computed by taking a cut-off radius of 2.5 Å, a value determined based on the Zn–N potential of mean force, and validated in previous *ab initio* studies [92, 123, 149]. We checked that the outcome of the calculations for ReaxFF systems is not strongly dependent on the exact value chosen, in the 2.5–2.7 Å range. Table 2.2 contains an example for various *a*ZIF-4 models.

System	AIMD	CRN	RMC	ReaxFF
Zn-N coordination number	3.93	4.00	3.96	3.56

Table 2.2: Coordination numbers for nitrogen atoms around the zinc cation of various *a*ZIF-4 models.

BOND ANGLE DISTRIBUTION

The bond angle distribution of a species A with respect to species B is the histogram of the bond angles calculated between atoms A and all their B neighbors (in their first coordination sphere). For an atom A and two neighbors B and C the bond angle is:

$$\theta_{BAC} = \cos^{-1} \left(\frac{(\mathbf{r}_B - \mathbf{r}_A) \cdot (\mathbf{r}_C - \mathbf{r}_A)}{|\mathbf{r}_B - \mathbf{r}_A| |\mathbf{r}_C - \mathbf{r}_A|} \right) \quad (2.47)$$

where \mathbf{r}_X is the position of atom X [230].

This distribution depends on the cut-off radius R_c defining the first coordination sphere, which is in this work the same as for coordination numbers introduced above. An example is shown on figure 2.14.

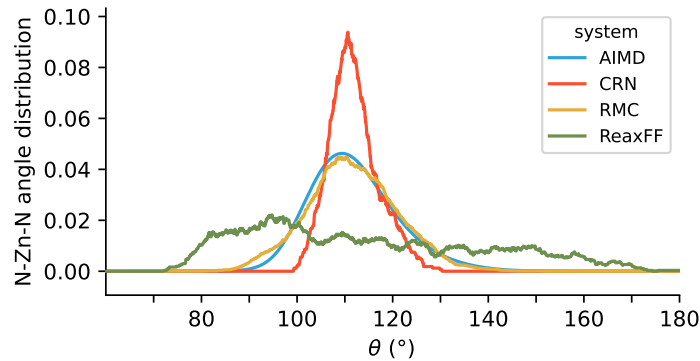


Figure 2.14: Distribution of the N–Zn–N angle for various *a*ZIF-4 models.

POTENTIAL OF MEAN FORCE

The potential of mean force (PMF) [231] is computed from partial radial distribution functions $g(r)$ through the relation:

$$F(r) = -k_B T (\ln g(r) - \ln g_{\max}) \quad (2.48)$$

where g_{\max} is the maximum of $g(r)$ over r which is used to arbitrarily enforce $F(r) = 0$ for the lowest free-energy minimum [92].

The angular PMF is computed from the angle distribution $P(\theta)$ through the analog relation [232]:

$$F_{ang}(\theta) = -k_B T (\ln P(\theta) - \ln P_{max}) \quad (2.49)$$

The PMF curves can highlight areas of the coordinate space where the RDF and bond angle distributions have very small, but nonzero, values. They are not shown for the models of this section as it requires a trajectory with a sufficient number of frames to remove the noise in g or P before taking the logarithm. Figure 3.2 later in the thesis provides an example plot.

2.5.2 Bulk properties**DENSITY**

Although the density is straightforward to compute numerically $\rho = m_{cell}/V_{cell}$, it is a key characteristic of amorphous systems that is particularly hard to measure experimentally. The density that can be computed numerically corresponds to the *crystallographic* density, *i.e.* the density obtained from diffraction experiments, sometimes called *skeletal* density [233]. It is different from the pycnometric density, obtained through *pycnometric* densities measurements, sometimes called *apparent* density. This crystallographic density is particularly hard to estimate experimentally for amorphous solids as diffraction experiments are severely complicated [233] (see section 3.2.2 for further discussion).

Table 2.3 illustrates how different models show remarkably distinctive values and I will discuss later in chapter 3 and chapter 5 the impact of the model density on the structural and mechanical properties of the frameworks.

System	AIMD	CRN	RMC	ReaxFF
Density (g cm ⁻³)	1.21	1.00	1.58	1.59

Table 2.3: Densities of various *a*ZIF-4 models.

PORE STATISTICS

Pore statistics were computed on individual frames with the Zeo++ software [234–236], which uses a geometric decomposition of space to compute the accessible and non-accessible volume to a sphere of a given radius. I generally report the total porous volume, which is defined as the sum of accessible and non-accessible volumes. I used a helium probe of radius 1.2 Å and the high accuracy (-ha) option.

Total porous volumes of the four *a*ZIF-4 models are reported on table 2.4. In this case it is a single value, but distributions can be reported for trajectories with multiple frames as illustrated on figure 3.14.

System	AIMD	CRN	RMC	ReaxFF
Total porous volume (cm ³ kg ⁻¹)	68.1	111.8	4.9	7.1

Table 2.4: Total porous volume of various *a*ZIF-4 models.

2.5.3 Topology

While amorphous systems have no long-range order by definition, investigating the medium-range order of various glasses allows contrasting their structures. Characterizing the topology [237] at larger scale, known to be key to the properties of these framework materials [70], is usually done by examining the coordination network. This network is built from the alternating node-ligand units, *i.e.* Zn and imidazolates (Im) in the case of ZIF-4 as illustrated on figure 2.15a.

RINGS STATISTICS

Ring analysis, routinely used to characterize zeolites [238] or amorphous systems such as SiO₂ [239], determines the number and size of rings present in the ZIF network. Ring sizes are computed by counting the number of different units (Zn and Im) in each ring; always even, they are equal to twice the T-based ring sizes usually reported for zeolitic nets [69].

Ring statistics were computed using the R.I.N.G.S. code [239] on the Zn–Im periodic graph (due to PBC) obtained after identification of the building units. The vertices of this graph are the Zn atoms and Im linkers, and its edges are the Zn–Im bonds.

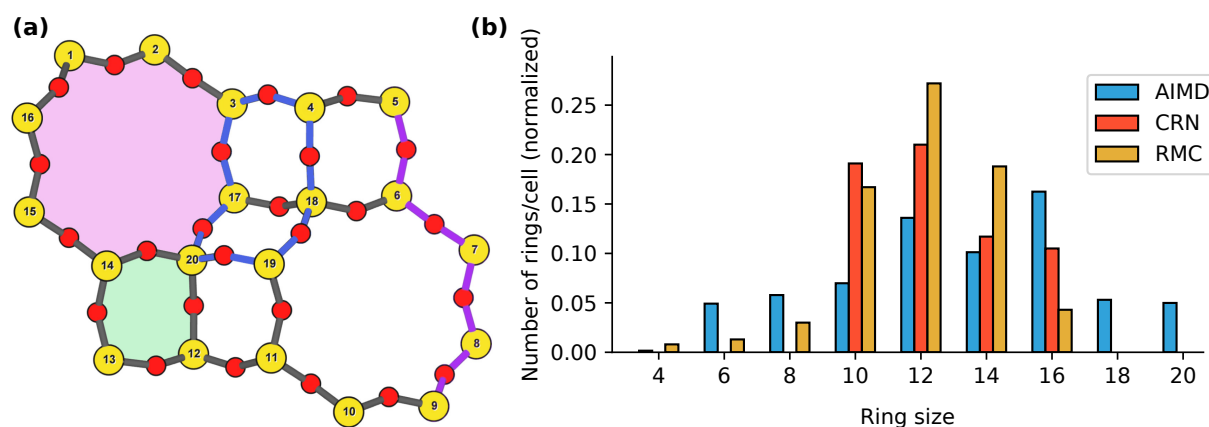


Figure 2.15: (a) Cartoon Zn (yellow)–Im (red) graph showing a path (5-6-7-8-9, purple), a cycle (3-4-18-19-20-17, blue) bonds, and primitive rings of size 16 (pink) and 8 (green). (b) Distributions of size of Zn–Im alternate rings for three *a*ZIF-4 models. (a) is reproduced from Ref. [238].

Out of the multiple definitions and enumerations of rings presented in the literature [238], the definition of rings used in this work corresponds to the definition of “primitive rings”, first introduced by Mariani [240] and used in the R.I.N.G.S. code [239]. Several names referring to the same mathematical object can be found in the literature, and this definition is equivalent to that of “shortest path ring” by Franzblau [241], of “minimal ring” by Guttman [242], of “irreducible ring” by Wooten [243] and of “rings” by Goetzke and Klein [244].

A path between vertices y and z of length k is a chain of k edges joining y to z , in which at most two edges share any vertex. A cycle is a closed path, *i.e.* which returns to its starting point. A ring is a cycle of a graph which contains a shortest path for each pair of vertices. A detailed outline of this terminology can be found in Franzblau [241] or in any of the other references above, with multiple concepts illustrated on figure 2.15a.

During my PhD I used a maximum search depth of 32, safely above the largest rings of the ZIF-4 crystal (16), and checked that for the studied ZIF-4 glasses the choice of the maximum search depth did not significantly affect the analysis and conclusions drawn.

These distributions of ring sizes in our three examples reported on figure 2.15b, show that *a*ZIF-4 models have distinct topologies, highlight structures more or less ordered at medium range. ReaxFF

is not reported as the model provided to us showed open imidazolate rings (see discussion later in section 3.1.3).

IDENTIFICATION OF BUILDING UNITS

The identification of building units – Zn and Im – is a prerequisite to the creation of the Zn-Im graph that is used to compute ring statistics. As it is more challenging for glasses than for crystals, I developed a Python module, part of the *aMOF* library (see section 2.5.5) to reduce the atomic structure into a structure made of Zn and Im units.

The goal of this code is to reduce the ZIF-4 atomic structure (composed of Zn, N, C and H atoms) into a structure made of Zn bonded to Im ($C_3N_2H_3$), which requires the identification of the imidazolates. It is illustrated on figure 2.16. Several codes exist to make this identification for crystalline MOFs, such as *molsys* from the Computational Materials Chemistry (CMC) group at the Ruhr-University Bochum [205], the clustering tools of ToposPro [245], CrystalNets.jl [246], or MOFid [247].

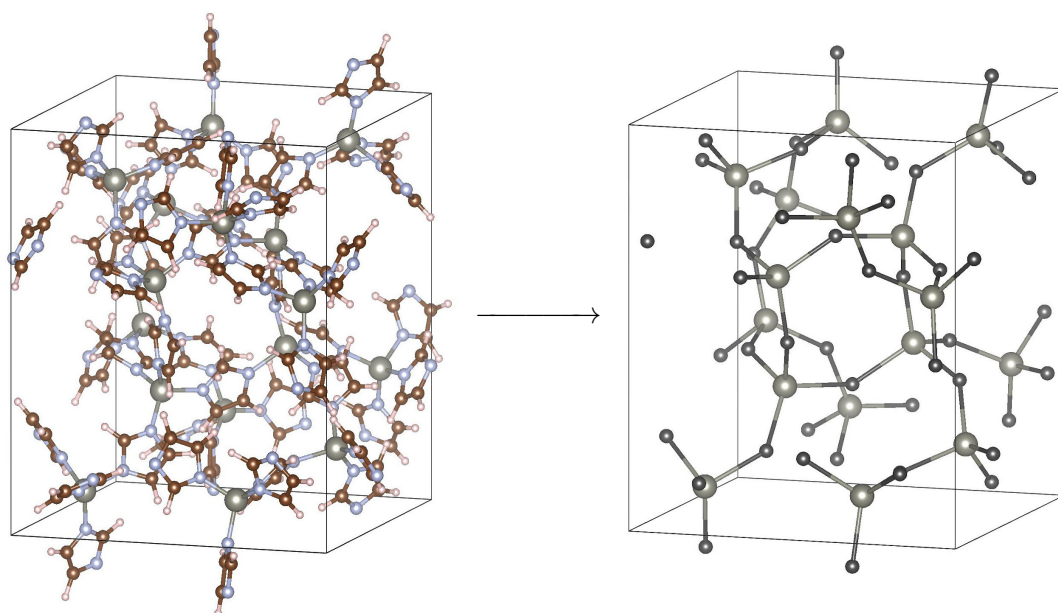


Figure 2.16: ZIF-4 crystal before and after identification of building units and reduction to a Zn-Im graph. Zn, grey; C, brown; N, blue; H, white; Im, black.

Yet, amorphous models are by definition not as regular as crystals. This calls for a robust method to identify the building units, which requires an adaptation of the routines designed for crystals. One particular issue comes from the broad distribution of atomic positions, especially in high-temperature liquids. For example, it is frequent in these amorphous structures to find a C or N atom in an imidazolate Im_1 , to be closer to a C/N atom of another imidazolate Im_2 than to the expected C/N atoms of Im_1 . Therefore, “neighboring” atoms cannot straightforwardly be deduced from their distance.

I have developed the method presented here, and designed to be compatible with *molsys* [205]. It is *ad hoc* for ZIF-4 and has been tested on several amorphous ZIF-4: *ab initio* liquids [92] and glasses [123], RMC glasses [87, 92], a CRN glass [141], and the liquids and glasses of this present work (ReaxFF of chapter 3 and AIMD and MLP of chapter 4).

Throughout the algorithm, two atoms are said to be “nearby” if their relative distance is smaller than a cutoff distance. The cutoff is a function of the atomic species and computed from the covalent radii as in *molsys* [205]. The explicit values used in this thesis are 1.752 Å, 1.728 Å, 1.4976 Å and 2.895 Å respectively for C–C, C–N, C–H and Zn–N.

Imidazolates (Im) are then identified with the following procedure:

1. Construct a graph whose vertices are the C and N atoms, and with edges between nearby [C, N] and [C, C] atoms.
2. Find every cycle C,N,C,N,C in this graph. Each atom in a given cycle is part of the same Im.
3. For every C atom, find nearby H atoms¹ and add them to the Im containing C.

Zn and Im are considered bonded if there is an N atom in Im which is nearby Zn.

2.5.4 Characterizing liquids

Contrasting liquids from solids is crucial for the production of glass systems by melt-quenching. As it is not straightforward to distinguish static structural properties between a liquid and an amorphous solid, I used in my PhD two metrics to identify liquids.

MEAN SQUARE DISPLACEMENT

Melting can first be evidenced by computing the mean square displacement (MSD). The MSD $\langle \mathbf{r}^2 \rangle$ of an atomic species A is defined as the mean-squared distance over which the atoms A have moved in a time interval t : [178]

$$\langle \mathbf{r}^2 \rangle(t) = \langle (\mathbf{r}(t) - \mathbf{r}(0))^2 \rangle = \lim_{T \rightarrow \infty} \frac{1}{T} \int_{-T/2}^{T/2} d\tau (\mathbf{r}(t + \tau) - \mathbf{r}(\tau))^2 \quad (2.50)$$

defined when the system is at equilibrium in $] - T/2, T/2[$ and $T \gg t$ [248].

For clarity, displacements $\mathbf{r}_i(t)$ can formally be defined based on velocities $\mathbf{v}_i(s)$ to implicitly consider that the periodic boundary conditions are properly handled:

$$\mathbf{r}_i(t) - \mathbf{r}_i(0) = \int_0^t \mathbf{v}_i(s) ds \quad (2.51)$$

In a liquid-like system, the MSD is linear with time t , following the relation:

$$\frac{\partial \langle \mathbf{r}^2 \rangle}{\partial t} = 6D \quad (2.52)$$

where D is the diffusion coefficient and 6 the numerical prefactor for 3D systems [178]. As illustrated on figure 2.17, it is therefore straightforward to contrast it from a solid for which the MSD will quickly reach a plateau as the atoms do not migrate.

In practice, from a MD trajectory the MSD can be directly computed compared to the first frame:

$$\langle \mathbf{r}^2 \rangle(t) = \frac{1}{N_A} \sum_{i=1}^{N_A} |\mathbf{r}_i(t) - \mathbf{r}_i(0)|^2 \quad (2.53)$$

Or when the first frame has no specific physical meaning, it is possible to use a so-called window MSD with a double average over time and over the atoms of the systems:

$$\langle \mathbf{r}^2 \rangle(t) = \frac{1}{N_A} \sum_{i=1}^{N_A} \frac{1}{T-t} \sum_{\tau=0}^{T-t-\delta t} (\mathbf{r}_i(t + \tau) - \mathbf{r}_i(\tau))^2 \quad (2.54)$$

¹There should be one and only one H for non-defective models

where T is the time of the last frame of the trajectory, and δt the time step. Although both methods are implemented in *aMOF*, I used the window MSD in this PhD.

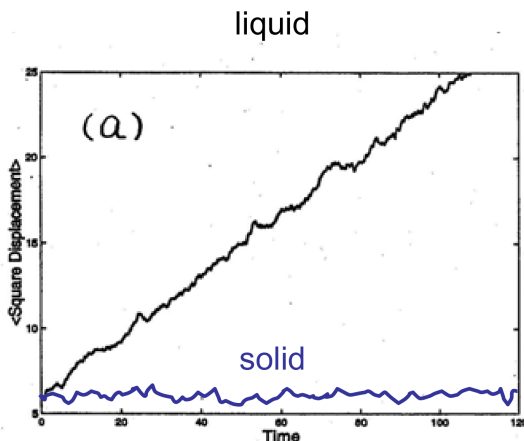


Figure 2.17: Typical MSD for liquid and solid states. Reproduced from [208].

LINDEMANN RATIO

The generalized Lindemann ratio Δ is a property which quantifies the liquid nature of the system [249]. A solid is usually considered to be melting when the value of this ratio is between 10 and 15%.

Δ is computed from partial radial distribution functions $g(r)$, following the same procedure as previous *ab initio* studies [92, 123, 149]:

$$\Delta = \frac{\text{FWHM}}{d_0} \quad (2.55)$$

where FWHM is the full width at half-maximum of the first peak in $g(r)$ and d_0 corresponds to the mean interatomic distance. d_0 is calculated as the distance r corresponding to the maximum of the first peak of $g(r)$. FWHM is estimated by a Gaussian fit, illustrated on two examples on figure 2.18. To be able to fit a Gaussian on noisy data (e.g. high temperature, few neighbors and time steps), I first used signal processing routines from *scipy* [250] to find the peaks. A Gaussian was then fitted on the upper part ($g(r) \geq \text{FWHM}_{\text{peak}}$) of the first peak. Both MSD and Δ are shown on the same trajectories later in the manuscript in figure 3.11.

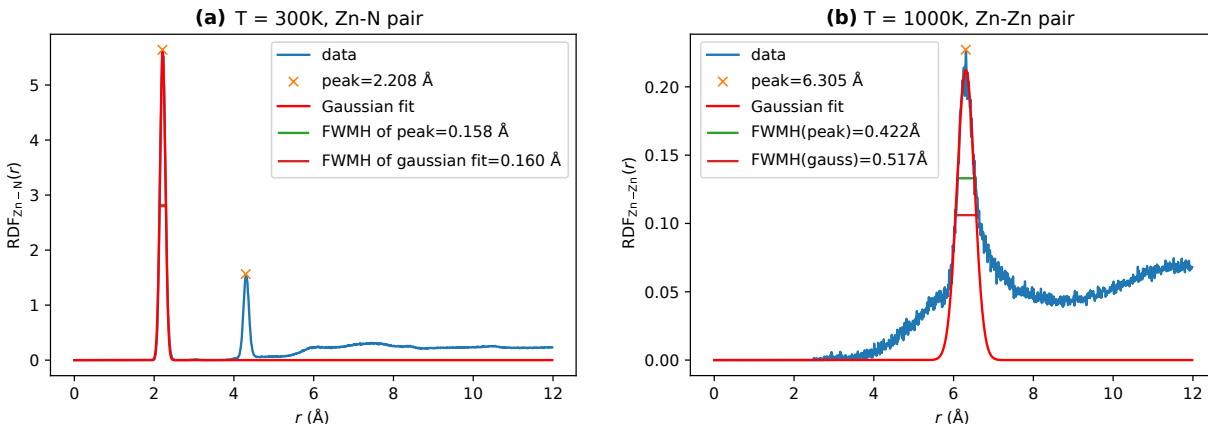


Figure 2.18: Computation of the FWHM with a Gaussian fit on (a) nicely defined and (b) noisy RDFs depending on the temperature (T) and atom pair.

2.5.5 *aMOF*, a Python library

To systematize all the trajectory analyses performed during my PhD, I developed *aMOF*, a Python package gathering a collection of tools to analyze MD trajectories of *aMOFs*

FUNCTIONALITIES

This package brings together a number of analyses that can be performed on every MD trajectory (not necessarily MOFs), heavily using both other Python packages and non-Python codes. It can compute the following properties:

- Radial distribution functions (RDF), based on ASAP, an ASE calculator [251].
- Bond angle distributions
- Coordination numbers
- Mean square displacement (MSD)
- Elastic constants from cell properties, and mechanical properties from elastic constants by calling ELATE [252]
- Pore analysis by wrapping Zeo++ [234–236], reusing code from pysimm [253]
- Ring statistics by wrapping the R.I.N.G.S. code [239]

The backend for manipulating trajectories is the atomic simulation environment (ASE) [251], by using ASE trajectory objects.

A module called `coordination` allows the identification of the different building blocks of amorphous MOFs with an *ad hoc* approach per MOF system. Only ZIF-4 is officially supported in the current stable release, although any (Zn, Im) or (Zn, mIm) ZIFs are *a priori* supported.

This code is designed to be compatible with `molsys` [205], and can be used to generate input files in the `mfpX` format.

AVAILABILITY

aMOF is available online on <https://github.com/coudertlab/amof>. This github repository also contains example analyses as well as instructions to construct the documentation.

aMOF can be installed directly from source or alternatively from PyPI:

```
pip install amof
```

CHALLENGES IN MOLECULAR DYNAMICS OF *a*ZIFs USING REACTIVE FORCE FIELDS

3.1	Producing glass models with <i>in silico</i> melt-quenching	73
3.1.1	System and methods	73
3.1.2	Preparation of the crystal	74
3.1.3	Melt-quenching	75
3.1.4	Choice of the melting temperature	76
3.1.5	Equilibration	79
3.2	Properties of the glass models	80
3.2.1	Local order: interatomic distances and bond angles	80
3.2.2	Bulk properties: density and porosity	83
3.2.3	Topological properties of the coordination network	83
3.3	Challenges in using ReaxFF	85
3.3.1	(<i>N, P, T</i>) ensemble and densification.	85
3.3.2	Description of the crystal.	86
	Conclusions and perspectives	91



I first explained in chapter 1 that the determination of the framework structure of amorphous MOFs at the microscopic scale is experimentally difficult, with diffraction experiments only providing indirect structural information. I then highlighted that in order to work around or alleviate this challenge, an array of computational methods coexist to model these disordered materials, with different scopes, scales and computational costs. One possible strategy consists in simulating the phase transition from a crystalline MOF to the amorphous state using molecular dynamics (MD) to mimick *in silico* the experimental formation routes. It is this strategy that I have explored during my PhD and that I will describe in detail in the next two chapters.

In prior work in my group by Romain Gaillac, *ab initio* molecular dynamics have successfully been used to model the melting of crystalline MOFs into liquids [92, 93, 149], and generate configurations of melt-quenched glasses [123]. However, this approach has a very significant computational cost which limits its use to small systems and short time scales. Classical MD simulations, routinely used for crystalline MOFs, do not provide a computationally efficient alternative as they are unable to simulate

bond breaking or reformation, two processes inherent to the formation of most amorphous MOFs [146].

Reactive force fields have then been proposed as a trade-off between chemical accuracy and computation cost. These empirical force fields, whose principles have been detailed in section 2.3.3, possess connection-dependent terms that enable the simulation of bond breaking and reformation [153]. We saw in section 1.3.5 that, starting with the work of Yang et al. [155], several studies relied on reactive force fields to generate models of zeolitic imidazolate frameworks (ZIFs) glasses by melt-quenching. However, I want to highlight that in the existing literature, the generated models have not been subjected to direct and in-depth comparison with those obtained by alternative approaches.

In this chapter, I probe the accuracy and reliability of modeling the formation and structure of amorphous ZIFs using the ReaxFF reactive force field. I first reproduced the melt-quenching procedure used in prior works [155], highlighting several difficulties and suggesting adaptations to the scheme. I then detailed the structure of the resulting glasses and compared it to *ab initio* data [123], contrasting their properties and commenting on some peculiarities of the glasses obtained with reactive force fields. This study has been published in *The Journal of Physical Chemistry C* (2022) [254].

3.1 PRODUCING GLASS MODELS WITH *IN SILICO* MELT-QUENCHING

In order to generate atomistic models of ZIF glasses, I have decided to follow the melt-quenching route, reproducing with molecular dynamics simulations the increase in temperature to produce a liquid ZIF [92], followed by a quench back to room temperature to produce a glass. This general procedure, mimicking the experimental reality (albeit at length and time scales that are much shorter), has long been used to model the structure of multiple glass-forming materials such as chalcogenide compounds or silicates [121, 122, 255]. It has previously been used in simulations of ZIFs, both with a reactive force field [155] and with *ab initio* MD [123].

In this work, I followed the same general melt-quenching procedure with small adaptations. Using the ReaxFF force field introduced by Yang et al. [155], an initial crystalline structure was prepared and heated up to 300 K, allowing us to measure the properties of the ZIF in its crystalline phase. Then, the system was melted by heating it up to a maximal temperature (well above the melting point). The produced liquid was then quenched to room temperature, transitioning into the glass state. Finally, the system was equilibrated, and its structural and dynamic properties were calculated. Both the melt-quenching and the equilibration were performed in the constant-pressure (N, P, T) ensemble to be able to capture changes in density during the formation. The four steps of this procedure are represented on figure 3.1 and are detailed in the following sections.

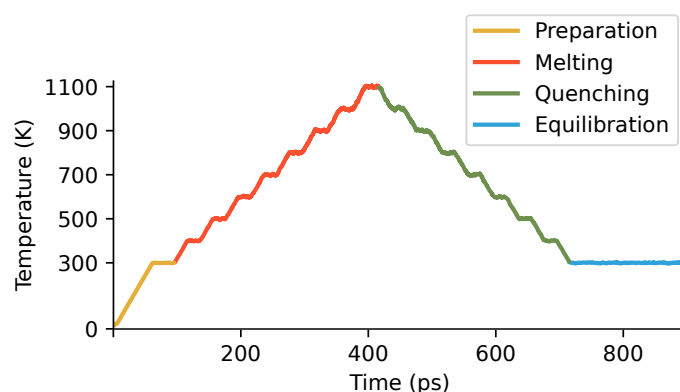


Figure 3.1: Temperature as a function of time during the glass formation procedure with ReaxFF, consisting of preparation (orange), melting (red), quenching (green) and equilibration (blue). Plateaux are present to collect statistics during melt-quenching. For clarity, only the start of the equilibration is shown, and a moving average over 250 fs is used. An enlarged plot of the preparation is presented on figure 3.3.

3.1.1 System and methods

Our system throughout this study will be ZIF-4, which is built up from Zn^{2+} metal nodes and imidazolate (Im) organic linkers and that I previously described in section 1.2.3. The first discovered amorphous MOF [84], it has since been the subject of numerous studies, both experimental and numerical (see chapter 1), thus providing a prototypical amorphous ZIF system.

All simulations were performed using LAMMPS [211, 256], with the ReaxFF force field introduced by Yang et al. [155] and further detailed in section 1.3.5 and section 2.3.3. A timestep of 0.25 fs was used in the MD runs and, the temperature (and pressure when applicable) were controlled using a Nosé–Hoover thermostat (and barostat), introduced in section 2.1.3. Unless otherwise specified, temperature and pressure damping parameters were fixed at 100 fs and 1000 fs respectively. At every stage, several values were tested to check the relevance of this range. By default, constant-pressure (N, P, T) simulations were performed using an isotropic cell, using the LAMMPS keyword `i so`. To reduce finite size effects, a

($2 \times 2 \times 2$) supercell of ZIF-4 with 2176 atoms was simulated with PBCs, as in Yang et al. [155]. I checked that it does not significantly affect the properties of the generated glasses, as shown on figure 3.2.

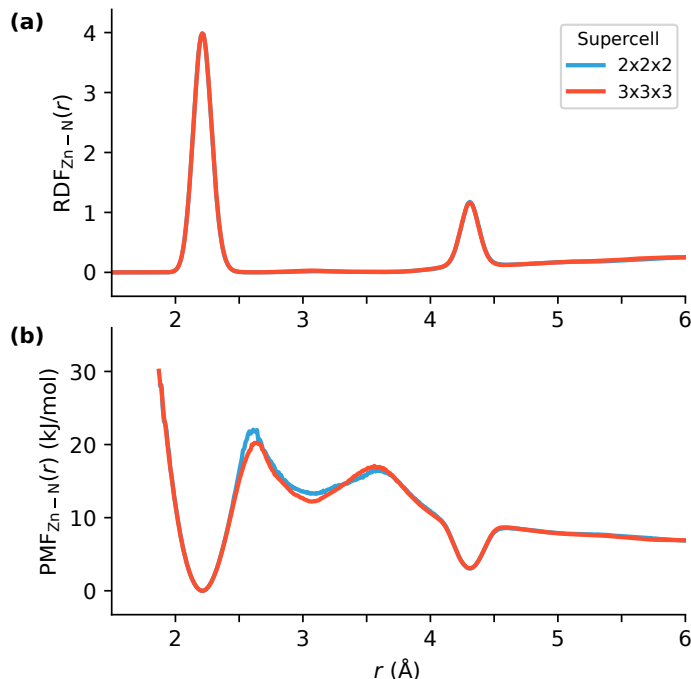


Figure 3.2: (a) Radial distribution functions (RDF) and (b) potentials of mean force (PMF) for the Zn-N atom pair of ReaxFF glasses generated with different supercells, after 1 ns of equilibration in the (N, V, T) ensemble.

3.1.2 Preparation of the crystal

While it may seem trivial to equilibrate the crystal structure at room temperature, I want to detail this here because I have found that it is a crucial step. This is true in particular when one wants to simulate with ReaxFF structures that originate from different levels of theory or come from experiments, therefore with different structural characteristics – for which features of the original model should be retained. I do this by imposing constraints on the energy, temperature and volume of the system, and successively releasing them. The entire procedure is represented on figure 3.3

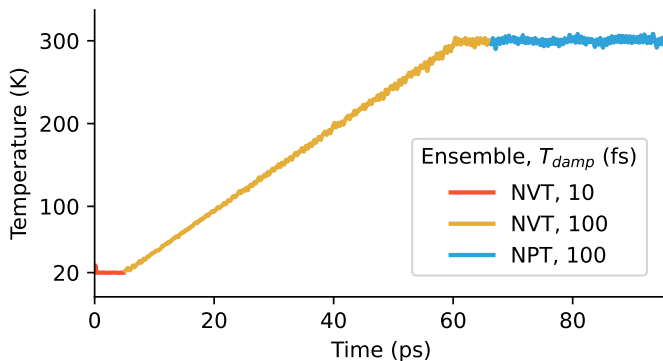


Figure 3.3: Temperature as a function of time during the crystal preparation procedure with ReaxFF, consisting in the use of various thermodynamic ensembles (constant-volume (N, V, T) and constant-pressure (N, V, T)) and temperature damping parameters (T_{damp}). A moving average over 250 fs is used.

After an initial energy minimization, the system is relaxed at a very low temperature, using a constant-volume (N, V, T) ensemble at 20 K for 5 ps with a temperature damping parameter of 10 fs (necessary to avoid having too large forces and a high temperature in the initial dynamics, as can be seen otherwise by checking the thermodynamic properties of this initial low-temperature relaxation).

The system then needs to be brought to 300 K, staying in the (N, V, T) ensemble to decouple temperature and pressure equilibration. I tried various heating rates from 2.5 K/ps to 116 K/ps, the value chosen in Yang et al. [155]. I found that rates above 10 K/ps lead to the breaking of Zn–N bonds, with a coordination number dropping from the expected value of 4. This undesirable and unphysical decoordination has consequences on the final structural properties of the obtained crystals, illustrated with the potentials of mean force (PMF) shown in figure 3.4. Due to the reactive nature of this force field, it is advised to carefully check that no bond breaking happens in the crystalline state [92]. I therefore chose a safe value of 5 K/ps for the heating rate of the preparation.

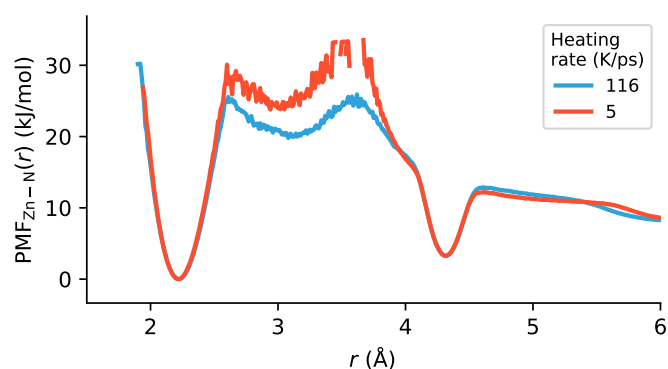


Figure 3.4: Potential of Mean Force (PMF) for Zn–N of ReaxFF crystals prepared with two different heating rates, after 1 ns of equilibration in the (N, V, T) ensemble.

Finally, once 300 K is reached, we switched to the constant-pressure (N, P, T) ensemble at $P = 0$ Pa, with a pressure damping parameter of 1000 fs and using an isotropic cell. After a short equilibration period of 30 ps, we found that this constant-pressure simulation led to an increase in density from 1.21 to 1.3. I checked that using a longer equilibration period of 500 ps does not change the properties of the resulting glass. I tried using a flexible cell (LAMMPS keyword `tr i`) and found that it led to a dramatic increase in density (up to 1.6), shown in figure 3.5. The goal being the system stabilization, it led us to keep the isotropic constraint on the cell shape. This tendency to densify will be discussed in the final section 3.3.1. Several pressure damping parameters in the range of 250 to 4000 fs were tested, leading to no significant change in the final density.

3.1.3 Melt-quenching

The equilibrated ZIF-4 crystal is then heated up above its melting temperature before being cooled down, with constant heating and cooling rates. While these rates are necessarily several orders of magnitude higher than in any achievable experiment, due to the small time scales tractable by MD simulations [122], they should be low enough to simulate a quasistatic process. Yang et al. opted for 96 K/ps [155] and the subsequent ReaxFF works used the lower value of 24 K/ps [156–158]. A cooling rate of 50 K/ps was chosen for the *ab initio* work to ensure the tractability of the simulation but was then seen as a limitation of the work [123]. Using the computational effectiveness of reactive force fields, I opted here for heating and cooling rates of 2.5 K/ps.

To monitor structural properties as a function of temperature during melt-quenching, such as the radial distribution function (RDF) plotted on figure 3.6, I opted for subsequent steps of temperature ramp up of 100 K at 5 K/ps and plateaux of 20 ps. Shown on figure 3.1, this succession of steps is equivalent to

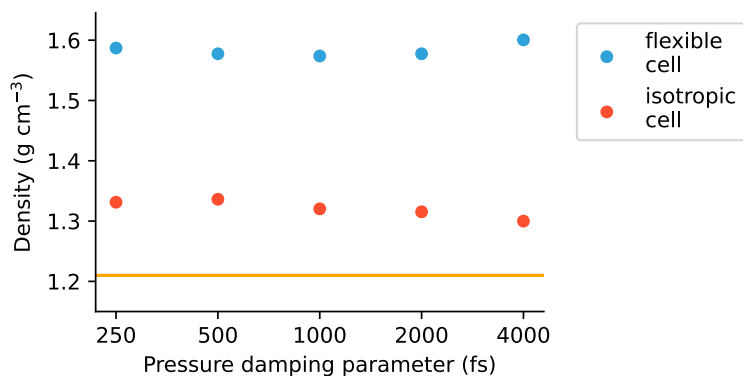


Figure 3.5: Crystal final density after 500 ps of equilibration in the (N, P, T) ensemble with various pressure damping parameters and cell types. The horizontal line is the density of the crystallographic crystal (1.21 g cm^{-3}) before its preparation with ReaxFF.

effective heating and cooling rates of 2.5 K/ps. I checked that the presence or absence of plateaux (with the same effective rate) has no influence on the final glasses properties, as expected for a quasistatic simulation. I also checked, and demonstrate on figure 3.7, that in the 1.25 – 5 K/ps range, the precise value does not significantly change the outcome of the simulation. I note here again that melt-quenching simulations were performed in the (N, P, T) ensemble with an isotropic cell, as the use of a flexible cell led to an undesirable fast density increase in the first tens of picoseconds, which affects the final properties of the melt-quenched glass.

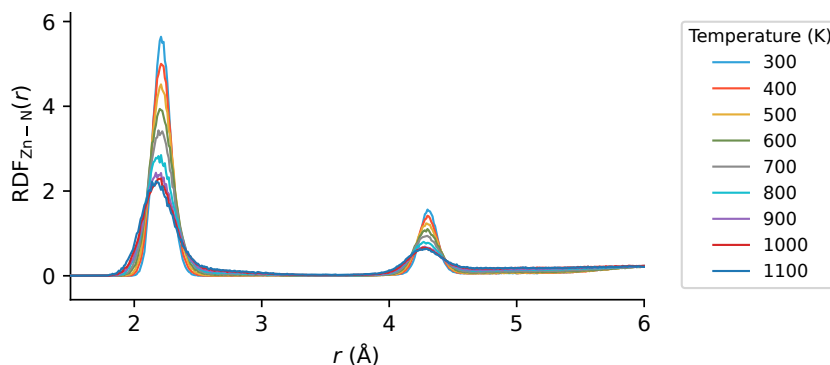


Figure 3.6: Radial distribution functions (RDF) for Zn–N shown for different temperatures during melting of the ReaxFF crystal. RDFs are computed over the constant temperature plateaux, each lasting 20 ps.

3.1.4 Choice of the melting temperature

The choice of the maximal temperature, necessarily above the melting temperature, is a trade-off between the need to gather statistics on relatively rare events during the relatively short times explored in MD [92], and the necessity to preserve the physical consistency of the model. A value of 1500 K was chosen for both the previous *ab initio* [123] and ReaxFF [155–158] works. While *ab initio* MD simulations of the liquid ZIF have been performed up to 2000 K while preserving the integrity of the imidazolate linkers [92], no published work investigated the temperature stability of ReaxFF simulations of the ZIF liquid.

During melting with a 2.5 K/ps heating rate, I report that when the maximal temperature exceeds 1300 K for more than a few tens of ps, the system vaporizes (as shown on figure 3.8). This effect is kinetically hidden when using the faster heating rates of 24 – 96 K/ps that do not provide sufficient time for the system to equilibrate, explaining why it was not observed in the previous ReaxFF works [155–158]. It

suggests a tendency of this reactive force field to be overly favorable to zinc–imidazolate bond breaking events, which is exacerbated at such high temperatures.

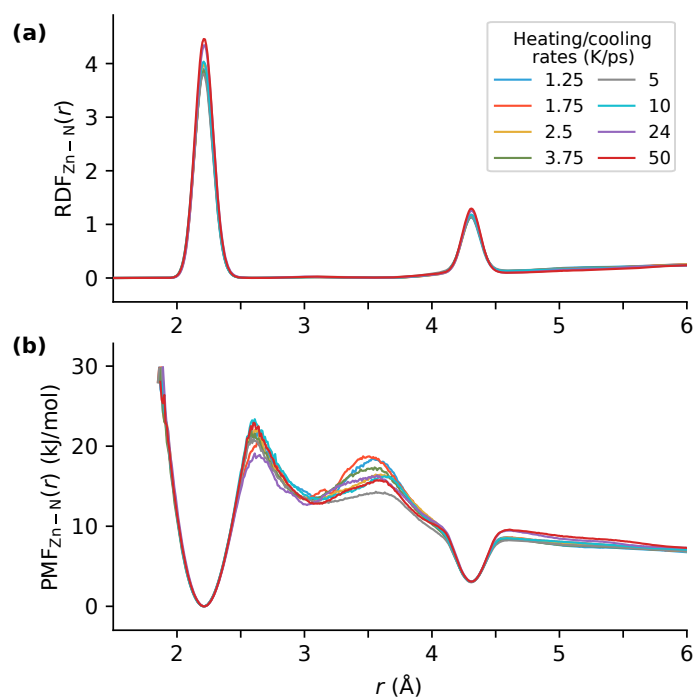


Figure 3.7: (a) Radial distribution functions (RDF) and (b) potentials of mean force (PMF) for the Zn–N atom pair of ReaxFF glasses generated with various heating/cooling rates and a maximal temperature of 1100 K, after 1 ns of equilibration in the (N, V, T) ensemble. For values below 3.75 K/ps we see no noticeable difference in the final properties of the glasses, confirming the choice of 2.5 K/ps. The larger cooling rates in the 10 – 50 K/ps range do not lead to significantly different properties, although they may have hastened the phase transition.

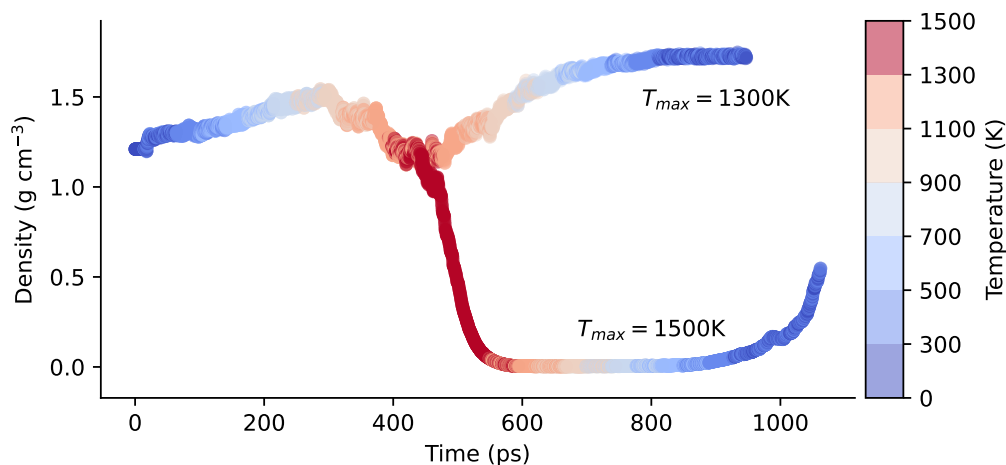


Figure 3.8: Density as a function of time and temperature during two melt-quenching ReaxFF trajectories with maximum temperatures T_{max} of 1300 K and 1500 K. Above 1300 K, the density drops to 0 g cm^{-3} as the system transitions into a gas.

Additionally, we observe that when the system temperature is above 1100 K for a sufficiently long time, a number of imidazolates are no longer properly treated, for example with an opening of the imidazolate ring as reported on figure 3.9. This unphysical treatment of the organic linkers, which should be stable at the melting temperature [92], is more visible for lower heating/cooling rates as they lengthen the time spent at high temperatures and increase the proportion of open rings. It could nonetheless be

observed when we reproduced the high melting rate of 96 K/ps and maximal temperature of 1500 K of Yang et al. [155].

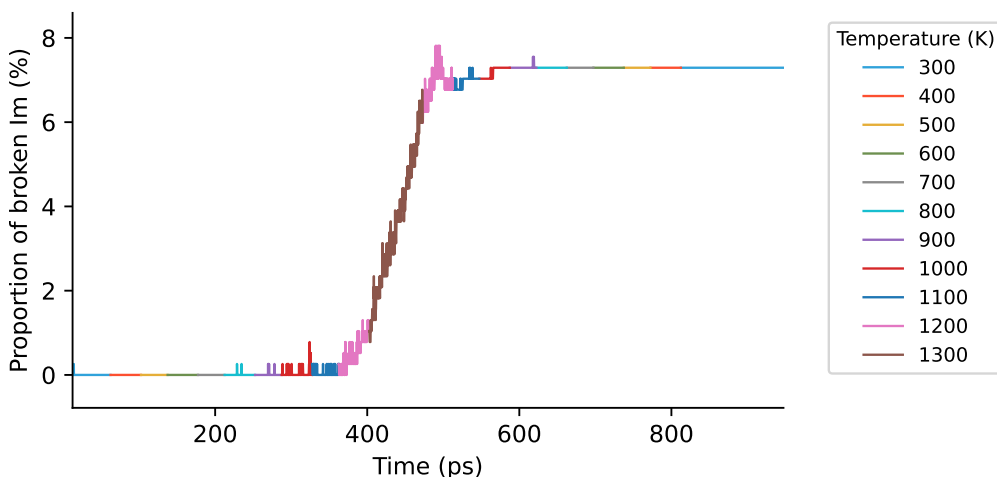


Figure 3.9: Proportion of broken (i.e. open) imidazolate cycles (Im) as a function of time for a melt-quenching ReaxFF trajectory with a maximum temperature of 1300 K. Detected during the cycle search step of the code identifying the building units described in section 2.5.3.

Changing the maximal temperature to 1100 K to avoid these undesired effects has significant implications for the computed structural properties. As shown on table 3.1, the decoordination of the Zn atoms compared to the crystal is now in better agreement with *ab initio* data [123] than in previous ReaxFF works. Similarly, the Zn–N potential of mean force (PMF) shown on figure 3.10, indicates a higher free-energy barrier to bond breaking, closer to the *ab initio* structure (see next section 3.2). This suggests that these imidazolate breaking events are frequent enough to statistically change the structural properties, and thus we recommend verifying that they do not appear during melt-quenching.

	This work		Yang et al. [155]	<i>ab initio</i> [123]
Maximal temperature	1100 K	1300 K	1500 K	1500 K
Zn–N average coordination	3.85	3.59	3.56	3.93

Table 3.1: Coordination numbers for nitrogen atoms around the zinc cation of ZIF-4 glasses for different maximal temperatures, compared to previous ReaxFF [155] and *ab initio* [123] works.

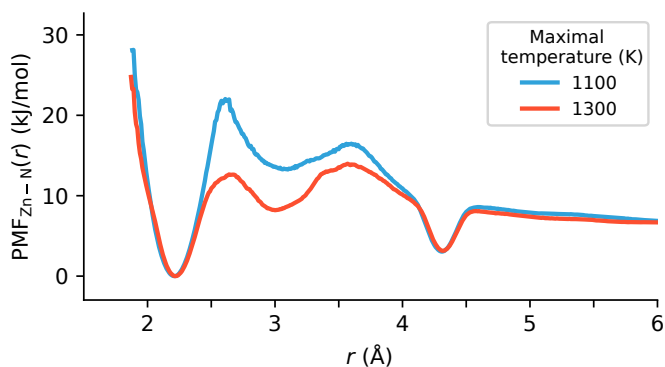


Figure 3.10: Potential of Mean Force (PMF) for Zn–N of melt-quenched ReaxFF glass produced with two different maximal temperatures.

Having opted for a lower maximal temperature of 1100 K, it is crucial to check that this value is still high enough for the crystal to melt. This is first evidenced by computing the mean square displacement (MSD) over time, shown in figure 3.11a for Zn. At temperatures above 1000 K, I identify a diffusive behavior

for the system, as expected for a liquid. In addition, similarly to previous *ab initio* works [92, 149], we computed the generalized Lindemann ratio [249] from the width of the first peak in the Zn–N partial RDF. A solid is usually considered to be melting when the value of this ratio, which quantifies the liquid nature of the system, is between 10 and 15%. Although less precise than the MSD, this estimate, shown on figure 3.11b, provides further evidence that the system is in a liquid state at 1100 K.

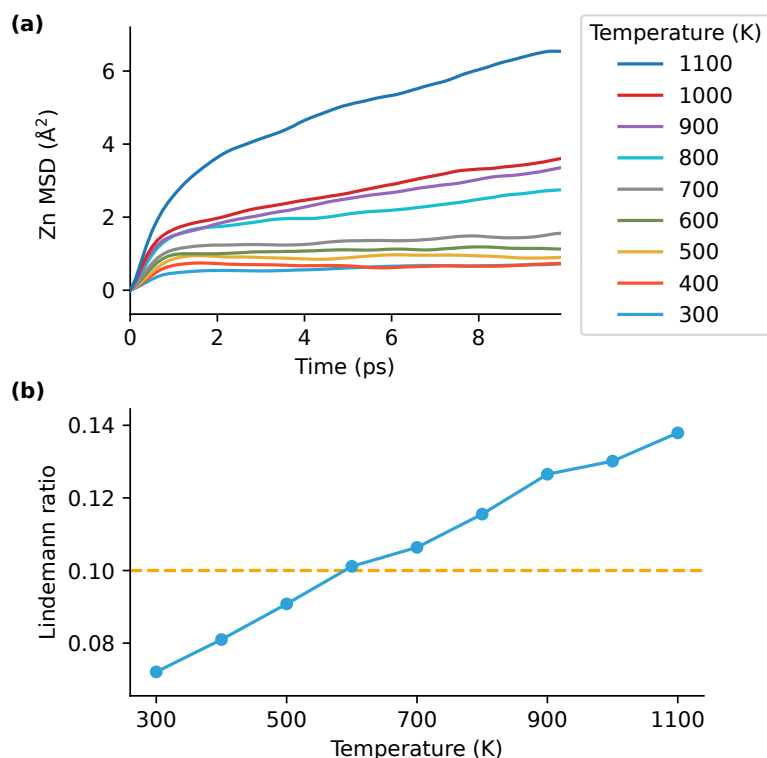


Figure 3.11: Evidence of melting during the ReaxFF glass generation. (a) Mean square displacement (MSD) as a function of time for Zn for temperatures ranging from 300 K to 1100 K. (b) Generalized Lindemann ratio, as a function of temperature, calculated for Zn–N interatomic distances. The orange horizontal line represents a “critical ratio” at 10%.

3.1.5 Equilibration

Finally, after the melt-quenching procedure, the glass model obtained was then equilibrated for 20 ps in the same (N, P, T) ensemble as during melt-quenching, the duration of one constant temperature plateau. The simulation was then further run for production during 1 ns in the (N, V, T) ensemble to gather statistics of structural and dynamical properties of the glass. I checked that up to 10 ns of further equilibration in the (N, P, T) ensemble, even with a flexible cell, does not perceptibly change the measured properties of the glass.

3.2 PROPERTIES OF THE GLASS MODELS

In order to quantitatively evaluate the validity of the ReaxFF melt-quenched glass model, I have compared its structural characteristics with that of glass models generated at a higher level of theory, namely the *ab initio* models of the work by Gaillac et al. [123], obtained with density functional theory (DFT)-based molecular dynamics. Such *ab initio* simulations allow for a full description of the electronic state of the system at the quantum chemical level, and still represent the most reliable atomistic description of ZIF-4 glasses published to date in the literature as discussed in section 1.3.

Due to the significant computational cost of *ab initio* MD, a faster melt-quenching procedure was used: only the quenching from a 1500 K liquid was simulated, with a faster cooling rate (50 K/ps), on a smaller system (unit cell) and with a shorter equilibration (~ 100 ps). To limit the impact of finite size effects, 10 quenched glasses were generated and their properties averaged. Due to the difficulty of performing (N, P, T) *ab initio* simulations of such flexible frameworks [150], all *ab initio* simulations were performed in the (N, V, T) ensemble. Although the influence of the density on the crystal and liquid properties was evaluated in a previous work [92], the inability to capture changes in density remains an important limitation of this *ab initio* methodology. The *ab initio* simulation of a crystal at 300 K reported here comes from the same work [92, 123].

Unless explicitly stated in the legend, properties were averaged over an (N, V, T) trajectory of 1 ns for ReaxFF systems and 60 ps for *ab initio*. For ReaxFF simulations, frames were taken every 125 fs for the radial distribution function (RDF), bond angle distribution and coordination number, every 250 fs for the mean square displacement (MSD), every 10 ps for ring statistics and every 25 ps for pore statistics. For *ab initio*, those intervals are respectively of 0.5 fs, 5 fs, 0.5 ps and 0.5 ps. The computed properties are extensively described in section 2.5.

3.2.1 Local order: interatomic distances and bond angles

I first investigated the difference in local order between ReaxFF and *ab initio* glasses by examining the metal–ligand bonds (Zn–N), central to the $\text{Zn}(\text{Im})_4$ tetrahedral structure represented on figure 1.19. For the two models, I plot and compare the partial radial distribution functions (RDF) $g(r)$ for the Zn–N and Zn–Zn atom pairs on figure 3.12. As outlined in table 3.2, we find a shift in Zn–N atomic distances of 0.2 Å between ReaxFF and both the *ab initio* and experimental values. To contrast the differences of the partial RDF in the region between the first two peaks, I also present it in the form of a potential of mean force (PMF). From the resultant free energy profiles, we observe similar values for the free energy barriers ($\simeq 23$ kJ/mol), although with different shapes. The wider well and narrower barrier for the ReaxFF glass suggest a tendency of ReaxFF to allow Zn–N bonds to break more easily.

	Zn–N (Å)	Zn–Zn (Å)
ReaxFF glass	2.21	6.35
AIMD glass	2.00	5.97
AIMD crystal	2.00	5.97
Experimental crystal	1.97 (XRD [65]), 1.98 (NMR [166])	5.87 (XRD [65])
Experimental glass	1.99 (RMC [92])	5.95 (RMC [92])

Table 3.2: Interatomic distances (Zn–N and Zn–Zn) of the ReaxFF ZIF-4 glass compared to *ab initio* and experimental values. Experimental data is obtained from X-ray diffraction (XRD) studies [65] and NMR (Nuclear magnetic resonance) [166] for the crystal, and from a Reverse Monte Carlo (RMC) refinement of Neutron and X-ray scattering data of a melt–quenched glass [92].

Yet, the most stringent distinctive feature of the ReaxFF glass compared to its *ab initio* counterpart lies in the N–Zn–N bond angle distribution $P(\theta)$, shown on figure 3.13. From the $\text{Zn}(\text{Im})_4$ tetrahedral structure, we expect a unimodal distribution around 109° for the crystal. Experimentally measured by NMR [166],

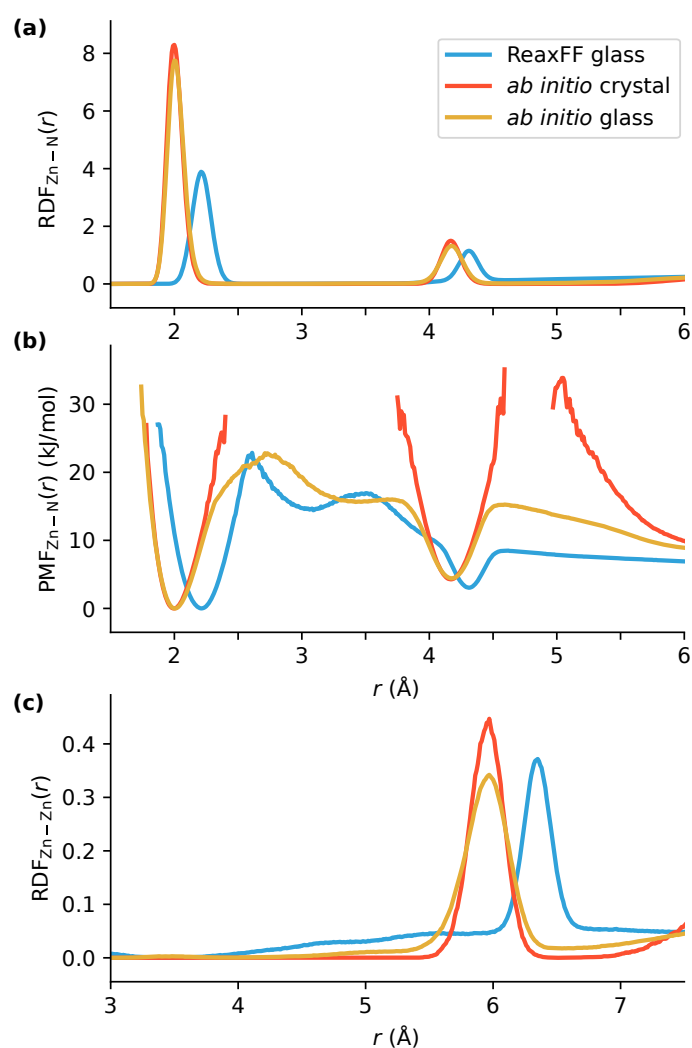


Figure 3.12: (a) Radial distribution functions (RDF) and (b) potentials of mean force (PMF) for the Zn–N atom pairs of the ReaxFF glass (blue), *ab initio* glass (orange) and *ab initio* crystal (red). (c) RDF for the Zn–Zn atom pair of the same systems.

this feature is well reproduced for the *ab initio* crystal. Due to the undercoordination of a small fraction of the Zn^{2+} nodes in the glasses, a small deviation is expected, and observed for the *ab initio* glass, with a wider distribution and tail at higher angle values. However, the ReaxFF glass distribution is very different, with a broad distribution of angles on the $70-170^\circ$ spectrum. This distribution is unphysical, and does not reproduce the known tetrahedral chemistry of the system, suggesting ill-adjusted angle constraints in the force field. The angular PMF shown on figure 3.13 further evidences the tendency of this force field to have the ReaxFF glass deform too easily.

Despite the importance of the N–Zn–N angle for the framework properties, key to the features of ZIFs, I found that statistical distributions of bond angles have never been published in the existing literature on ReaxFF simulations of these materials: Yang et al. showed the results of a single frame [155] while a later work by To et al. only looked at the average bond angle [157]. I recommend computing and reporting this distribution, in the same way as it is routinely done for the development of classical force fields [203].

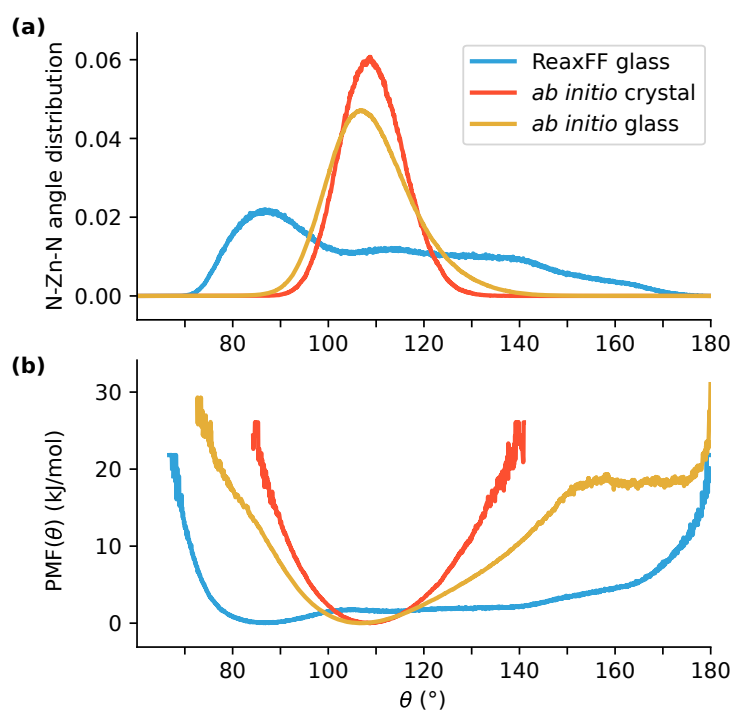


Figure 3.13: (a) Distribution and (b) potentials of mean force (PMF) of the N-Zn-N angle for the ReaxFF glass (blue), *ab initio* glass (orange) and *ab initio* crystal (red).

3.2.2 Bulk properties: density and porosity

By allowing exaggerated deformation of the framework, the underconstrained Zn–imidazolate interactions described above impacts the bulk properties of the ReaxFF glass. I report from our simulations a density of 1.68 g cm^{-3} , significantly larger than the crystal density of 1.21 g cm^{-3} . Comparison with the *ab initio* glass is not possible as they were generated using a constant-volume (N, V, T) ensemble, which does not capture changes in density. Direct experimental comparison of these densities computed from the atomic structure is limited: they correspond to crystallographic densities, while almost all densities measurements performed for glasses utilized pycnometry [233]. Nevertheless, pycnometric densities of 1.63 g cm^{-3} for the glass and 1.50 g cm^{-3} for the crystal [86] indicate that a larger value is expected for the glass. Although we could expect the difference in crystallographic densities between the glass and crystal to be much smaller, the complex diffusion behavior of helium into the ZIF-4 pores makes pycnometric densities measurements difficult to interpret. As an alternative to pycnometry, a recent work determined the crystallographic density for the ZIF-4 glass from CO_2 physisorption studies [233]. Estimated to be 1.38 g cm^{-3} , this value hints that ReaxFF overestimates the glass density.

Additionally, I computed the porosity of the glasses (see figure 3.14) and found a total porous volume of $4.6 \text{ cm}^3 \text{ kg}^{-1}$ for the ReaxFF glass, down from the $54 \text{ cm}^3 \text{ kg}^{-1}$ of the crystal (computed for *ab initio*). As the porosity is greatly impacted by the density of a system, direct comparison to the *ab initio* glass ($68 \text{ cm}^3 \text{ kg}^{-1}$) is limited but does suggest that the ReaxFF glass porosity is one order of magnitude too low. This all but complete loss of porosity also contradicts the experimental measurements of the porosity of a ZIF-4 glass made by positron annihilation lifetime spectroscopy (PALS) [164], and further confirms that the density of the ReaxFF glass is excessively large.

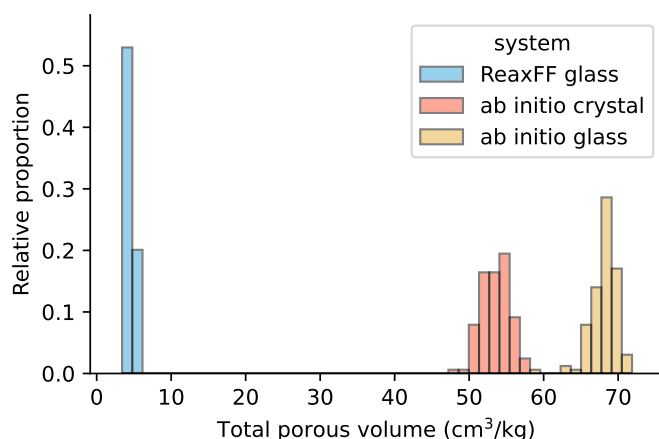


Figure 3.14: Total porous volume of the ReaxFF glass (blue), *ab initio* glass (orange) and *ab initio* crystal (red).

3.2.3 Topological properties of the coordination network

Finally, I investigated the differences in the medium-range order of the glasses, highlighted by their contrasting structure factors shown on figure 3.15, by examining the coordination network built from the alternating Zn–Im (imidazolate) units. I first calculated the average Zn–N coordination numbers and found a lower coordination of 3.85 for the ReaxFF glass compared to 3.93 for the *ab initio* glass, confirming the ReaxFF tendency to underconstrain Zn–N bonds.

In order to characterize the topology at larger scale, known to be key to the properties of these framework materials [70], I computed Zn–Im ring statistics. This analysis, routinely used to characterize amorphous systems such as SiO_2 [239] and first applied to amorphous MOFs for the *ab initio* glasses [123], determines the number and size of rings present in the ZIF network. Ring sizes are computed by counting the number of different units (Zn and Im) in each ring; always even, they are equal to twice the T-based ring

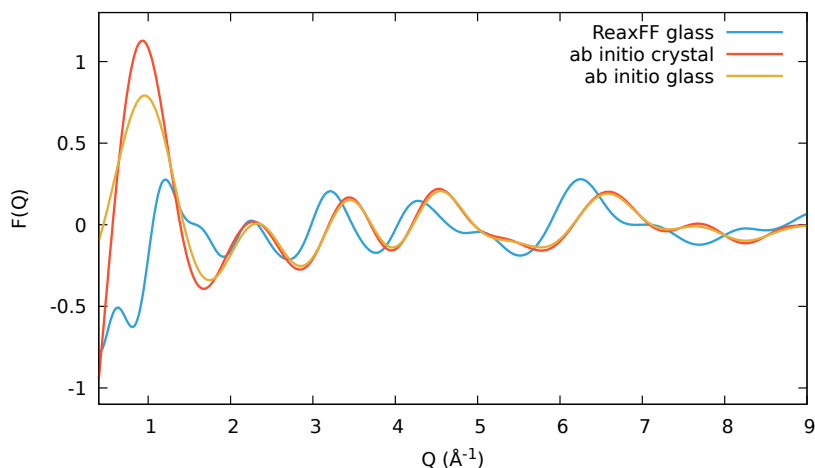


Figure 3.15: X-ray total-scattering structure factors $F(Q)$ of the ReaxFF glass (blue), *ab initio* glass (orange) and *ab initio* crystal (red). Computed following the same methodology as in Gaillac et al. [92].

sizes usually reported for zeolitic nets [69]. These distributions of ring sizes, reported on figure 3.16, show that both glasses have topologies that deviate from the crystal perfectly defined 8, 12 and 16 rings. However, the two glass models display very different topologies, with the ReaxFF glass having a higher proportion of larger rings than the *ab initio* glass. It demonstrates that it is less ordered at medium range, a result arising from the too weak constraints on the Zn–imidazolate interactions.

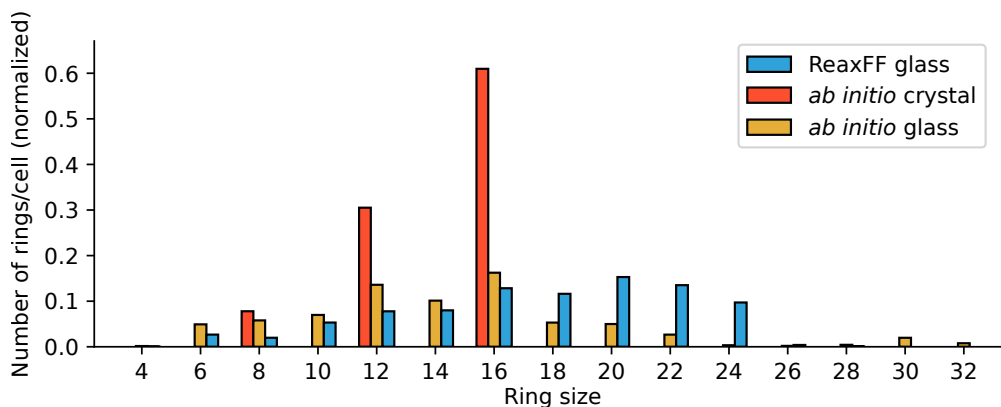


Figure 3.16: Distributions of size of zinc–imidazolate alternate rings for the ReaxFF glass (blue), *ab initio* glass (orange) and *ab initio* crystal (red).

3.3 CHALLENGES IN USING REAXFF

In addition to generating a glass model markedly different from its *ab initio* counterpart, I identified several challenges when using the ReaxFF force field for ZIFs. I highlight them here, as they should be kept in mind and may be applicable to other molecular simulations of MOF glasses.

3.3.1 (N, P, T) ensemble and densification

Molecular dynamics simulations in the constant-pressure (N, P, T) ensemble are remarkably insightful, notably for the study of mechanical and thermal properties [146, 257]. In particular, the use of a flexible cell, more general than an isotropic cell, enables the computation of multiple mechanical properties as we will see in chapter 5.

Yet, previous work has shown that (N, P, T) are particularly challenging to use with soft porous materials, due to the sensitive response of these frameworks to small external stimuli, in particular for *ab initio* calculations [150]. While every published work on ZIFs with ReaxFF used (N, P, T) ensembles, no systematic validation has been published to this day.

SYSTEM DESCRIPTION

In order to evaluate the robustness of such constant-pressure simulations, we equilibrated at $T = 300$ K and $P = 0$ Pa several ZIF-4 systems with a flexible cell:

- The ReaxFF glass prepared in the first section, equilibrated for 10 ns.
- The crystal prepared in the first section, equilibrated for 5 ns.
- Three *ab initio* glasses obtained from the work by Gaillac et al. [123] that went through the same preparation process as the crystal (see section 3.1.2). I took $(2 \times 2 \times 2)$ supercells of these systems to have the same system size as the ReaxFF glass and the crystal (2176 atoms). Their equilibration times were comprised between 7 ns and 18 ns. Densities reported in the article are averaged over the three glasses.
- A glass obtained by Reverse Monte Carlo (RMC) modeling [129] in another work by Gaillac et al. [92]. The system, made of 8704 atoms, was prepared as the crystal, and was then equilibrated for 22 ns.

The criteria for the convergence of the cell shape was the convergence of the elastic constants obtained from the cell parameters by the strain-fluctuation method [146, 258]. We note that it can be a lengthy process for some systems as illustrated on figure 3.17 for the RMC glass.

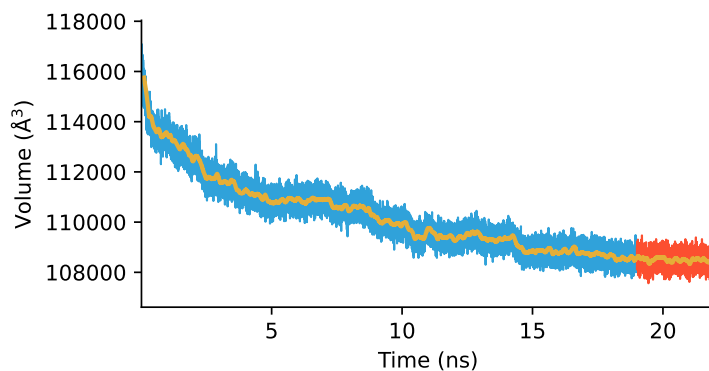


Figure 3.17: Volume as a function of time during a long 22 ns equilibration in the (N, P, T) ensemble with a flexible cell for the RMC glass. The red part of the figure corresponds to the region where the convergence of the elastic constants was achieved. The orange line shows a moving average over 100 ps.

IMPACT ON THE DENSITY

As reported on table 3.3, we see that the density of every equilibrated system is in the range of 1.5 to 1.7 g cm⁻³, regardless of their initial density. I conclude that the large density observed for the ReaxFF glass may not be due to its specific structure, but is rather a symptom of ReaxFF tendency to densify systems.

	Initial density (g cm ⁻³)	Density after equilibration (g cm ⁻³)
Crystal	1.21	1.61
ReaxFF glass		1.68
RMC glass	1.58	1.56
<i>ab initio</i> glass	1.21	1.57

Table 3.3: Densities after preparation and equilibration in ReaxFF for the ZIF-4 crystal and three ZIF-4 glasses, compared to their initial densities.

I have found that using an isotropic cell for the crystal and *ab initio* glasses reduces the magnitude of the densification respectively by 0.25 g cm⁻³ (see figure 3.5) and 0.14 g cm⁻³ (see figure 3.18). This difference, which should *a priori* not be observed for the crystal as the cell shape is not supposed to vary much, highlights once again that this ReaxFF force field is very sensitive and does not fare well when we reduce the number of constraints on the system. Nevertheless, I recommend using an isotropic cell if one has no interest in the fluctuations of the cell, as it provides a behavior closer to the physical reality.

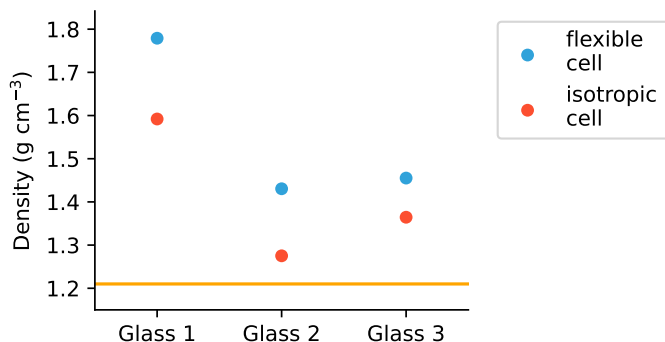


Figure 3.18: Final density of three *ab initio* glasses after 500 ps of equilibration in the (N, P, T) ensemble with isotropic or flexible cells. The horizontal line is the density of the *ab initio* glasses (1.21 g cm⁻³) before their preparation with ReaxFF.

Another option to avoid this undesired densification may consist in staying in the constant-volume (N, V, T) ensemble, similarly to what was done in the *ab initio* works [92, 123]. For example, pressure equilibration can be achieved by successive slow deformation of the cell until zero pressure is reached. When I performed this procedure in the case of the ZIF-4 crystal, it leads to a density of 1.26 g cm⁻³, not far from the experimental crystal density. However, although this approach could fix the troublesome densification, we end up losing all the benefits of the (N, P, T) ensemble that every ReaxFF work published so far was interested in.

3.3.2 Description of the crystal

Surprisingly, I found that the ReaxFF parametrization for Zn-based ZIFs have not been systematically validated on any crystalline structure in the existing literature. Therefore, I report here the properties of a ZIF-4 crystal prepared as described in the first section 3.1.2. The goal is to differentiate the intrinsic properties of the ReaxFF glass from the numerical artifacts linked to the use of this force field. Due to

the ReaxFF tendency to densify the crystal, I investigated various equilibration procedures using either (N, V, T) or (N, P, T) ensembles.

SYSTEM DESCRIPTION

Four ReaxFF crystal systems are compared to the *ab initio* crystal in the final section. The starting point of these crystals is the last (N, V, T) state of the prepared crystal at 300 K of section 3.1.2. Before computing their properties – gathered during a 1 ns equilibration in the (N, V, T) ensemble – these systems went through different preliminary equilibration procedures:

- (N, V, T) *initial density*: no preliminary equilibration, implying no change in density from the crystallographic crystal.
- (N, V, T) *zero pressure*: successive (N, V, T) runs of slow deformations of the system volume were applied until a state of zero pressure was achieved. The system went through three sequences of 250 ps of isotropic volume reduction by 1.5% and 250 ps of equilibration. During the deformation, each dimension of the box changed linearly with time from its initial to final value.
- (N, P, T) *isotropic cell*: (N, P, T) run of 500 ps with an isotropic cell.
- (N, P, T) *flexible cell*: (N, P, T) run of 500 ps with a flexible cell. I checked that there is no significant difference in the computed properties compared to an equilibration time of 5 ns.

All these simulations are performed at 300 K and – if applicable – 0 Pa, using the same temperature and pressure damping parameters than for the preparation (respectively 100 fs and 1000 fs).

STRUCTURAL PROPERTIES

These various strategies led to ReaxFF crystals of different densities, reported in table 3.4, which ineluctably lead to different porosities (see figure 3.19).

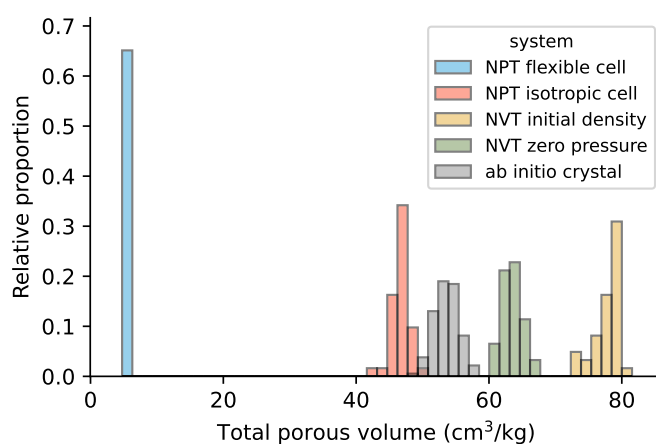


Figure 3.19: Total porous volume of the ReaxFF crystals with four different equilibrations compared to the *ab initio* crystal.

Under (N, V, T) simulations, I systematically found no change in the connectivity (see table 3.4) or topology of the crystal (see figure 3.20). However, this does not hold true for the (N, P, T) schemes for which we observe a small deviation, evidencing that an (N, P, T) equilibration at 300 K causes undesired bond breaking, even when enforcing an isotropic cell.

An investigation of the local order with the RDF and PMF (see figure 3.21), evidence a similar shift in interatomic distances compared to *ab initio* data than what was observed for the glass. Additionally, we observe a significant lowering of the free energy barrier in the PMF between the first two minima compared to the *ab initio* data, even for the crystal systems that never went through an (N, P, T) ensemble.

		Density (g cm^{-3})	Zn-N coordination number
ReaxFF	(<i>N, V, T</i>) initial density	1.21	3.99
	(<i>N, V, T</i>) zero pressure	1.27	4.00
	(<i>N, P, T</i>) isotropic cell	1.30	3.95
	(<i>N, P, T</i>) flexible cell	1.59	3.98
<i>ab initio</i>		1.21	4.00

Table 3.4: Densities and coordination numbers of crystal systems with different preliminary equilibrations in ReaxFF.

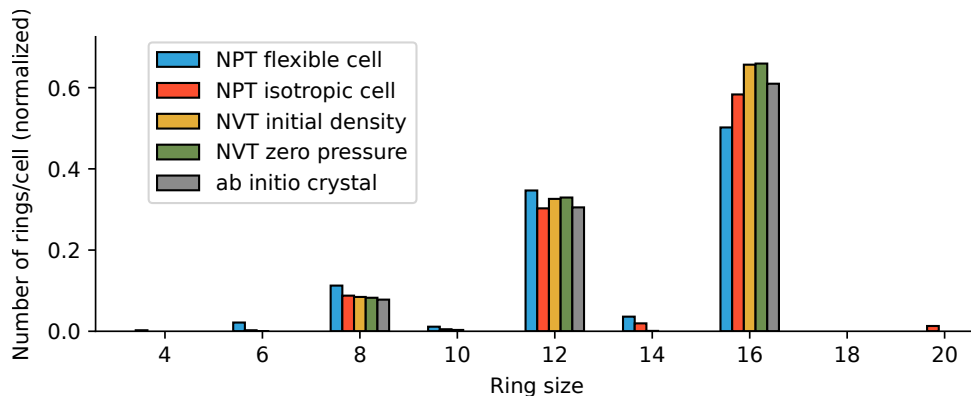


Figure 3.20: Distributions of size of zinc-imidazolate alternate rings for the ReaxFF crystals with four different equilibrations compared to the *ab initio* crystal.

This tendency to systematically underconstrained the Zn-N interaction is further evidenced by the unphysical bond angle distribution shown on figure 3.22.

Unphysical angles are also observed on two other ZIF crystals – ZIF-8 and SALEM-2 – evidencing that this issue is not linked to the choice of ZIF-4 as a prototypical system (see figure 3.23). I conclude that the unphysical description of the zinc-imidazolate coordination in the ReaxFF force field is also manifest in the detailed analysis of the structural properties of the crystalline phase, further questioning the validity of this force field.

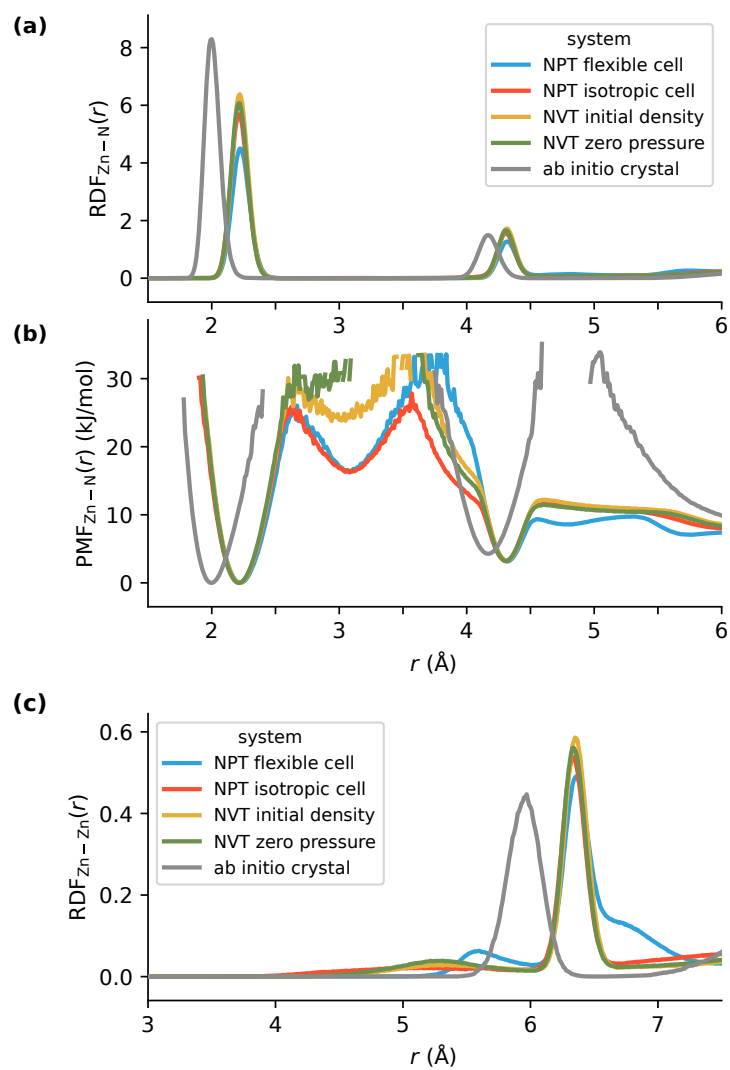


Figure 3.21: (a) Radial distribution functions (RDF) and (b) potentials of mean force (PMF) for the Zn-N atom pair of the ReaxFF crystals with four different equilibrations, compared to the *ab initio* crystal. (c) RDF for the Zn-Zn atom pair of the same systems.

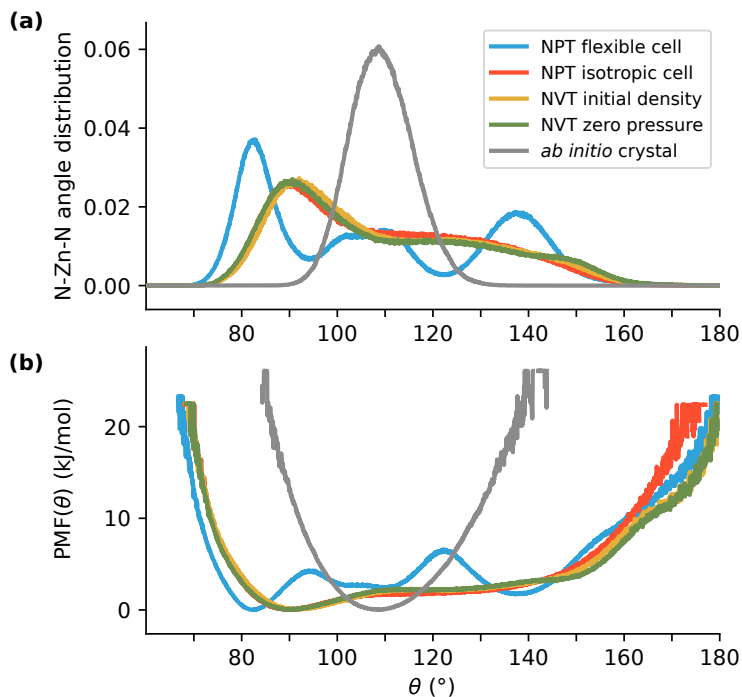


Figure 3.22: (a) Distribution and (b) potentials of mean force (PMF) of the N-Zn-N angle for the ReaxFF crystals with four different equilibrations, compared to the *ab initio* crystal.

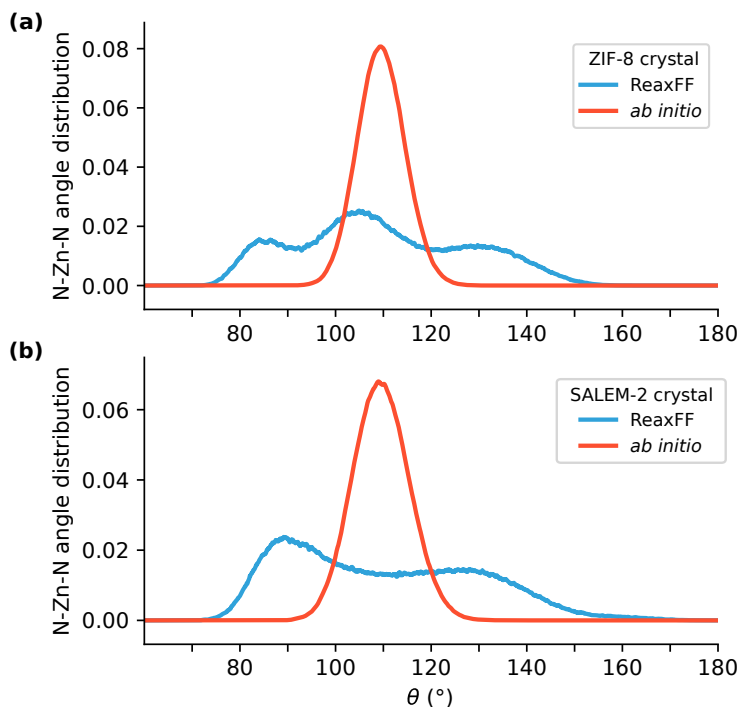


Figure 3.23: Distribution of the N-Zn-N angle of the crystalline phases of (a) ZIF-8 and (b) SALEM-2, simulated with ReaxFF (blue) and *ab initio* MD (red). ReaxFF crystals are prepared with the same procedure as the ZIF-4 crystal detailed in this paper, and their properties are computed over a subsequent 100 ps of equilibration in the (N, V, T) ensemble. *Ab initio* data is obtained from the same previous work the ZIF-4 glasses and crystal were obtained [123], consisting of between 80 and 100 ps of (N, V, T) equilibration.

CONCLUSIONS AND PERSPECTIVES

In this work, I have reported the results of an extensive study of the use of the ReaxFF reactive force field to generate atomistic models of ZIF glasses. I demonstrated that the molecular simulations performed so far in the literature are extremely sensitive to the choice of simulation methodology and parameters: thermodynamic ensemble, damping parameters, heating/cooling rate, maximal temperature, etc. The physical consistency of the system should always be carefully checked, for example by drawing inspiration from the procedure presented in this study.

I have also shown that the glass models generated with ReaxFF are markedly different from their *ab initio* counterparts, with extensive differences in both local environment, medium-range and bulk properties. This is due in large part to an underconstrained representation of the Zn–N interactions in the ReaxFF model, which do not faithfully reproduce one of the key characteristics of the chemistry of ZIFs, namely the directional nature of the Zn–N coordination. This issue in the intermolecular potential, in turns, significantly impacts the crystal properties obtained through molecular simulations. Additionally, I have reported and analyzed a tendency of simulations performed in the constant-pressure (N, P, T) ensemble to densify the system.

All these observations suggest that structural properties obtained from the use of ReaxFF force field for ZIFs should be interpreted with caution, and makes a strong case for the use of alternative methodologies, or the further optimization of the ReaxFF force field. They also call for further methodological development to assess the possibility to explore mechanical properties of these soft porous materials with ReaxFF. Moreover, I think it is imperative, for future developments of ZIF reactive force fields, to systematically check their ability to simulate an (N, P, T) equilibration of the crystal at ambient conditions. A good example of such practice is the recent development of a ReaxFF force field for zirconium-based MOFs by the same group, for which the authors reported the density profile for a 1 ns equilibration [259].

Finally, this work exemplifies the need for direct and in-depth comparison of the different models of ZIF glasses available by systematically contrasting their properties. It shows that, apart from expensive *ab initio* calculations, no molecular dynamics scheme used to this date in the literature can yield an accurate microscopic representation of the ZIF melt-quenched glasses, and suggests the development of multi-scale modeling strategies that I will explore in the next chapters.

GENERATION OF *a*ZIF MODELS WITH MACHINE-LEARNED POTENTIALS

4.1	MLPs for MOFs and amorphous systems	95
4.1.1	MLPs for MOFs	95
4.1.2	Generation of glass models with MLPs.	96
4.2	Construction of MLPs for ZIF-4	97
4.2.1	<i>Ab initio</i> reference data	97
4.2.2	Training	97
4.2.3	Reproducing structural properties	99
4.3	Generating <i>a</i> ZIF-4 glass models	103
4.3.1	Producing glass models by melt-quenching	103
4.3.2	Properties of the glass models	104
4.4	Towards a universal MLP for ZIFs	108
4.4.1	Multiple ZIF structures	108
4.4.2	Multiple volumes.	108
4.4.3	Simulation of liquid systems	109
	Preliminary conclusions and perspectives	112



As ReaxFF represented the only tractable alternative to *ab initio* molecular dynamics published in the literature to generate ZIF glasses, the significant challenges evidenced in chapter 3 left us with no off-the-shelf option and the necessity to develop new potentials for ZIFs. One area of active research that appeared very promising was the development of machine-learned potentials (MLP) for the description of atomic interactions [213]. I have given a description of MLPs in section 2.4. Their use could lead to a new generation of specific and accurate reactive potentials for the description, in particular, of the coordination interactions that are key to the metal–ligand bond breaking and formation during amorphization, as well as in the glassy state.

Several MLPs have successfully been developed either for MOFs [221, 260] or to generate amorphous systems or glasses [261, 262], but none was ever used to model amorphous MOFs so far. This work ambitions to bridge the gap between these two bodies of work, by developing the first MLP used to generate amorphous MOF, focusing on the example of *a*ZIFs.

This chapter relates an ongoing work performed in collaboration with Jack D. Evans from the University of Adelaide. He performed the training of the MLPs, while I focused on the generation of the training

data and use of the trained MLP to run MDs. His contributions are explicitly mentioned where relevant in this manuscript. In this chapter, after discussing the literature on MLPs for MOFs and amorphous systems, I introduced the prototypical MLPs for ZIF-4 we developed, which I then used to generate realistic *a*ZIF-4 models by melt-quenching. Finally, I generated an enlarged training set as a first step towards the training of a universal MLPs for ZIFs. Due to the ongoing nature of this work, this chapter is rather a proof of concept than a definitive answer. I nonetheless evidenced that the MLP route is particularly promising and mentioned the next steps that we will take in this research.

4.1 MLPS FOR MOFS AND AMORPHOUS SYSTEMS

4.1.1 MLPs for MOFs

Despite the dramatic increase in the use of MLPs for both molecules and materials, only five articles proposed MLPs for MOFs at the time of writing, all of them consisting of neural network potentials (NNP). MOFs are particularly challenging for multiple reasons, in particular because of the different interactions that need to be correctly modeled – from strong covalent bonds and ionic interactions to weak van der Waals interactions –, along with their chemically complex composition. In addition, the (often) large unit cell size impedes *ab initio* simulations from generating training data [260, 263]. Approaches based on parametrization (e.g. MOF-FF described in section 2.3.2) have been much more used in this community.

In 2019, Eckhoff and Behler [260] proposed the first MLP for a MOF system, using the prototypical MOF-5 [45]. They circumvented the need for large *ab initio* calculations by using DFT calculations of small molecular fragments to train their MLP for the periodic bulk framework. This neural network potential [219], constructed using the RuNNer code [264], was used to predict a number of properties (energies, forces, thermal and mechanical properties) which the authors found to be in good agreement with *ab initio* calculations. This method was refined and further validated in a later work from the same group [265].

Two other works published in 2022 followed this approach, relying on molecular fragments for the construction of MLPs for the bulk material. Yu et al. [266] constructed a NNP for MOF-808 – a Zr-based MOF –, using the Large-scale Atomic Simulation with neural network Potential (LASP) software [267], to investigate adsorption and migration mechanisms of Pt clusters inside the framework. It is illustrated on figure 4.1. Another NNP was developed by Tayfuroglu et al. [268] to study the isorecticular metal–organic framework (IRMOF) series and predict a number of structural and mechanical properties. It was an invariant message-passing neural network (MPNN) (see section 2.4.3 for details) constructed using SchNet [227], which was shown to work on multiple frameworks (IRMOF- n with $n \in \{1, 4, 6, 7, 10\}$).

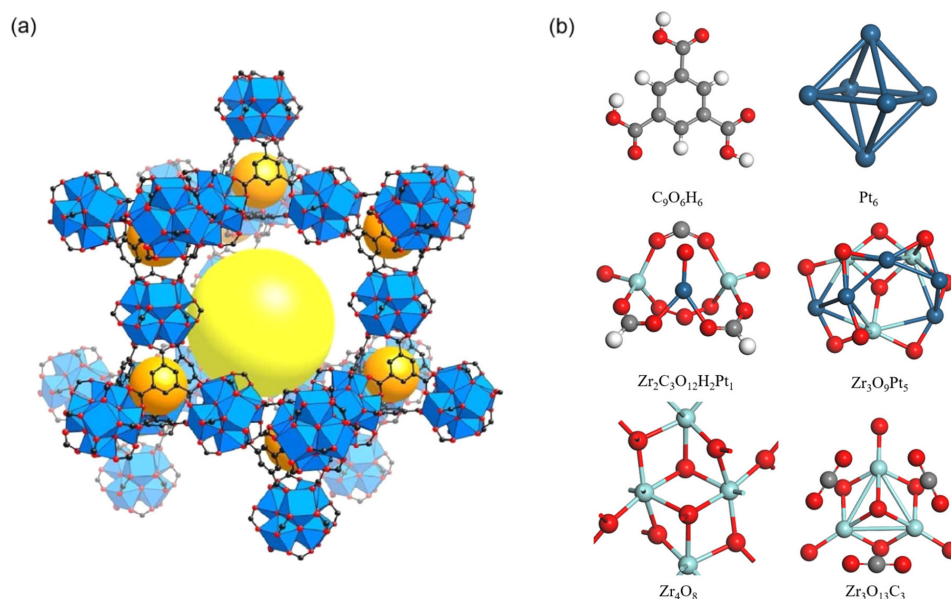


Figure 4.1: (a) MOF-808 structure and (b) examples of molecular fragments used for the construction of a NNP by Yu et al. [266]. Adapted from Ref. [266, 269].

However, the molecular fragments approach suffers from a lack of universal method to choose the fragments working on all MOFs, and from the sensitivity of its predicted energies to the choice of fragments. To overcome its shortcomings, Achar et al. [263] used for the first time periodic DFT calculations on the primitive cell of the framework to train a NNP for UiO-66. They relied on DeePMD [228], another popular invariant MPNN, to construct a NNP that predicted a number of dynamic properties with good accuracy and was used to study diffusion.

This work, however, did not solve the high computational cost of running *ab initio* simulations with large unit cells. One option proposed by Vandenhoute et al. [221] in a very recent work published in February 2023 was to use a data-efficient NNP to reduce the number of *ab initio* calculations. They employed NequIP [212], an equivariant MPNN with proved data efficiency described in section 2.4.3, and developed an active learning strategy [219] to train NNPs for two representative frameworks: UiO-66 (Zr) and MIL-53(Al). The NNPs were shown to possess good transferability, evaluated by considering a set of 10 similar frameworks which differed from MIL-53(Al) and UiO-66(Zr) in either the topology or the organic ligand. Interestingly, this work demonstrated that it was possible to simulate a phase transition for MOFs with MLPs, although the transition was non-displacive and did not involve any bond breaking.

4.1.2 Generation of glass models with MLPs

While they were not concerned with MOFs, multiple studies have successfully developed MLPs for the simulation of amorphous solids – including multiple glass-forming materials – such as oxide glasses [270], chalcogenide compounds [271], silicates [261] or amorphous carbons [262]. These studies were made possible by the reactive nature of MLPs which enables simulating various phase transitions such as vitrification. They further benefited from the low computational cost of MLPs, which could accommodate slower cooling rates and much larger systems than AIMD (e.g. 100,000 Si atoms in [261]), allowing probing the medium and long-range orders of such amorphous systems. MLPs are typically trained on data generated by high-temperature MD trajectories, to enhance coverage of off-equilibrium conformations and potentially include bond-breaking and reforming events.

A number of these studies used MPNNs, with DeePMD [228] being used to study liquid silica [272] or amorphous carbon [262]. The latter work is of particular interest as it focused on the transferability of the MLPs over multiple carbon allotropes. It was achieved by using training data made of liquid carbon at different densities and temperatures, as well as various crystalline phases.

In our work we ambition to bridge the gap between these two bodies of work and develop the first MLP used to generate MOF glasses, by drawing inspiration from both corpora.

4.2 CONSTRUCTION OF MLPs FOR ZIF-4

In this work, we chose to generate *ab initio* reference systems composed of entire unit cells, combined with a data-efficient architecture. We used the Neural Equivariant Interatomic Potential (NequIP), an equivariant MPNN described in section 2.4.3, which has demonstrated high accuracy across a wide variety of systems, including MOFs [221] and amorphous solids [212]. To evaluate the potential of the NequIP architecture to obtain MLPs for ZIFs, we first focused on ZIF-4, the same framework investigated with ReaxFF in chapter 3 and extensively described in section 1.2.3. The developed MLPs should be able to successfully describe the different phases necessary to obtain melt-quenched glasses, *i.e.* the crystal, liquid and glassy phases.

4.2.1 *Ab initio* reference data

Reference data was extracted from *ab initio* molecular dynamics (AIMD) simulations (see section 2.2 for the method). We started with limited training data by only considering two AIMD trajectories performed in the (N, V, T) ensemble: one simulating the ZIF-4 crystal at 300 K and another a ZIF-4 liquid at 1500 K. These trajectories were taken from the work by Gaillac et al. [92] (described in section 3.2) and were rerun to obtain at least 100 ps of simulation data for each system.

DFT-based Born-Oppenheimer MD simulations were performed using the Quickstep module [198] of the CP2K software package [273], a general open source quantum chemistry and solid-state physics simulation package. I used parameters already fine-tuned for several ZIFs (ZIF-4, ZIF-8, ZIF-62, ZIF-zni, SALEM-2) in previous works by Gaillac et al. [92, 93, 123, 149].

As mentioned in section 2.2, I used the hybrid Gaussian and plane wave method GPW [198], the exchange–correlation energy was evaluated in the PBE approximation [274], and the dispersion interactions were treated at the DFT-D3 level [197]. The multigrid system was set up with four different grids, a plane wave cutoff for the electronic density of 600 Ry, and a relative cutoff of 40 Ry. Valence electrons were described by double- ζ valence polarized basis sets and norm-conserving Goedecker–Teter–Hutter [275] pseudopotentials, all adapted for PBE (DZVP-GTH-PBE) for H, C, and N or optimized for solids (DZVP-MOLOPT-SR-GTH) in the case of Zn.

Simulations were performed in the constant-volume (N, V, T) ensemble with a fixed size and shape of the unit cell. A time step of 0.5 fs was used in the MD runs, and the temperature was controlled by velocity rescaling [185] with a time constant of 1000 fs.

4.2.2 Training

Unlike the rest of this chapter 4, the work presented in this section 4.2.2 was mainly performed by Jack D. Evans, as part of a collaboration that I started during my PhD project.

NETWORK ARCHITECTURE AND TRAINING PROCEDURE

We used NequIP version 0.5.5 [212], and tested several hyperparameters. All MLPs presented in this manuscript were trained with the network architecture described in table 4.1 and in the remainder of this paragraph. Training was performed with the Adam optimizer [276] with a learning rate of 0.005. We employed a batch size of 5, and disabled the learning rate decay scheduler. The weights used during validation or test error evaluation were obtained after an exponential moving average filter, with weight 0.999. Among the multiple parameters, it is worth mentioning that we tested several rotation orders in $l \in \{1, 2, 3\}$ (defined in section 2.4.3) and found that $l = 2$ led to the best compromise between precision and efficiency.

Out of a given trajectory of 100 ps, corresponding to 200 000 frames, 2500 were taken randomly to constitute the training dataset, and 100 other to be used as validation data. Therefore, each frame was on average separated from the others by 75 fs, leaving room for improvement in the reduction of

Cutoff radius R_c	6 Å
Number of interaction layers	4
Maximum rotation order l	2
Parity	even and odd
Number of radial basis functions	8

Table 4.1: Network architecture parameters for every MLP presented in this work.

correlation between frames. The data efficiency of the training, and the amount of time required to separate different configurations should be explored further in future work.

MULTIPLE MLPs

Despite having all these hyperparameters in common, MLPs discussed in this manuscript differ in their training data and choice of loss function. Most MLPs were trained on the high temperature trajectory, which we consider to be more promising as it contains more diverse configurations (explores better the configuration space). To enable comparison, some MLPs were trained on the crystalline trajectory, at 300 K.

Several loss functions were used to simultaneously minimize the errors on the energy (E), forces ($\{F_i\}$) and stress (σ). The respective contribution of each error in the total loss functions are parameterized by three weights $\lambda_F, \lambda_E, \lambda_\sigma$. In all models presented here $\lambda_F = \lambda_E = 1$. For some MLPs we wanted to bias learning for stress by choosing large λ_σ . We otherwise used $\lambda_\sigma = 1$, which in practice led to similar results than $\lambda_\sigma = 0$ due to the choice of prefactor for each error.

Let us denote the different MLPs as MLP(system| \mathcal{L}), where “system” refers to the training data (either crystal or liquid), and \mathcal{L} is the loss function which is denoted by the relative weights $\lambda_F : \lambda_E : \lambda_\sigma$.

	λ_σ	1	10	100	1000
Energy MAE (meV/atom)		0.396	0.775	0.899	1.01
Forces MAE (meV Å ⁻¹)		19.2	20.9	19.7	22.6
Stress MAE (MPa)		351	163	75.8	73.4

Table 4.2: MAEs of the trained models for MLP(liquid|1:1: λ_σ) with $\lambda_\sigma \in \{1, 10, 100, 1000\}$, evaluated on unseen frames of the liquid trajectory.

Figure 4.2 compares the learning curves for MLP(liquid|1:1: λ_σ) for $\lambda_\sigma \in \{1, 10, 100, 1000\}$, and highlights that although forces are well learned in every case, one needs to find a balance between an accurate reproduction of the energies ($\lambda_\sigma = 1$), and any actual learning of the stress ($\lambda_\sigma \in \{100, 1000\}$). We found satisfying final mean absolute errors (MAE) on energy and forces reported in table 4.2, compared to previous NequIP works on liquid systems [212] and MOFs [221]. Stress MAEs however, are satisfying only for $\lambda_\sigma \in \{100, 1000\}$.

In the remainder of this thesis, I will use MLP(sys) and MLP(sys| σ) as shorthands for respectively MLP(sys|1:1:1) and MLP(sys|1:1:100). They respectively represent MLPs learned without and with stress.

TRANSFERABILITY OF LEARNED PROPERTIES

While the various MAEs showed that the training was successfully performed, it is necessary to further validate the generated MLPs, for example by investigating their transferability.

A first option is to compute the MAEs of the learned properties ($E, \{F_i\}, \sigma$) for a system other than the one used for training. Table 4.3 compares how two MLPs, learned either on the crystalline or liquid trajectory, reproduce the properties of the AIMD crystalline trajectory. It evidences that both the energy and forces learned on the liquid trajectory suffice to predict the crystal properties. However this result

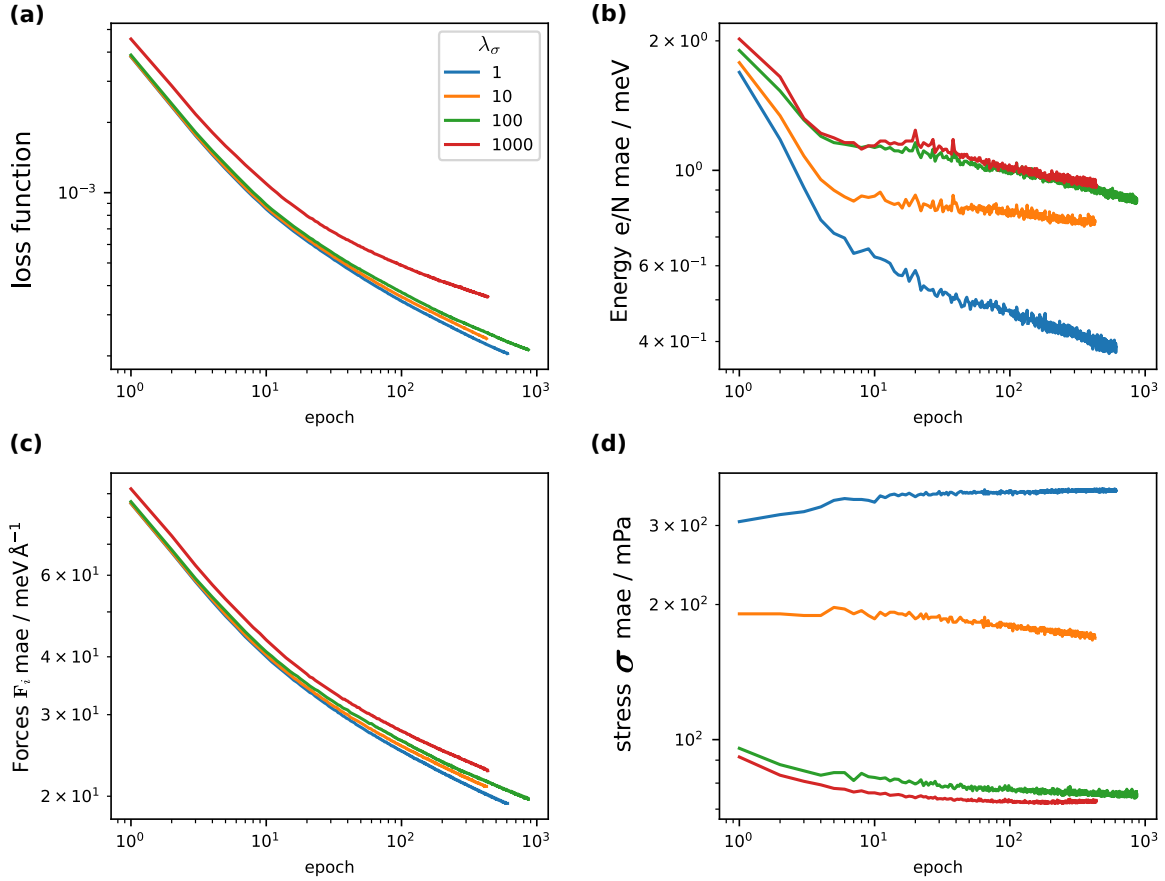


Figure 4.2: (a) Loss function and mean absolute errors (MAE) for (b) normalized energy E/N , (c) forces $\{F_i\}$ and (d) stress (σ) as the function of epoch for MLP(liquid|1: λ_σ) with $\lambda_\sigma \in \{1, 10, 100, 1000\}$.

do not hold for the stress, which do not appear to transfer to the crystal structure at low temperature, suggesting that the procedure for learning stress is perfectible.

	MLP	MLP(crystal σ)	MLP(liquid σ)
Energy MAE (meV/atom)		1.26	1.29
Forces MAE (meV \AA^{-1})		7.17	8.69
Stress MAE (MPa)		23.7	322

Table 4.3: MAEs of the trained models for MLP(crystal| σ) and MLP(liquid| σ), evaluated on unseen frames of the crystal trajectory.

A similar comparison showed that MLPs learned on the crystalline trajectory do not transfer well to the liquid structure, as expected because the latter contains configurations too far from the training dataset (e.g. undercoordinated Zn atoms). Both observations confirm that MLPs learned on the liquid trajectory are promising candidates to be used on multiple structures.

4.2.3 Reproducing structural properties

To further evaluate the quality of the generated MLPs, I looked at the same structural properties investigated for ReaxFF in chapter 3 for both systems used for training: the crystal and the liquid.

MD WITH NEQUIP

MD simulations with NequIP can be performed either using the atomic simulation environment (ASE) [251] or using LAMMPS [211]. Although LAMMPS was generally preferred, due to its extensive, robust and validated methods, along with better performance, the (N, P, T) ensemble is not yet implemented for NequIP potentials. In this chapter, I therefore stick to the (N, V, T) ensemble and, unless other-

wise mentioned, used LAMMPS. I nonetheless checked that both simulation engines gave consistent results.

By default, a time step of 0.5 fs was used in the MD runs, which could occasionally be changed to 0.25 fs to simulate high temperatures (above 1500 K). The temperature was controlled using a Nosé–Hoover thermostat with a temperature damping parameter fixed at 100 fs. Several values were tested, with the 50–400 ps range leading to satisfying behaviors. In most cases, I report simulations of the unit cell, although the impact of the use of supercells was explored.

Unless explicitly stated in the figure caption, properties were averaged over an (N, V, T) trajectory of 100 ps for NequIP simulations. Frames were taken every 100 fs for the radial distribution function (RDF), bond angle distribution and coordination number, every 500 fs for the mean square displacement (MSD), every 1 ps for ring statistics and every 10 ps for pore statistics. *Ab initio* properties were computed as in section 3.2.

A typical (N, V, T) simulation of a ZIF-4 unit cell (272 atoms) for 100 ps, required around 5 hours of computation on a single NVIDIA V100 GPU. It is a significant speedup compared to AIMD, for which 4 days and 160 CPUs (4 nodes of Intel Cascade Lake 6248) are required for the same system and duration. As a comparison, a ReaxFF simulation for the same system (with the parameters than in section 3.1.1 except for the system size) required one hour on one node (40 CPUs).

EVALUATION ON THE TRAINED SYSTEMS

Structural properties were evaluated over two (N, V, T) trajectories of crystal and liquid for three models: MLP(crystal), MLP(liquid) and MLP(liquid| σ). The crystal trajectory was started from the crystallographic reference structure, immediately raised to 300 K and was then equilibrated for 100 ps. The liquid was started from the same crystallographic reference structure immediately raised to 1500 K, and consisted of a melting part of 100 ps, followed by another 100 ps to collect statistics. While every MLP was used to simulate the crystal, MLP(crystal) could not be used for the liquid as it contained configurations too far from its training dataset. This was manifested by the systematic crashing of LAMMPS simulations at 1500 K.

Figure 4.3 shows three local properties (RDF, PMF and angle distributions) for the different combinations of phases (liquid or crystal) and MLPs. In every case, we note an excellent reproduction of the *ab initio* properties. Both MLP(liquid) and MLP(liquid| σ) emulate the crystal properties as accurately as MLP(crystal), thus demonstrating excellent transferability on this system. It is also worth mentioning that MLP(liquid) and MLP(liquid| σ) lead to the same reproduction of local properties, despite the difference in energies and forces MAEs reported above.

Additionally, no change in coordination nor ring statistics is observed for the crystal. Similarly, Zn–N coordination numbers for the liquid are almost identical ($\leq 1\%$ difference between MLPs and *ab initio*). However, ring statistics are not straightforwardly interpretable, as their convergence on liquid trajectories would require much longer equilibration times. Finally, the computed porous volumes are fairly similar for every phase, another evidence of the excellent reproduction of the structural properties of both the system they were trained on, and the crystal.

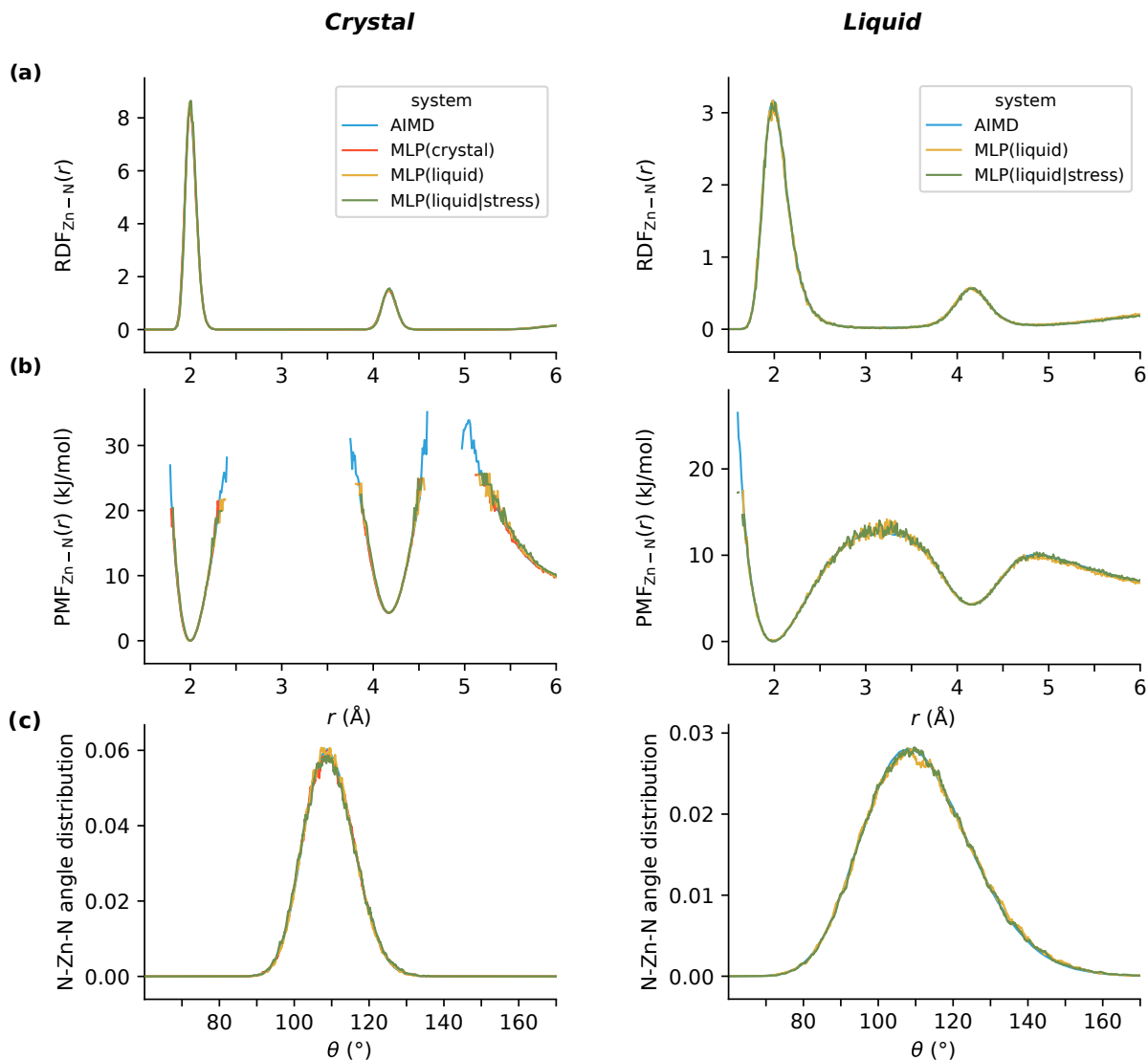


Figure 4.3: (a) Radial distribution functions (RDF), (b) potentials of mean force (PMF) for the Zn–N atom pairs, and (c) distribution of the N–Zn–N angle for the ZIF-4 crystal (left) and liquid (right) with multiple MLPs compared to AIMD.

VALIDATION ON *AB INITIO* GLASSES

To further explore the transferability on these MLPs, I deployed the same strategy, *i.e.* MD runs and computation of structural properties, for unseen ZIF-4 systems consisting in the 10 *ab initio* glasses generated by Gaillac et al. [123] I introduced in section 1.3.4.

Ten (N, V, T) MD simulations were run at 300 K for 100 ps starting from the glass models, with MLP(crystal), MLP(liquid) and MLP(liquid| σ). All reported structural properties were averaged over the ten glasses. Their local properties are reported on figure 4.4, which demonstrates the excellent reproduction of the *ab initio* RDF by every MLP. However, a closer investigation with the PMF highlights differences between MLPs. MLP(crystal) is shown to fail to reproduce the region between the two first minima in the PMF, a region absent from the crystalline training data (see figure 4.3). On the contrary, both MLP(liquid) and MLP(liquid| σ) were able to describe this region, with MLP(liquid) performing better. The gain in accuracy of MLP(liquid) over MLP(liquid| σ) is also visible on the angle distribution, for which MLP(liquid| σ) led to a slight deviation from the *ab initio* properties. Additionally, no change in coordination by every MLP and AIMD data was reported, with coordination numbers and ring statistics being identical.

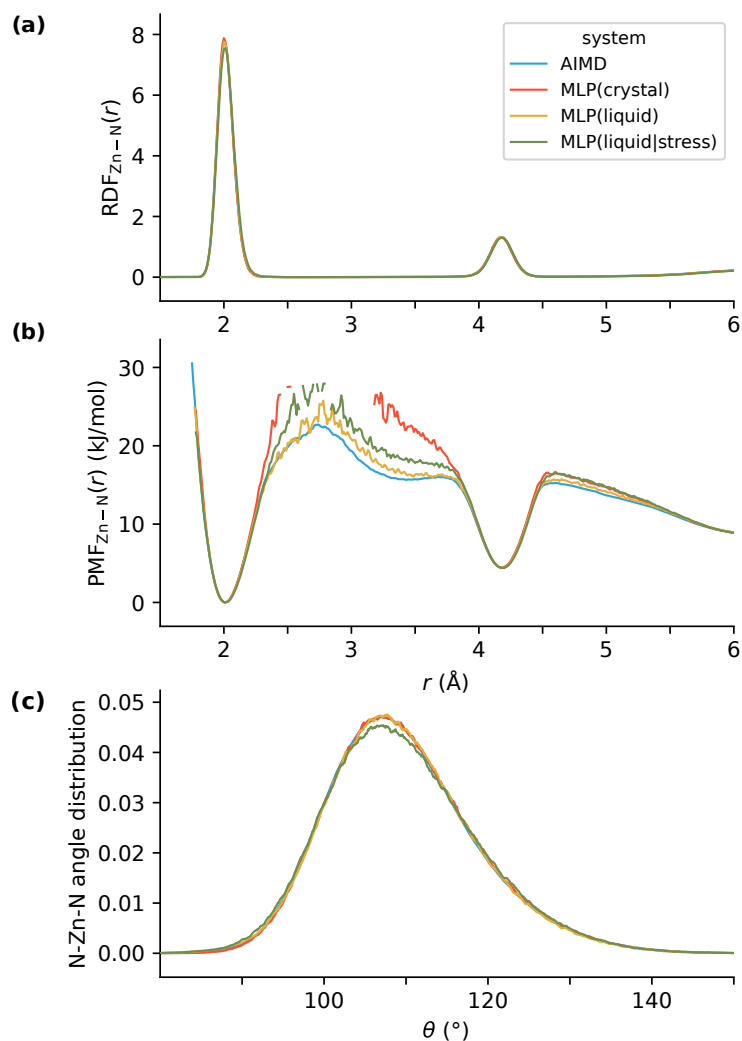


Figure 4.4: (a) Radial distribution functions (RDF), (b) potentials of mean force (PMF) for the Zn–N atom pairs, and (c) distribution of the N–Zn–N angle for the ZIF-4 *ab initio* glasses with multiple MLPs compared to AIMD.

At this stage, we were therefore confident that the strategy employed in this work to train MLPs is promising. It suggests that the data contained in the liquid trajectory are sufficient to model a variety of ZIF-4 phases. Among the multiple models developed, MLP(liquid) led to an overall higher accuracy and was therefore chosen for the rest of this chapter.

4.3 GENERATING *a*ZIF-4 GLASS MODELS

Using MLP(liquid) as a prototypical MLP to model ZIF-4, I used the same methodology as the work done with ReaxFF in chapter 3. I generated glass models and then compared their properties to *ab initio* data to evaluate the applicability of MLPs for this task.

4.3.1 Producing glass models by melt-quenching

PRODUCTION PROCEDURE

The melt-quenching procedure is similar to the one devised for ReaxFF in section 3.1. Starting with an initial preparation of the crystalline structure at 300 K, the system was first melted to 1500 K, then quenched to room temperature, leading to the creation of a glassy state. The system was finally equilibrated for 100 ps to collect statistics. The four steps of this procedure are represented on figure 4.5.

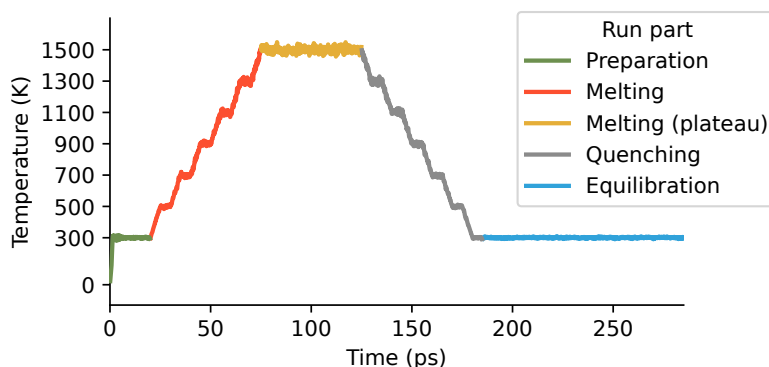


Figure 4.5: Temperature as a function of time during the glass formation procedure, consisting of preparation (green), melting (red and orange), quenching (grey) and equilibration (blue). For clarity, a moving average over 25 fs is used.

The entire procedure was performed in the (N, V, T) ensemble, as (N, P, T) simulations are not yet supported in LAMMPS with NequIP (see section 4.2.3). The preparation only consisted of a simple (N, V, T) run at 300 K, as I found that MDs with MLPs are not as sensitive as with ReaxFF. To reduce finite size effects, a $(2 \times 2 \times 2)$ supercell of ZIF-4 with 2176 atoms was simulated, with periodic boundary conditions. I checked that the use of a supercell did not significantly affect the properties of the generated glasses, compared to only simulating one unit cell. I also checked that the use of MLP(liquid) and MLP(liquid| σ) led to glasses of very close structural properties.

MELT-QUENCHING

As discussed in section 3.1.3, melt-quenching is mainly parameterized by the maximal temperature T_{max} and the heating/cooling rate r . Consistently with the previous *ab initio* work [123], I aimed for a maximal temperature of 1500 K, and chose a rate of 20 K/ps.

Contrary to ReaxFF simulations which led to excessive decoordination, MD simulations with MLP did not melt that easily. After a procedure consisting of only two ramps (one for heating, one for cooling), as with ReaxFF, the final system was still crystalline for $T_{max} = 1500$ K and r in the 50–2.5 K/ps region. Either lowering the rate to $r = 1$ K/ps, or increasing the temperature to $T_{max} = 1900$ K, both led to the successful formation of glasses. However the first option requires rather long simulations, while the second leads to an increased risk of loss of physical integrity.

Even if no breaking of the imidazolate rings was observed for $T \in [1500 \text{ K}; 1900 \text{ K}]$, I chose a safer third option which consisted in keeping $T_{max} = 1500$ K and spending more time at the maximal temperature as represented on figure 4.5. A plateau of 50 ps at T_{max} was enough to ensure melting, and therefore obtain a glass as highlighted on figure 4.6. I tested different plateaux in the 50–300 ps which all led to glasses of similar properties.

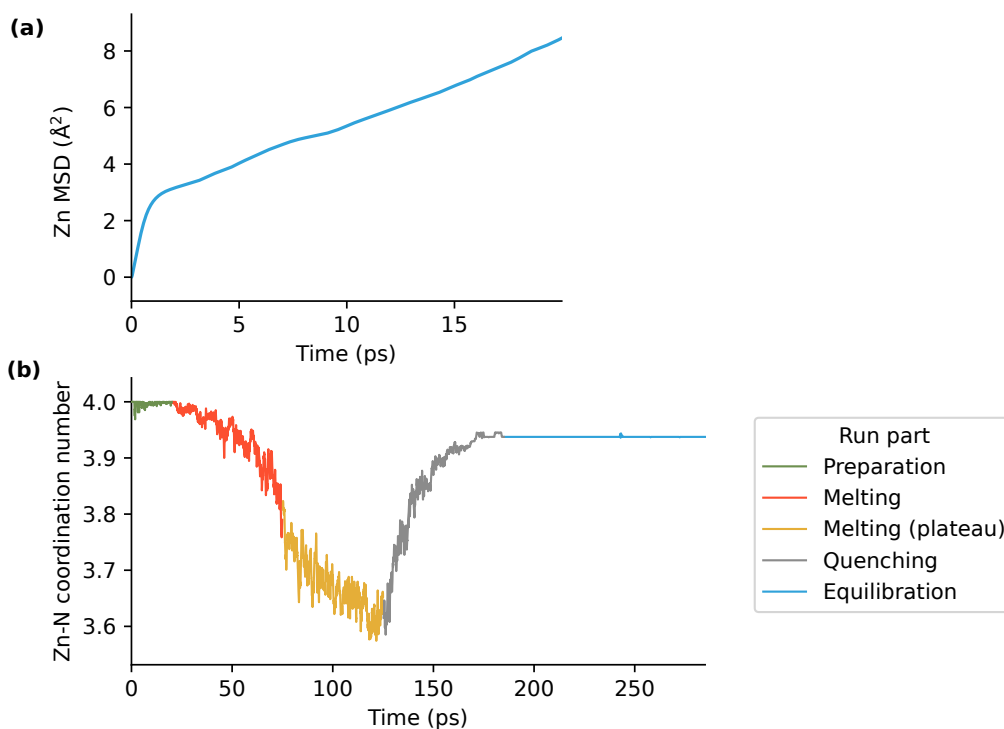


Figure 4.6: Evidence of melting and glass generation. (a) Mean square displacement (MSD) as a function of time for Zn during the 1500 K plateau. (b) Zn–N coordination number as the function of time with the final value for the glass system distinct from that of the initial crystal.

The option used for the *ab initio* glasses – *i.e.* starting straight away at 1500 K from the crystallographic crystal without a slow ramp up – was also tested. While it also led to glassy states, the low computational cost of MLPs makes a smooth ramp-up in temperature too affordable to justify an abrupt heat-up.

4.3.2 Properties of the glass models

I then investigated the exact same properties looked for the ReaxFF glass in section 3.2, and compared them to the same *ab initio* crystal and glasses.

LOCAL ORDER

I first investigated the local order by examining the Zn–N bonds. On figure 4.7 I plot the partial RDFs for the Zn–N and Zn–Zn atom pairs, which highlights a remarkable agreement of the MLP glass with its *ab initio* counterpart. To contrast the differences in the region between the first two peaks, the Zn–N PMF is shown on the same figure. Although the PMF of the MLP glass resembles that of a glass, with the region between the first two peaks populated, its profile is distinct from the one of the *ab initio* glass and shares some features of the crystalline PMF. In particular, the free energy barrier is larger for the MLP glass than for the *ab initio* one, with a value of $\simeq 32$ kJ/mol.

I then investigated the N–Zn–N angle, key to the features of ZIFs, by plotting the bond angle distribution on figure 4.8a. The MLP glass demonstrates an excellent reproduction of the *ab initio* data, while ReaxFF failed to do so. The angular PMF shown on figure 4.8b further confirms this accuracy, while hinting at small deviations for angles away from the 109° of the $\text{Zn}(\text{Im})_4$ tetrahedral structure. Once again, the MLP glass shows intermediate properties between those of the *ab initio* crystal and glass.

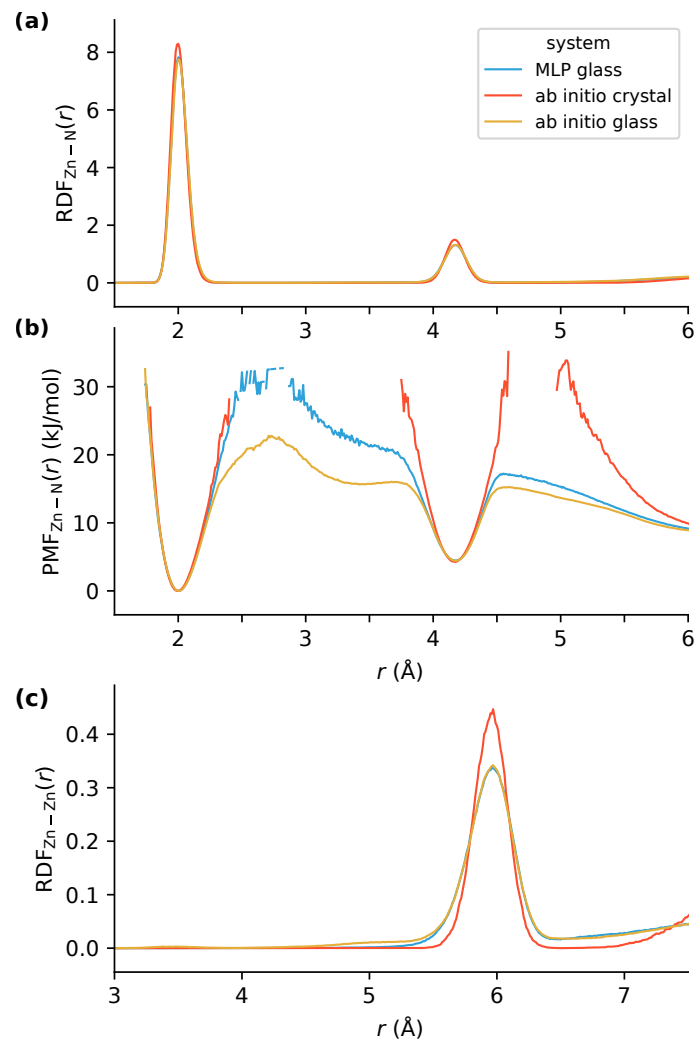


Figure 4.7: (a) Radial distribution functions (RDF) and (b) potentials of mean force (PMF) for the Zn–N atom pairs of the MLP glass (blue), *ab initio* glass (orange) and *ab initio* crystal (red). (c) RDF for the Zn–Zn atom pair of the same systems.

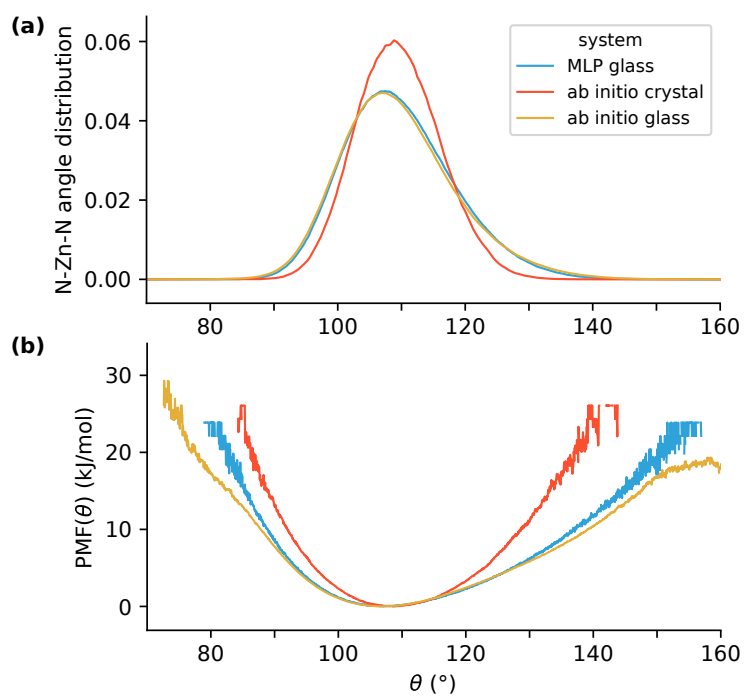


Figure 4.8: (a) Distribution and (b) potentials of mean force (PMF) of the N-Zn-N angle for the MLP glass (blue), *ab initio* glass (orange) and *ab initio* crystal (red).

BULK PROPERTIES

I computed the porosity of the glasses (see figure 4.9) and found a total porous volume of $61 \text{ cm}^3 \text{ kg}^{-1}$ for the MLP glass, comprised between the $54 \text{ cm}^3 \text{ kg}^{-1}$ of the crystal and $68 \text{ cm}^3 \text{ kg}^{-1}$ of the *ab initio* glass. This is in good agreement with the experimental measurements of the porosity of a ZIF-4 glass made by positron annihilation lifetime spectroscopy (PALS) [164]. Due to the reliance on the (N, V, T) ensemble, no comment can be made on the density of the MLP glass. This will be a key issue to characterize and validate in future work.

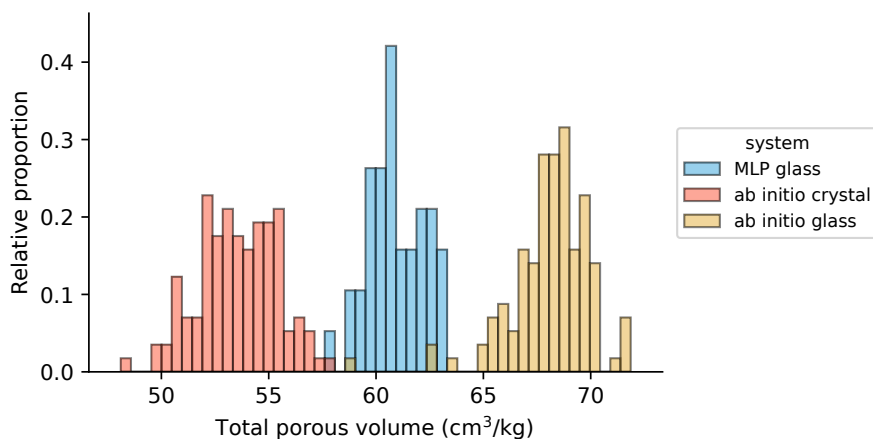


Figure 4.9: Total porous volume of the MLP glass (blue), *ab initio* glass (orange) and *ab initio* crystal (red).

TOPOLOGICAL PROPERTIES

Finally, I investigated the differences in the medium-range order of the glasses, by examining the coordination network built from the alternating Zn–Im units. I first calculated the average Zn–N coordination numbers and found a coordination of 3.94 for the MLP glass, in excellent agreement with the value of 3.93 found for the *ab initio* glass.

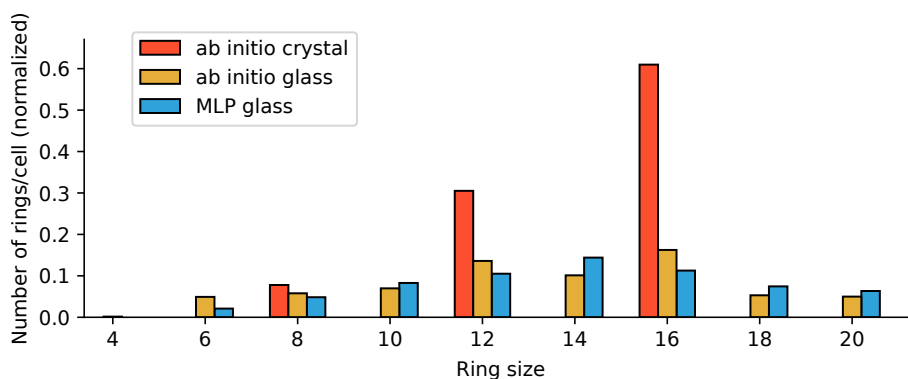


Figure 4.10: Distributions of size of zinc–imidazolate alternate rings for the ReaxFF glass (blue), *ab initio* glass (orange) and *ab initio* crystal (red).

In order to characterize the topology at a larger scale, I also computed Zn–Im ring statistics. Figure 4.10 evidences that both glasses have topologies that deviate from the crystal perfectly defined 8, 12 and 16 rings. While not identical, the two glass models display rather similar topologies.

Overall, these elements show that the generated MLP glass model demonstrates an excellent reproduction of a number of properties of the *ab initio* glasses, all the more when compared to how ReaxFF fared. It is interesting to note that a number of the properties of the MLP glass are intermediate between those of the *ab initio* crystal and glass models. While not identical to *ab initio* glass models, the MLP model is unambiguously a glass, with characteristics in line with known experimental data [92]. It provides strong evidence that *aZIF* models can be generated by MD simulations of melt-quenching.

4.4 TOWARDS A UNIVERSAL MLP FOR ZIFs

In the previous two sections, we limited ourselves to ZIF-4 and its different phases to develop a proof of concept. Our current work aims at going beyond this single system by going towards a “universal” MLP for ZIFs, which should work on multiple ZIF structures. To do that I generated *ab initio* training data for different structures, volumes and phases, aiming to build liquid trajectories. At the time of writing, training is still an ongoing work, as part of my collaboration with Jack D. Evans. I present in this thesis the general approach and some preliminary results.

4.4.1 Multiple ZIF structures

First, I selected several Zn-based ZIF structures, chosen to display diverse topologies and a selection of linkers. The latter are described on figure 4.11.

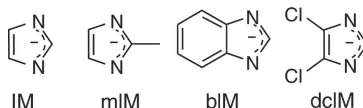


Figure 4.11: Different linkers present in the structures investigated: imidazolate (IM), benzimidazolate (bIM), 2-methylimidazolate (MeIM) and 4,5-dichloroimidazole (dcIM). Adapted from Ref. [71].

The different ZIFs are described in table 4.4 along with their composition, topology and number of atoms of unit cell N_{atoms} . The table also mentions the source of the structural files, which were either taken from previous works of the group or straight from the CSD [46] and CoRE MOF [170] databases.

ZIF-n	Composition	Net	Zeolite	N_{atoms}	Source
ZIF-4	Zn(IM) ₂	cag	–	272	[92]
ZIF-7	Zn(bIM) ₂	sod	SOD	522	[65, 170]
ZIF-8	Zn(MeIM) ₂	sod	SOD	276	[149]
ZIF-11	Zn(bIM) ₂	rho	RHO	1392	[65]
ZIF-62	Zn(IM) _{1.75} (bIM) _{0.25}	cag	–	296	[93]
ZIF-71	Zn(dcIM) ₂	rho	RHO	816	[46, 71]

Table 4.4: ZIF structures for which training data was generated long with their composition, structure, topology, number of atoms in the unit cell N_{atoms} and source of the structural file. Topology is expressed both with net three-letter abbreviations and the corresponding zeolite symbol (if it exists), described in Ref. [66] and retrieved from Ref. [65, 71].

Structures first went through a full geometry optimization (atomic positions and unit cell parameters) of the crystallographic files at 0 K, before being used in any MD simulation. I used for ZIF-7,11, and 71 the same configuration as the one used by Gaillac et al. for ZIF-4, 8 and 62 [92, 93, 149]. I used the same *ab initio* parametrization as the one thoroughly tested on multiple ZIFs and described in section 4.2.1. The only adaptation concerned Cl atoms, which were treated in a similar fashion to Zn atoms, *i.e.* they were described by double- ζ valence polarized basis sets and norm-conserving Goedecker–Teter–Hutter [275] pseudopotentials optimized for solids (DZVP-MOLOPT-SR-GTH). It is worth noting that ZIF-7,11, and 71 have considerably larger cells than the previously studied ZIF-4, 8, and 62. It is therefore more computationally demanding to run AIMD simulation of these systems, and I chose to generate fewer trajectories per ZIF structure.

4.4.2 Multiple volumes

While (N, V, T) simulations are an efficient way to generate training data at high temperature, we ambition to develop an MLP that could also be used for (N, P, T) simulations, which therefore requires to an accurate reproduction of the stress. An option is to learn from structures simulated at different volumes, by applying deformation to the initial cell of the crystal.

For each ZIF crystal, I created four (N, V, T) trajectories at 300 K with different deformations. Successive simulations at different volumes were performed, consisting in an instantaneous and isotropic volume change by 2% from the previous volume, followed by an equilibration time of around 10 ps. The final volume deformations were {2%, 0%, -2%, -4%}, as exemplified in the case of ZIF-8 with figure 4.12. These small changes in volume did not lead to many changes to the crystalline structure, with the local structural properties staying similar as exemplified on figure 4.12a, and the coordination remaining unchanged. Porosity is however impacted, with figure 4.12b highlighting the expected decrease in porous volume associated with a reduction of the total volume.

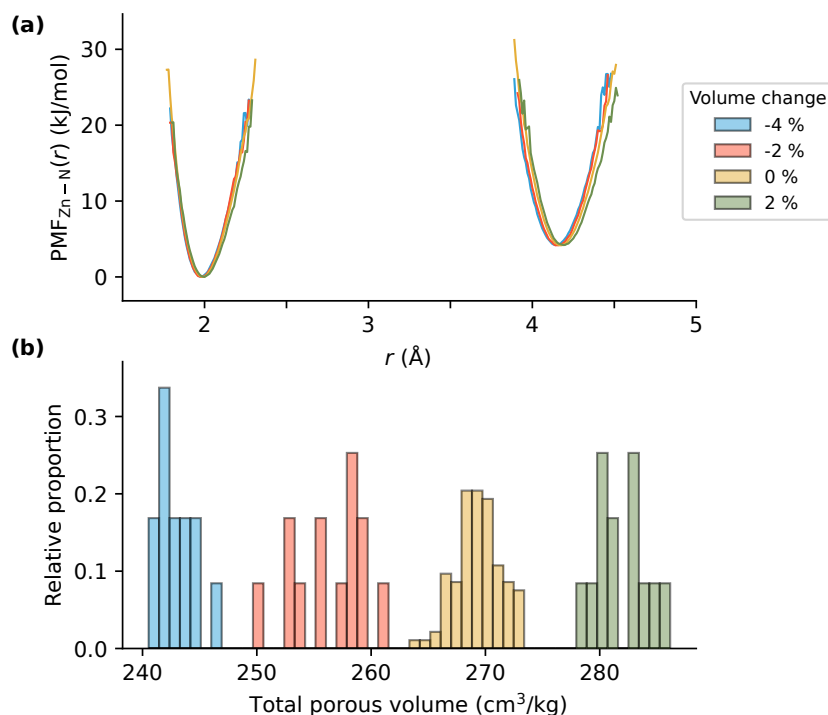


Figure 4.12: (a) Potentials of mean force (PMF) for the Zn-N atom pair and (b) total porous volume of the ZIF-8 crystal at various volume deformations. The volume deformation of 0% corresponds to the state of crystallographic density. Properties are averaged over the entire (N, V, T) trajectory of each volume.

4.4.3 Simulation of liquid systems

Once the 300 K crystal models at various volumes are prepared, they must be heated up to obtain high temperature trajectories, that should preferably simulate liquid systems. The choice of the high temperature value is a trade-off between the need to gather statistics on relatively rare events, and the necessity to preserve the physical consistency of the model. While previous *ab initio* MD simulations of the liquid ZIF-4 have been performed up to 2000 K while preserving the integrity of the imidazolate linkers [92], I found that for another system (ZIF-7) 2000 K was enough to break its linkers. Previous work on the melting of ZIFs [92, 149] showed that a duration of 50 ps is often sufficient to observe melting. I therefore ran multiple (N, V, T) trajectories of 50 ps at either 1200 K, 1500 K and 1750 K.

As previously discussed in section 3.1.4, detecting melting is insightful but not straightforward. If a trajectory is sufficiently long, it is possible to identify melting by spotlighting a loss in coordination as table 4.5 or a change in the behavior of the MSD as in figure 4.13a.

Volume change (%)	-4	-2	0	2
Average Zn-N coordination number	3.84	3.76	3.59	3.64

Table 4.5: Coordination numbers for nitrogen atoms around the zinc cation for 1500 K MD trajectories of ZIF-4 with various deformations. Computed over the last 10 ps of each trajectory.

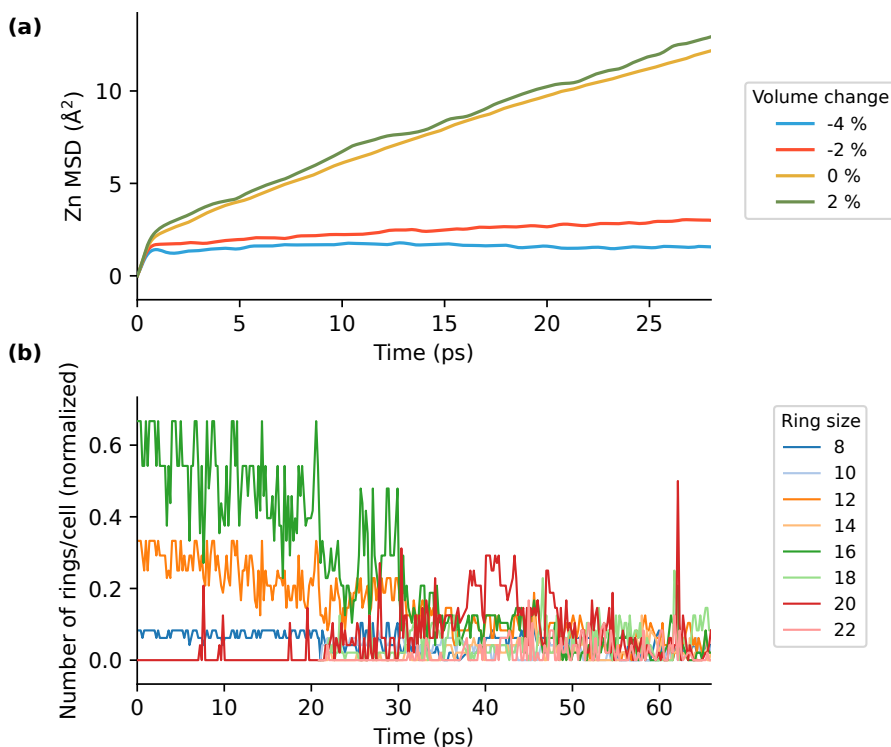


Figure 4.13: Evidence of melting during 1500 K MD trajectories of ZIF-4. (a) Mean square displacement (MSD) as a function of time for Zn with various deformations. (b) Number of zinc–imidazolate alternate rings of different sizes as the function of time for the trajectory with a deformation of 2%. For clarity, only rings of size comprised between 8 and 22 are shown.

As a complement, ring statistics can provide clear evidence of the onset of the melting transition. By monitoring the number of rings of different sizes as the function of time, as shown on figure 4.13b, one can easily identify a transition from the ring statistics of the crystal towards a less ordered system. This had not been used before, but I think it is a powerful descriptor to detect melting.

The choice of the temperature required to observe melting is not straightforward, as I found that it could depend on the deformation. Table 4.5 and figure 4.13a provide evidence in the case of ZIF-4 at 1500 K that systems with volume deformations of 0% and 2% ended up melting after a few tens of picoseconds, while -2% and -4% did not. Interpreting the relationship between deformation and melting behavior is not forthright, as the opposite behavior was observed for ZIF-8 at 1500 K (-2% and -4% melted while 0% and 2% did not).

As a result, I tried to melt every framework by raising the temperature up to 1750 K. Table 4.6 reports the different 50 ps runs that were performed at various temperatures, and whether they yielded solid or liquid systems. While melting was observed for four frameworks, I did not manage to obtain liquids of either ZIF-7 or ZIF-11. Heating up the system at 2000 K was tried, but led to the loss of the physical integrity of the linkers.

ZIF-n	T = 1200 K	T = 1500 K	T = 1750 K	$N_{trajectories}$	$N_{liquids}$
ZIF-4		2 solids, 2 liquids	2 liquids	6	4
ZIF-7	4 solids		1 solid	5	0
ZIF-8		2 solids, 2 liquids	2 liquids	6	4
ZIF-11	4 solids		1 solid	5	0
ZIF-62	4 solids		4 liquids	8	4
ZIF-71	4 solids		1 liquid	5	1

Table 4.6: Total number of 50 ps solid and liquid trajectories generated per system and temperature. For each ZIF, the total number of trajectories $N_{trajectories}$ and the number of liquid ones $N_{liquids}$ are reported.

An open question that should be tested when training the next MLPs, is whether these “hot solids” contain enough information about the potential energy surface of these frameworks for accurate training. If we consider all these high-temperature trajectories and still use 2500 frames for training, two frames will on average separated by typically 0.5–1 ps, ensuring a weak correlation [221]. If only the liquid trajectories end up being used, frames will be more correlated but still far less than for our ZIF-4 test case, which already showed promising results.

PRELIMINARY CONCLUSIONS AND PERSPECTIVES

In this chapter, I provided strong evidence that the development of MLPs can pave the way towards the generation of multiple amorphous MOF models and the study of their properties. Using a limited dataset consisting of *ab initio* trajectories of ZIF-4, we trained MLPs that led to an exceptional reproduction of the structural properties of multiple phases – crystal, liquid and several glasses – of ZIF-4.

By generating new *aZIF*-4 models by melt-quenching, I demonstrated the potential of these MLPs to generate disordered models of MOFs at a fraction of the computational cost of AIMD. A next step would consist in overcoming the reliance on the (N, V, T) ensemble, to capture the effects of vitrification on the system density.

While this work is promising, multiple challenges await to be overcome before being able to generate *aZIFs* for a larger variety of ZIF structures. As a first step towards the development of a more universal MLP for ZIFs, I generated multiple *ab initio* high-temperature trajectories of various ZIFs under different deformations. Our ongoing work is dedicated to the use of this training data to obtain and validate new MLPs that ought to be used on a variety of frameworks.

Finally, this work opens multiple perspectives that we plan to explore in the group. A first extension could consist in the exploration of even larger scales with another neural network architecture, Allegro [277], which uses a similar framework for training and MD simulations than NequIP. Another possible extension would be to use of the generated MLPs to simulate large *aZIF* structures generated by other means, for example using polymerization algorithms [82, 163] described in section 1.3.6.

FINITE TEMPERATURE MECHANICAL PROPERTIES OF *a*ZIFs

5.1	Computation of mechanical properties with molecular dynamics117
5.1.1	Extracting mechanical properties from simulations117
5.1.2	Finite difference methods.117
5.1.3	Strain-fluctuation method118
5.1.4	Mechanical properties of ZIFs119
5.2	<i>Ab initio</i> molecular dynamics121
5.2.1	Systems and methods121
5.2.2	Finite strain difference method.121
5.2.3	Reference values123
5.3	Reactive force fields125
5.3.1	Finite strain difference method.125
5.3.2	Finite stress difference method.126
5.3.3	Strain-fluctuation method128
5.4	Classical force fields131
5.4.1	Adaptation of the force fields131
5.4.2	Validation with AIMD results133
5.4.3	Exploring other methods134
5.5	Machine-learned potentials138
5.5.1	Finite strain difference method with NequIP.138
5.5.2	Accurately training for stress139
5.5.3	Reproduction of <i>a</i> ZIF-4 mechanical properties140
5.5.4	Exploratory use of the (N, P, T) ensemble.141
	Conclusions and perspectives143



I presented in chapter 1 the significant potential of MOFs for a series of applications, including CO₂ separation. However, while their mechanical stability is also essential for MOFs to fully achieve their potential in industrial-scale processes – in particular for processing (extrusion and pellet formation) –, the study of how these materials respond to mechanical stress is comparatively still emerging [278, 279]. *a*MOFs are particularly promising in this regard, as they yield the potential of increased mechanical robustness and would allow for greater ease of processing, notably by circumventing the performance

drop due to the necessary densification of the MOF powders [105, 106]. However mechanical properties of *a*MOFs are difficult to determine experimentally.

In this chapter, building on the knowledge about *a*ZIF models and MD schemes acquired in chapter 3 and chapter 4, I extensively investigated the computation of finite temperature mechanical properties of ZIF-4 in the crystal and glass phases. I critically assessed computational methodologies including *ab initio* molecular dynamics (section 5.2), reactive force fields (section 5.3), classical force fields (section 5.4), and machine-learned potentials (section 5.5) based on a variety of glass models. I found that ZIF-4 glasses have a larger bulk modulus than the crystal and confirm previous studies that the density is larger for the glass phases. Moreover, I confirmed in the case of ZIF glasses the relationship between density and bulk modulus, showing that obtaining models of correct density is key to the prediction of physical properties for these systems. At the exception of section 5.5 on machine-learned potentials which is an ongoing work, this study has been published in *Chemistry of Materials* (2023) [280].

5.1 COMPUTATION OF MECHANICAL PROPERTIES WITH MOLECULAR DYNAMICS

5.1.1 Extracting mechanical properties from simulations

While a series of experimental techniques have successfully been employed to determine the mechanical properties of crystalline MOFs, there is a lack of studies on the amorphous phases [81]. Some methods such as those relying on high-pressure X-ray diffraction [281] are not straightforwardly applicable to disordered materials, and many others require large bulk glass samples which are challenging to prepare [81, 282]. Fortunately, the same mechanical properties can be studied by computational simulations [167], which have been used extensively as a complement to experiments on MOF crystals and can lead to systematic studies of the structure–property relationships [283, 284].

We saw in section 1.3 that despite the challenges in the determination of the framework structure of amorphous states at the microscopic scale, several methodologies are available to generate the atomistic models which are a prerequisite of any computational determination of the mechanical properties. One family of approaches to computing finite temperature mechanical properties consists in using molecular dynamics (MD), either to mimic *in silico* the high-pressure experiments [285–287] or by using the strain-fluctuation method [257, 258]. Unlike most computational works which led to the determination of mechanical properties at 0 K, often using the stress-strain approach [288], the temperature dependence of these methods allows for a better prediction and understanding of the mechanical strength and stability of the studied materials [289]. It is key for disordered MOFs which can display complex pressure and temperature behaviors at both low and high temperature [93, 290].

In this work, I used a range of MD schemes to extract the finite temperature mechanical properties of ZIF crystals and glasses. I first report in section 5.2 how *ab initio* MD can be used to obtain reference values, which have never been determined for a MOF glass in the literature before. I then investigate three MD schemes with lower computational cost: reactive force fields (section 5.3), classical force fields (section 5.4) and machine-learned potentials (section 5.5).

Out of the many finite temperature mechanical properties that characterize anisotropic materials, in this study I will mostly focus on the bulk modulus (K) which characterizes the variation of the volume (V) of a solid under uniform hydrostatic pressure (P). It is defined as [291]:

$$K = -V \left(\frac{\partial P}{\partial V} \right)_T \quad (5.1)$$

Values of K reported in this work correspond to the equilibrium volume. This property is the most readily available experimentally, and provides key information relating to applications, including about the MOF stability during the shaping process [292] or pressure swing adsorption (PSA) cycles [278].

Two approaches were used in this work to obtain finite temperature mechanical properties: finite difference methods and strain-fluctuation methods.

5.1.2 Finite difference methods

The finite difference approach consists in first establishing the P – V relationship, and then fitting it with an equation of state (EoS). Widely used experimentally [85, 293], it is also within the reach of computational methods that can generate P – V data by running multiple MD simulations at various values of pressure or volume. This computational approach has been used on multiple materials such as molten salts [287, 294], ceramics [295] or silicates [285], and can be used with MD schemes ranging from *ab initio* [286, 287, 294] to classical [285, 295] and reactive [296] force fields.

P - V data is generated by running multiple MD simulations, enforcing either various values of pressure (stress) or volume (strain), and measuring the other variable. I will talk about the *finite strain difference* method if the MD simulations are performed in the constant-volume (N, V, T) ensemble by enforcing the volume V , with the resulting pressure $P(V)$ of the equilibrated system being measured. Alternatively, if they are performed in the constant-pressure (N, P, T) ensemble, with the volume $V(P)$ being measured for a given P , I talk about the *finite stress difference* method.

In both cases, the well-behaved region of the P - V data was fitted with the second order Birch–Murnaghan EoS [291, 297]:

$$P = 3Kf_E(1 + 2f_E)^{5/2} \quad (5.2)$$

where V_0 is the volume at zero pressure and f_E the Eulerian strain defined as

$$f_E = \frac{1}{2} \left[\left(\frac{V_0}{V} \right)^{2/3} - 1 \right] \quad (5.3)$$

In addition to providing K , this EoS fit returns V_0 and thus the density at zero pressure ρ_0 .

I systematically tried to use the third order Birch–Murnaghan EoS, and found that it leads to overfitting in the large majority (> 80%) of cases due to the small number of P - V data points, therefore it is not reported in this work.

5.1.3 Strain-fluctuation method

Mechanical properties at a given temperature T can also be evaluated from the fluctuations of a system at equilibrium, simulated under a constant stress in the (N, σ, T) ensemble [258]. The bulk modulus can be obtained directly from the fluctuations of the volume [258]:

$$\langle (\Delta V)^2 \rangle = \frac{k_B T \langle V \rangle}{K} \quad (5.4)$$

where k_B is the Boltzmann constant, $\Delta V = V - \langle V \rangle$, and $\langle X \rangle$ denotes the time average of any quantity X .

With this method, it is possible to obtain more than the bulk modulus, and access anisotropic mechanical properties. The elastic stiffness tensor \mathbf{C} can be obtained from the fluctuations of the unit cell matrix \mathbf{h} through the following relation [257, 258]:

$$\left(\frac{k_B T}{V} \right) C_{ijkl}^{-1} = \langle \varepsilon_{ij} \varepsilon_{kl} \rangle - \langle \varepsilon_{ij} \rangle \langle \varepsilon_{kl} \rangle \quad (5.5)$$

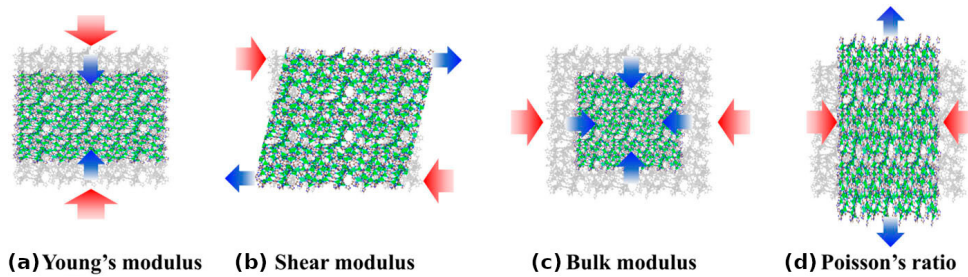


Figure 5.1: Schematic diagram of (a) Young's modulus (E), (b) shear modulus (G), (c) bulk modulus (K) and (d) Poisson's ratio (ν) illustrated for *azIF-4*. Red and blue arrows respectively represent the exerted stress and response. Adapted from Ref. [300].

In this equation, C_{ijkl} are the components of the fourth-order tensor \mathbf{C} , called elastic constants, and $\boldsymbol{\varepsilon}$ is the unit cell strain defined by: [298]

$$\boldsymbol{\varepsilon} = \frac{1}{2} \left(\left(\mathbf{h}_0^T \right)^{-1} \mathbf{h}^T \mathbf{h} \mathbf{h}_0^{-1} - \mathbf{1} \right) \quad (5.6)$$

with \mathbf{h}_0 the reference unit cell, corresponding to the first frame of the equilibrated trajectory.

From this elastic stiffness tensor, multiple mechanical properties – bulk modulus K , Young’s modulus E , shear modulus G , and Poisson’s ratio ν – were computed using the ELATE code [252] and are illustrated on figure 5.1. Values reported in this work were obtained with the Hill averaging scheme [299].

The computation of \mathbf{C} was performed using the Python library *aMOF*, presented in section 2.5.5, in which I adapted and implemented a code developed for previous works in the group [93, 257].

5.1.4 Mechanical properties of ZIFs

SYSTEMS OF THIS STUDY

Systems throughout this study belong to two different phases of ZIF-4: the crystal and the melt-quenched glasses [92]. ZIF-4 was further described in section 1.2.3.

Several structural analyses are presented in this chapter. They were performed using the parameters used and further detailed in section 2.5. Unless explicitly stated in the caption, properties are averaged over an (N, V, T) trajectory of 1 ns for classical MD simulations and 60 ps for *ab initio* simulations. For classical MD, frames are taken every 1 ps for the radial distribution function (RDF) and bond angle distribution, and every 50 ps for pore statistics. For *ab initio* MD, those intervals are respectively of 0.5 fs and 0.5 ps.

PREVIOUSLY REPORTED BULK MODULI

To this date, multiple experimental and computational values for the ZIF-4 crystal have been determined and are listed in table 5.1. K is comprised in the 1.4–2.7 GPa range for systems at a density (ρ_0) around the crystallographic density [65] of 1.22 g cm^{-3} , corresponding to a phase called open-pore (op) in the two latest experimental works that have focused on low-pressure behavior [290, 293]. Comparison between experiments and computational works is not straightforward as the measurements are complicated by subtle differences between MOFs from different batches (e.g. unintended defects incorporation during synthesis and different degrees of activation) and are dependent on the experimental setup (e.g. pressure transmitting medium) [293, 301]. Additionally, computational values reported so far are either computed at 0 K [302–304] or performed at a low level of theory [93, 257], with no *ab initio* value at finite temperature reported in the literature for the ZIF-4 crystal.

Though some mechanical properties of amorphous ZIF-4 such as the Young’s modulus [86] or the fracture toughness [157] have been determined [306], studies are significantly scarcer than for crystals. There are only two reported values of a bulk modulus, which stems from computational studies with the stress-strain approach performed on the same Continuous Random Network (CRN) model. A first work [141] found a bulk modulus of 8.88 GPa for a density of 1.07 g cm^{-3} , while a second one [300] reported $K = 4.47 \text{ GPa}$ and $\rho_0 = 0.99 \text{ g cm}^{-3}$. However, the physical realism of the CRN model has not been thoroughly demonstrated in the first place (see section 1.3.2), notably as it features a surprisingly low density (see section 3.2.2). Additionally, the mismatch in reported K values was left unexplained in the latest study, leaving us with no reliable value.

	Method	Ref.	K (GPa)	ρ_0 (g cm ⁻³)	Phase
Exp.	High-Pressure	[85]	2.6 ± 0.1	1.21	
	Crystallography	[293]	2.01 ± 0.05	1.22	(op)
			4.39 ± 0.20	1.56	(cp)
	Mercury intrusion	[290]	1.42	1.22	(op)
			4.88	1.53	(cp)
Comp.	Strain-fluctuation with classical FF [305]	[257]	2.58	1.31	
		[93]	2.69	1.31	
	Stress-strain from first principles [288]	[302]	2.41	1.16	
		[303]	1.54	1.03	
		[304]	1.76	1.18	

Table 5.1: Bulk moduli (K) and densities at zero pressure (ρ_0) of crystalline ZIF-4, as reported in previous experimental (top panel) and computational (bottom panel) works. With the exception of values computed by stress–strain (at 0 K), they are measured or computed at room temperature. The two most recent experimental works identified two low-pressure phases, open-pore (op) and closed-pore (cp), which are both reported.

5.2 AB INITIO MOLECULAR DYNAMICS

As we saw in section 2.2, *ab initio* methods, and in particular density functional theory (DFT)-based methods, allow for a full description of the electronic state of physical systems at the quantum chemical level. They are commonly used to compute mechanical properties at 0 K using the stress–strain approach [288], and have been applied to many MOF systems including for the ZIF-4 crystal [302–304] (see table 5.1). Combining the precision of *ab initio* methods with molecular dynamics allows the determination of finite temperature mechanical properties and can account for potential phase transitions that may occur under the application of both temperature and pressure [93, 290, 293]. Already applied to molten salts [287, 294] and metals [286], *ab initio* molecular dynamics (AIMD) has never – to my knowledge – been used to this aim for any MOF system. Despite its significant computational cost, AIMD can provide much needed reference values for ZIF glasses, where there are no experimental results currently available.

5.2.1 Systems and methods

As detailed in section 1.3, AIMD has successfully been used in prior works to model the melting of the ZIF-4 crystal [92], and to produce atomistic configurations of melt-quenched glasses [123]. All these models have been generated and equilibrated in the (N, V, T) ensemble, and thus are all at the same density (taken to be the crystallographic density 1.22 g cm^{-3}). Although this difficulty in capturing changes in density has been identified as an important limitation of the *ab initio* methodology [92], such glass models still represent the most chemically accurate atomistic description of ZIF-4 glasses published to date in the literature as seen in section 1.3.

Here, I have computed the bulk modulus K for four of these systems: the crystal and three melt-quenched glasses, chosen to preserve the diversity found in the Zn–N coordination environments. This restriction to 3 out of the 10 original glass models was guided by the significant computational cost of *ab initio* MD. AIMD simulations were performed using CP2K [273] with the exact same parameters presented in section 4.2.1.

5.2.2 Finite strain difference method

Due to the difficulty of performing (N, P, T) *ab initio* simulations of soft porous crystals [150] and to the reduced computational cost of (N, V, T) MD runs, I employed the finite strain difference method. All *ab initio* simulations were performed in the (N, V, T) ensemble to enforce a volume V and compute the resulting pressure $P(V)$ of the equilibrated system. Successive simulations at different volumes were performed, consisting in an instantaneous and isotropic volume change by 2% from the previous volume, followed by an equilibration time of around ~ 100 – 200 ps. Convergence was determined by monitoring the pressure as a function of time with a sufficiently large moving average of 5 ps, as illustrated on figure 5.2.

The value of the pressure for a given volume was taken as the average over the last 50 ps of the simulation. To estimate the uncertainty due to the fluctuations and limited simulation time, the last 50 ps were divided into blocks of 5 ps. The average pressure of each block was computed, and a standard deviation was calculated on these 10 values. Both the bulk modulus K and the extrapolated density at zero pressure ρ_0 were obtained by fitting the $P - V$ data with the second order Birch-Murnaghan EoS [291, 297]. Results are shown on table 5.2. The $P - V$ plot with the standard deviations as well as the fitted EoS is shown on figure 5.3 in the case of the crystal.

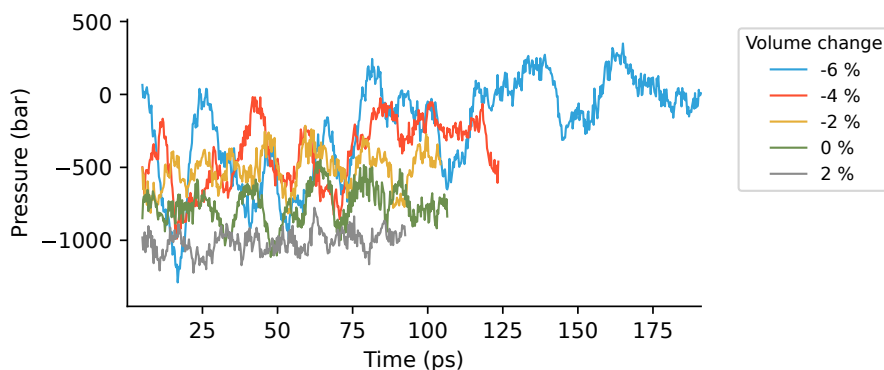


Figure 5.2: Pressure as a function of time for different deformations of the crystal. A moving average over 5 ps is used and deformation is defined as relative volume change to the reference volume of the crystal.

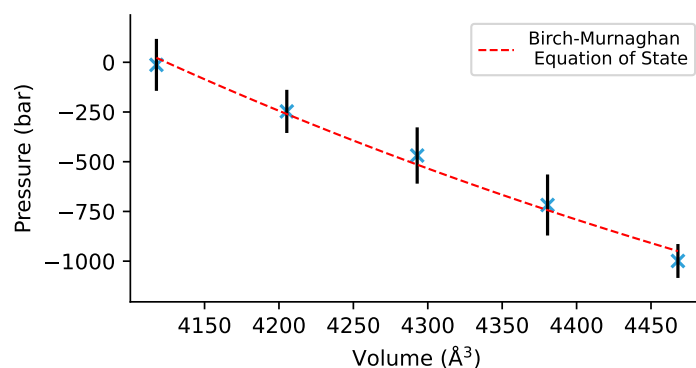


Figure 5.3: Pressure as a function of volume for the crystal, fitted with the second order Birch-Murnaghan Equation of State (red). Each volume corresponds to an (N, V, T) simulation with fixed deformation. Pressure is computed as the average over the last 50 ps of simulations. Error bars are the standard deviations of the pressure averaged with a rolling window of 5 ps.

	Crystal	Glass
K (GPa)	1.39	2.43 ± 0.09
ρ_0 (g cm^{-3})	1.29	1.34 ± 0.03

Table 5.2: Bulk moduli K and densities at zero pressure ρ_0 for the ZIF-4 crystal and glasses obtained by AIMD [123] with the finite strain difference method. Glass values are averaged over 3 models.

The same procedure was then used for the glass models, although the complex energy landscapes of ZIF systems – prone to polyamorphism [70, 307] – meant that it was not straightforward to observe a well-behaved $P(V)$ regime for a large range of volumes. As illustrated on figure 5.4, a structural rearrangement of the system caused by a large strain can lead to a change in the final pressure, although this structural change is not visible in local structural properties. Although 5 $P - V$ data points (as for the crystal) were obtained for one glass, fewer points were obtained for the other two glasses, which nonetheless confirm the results.

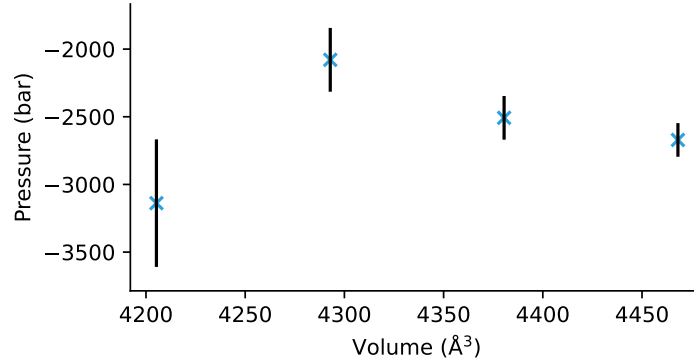


Figure 5.4: Pressure as a function of volume for one glass system, illustrating potential polymorphism. Each volume corresponds to an (N, V, T) simulation with fixed deformation. Pressure is computed as the average over the last 50 ps of simulations. Error bars are the standard deviations of the pressure averaged with a rolling window of 5 ps.

5.2.3 Reference values

As shown on table 5.2, I obtain a bulk modulus of $K_{\text{crystal}} = 1.39$ GPa, in reasonable agreement with previous experimental and computational works. It is in the lower range of values (see table 5.1), but further interpretation is limited, as the precise value determined depends on the computational methodology and – for experiments – also on subtle differences between MOFs from different batches or on the experimental setup [293, 301]. However, the comparison between two different systems within the same methodology is meaningful, and I find that the ZIF-4 glasses are less soft with $K_{\text{glass}} = 2.43 \pm 0.09$ GPa. This new result complements a previous nanoindentation study [86] that found that ZIF-4 melt-quenched glasses showed larger Young’s modulus ($E_{\text{glass}} = 8.2$ GPa) than in their parent crystalline phase ($E_{\text{crystal}} = 4.6$ GPa) [91].

Interestingly, this finite strain difference approach also yields the density at zero pressure ρ_0 which is of 1.29 g cm^{-3} for the crystal and of $1.34 \pm 0.03 \text{ g cm}^{-3}$ for the glass. We note that the glass density is higher than for the crystal, as expected from pycnometric measurements [86] ($\rho_{\text{glass}} = 1.63 \text{ g cm}^{-3}$ and $\rho_{\text{crystal}} = 1.50 \text{ g cm}^{-3}$) and from a recent CO_2 physisorption study [233] ($\rho_{\text{glass}} = 1.38 \text{ g cm}^{-3}$ which allows direct comparison to the crystallographic density [65] $\rho_{\text{crystal}} = 1.22 \text{ g cm}^{-3}$). An extended discussion can be found in section 3.2.2. However, the difference is not as large as what could be expected from these experiments and may come from the *ab initio* methodology, which led to glass models of the same density as the crystal before any deformation step.

It is worth mentioning that in the case of the crystal, the system was deformed enough to reach the density at zero pressure ρ_0 , without change in the local structural properties as shown on figure 5.5. However, no glass system was brought to its extrapolated ρ_0 .

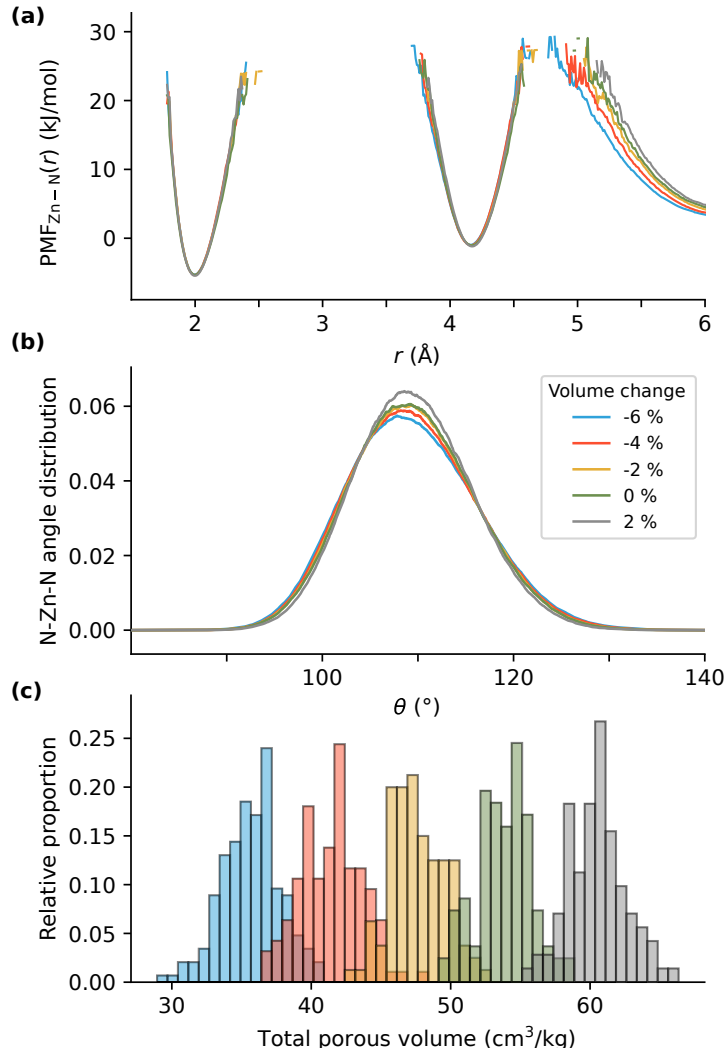


Figure 5.5: (a) Potentials of mean force (PMF) for the Zn–N atom pair, (b) distribution of the N–Zn–N angle, and (c) total porous volume of the *ab initio* crystal at various volume deformations. The volume deformation of 0% corresponds to the state of crystallographic density, while the volume deformation of -6% corresponds to the state of zero pressure. Properties are averaged over the entire (N , V , T) trajectory of each volume. All the local structural properties are similar, and the coordination is unchanged (evaluated with coordination numbers and ring statistics as in chapter 3, not reported here). As expected, the porous volume is decreasing with total volume.

In spite of the limitations discussed above, I find that *ab initio* simulations provide a reference value for the bulk modulus at room temperature of ZIF-4 glasses, which may be thought of as a lower bound due to the low density of the particular glass models used. We note that such a quantity had never been determined before at the quantum chemical level. By comparing two states of similar densities, it further demonstrates the influence of the system topology on the mechanical properties of ZIF-4 systems. It complements previous results on the high-density states which found the closed-pore ZIF-4 phase bulk modulus (~ 4.4 to 4.9 GPa) [290, 293] to be much lower than its polymorph ZIF-zni (~ 14 GPa) [308], while they all show similar densities (1.53 to 1.56 g cm⁻³).

5.3 REACTIVE FORCE FIELDS

With a reference value now at hand, it is possible to develop and validate more computationally efficient alternatives for the determination of finite temperature mechanical properties. To develop a method able to screen the mechanical properties of a large number of ZIF glasses, it would be convenient and consistent to use the same MD scheme for the glass model generation and the subsequent determination of its properties. An option is the use of reactive force fields (presented in section 2.3.3), which have been proposed to generate models of ZIF glasses by melt-quenching with the development of a ReaxFF parametrization for ZIFs [155] as we saw in section 1.3.5. They have previously been used to compute mechanical properties [156, 157, 159] and are a natural candidate for the task at hand. Able to explore larger spatial and time scales, they could in principle be used to obtain the bulk modulus with several methods while reducing the finite size effects inherent to AIMD. However, I showed in chapter 3 the atypical structural properties of the glasses obtained with this approach, and there is still no in-depth validation of the mechanical properties obtained with this force field in the existing literature.

In order to offer a meaningful comparison to other MD schemes, I consider several glass models: the ReaxFF glass obtained in chapter 3, the same three *ab initio* glass models studied in the previous section [123] and a glass obtained by Reverse Monte Carlo (RMC) modeling [92, 129]. MD simulations were performed using LAMMPS [211, 256] with the exact same parameters presented in section 3.1.1.

5.3.1 Finite strain difference method

To allow direct comparison to our *ab initio* results, I first computed K with the finite strain difference method. The reduced computational cost allowed for smoother volumetric deformations (1.5% change over 250 ps) and a longer equilibration (250 ps, shown on figure 5.6) than was possible with AIMD.

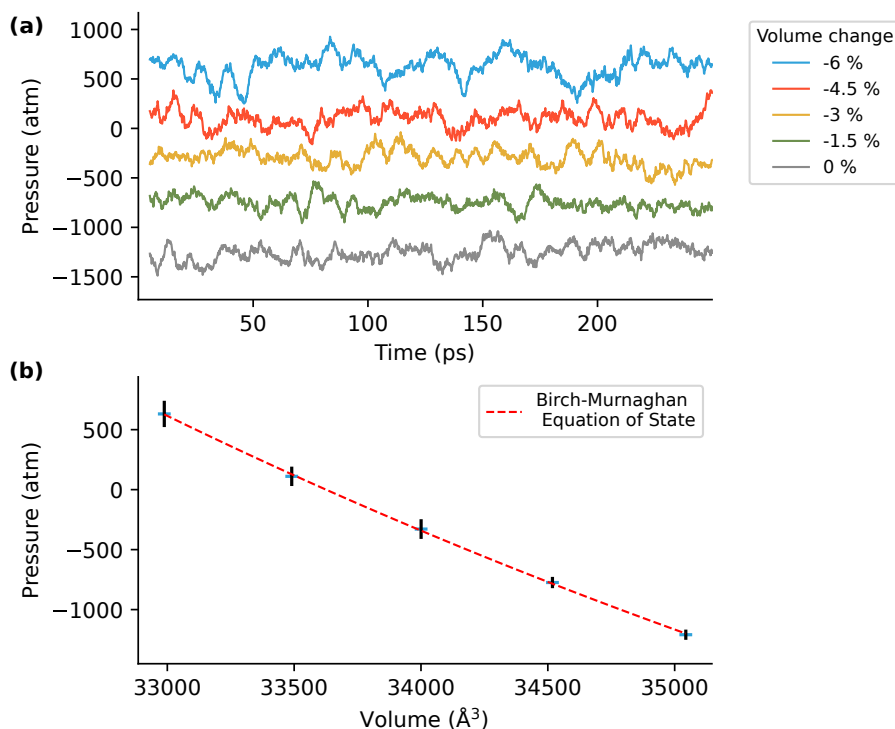


Figure 5.6: Finite strain difference method for the crystal with ReaxFF. (a) Pressure as a function of time for different deformations, shown with a moving average over 5 ps. (b) Pressure as a function of volume fitted with the second order Birch-Murnaghan EoS (red). Each volume corresponds to an (N, V, T) simulation with fixed deformation. Pressure is computed as the average over the last 100 ps of simulations. Error bars are the standard deviations of the pressure averaged with a rolling window of 10 ps.

All these systems were already introduced in section 3.3.1, and notably went through a careful preparation process. I took $(2 \times 2 \times 2)$ supercells of the crystal and *ab initio* glasses to have the same system size as the ReaxFF glass, and reported properties (K and ρ_0) for the *ab initio* glasses are averaged over the three models. For the finite strain difference method, the ReaxFF glass was taken at the last 300 K plateau of the quenching process, and the other systems were taken at the last (N, V, T) step of the preparation process. Therefore the latter still possess the initial model densities. They all went through a long (N, V, T) equilibration of 1 ns before any volume deformation.

Volume deformation in the (N, V, T) ensemble was a continuous process, during which each dimension of the box changed linearly with time from its initial to final value to achieve a volume reduction by 1.5%. The well-behaved region of the $P - V$ data for the fit with the second order Birch-Murnaghan EoS was selected to have 5 points at maximum and to include the region of zero pressure. While 5 points were found for the crystal, ReaxFF and RMC glasses, only between 3 and 4 points could be obtained for the *ab initio* glasses.

This approach led to well-behaved $P - V$ plots and to the values presented in table 5.3. Although of reasonable density, the ReaxFF crystal shows a larger bulk modulus by comparison with AIMD and experimental results. The bulk moduli and densities reported for the *ab initio* glasses do not contrast with the values computed for the crystal as clearly than with AIMD. The glass models which display higher K , represent states of considerably higher densities than the AIMD glass model and than the experimentally determined crystallographic density of ZIF-4 glasses [233], and are therefore not directly comparable.

	Crystal	ReaxFF glass	RMC glass	<i>Ab initio</i> glass
K (GPa)	3.15	10.36	6.29	3.57 ± 0.75
ρ_0 (g cm^{-3})	1.26	1.67	1.55	1.31 ± 0.03

Table 5.3: Bulk moduli K and densities at zero pressure ρ_0 for multiple ZIF-4 models obtained with the finite strain difference method with ReaxFF.

5.3.2 Finite stress difference method

An alternative option is the use of the finite stress difference method, in which the MD simulations are performed in the constant-pressure (N, P, T) ensemble at a given P , before measuring the volume $V(P)$. It is illustrated on figure 5.7. This approach is more commonly used in conjunction with classical and reactive force fields [296]. I evaluate the method using two possible variants, with an isotropic or a flexible cell (respective LAMMPS keywords `iso` and `tri`), as I have shown that this choice can impact the description of the glass. Section 2.1.3 provides a description of these thermodynamic ensembles.

For this method with a flexible cell, the initial systems for the finite strain difference method (see above) were taken and were further equilibrated in the (N, P, T) ensemble until convergence of the volume. The equilibration times t_{eq} are reported in table 5.4. For the finite stress difference method with an isotropic cell, at the exception of the ReaxFF glass, the initial systems for the finite strain difference method were taken and were further equilibrated for 500 ps in the (N, P, T) ensemble. For the ReaxFF glass, the initial system is the same as with the flexible cell.

	Crystal	ReaxFF glass	RMC glass	<i>Ab initio</i> glass
Finite stress difference with a flexible cell	5	10	20	7-7.5
Strain-fluctuation	5	10	22	7-18

Table 5.4: Equilibration times t_{eq} (in ns) spent in the (N, P, T) ensemble with a flexible cell for two methods.

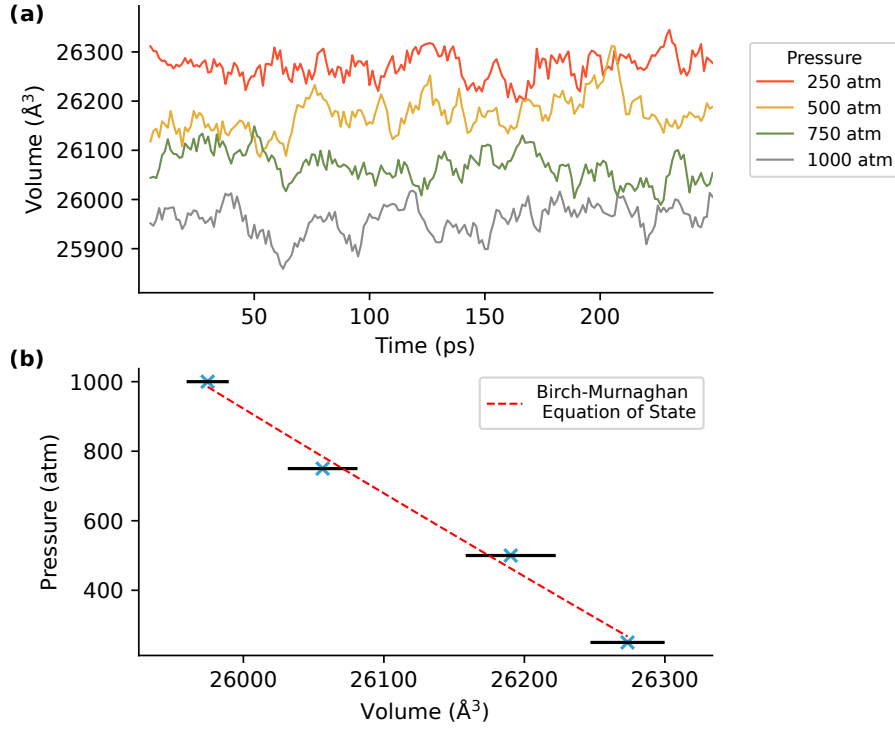


Figure 5.7: Finite stress difference method with a flexible cell (LAMMPS keyword `tri`) for the crystal with ReaxFF. (a) Volume as a function of time for different pressures, shown with a moving average over 5 ps. (b) Pressure as a function of volume fitted with the second order Birch-Murnaghan EoS (red). Each volume corresponds to an (N, P, T) simulation with fixed pressure. Volume is computed as the average over the last 100 ps of simulations. Error bars are the standard deviations of the pressure averaged with a rolling window of 10 ps.

Successive simulations at different pressures were applied, consisting in ramping up the pressure from 0 MPa to P_{max} by step of P_{step} and t_{step} . P_{max} , P_{step} and t_{step} values for the different systems are reported in table 5.5. The well-behaved region of the $P - V$ data was composed of 4 or 5 points for the crystal, ReaxFF and RMC glasses, and between 3 and 5 points for the *ab initio* glasses (average of 4.2).

System	cell	P_{max} (atm)	P_{step} (atm)	t_{step} (ps)
Crystal	tri	1000	250	250
	iso	1000	250	500
ReaxFF glass	tri/iso	2000	500	500
RMC glass	tri	1000	250	250
	iso	1000	250	500
<i>Ab initio</i> glass	tri	1000	250	1000
	iso	1000	250	500

Table 5.5: Maximal pressure P_{max} (in atm), pressure increment P_{step} (in atm) and time spent at each pressure t_{step} (in ps) for different systems and cell types, used for the finite stress difference method with ReaxFF.

While this method yields results for every studied system, as reported on table 5.6, the significant mismatch between values computed with different cell types, which should not exist for the crystal, severely questions the results and illustrate once again the tendency of ReaxFF to densify systems I highlighted in section 3.3.1. Additionally, the only two low-density states (the crystal and the *ab initio* glasses with an isotropic cell), have lower values than what was obtained with AIMD, the opposite of

what yielded the finite strain difference method with ReaxFF. This seriously discourages using the finite stress difference method with ReaxFF.

	cell	Crystal	ReaxFF glass	RMC glass	<i>Ab initio</i> glass
K (GPa)	iso	0.91	7.64	1.83	1.87 ± 0.75
	tri	6.11	10.60	7.89	4.07 ± 1.52
ρ_0 (g cm ⁻³)	iso	1.31	1.74	1.50	1.36 ± 0.06
	tri	1.61	1.68	1.57	1.46 ± 0.08

Table 5.6: Bulk modulus K and density at zero pressure ρ_0 for multiple ZIF-4 models obtained with the finite stress difference method with ReaxFF, either using an isotropic (iso) or a flexible (tri) cell.

5.3.3 Strain-fluctuation method

Another approach to obtain mechanical properties at a given temperature T is to evaluate them from the fluctuations of the unit cell of an equilibrated system simulated under a constant-stress (N, σ, T) ensemble [258]. Unlike the previous finite difference methods which only yield one property at a time, it leads to the estimation of the entire tensor of second-order elastic constants $C_{ij,kl}$ which in turns is linked to mechanical properties such as Young’s modulus, shear modulus, and Poisson’s ratio [252]. This approach, already used for the ZIF-4 crystal with a classical force field [93, 257], requires long equilibration times ($\sim 5 - 10$ ns). While out of reach of AIMD simulations, it is tractable with ReaxFF. The bulk modulus can also be directly computed from the fluctuations of the volume [258], a second method I used as a validation.

Starting from the initial systems for the finite strain difference method, I performed further (N, P, T) simulations with a flexible cell, corresponding to the (N, σ, T) ensemble required by the method, until convergence of the volume (see figure 5.8) and elastic constants (see figure 5.9), which may be a bit longer than the sole volume. It required a total equilibration time t_{eq} comprised between 5 ns and 22 ns, detailed in table 5.4. The elastic constants, the volume fluctuations and the volumes were computed over the last 3 ns of the simulation for the crystal, RMC glass and two *ab initio* glasses, and over the last 2.5 ns for the two other systems.

From the resulting bulk moduli, shown on table 5.7, we see that both strain-fluctuation methods are consistent. While such a long ReaxFF equilibration only yields highly densified states, with large K as a consequence, the results are consistent with the high-density states explored with finite difference methods.

	Crystal	ReaxFF glass	RMC glass	<i>Ab initio</i> glass
K - volume fluctuations (GPa)	5.65	12.73	7.47	4.30 ± 0.64
K - elastic constants (GPa)	7.58	12.85	7.62	4.77 ± 0.88
ρ_0 (g cm ⁻³)	1.61	1.68	1.56	1.46 ± 0.07

Table 5.7: Bulk moduli K and densities at zero pressure ρ_0 for multiple ZIF-4 models obtained with two strain-fluctuation methods with ReaxFF.

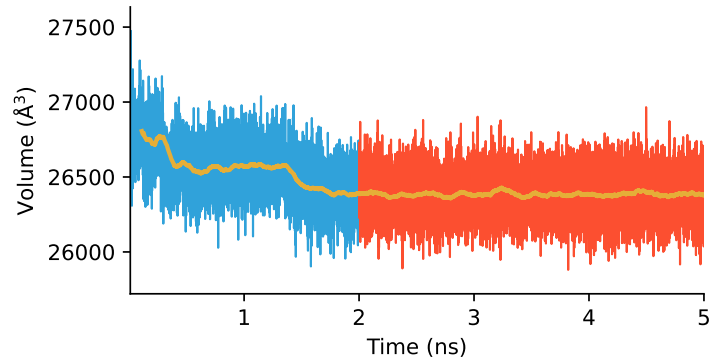


Figure 5.8: Volume as a function of time during a long 5 ns equilibration in the (N, P, T) ensemble with a flexible cell for the crystal. Elastic constants were computed on the red part of the figure. The orange line shows a moving average over 100 ps.

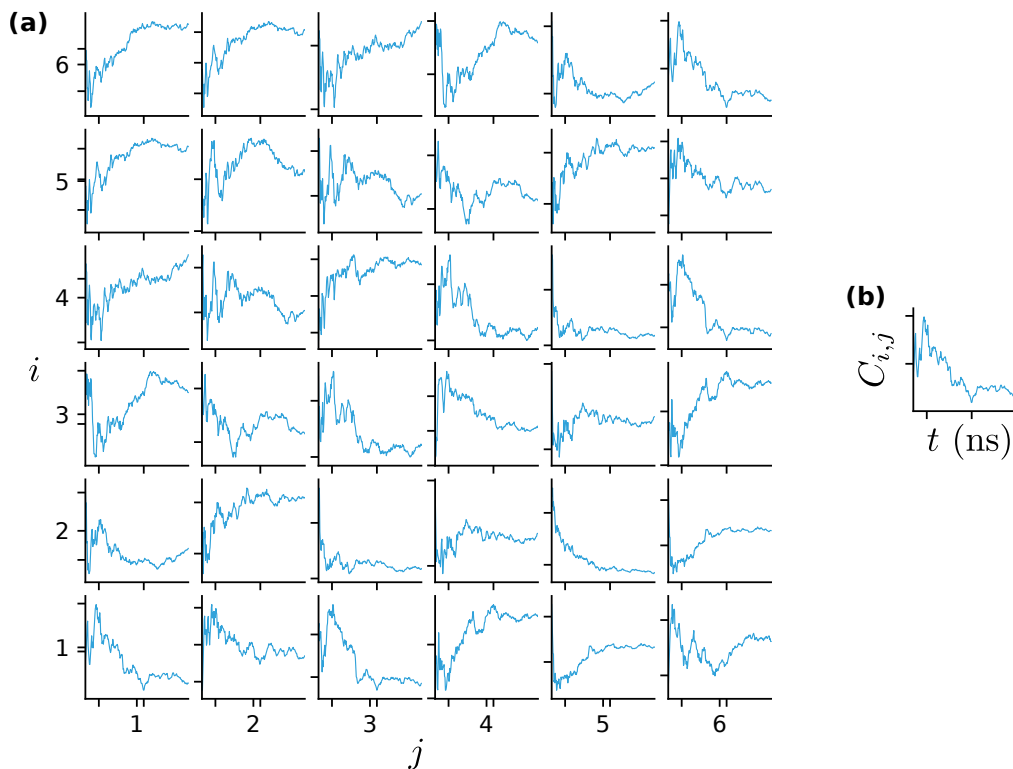


Figure 5.9: (a) Convergence of the elastic constants C_{ij} as function of time for the crystal with ReaxFF during a long 5 ns equilibration in the (N, P, T) ensemble with a flexible cell. (b) At time t , the represented $C_{ij}(t)$ corresponds to the elastic constant computed from the 2 ns to $(t + 2)$ ns part of the trajectory. The C_{ij} used for the computation of the mechanical properties thus correspond to the final $t = 3$ ns.

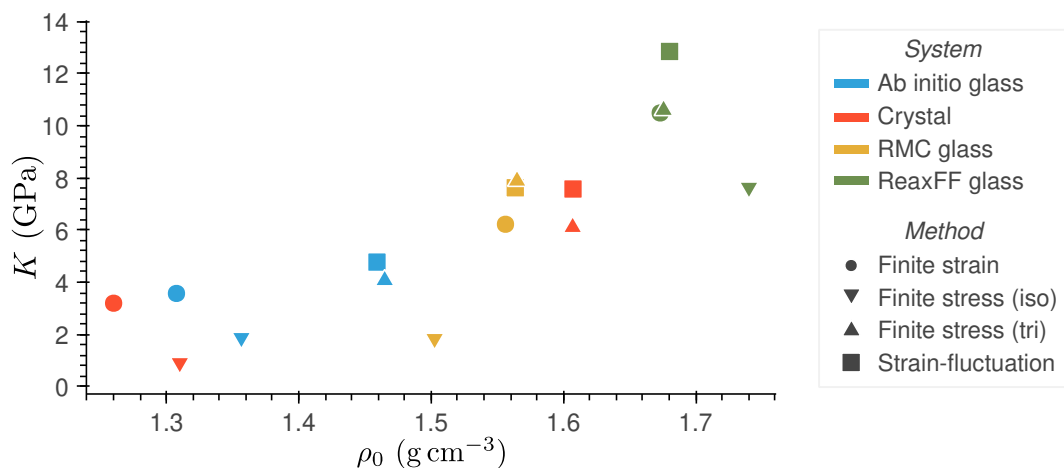


Figure 5.10: Bulk modulus K as function of the density at zero pressure ρ_0 for multiple ZIF-4 models and methods with ReaxFF.

This additional method confirms the very direct relationship between large K and ρ_0 , apparent on figure 5.10, which is found almost irrespective of the model – crystal or glass – and of the method used to compute K . It is therefore difficult to separate the influence of the topology (e.g. between different glasses) from the density, or to study low-density glass models. As a consequence, I cannot recommend the use of the ReaxFF parametrization for ZIFs [155] to compute mechanical properties, especially at finite temperature, and suggest that every work that intend to use it should first go through a detailed validation.

5.4 CLASSICAL FORCE FIELDS

Considering the strong limitations of the ReaxFF parametrization for ZIF glasses, no computationally efficient MD scheme published to this date in the literature can both generate ZIF melt-quenched glasses and provide their finite temperature mechanical properties. In this section, I look into a possible strategy to separate these two aspects and investigate the use of classical force fields (presented in section 2.3.2) to analyze the crystal and glass models generated by AIMD [92, 123] studied in the first section. Owing to the computational efficiency of classical MD, all 10 configurations of the melt-quenched glasses were simulated.

5.4.1 Adaptation of the force fields

As detailed in section 2.3.2, every classical FF for ZIFs published to this date has been developed for crystals and should thus first be adapted and validated before studying ZIF glasses. In my study, I chose to use the recently developed MOF-FF for ZIFs by Dürholt et al. [203], presented in section 2.3.2. This force field showed good transferability across a series of ZIF polymorphs, indicating that it can handle various network topologies, and led to mechanical properties in line with earlier FFs [204]. Developing a new FF for glasses from scratch is beyond the scope of this study, but the MOF-FF methodology for an automatic parametrization of FFs would make such a development achievable in future work [145].

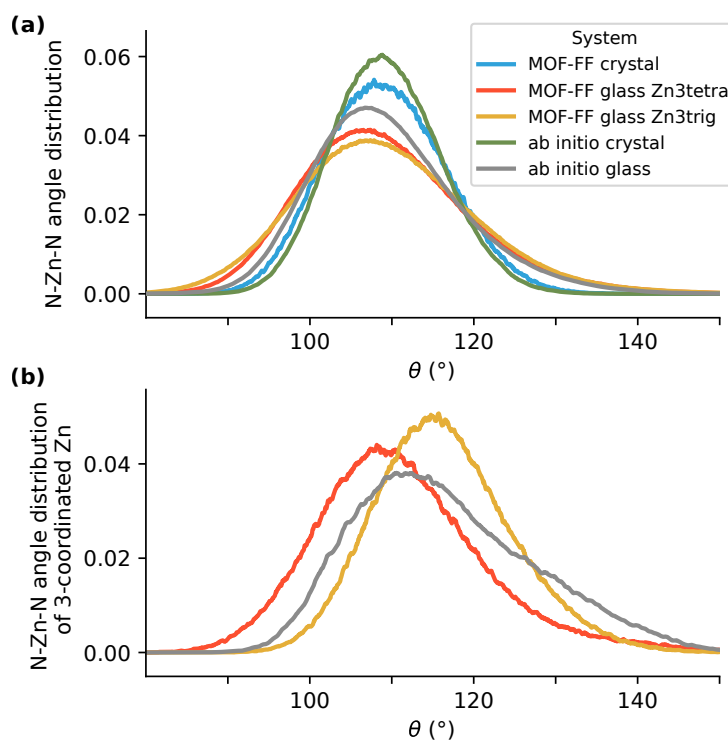


Figure 5.11: Distribution of the N–Zn–N angle for (a) every Zn atom and (b) only three-coordinated Zn atom, for the MOF-FF crystal (blue) and glasses (red and orange) compared the *ab initio* crystal (green) and glass (grey).

While ZIF-4 crystals are made only of $\text{Zn}(\text{Im})_4$ tetrahedra, a number of three-coordinated Zn ions can be found in ZIF-4 glasses, which are not readily parametrized in MOF-FF. On the N–Zn–N bond angle distribution of the *ab initio* glass shown on figure 5.11, we see that these three-coordinated Zn deviate from the 109° angle of the tetrahedra. To reproduce the glass properties and test the sensitivity of our results to our adaptation of MOF-FF, I introduced and evaluated two adaptations of the FF, which I name Zn3tetra and Zn3trig which respectively shift the N–Zn–N angle of the three-coordinated Zn towards

109° or 120° as shown on figure 5.11. Their construction is detailed in section 2.3.2. As it features no under-coordinated Zn atoms, the ZIF-4 crystal is simulated with the original FF.

In order to evaluate the validity of these FF adaptations, I compared the structural characteristics of ZIF-4 systems simulated with MOF-FF to the original *ab initio* models, using the same metrics as in chapter 3 on ReaxFF. An investigation of the local order with the partial radial distribution functions (RDF) and potentials of mean force (PMF) (see figure 5.12a,b), evidences an excellent reproduction of interatomic distances and similar energy landscapes close to the energy minima. The region between the two minima in PMF is qualitatively different, as MOF-FF is unable by design to simulate non-bonded but nearby Zn-N atoms. Despite differences in the angle distribution of the three-coordinated Zn atoms, figure 5.11 shows that the total distribution is similar for both FF adaptations, which reproduce the wider distribution of angles for the glasses than for the crystal. Although affected by the small difference in geometry imposed by the FF adaptations, both FF adaptations lead to glass models of higher porosity than the crystal, as shown on figure 5.12c. Finally, as classical MD cannot simulate bond breaking, the coordination and topology (e.g. ring statistics) are automatically preserved. Despite not being developed for ZIF glasses, both FF adaptations reasonably reproduce the structural properties of the *ab initio* systems, at least compared to the only force field available in the literature for amorphous ZIFs, namely ReaxFF.

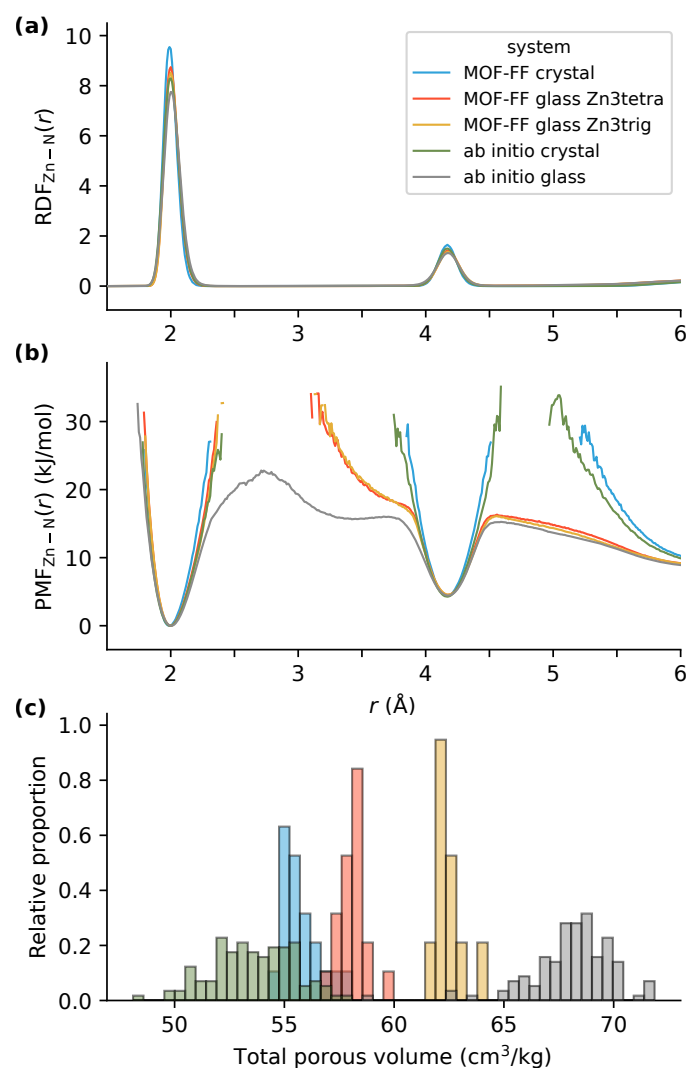


Figure 5.12: (a) Radial distribution functions (RDF), (b) potentials of mean force (PMF) for the Zn–N atom pairs, and (c) total porous volume of the MOF-FF crystal (blue) and glasses (red and orange) compared the *ab initio* crystal (green) and glass (grey).

Classical MD simulations were performed using LAMMPS [211]. A timestep δt of 1 fs was used in the MD runs and, the temperature (and pressure when applicable) were controlled using a Nosé–Hoover thermostat (and barostat). Temperature and pressure damping parameters T_{damp} and P_{damp} were fixed at 1 ps and 10 ps respectively.

5.4.2 Validation with AIMD results

I investigate the applicability of these classical FF adaptations by computing finite temperature bulk moduli, with the same methods I used on ReaxFF, starting with the finite strain difference method (illustrated on figure 5.13) to allow direct comparison with AIMD results.

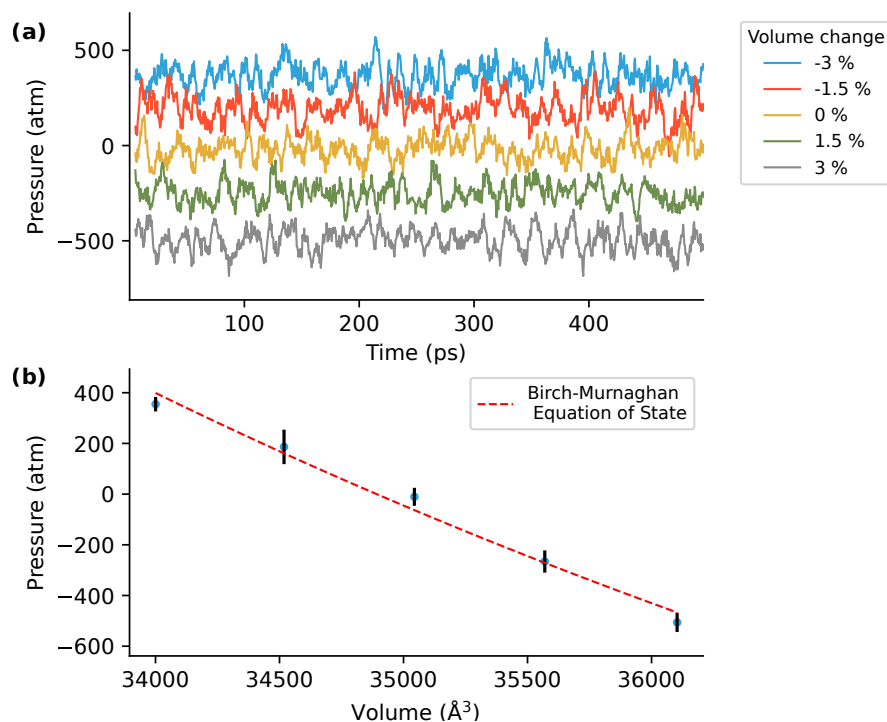


Figure 5.13: Finite strain difference method for the crystal with MOF-FF. (a) Pressure as a function of time for different deformations, shown with a moving average over 5 ps. (b) Pressure as a function of volume fitted with the second order Birch-Murnaghan EoS (red). Each volume corresponds to an (N, V, T) simulation with fixed deformation. Pressure is computed as the average over the last 100 ps of simulations. Error bars are the standard deviations of the pressure averaged with a rolling window of 10 ps.

The crystal [92, 123] and ten glasses [123] were prepared following a simplified preparation procedure compared to what was done for ReaxFF. It consisted in an initial energy minimization, followed by an (N, V, T) run at 300 K for 250 ps with the default temperature damping parameter of 1 ps. All the systems then went through a long (N, V, T) equilibration of 1 ns before any volume deformation. $(2 \times 2 \times 2)$ supercells of each system were considered, and reported properties (K and ρ_0) of the glasses are averaged over the ten models.

Successive simulations at different volumes were applied, consisting of a volume deformation by 1.5% and lasting 500 ps from the previous volume followed by an equilibration time of 500 ps. Volume deformation in the (N, V, T) ensemble was the same continuous process as for ReaxFF, the only difference being the longer time $\tau_{\Delta V} = 500$ ps. The well-behaved region of the $P - V$ data was chosen as for ReaxFF. 5 points were found for the crystal, 4.3 ± 0.9 for the Zn3trig glasses and 4.7 ± 0.5 for the Zn3tetra glasses

	Crystal	Glass w/ Zn3trig	Glass w/ Zn3tetra
K (GPa)	1.48	3.01 ± 1.15	2.46 ± 0.65
ρ_0 (g cm ⁻³)	1.22	1.29 ± 0.06	1.31 ± 0.05

Table 5.8: Bulk modulus K and density at zero pressure ρ_0 for ZIF-4 crystal and *ab initio* glasses obtained with the finite strain difference method with two different adaptations of MOF-FF.

From the results, summarized in table 5.8, we see that both FF adaptations lead to larger bulk moduli for the glasses than the crystal. As shown on figure 5.14, K values are in reasonable agreement with AIMD, where ReaxFF failed to differentiate the crystal from the glasses. The densities are also consistent with both AIMD and experiments.

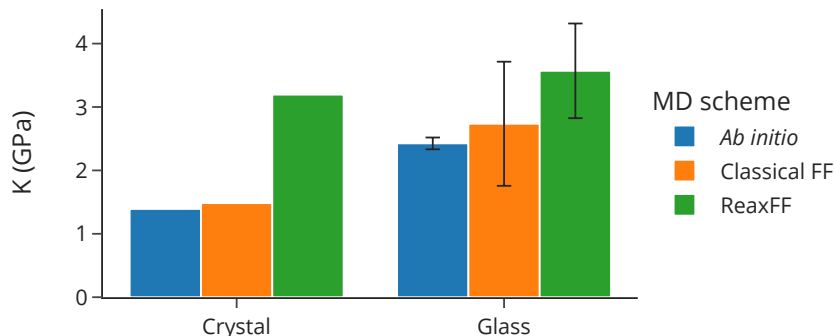


Figure 5.14: Bulk modulus K for ZIF-4 crystal and *ab initio* glasses with the finite strain difference method and different MD schemes. Average and standard deviation for classical FF are computed over every glass and FF adaptation.

We note, however, that there is an important variance in the bulk moduli of the glasses, with potentially divergent values with respect to the FF adaptation for the same glass model, as shown on figure 5.15. It highlights the importance of using a large enough number of glass configurations to obtain average mechanical properties for models with a small system size.

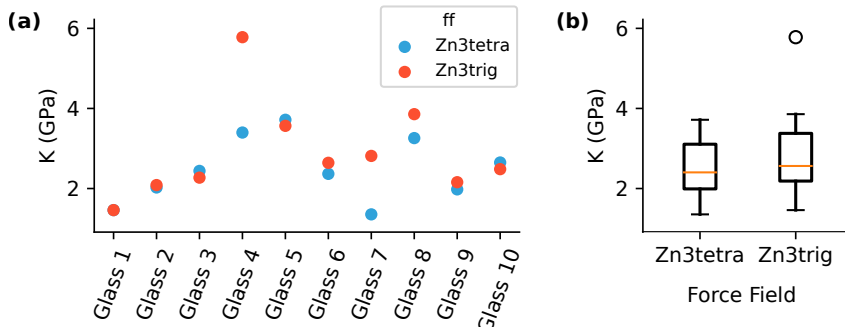


Figure 5.15: Bulk modulus K for ZIF-4 *ab initio* glasses obtained with the finite strain difference method with two different adaptations of MOF-FF.

5.4.3 Exploring other methods

FINITE STRESS DIFFERENCE METHOD

I then investigated the use of the (N, P, T) ensemble with our two FF adaptations, again with both an isotropic and a flexible cell as done for ReaxFF (see figure 5.16).

For the finite stress difference method with an isotropic cell (*iso*), the initial systems for the finite strain difference method were taken and were further equilibrated for 500 ps in the (N, P, T) ensemble. For the finite stress difference method with a flexible cell (*tri*), the initial systems for the finite strain difference method with an isotropic cell were taken and were further equilibrated in the (N, P, T)

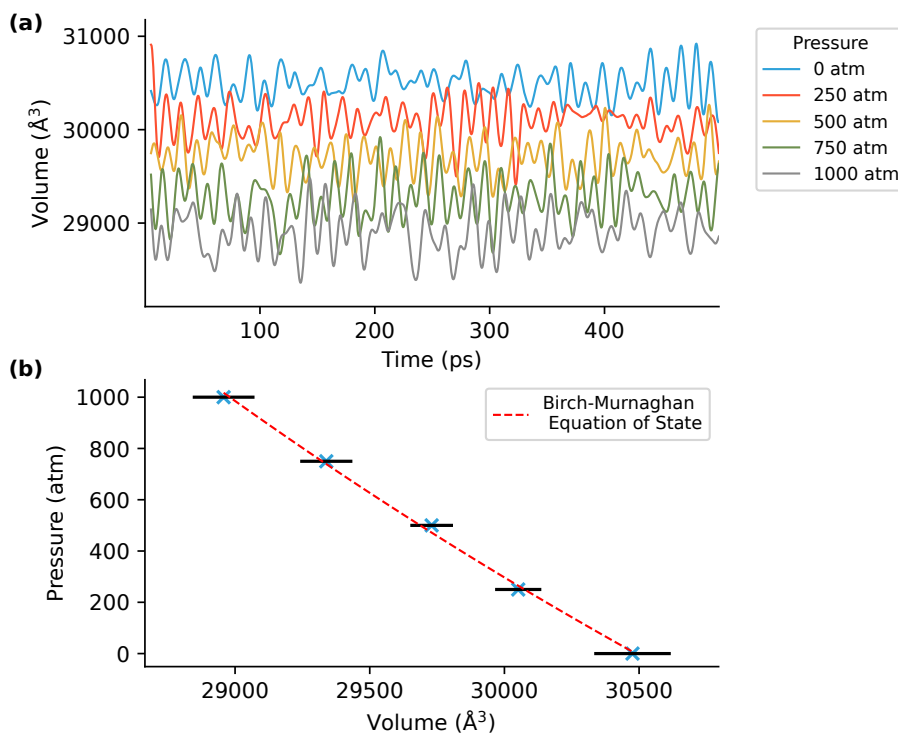


Figure 5.16: Finite stress difference method with a flexible cell (LAMMPS keyword `tri`) for the crystal with MOF-FF. (a) Volume as a function of time for pressures, shown with a moving average over 5 ps. (b) Pressure as a function of volume fitted with the second order Birch-Murnaghan EoS (red). Each volume corresponds to an (N, P, T) simulation with fixed pressure. Volume is computed as the average over the last 100 ps of simulations. Error bars are the standard deviations of the pressure averaged with a rolling window of 10 ps.

ensemble until convergence of the volume. The equilibration times are 6 ns for the crystal and 11 ns for the glasses.

Successive simulations at different pressures were applied, consisting in ramping up the pressure from 0 atm to 2500 atm by step of 250 atm and 500 ps. The well-behaved region of the $P - V$ data with an isotropic cell was composed of 3 points for the crystal, 4.0 ± 0.9 for the Zn3trig glasses and 3.9 ± 0.8 for the Zn3tetra glasses. With a flexible cell, those numbers are of 5 points for the crystal, 4.7 ± 0.6 for the Zn3trig glasses and 4.6 ± 0.7 for the Zn3tetra glasses.

We see on the results presented in table 5.9 that no system reaches a state of unreasonably high density (unlike with a reactive force field). In particular, MOF-FF handles better the additional degree of freedom brought by the free shape of the cell than does ReaxFF, although a flexible cell still leads to a larger densification, particularly for the crystal. We note that both FF adaptations give similar average results, with still a significant variance over the different glass models. Finally, K values are consistent with the

	cell	Crystal	Glass w/ Zn3trig	Glass w/ Zn3tetra
K (GPa)	iso	1.00	2.16 ± 0.89	2.24 ± 0.94
	tri	1.80	2.77 ± 0.98	2.59 ± 1.04
ρ_0 (g cm ⁻³)	iso	1.21	1.33 ± 0.08	1.31 ± 0.06
	tri	1.39	1.35 ± 0.08	1.35 ± 0.06

Table 5.9: Bulk modulus K and density at zero pressure ρ_0 for ZIF-4 crystal and *ab initio* glasses obtained with the finite stress difference method with two different adaptations of MOF-FF, either using an isotropic (iso) or a flexible (tri) cell.

finite strain difference method, and the previously observed trends of $K_{\text{glass}} > K_{\text{crystal}}$ and increasing K with respect to ρ_0 are found again.

STRAIN-FLUCTUATION METHOD

Finally, to obtain additional mechanical properties, I applied the strain-fluctuation method. The initial systems for the finite stress difference method with an isotropic cell were taken and were further equilibrated in the (N, P, T) ensemble with a flexible cell until convergence of the volume (see figure 5.17) the elastic constants. The equilibration times are 6 ns for the crystal and 21 ns for the glasses. The elastic constants, the volume fluctuations and the volumes were computed over the last 4 ns for every system.

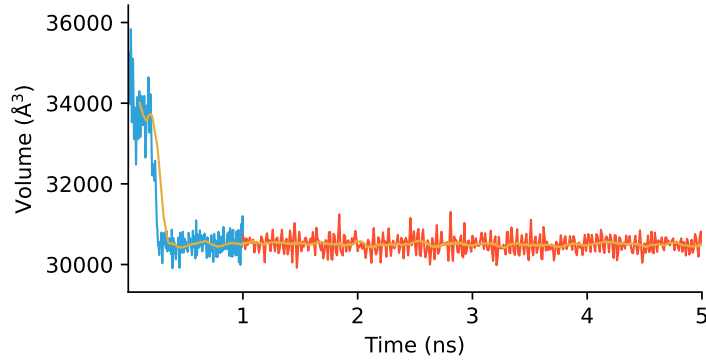


Figure 5.17: Volume as a function of time during a long 5 ns equilibration in the (N, P, T) ensemble with a flexible cell for the crystal with MOF-FF. Elastic constants were computed on the red part of the figure. The orange line shows a moving average over 100 ps.

From the results shown in table 5.10, we see that the values obtained from the elastic constants are consistent with the more robust volume fluctuations. While the values for the glass are consistent with the finite difference methods, the strain-fluctuation methods with MOF-FF fail to highlight the difference in K between the crystal and the glasses as shown on figure 5.18, which may be explained by the unreasonably large density of the crystal equilibrated in the (N, P, T) ensemble with a flexible cell. We note, however, that the value for the ZIF-4 crystal is similar to what was achieved in previous works [93, 257] with the strain-fluctuation method but another classical FF [305], and which reported K to be 2.6–2.7 GPa for a density of 1.31 g cm^{-3} (see table 5.1).

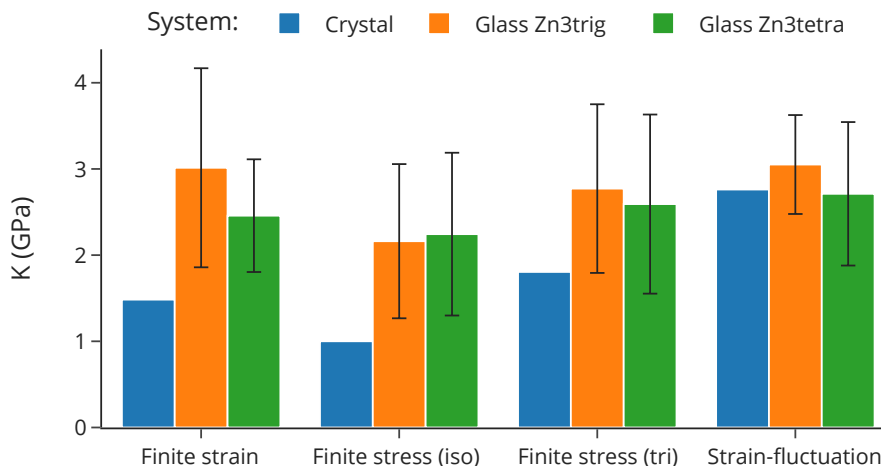


Figure 5.18: Bulk modulus K for ZIF-4 crystal and glasses with different methods and two different adaptations of MOF-FF.

	Crystal	Glass w/ Zn3trig	Glass w/ Zn3tetra
K - volume fluctuations (GPa)	2.67	2.66 ± 0.55	2.42 ± 0.82
K - elastic constants (GPa)	2.76	3.05 ± 0.57	2.71 ± 0.83
ρ_0 (g cm ⁻³)	1.39	1.35 ± 0.08	1.35 ± 0.06

Table 5.10: Bulk modulus K and density at zero pressure ρ_0 for ZIF-4 crystal and *ab initio* glasses obtained with two strain-fluctuation methods using two different adaptations of MOF-FF.

The important similarity between crystal and glasses is also present in the other mechanical properties computed with this method – Young’s modulus E , shear modulus G , and Poisson’s ratio ν – which are reported in table 5.11. For example, while nanoindentation studies found E to be significantly larger for the glass than for the crystal (respectively 8.2 GPa [86] and 4.6 GPa [84]), this effect is not convincingly captured by this approach (3.22 ± 0.74 GPa compared to 2.51 GPa). Carrying an (N, P, T) simulation of the ZIF-4 crystal with a flexible cell while preserving the low crystallographic density, previously known to be challenging with AIMD (see section 1.3.4) and ReaxFF (see section 3.3.1), would require further work on MOF-FF for ZIFs.

	Crystal	Glass Zn3trig	Glass Zn3tetra
Bulk modulus K (GPa)	2.76	3.05 ± 0.57	2.71 ± 0.83
Young’s modulus E (GPa)	2.51	3.48 ± 0.80	2.95 ± 0.57
Shear modulus G (GPa)	0.93	1.33 ± 0.32	1.13 ± 0.21
Poisson’s ratio ν	0.35	0.31 ± 0.02	0.31 ± 0.03

Table 5.11: Mechanical properties for the ZIF-4 crystal and *ab initio* glasses obtained with the strain-fluctuation method with the elastic stiffness tensor using two different adaptations of MOF-FF.

Despite this challenge, all finite difference methods are overall consistent, as illustrated on figure 5.18, albeit with a large variability across glass configurations. Both FF adaptations yield similar results, suggesting they are not ill adapted and that this procedure is not very sensitive to such a small perturbation in the MOF-FF parametrization. I thus showed that the finite difference methods with classical FFs are ready to be deployed, and that the development of a specific MOF-FF parametrization for amorphous ZIFs could prove useful.

5.5 MACHINE-LEARNED POTENTIALS

While adapted classical FFs seem promising to evaluate the mechanical properties of *a*ZIFs, they cannot be used for the systematic generation and subsequent study of the mechanical properties of multiple ZIF structures. Machine-learned potentials (MLP), whose principles are presented in section 2.4, represent potential candidates. Multiple studies showed that they can be used to study various mechanical properties, including three on MOFs. Two studies employed the stress-strain method to obtain elastic constants and bulk moduli [221, 260], while one computed K using the strain-fluctuation method [268].

In chapter 4, I reported the development of preliminary MLPs for ZIF-4 that led to an excellent reproduction of the *ab initio* structural properties of both ordered and disordered systems. In this section, I investigate their use to obtain finite temperature mechanical properties of ZIF-4 solids by using the same methods explored for other MD schemes. As chapter 4, this is an ongoing work whose goal is not to provide final answers but to probe whether this path is worth following. The results will have to be confirmed after the more universal MLPs for ZIFs under development will be ready for production.

5.5.1 Finite strain difference method with NequIP

The finite strain difference method, studied with every other MD scheme, is used as the platform for most of the evaluations of the developed MLPs. As mentioned in section 4.2.3, stress support in LAMMPS [211] was not yet implemented for NequIP at the time when I started this work. I therefore resorted to the use of the atomic simulation environment (ASE) [251], using a Nosé–Hoover thermostat shipped with NequIP.

Unlike LAMMPS or CP2K, this thermostat is not set up by a time constant but by a damping factor Q . Unlike in equation (2.4) presented in chapter 2, and according to the notes accompanying the NequIP code, this Q is of dimension $[ML^2]$, where M, L respectively designate mass and length. Using ASE default units (eV fs^2), I tested a range of values in the 10–10 000 eV fs^2 and chose $Q = 400 \text{ eV fs}^2$, as the 100–1000 eV fs^2 range provided consistent results. Unlike otherwise mentioned, I used single unit cells to speed up calculations in this development phase.

Successive simulations at different volumes were performed, consisting in an instantaneous and isotropic volume change by 1.5% from the previous volume, followed by an equilibration time of 200 ps. The value of the pressure for a given volume was taken as the average over the last 100 ps of the simulation. For simulations with a $(2 \times 2 \times 2)$ supercell, only 100 ps in total were simulated.

Figure 5.19 illustrates, in the case of the crystal with two different MLPs the pressure convergence and the $P - V$ data. We see that in these two cases the finite strain difference method worked accurately, in the sense that it provided well-behaved $P - V$ data and Birch-Murnaghan fits. It is worth noting that the pressure fluctuations were different depending on the model, with MLP(liquid) (trained without biasing for stress) having larger fluctuations than MLP(liquid| σ) (trained by biasing for stress). In both cases, these fluctuations were significantly reduced by the use of a $(2 \times 2 \times 2)$ supercell.

	supercell	K (GPa)	ρ_0 (g cm^{-3})
MLP(liquid 1:1:1)	1	1.31	1.24
	$(2 \times 2 \times 2)$	1.37	1.24
MLP(liquid 1:1:100)	1	0.84	0.80
	$(2 \times 2 \times 2)$	0.82	0.80

Table 5.12: Bulk modulus K and density at zero pressure ρ_0 for ZIF-4 crystal obtained with the finite strain difference method with multiple MLPs and different supercells.

Before further study of the different MLPs, it is worth mentioning that the use of a supercell did not seem to significantly impact the resulting bulk moduli K and density at zero pressure ρ_0 . Table 5.12 shows that for a ZIF-4 crystal, both tested MLPs led to almost identical results.

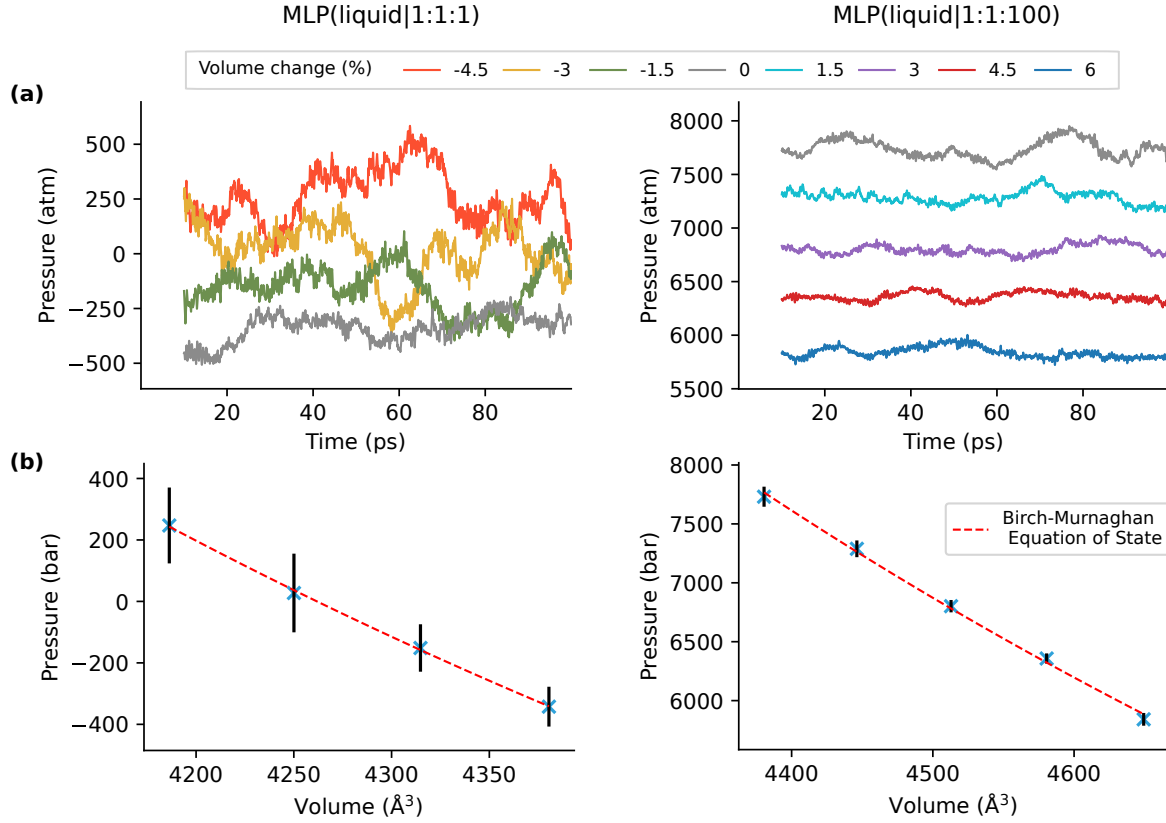


Figure 5.19: Finite strain difference method for the crystal with MLP(liquid) (left) and MLP(liquid| σ) (right). (a) Pressure as a function of time for different deformations during the last 100 ps of simulation, shown with a moving average over 10 ps. (b) Pressure as a function of volume fitted with the second order Birch-Murnaghan EoS (red). Each volume corresponds to an (N, V, T) simulation with fixed deformation. Pressure is computed as the average over the last 100 ps of simulations. Error bars are the standard deviations of the pressure averaged with a rolling window of 10 ps.

5.5.2 Accurately training for stress

In section 4.2.2, I introduced and contrasted several MLPs that differed in their training data (liquid or crystal), and choice of loss function \mathcal{L} . This \mathcal{L} was parameterized by three weights (λ) representing the respective influence of the energy (E), the forces ($\{F_{ij}\}$) and the stress (σ) during training, and is denoted by $\lambda_F : \lambda_E : \lambda_\sigma$.

Figure 5.20 clearly evidences that the pressure outputs were singularly different depending on whether the loss function is biased for stress, regardless of the training data. Strongly biased systems displayed pressure ranges located far from the state of zero pressure, resulting in the extremely low values for the fitted ρ_0 reported in table 5.13. Additionally, the associated values of K varied significantly as a function of the chosen value $\lambda_\sigma \in \{100, 1000\}$, providing further evidence to discard these MLPs. On the contrary, the unbiased MLPs – MLP(crystal) and MLP(liquid)– led to K and ρ_0 values in line with each other and with previous AIMD results. It suggests that training MLPs on energy and forces only is sufficient to reproduce the mechanical properties with reasonable accuracy.

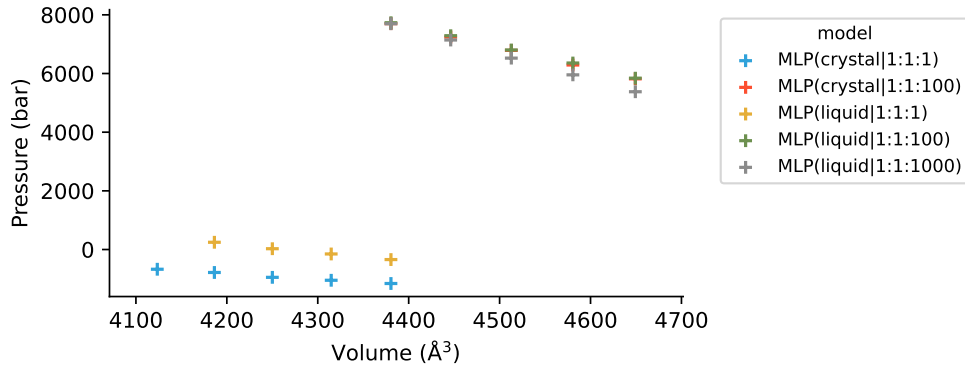


Figure 5.20: Pressure as a function of volume for the ZIF-4 crystal with different MLPs obtained by the finite strain difference method.

Training data	\mathcal{L}	K (GPa)	ρ_0 (g cm ⁻³)
crystal	1:1:1	1.21	1.37
crystal	1:1:100	0.85	0.81
liquid	1:1:1	1.31	1.24
liquid	1:1:100	0.84	0.80
liquid	1:1:1000	1.57	0.91

Table 5.13: Bulk modulus K and density at zero pressure ρ_0 for ZIF-4 crystal obtained with the finite strain difference method with multiple MLPs. MLP(sys| \mathcal{L}) are defined by their training data and their loss function \mathcal{L} denoted by $\lambda_F : \lambda_E : \lambda_\sigma$

5.5.3 Reproduction of *aZIF-4* mechanical properties

Unbiased MLPs were therefore employed for the computation of finite temperature mechanical properties. MLP(liquid) was chosen, provided that the difference between MLP(liquid) and MLP(crystal) was not that significant on the ZIF-4 crystal, and that MLP(liquid) led to better transferability (see section 4.2).

In order to offer a meaningful comparison to other MD schemes, I considered several glass models: the same three *ab initio* glass models studied with AIMD and ReaxFF, and the MLP glass obtained by melt-quenching in section 4.3. The original size of the systems was preserved, *i.e.* a single unit cell for both the crystal and the *ab initio* glasses, and a $(2 \times 2 \times 2)$ supercell for the MLP glass.

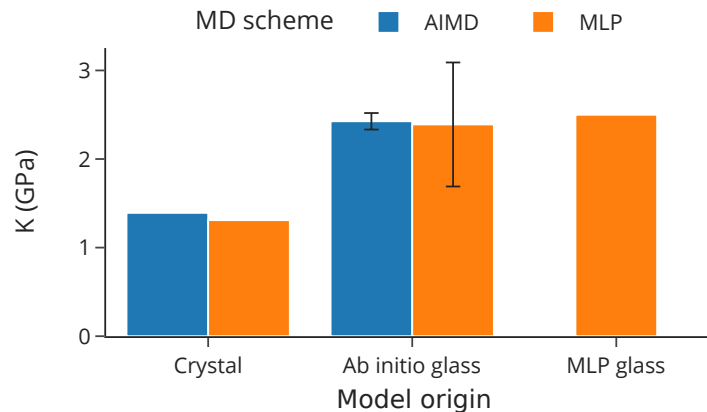


Figure 5.21: Bulk modulus K for the ZIF-4 crystal and two glasses with the finite strain difference method with MLP(liquid) compared with AIMD.

As evidenced in table 5.14, calculations with MLP(liquid) reproduced the trend previously identified with other MD schemes, where glasses have both larger K and ρ_0 than the crystalline phase. Reported values were in very good agreement with AIMD data, as shown on figure 5.21, making a strong case for

the use of MLPs to obtain the mechanical properties of *a*ZIF-4. We note, however, that the fluctuations are larger than for the *ab initio* glasses, which can be reduced in the future by computing the mechanical properties on all ten *ab initio* glasses as done in section 5.4 with classical FFs.

	Crystal	<i>ab initio</i> glass	MLP glass
K (GPa)	1.31	2.39+/-0.70	2.50
ρ_0 (g cm ⁻³)	1.24	1.37+/-0.10	1.31

Table 5.14: Bulk modulus K and density at zero pressure ρ_0 for the ZIF-4 crystal and two glasses obtained with the finite strain difference method with MLP(liquid).

While it is interesting to note that both the *ab initio* and MLP glasses display very similar values, only one glass model generated with MLP was chosen. Further investigation on the influence of the melt-quenching parameters (rate, length of high-temperature plateau) should be in order once the final MLP for multiple ZIFs is ready. Another methodological question worth investigating is that of the comparison between the use of multiple single cell models against a single model generated with a larger supercell.

5.5.4 Exploratory use of the (N, P, T) ensemble

I also investigated the use of the (N, P, T) ensemble with our prototypical MLP. As LAMMPS was not yet supported, I used ASE which only supported an isotropic cell, therefore only enabling the use of the finite stress difference method at the expense of the strain-fluctuations method.

I used a Nosé–Hoover–Parrinello–Rahman thermostat/barostat [251] with a temperature damping constant τ_T of 50 fs and pressure damping constant τ_P of 500 fs. The barostat constant required as input by ASE was calculated as $\tau_P^2 * B$, where B is a typical bulk modulus for the studied materials, set up at $B = 1$ GPa. I first set up τ_T by disabling the barostat and probing the 10–1000 fs range, before fixing τ_P by exploring the 10–10 000 fs range. Starting from the initial structural files, successive simulations at different pressures were applied, consisting in ramping up the pressure from 0 MPa to 250 MPa by step of 25 MPa and 100 ps, as illustrated on figure 5.22.

I first tested the finite stress difference methods by studying the ZIF-4 crystal with multiple MLPs: both biased and unbiased for stress, and trained either on the crystal or the liquid. As reported in figure 5.23, both K and ρ_0 were consistent across both finite difference methods. We note that systems biased for stress converge to states of unreasonably low density, confirming the low ρ_0 fitted with the finite strain difference method.

Using the previously chosen MLP(liquid), I applied the finite stress difference method on both the ZIF-4 crystal and the same three *ab initio* glasses. Table 5.15 highlights that although K and ρ_0 values for the crystal were consistent between methods, it did not hold true for the *ab initio* glasses. Therefore, the use of the (N, P, T) ensemble is not yet ready to use for production and should be further evaluated. A safer option may be to wait for the support of (N, P, T) simulations with NequIP in LAMMPS to benefit from its more robust and consistent methods.

	Method	Crystal	<i>ab initio</i> glass
K (GPa)	Stress	1.07	1.24±0.38
	Strain	1.31	2.39±0.70
ρ_0 (g cm ⁻³)	Stress	1.24	1.14±0.05
	Strain	1.24	1.37±0.10

Table 5.15: Bulk modulus K and density at zero pressure ρ_0 for the ZIF-4 crystal and *ab initio* glasses obtained with MLP(liquid) and with the finite stress difference method compared to the finite strain method.

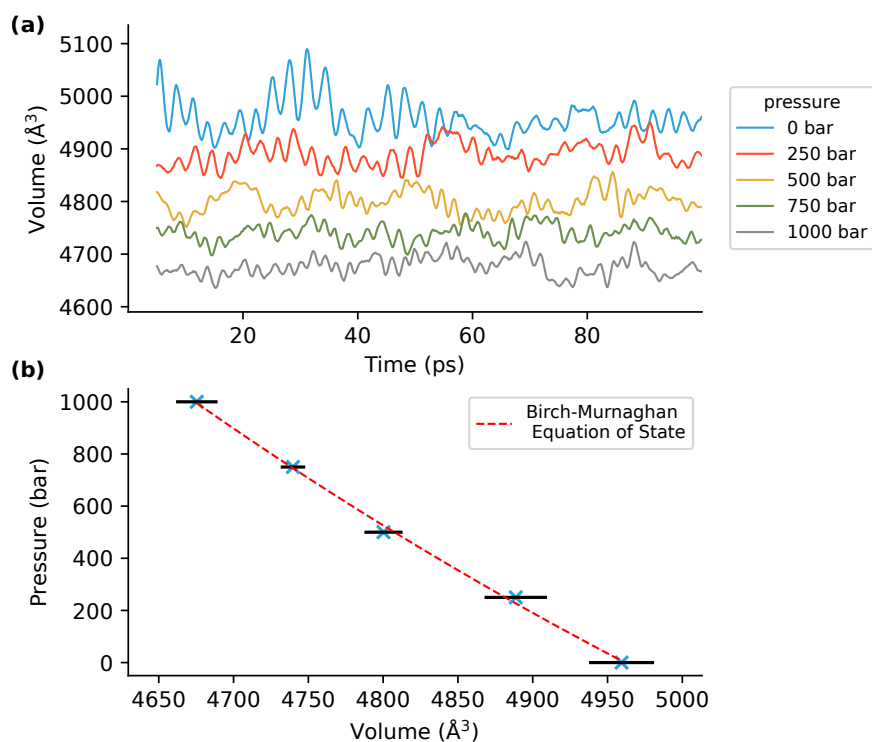


Figure 5.22: Finite stress difference method with an isotropic cell for the crystal with MLP(liquid). (a) Volume as a function of time for pressures, shown with a moving average over 5 ps. (b) Pressure as a function of volume fitted with the second order Birch-Murnaghan EoS (red). Each volume corresponds to an (N, P, T) simulation with fixed pressure. Volume is computed as the average over the last 100 ps of simulations. Error bars are the standard deviations of the pressure averaged with a rolling window of 10 ps.

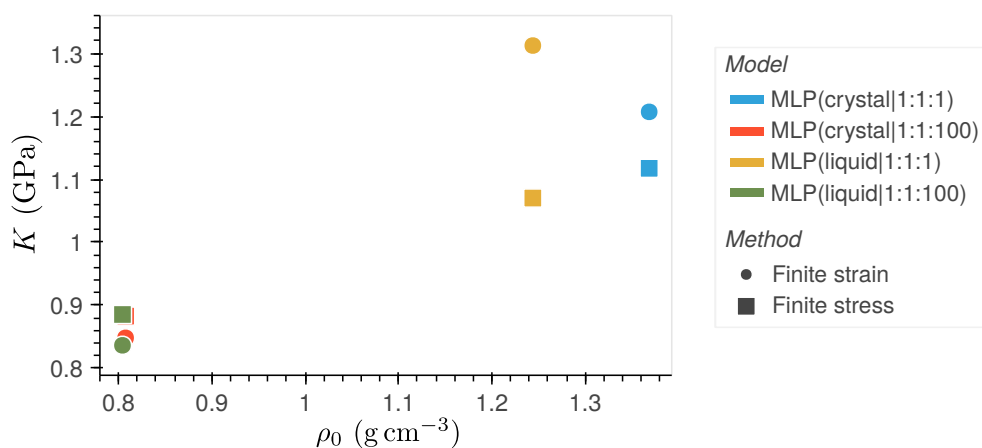


Figure 5.23: Bulk modulus K as function of the density at zero pressure ρ_0 for the ZIF-4 crystal with different MLPs for the finite strain and finite stress difference methods.

Overall, I provided strong evidence that MLPs for ZIFs may constitute a promising option to generate finite temperature mechanical properties of *azifs*. This will have to be confirmed when our final version of a MLP for ZIFs is ready for production.

CONCLUSIONS AND PERSPECTIVES

In this chapter, I have extensively investigated the computation of finite temperature mechanical properties of ZIF-4 in the crystal and glass phases. I have compared different molecular dynamics schemes and computational methods on a series of glass models. This is important because such mechanical properties are difficult to access experimentally, especially for the glasses.

Demonstrating for the first time the applicability and accuracy of the finite strain difference method with *ab initio* molecular dynamics to MOF systems, I provided the first reliable value for the bulk modulus of an amorphous ZIF in the literature. I found that ZIF-4 glasses have a larger bulk modulus than the crystal, and confirm previous results which found the density to be larger for the glass phase. Not only does this study provide intrinsically valuable data, it yields reference values for the computation of finite temperature mechanical properties, making it possible to validate alternative methods with less computationally expensive MD schemes.

I have investigated the use of ReaxFF, the only alternative MD scheme present in the literature that could be used to both generate melt-quenched glass models and study their mechanical properties. I have reported and analyzed a tendency of ReaxFF simulations to densify the systems, particularly if they are performed in the constant-pressure (N, P, T) ensemble, making it all but inapplicable to low-density models. Additionally, I have shown that the bulk moduli reported were primarily a function of the density and not of its phase or topology. All these observations suggest that mechanical properties obtained from the use of the ReaxFF force field for ZIFs should be interpreted with caution, and makes a strong case for the use of alternative methodologies, or for the further optimization of the ReaxFF force field.

Looking for another tractable alternative, I examined the use of classical force fields for the computation of mechanical properties of models created through other methodologies, demonstrating that all finite difference methods were consistent, and that the values were in good agreement with AIMD. I have thus shown that this method is ready to be deployed, and that the development of a specific MOF-FF parametrization for amorphous ZIFs could prove useful.

Finally, I investigated the use of machine-learned potentials as a novel alternative. Using the finite strain difference method, I showed that the MLPs developed in chapter 4 led to a satisfactory reproduction of the AIMD mechanical properties, provided that learning was not overly biased for stress. However, methods relying on the (N, P, T) ensemble are not yet ready for production. I nonetheless provided strong evidence that MLPs constitute a promising option to be used on multiple *a*ZIF models. Further work is ongoing and the results will have to be confirmed with the final MLPs when released.

GENERAL CONCLUSIONS

The work presented in this thesis contributed to a broader research effort to characterize and discover new materials for applications in various industrial-scale processes, with a focus on CO₂ separation. I investigated the relatively uncharted territory of amorphous MOFs, and compared and developed computational methods to obtain atomistic models and study their properties. In addition to exploring the material space of MOFs, progress in the study of non-crystalline states is beneficial to the understanding of a number of phenomena in the MOF field, as the role of disorder is increasingly investigated and linked to novel features at the macroscopic level.

I reviewed and compared the existing methodologies available in the literature for *a*MOFs, based on both experimental data and numerical simulations, and chose during my PhD to focus on molecular dynamics to simulate the phase transition from a crystalline MOF to an amorphous state by mimicking *in silico* one of the most common experimental formation routes. Using ZIF-4 as a test case, I employed several simulation methods with different scopes, scales and computational costs – *ab initio* molecular dynamics, classical and reactive force fields, and machine-learned potentials – to generate atomistic models of *a*MOFs and study their properties.

I have first extensively studied the use of the ReaxFF reactive force field to generate atomistic models of ZIF glasses, which have been proposed as a tractable alternative to the successful but computationally expensive *ab initio* simulations. I have demonstrated that the molecular simulations performed so far in the literature with ReaxFF were extremely sensitive to the choice of simulation methodology and parameters, and showed that the glass models it generated were markedly different from their *ab initio* counterparts. All these observations demonstrate that structural properties obtained from the use of the ReaxFF force field for ZIFs should be interpreted with caution, and makes a strong case for the use of alternative methodologies, or for the further optimization of this force field by drawing inspiration from this work.

Having shown that no tractable MD scheme used to this date in the literature could yield an accurate microscopic representation of the ZIF melt-quenched glasses, the development of new reactive interatomic potentials appeared as an attractive alternative. Therefore I proposed in this thesis the first machine-learned potentials to generate *a*MOF models. Using a limited training dataset consisting of *ab initio* trajectories of ZIF-4, I obtained MLPs that led to an exceptional reproduction of the structural properties of multiple phases and were used to generate new *a*ZIF-4 models by melt-quenching. As a step towards the development of a more universal MLP for ZIFs, I generated multiple *ab initio* high-temperature trajectories of various ZIFs under different deformations. This was performed as part of a collaboration with Jack D. Evans (University of Adelaide) and is a direction that will continue in the group in the future.

Finally, as a demonstration of the interest of this methodology of molecular simulations, I have computed finite temperature mechanical properties which, while essential for MOFs to fully achieve their potential in industrial-scale processes, are difficult to determine experimentally. Demonstrating for the first time the applicability and accuracy of the finite strain difference method with AIMD to MOF systems, I

provided the first reliable value for the bulk modulus of an *a*ZIF in the literature. This reference value was then used to compare and validate alternative methods with less computationally expensive MD schemes. I first investigated the use of ReaxFF, and showed that the bulk moduli reported are primarily a function of the density of the models and not of their phase or topology, calling for alternative methodologies. I then examined the use of classical force fields adapted to *a*ZIFs and machine-learned potentials (MLP) developed in this work, which both provided values in good agreement with AIMD, and could therefore be applied on other ZIF systems.

Overall, this thesis evidenced the too often lack of direct and in-depth comparison of the models in the existing literature despite their significant differences, and exemplified how such a comparison could be performed.



The work performed during this PhD opens multiple perspectives for the development and use of *a*MOF models, by building on the expertise built with multiple MD schemes on the prototypical ZIF-4 system. First, the ongoing development of a more universal MLP for ZIFs should enable the generation of multiple ZIF glasses, and their structural characterization. It could in turn lead to a systematic screening of the finite temperature mechanical properties of these glasses. If MLPs fail to materialize their promises regarding the computation of mechanical properties, they could alternatively be obtained with the parametrization of a classical force field for *a*ZIFs.

More generally, and in order to improve the quality of amorphous models in the future, I see the need for wider studies, integrating many different experimental techniques (e.g. infrared and Raman, NMR, etc), in order to provide *in situ* data. In addition to providing direct insight into the nature of the amorphous phases of MOFs, such data could be used as a benchmark to test the different types of microscopic models generated. Databases of amorphous porous materials could then be expanded, along the lines of what has been done for years for the crystalline phases, and help accelerate efforts to model these systems.

Finally, as it appears that no single modeling method can currently yield an accurate microscopic representation of the MOF glasses, the development of multi-scale modeling strategies could prove fruitful. It would enable to combine the strength of different methods already available, such as those devoted to the generation of amorphous structures (*i.e.* polymerization algorithms), and MD schemes to analyze them such as classical force fields or MLPs.



LIST OF PUBLICATIONS

PUBLISHED

1. Nicolas Castel and François-Xavier Coudert. “Atomistic Models of Amorphous Metal–Organic Frameworks”. In: *The Journal of Physical Chemistry C* 126.16 (Apr. 2022), pp. 6905–6914. DOI: [10.1021/acs.jpcc.2c01091](https://doi.org/10.1021/acs.jpcc.2c01091).
2. Nicolas Castel and François-Xavier Coudert. “Challenges in Molecular Dynamics of Amorphous ZIFs Using Reactive Force Fields”. In: *J. Phys. Chem. C* 126 (45 2022), pp. 19532–19541. DOI: [10.1021/acs.jpcc.2c06305](https://doi.org/10.1021/acs.jpcc.2c06305).

IN PRESS

3. Nicolas Castel and François-Xavier Coudert. “Computation of Finite Temperature Mechanical Properties of Zeolitic Imidazolate Framework Glasses by Molecular Dynamics”. In: *Chemistry of Materials* (2023). DOI: [10.1021/acs.chemmater.3c00392](https://doi.org/10.1021/acs.chemmater.3c00392).

BIBLIOGRAPHY

- [1] IPCC. “Summary for Policymakers”. In: *Climate Change 2021: The Physical Science Basis. Contribution of Working Group I to the Sixth Assessment Report of the Intergovernmental Panel on Climate Change*. Ed. by V. Masson-Delmotte, P. Zhai, A. Pirani, S. L. Connors, C. Péan, S. Berger, N. Caud, Y. Chen, L. Goldfarb, M. I. Gomis, M. Huang, K. Leitzell, E. Lonnoy, J. B. R. Matthews, T. K. Maycock, T. Waterfield, O. Yelekçi, R. Yu, and B. Zhou. Cambridge, United Kingdom and New York, NY, USA: Cambridge University Press, 2021.
- [2] Q. Perrier, C. Guivarch, and O. Boucher. “Zéro émissions nettes: Signification et implications”. In: *Note scientifique* 34 (2018).
- [3] K. Riahi, R. Schaeffer, J. Arango, K. Calvin, C. Guivarch, T. Hasegawa, K. Jiang, E. Kriegler, R. Matthews, G. Peters, A. Rao, S. Robertson, A. Sebbit, J. Steinberger, M. Tavoni, and D. Van Vuuren. “Mitigation pathways compatible with long-term goals.” In: *IPCC, 2022: Climate Change 2022: Mitigation of Climate Change. Contribution of Working Group III to the Sixth Assessment Report of the Intergovernmental Panel on Climate Change*. Ed. by P. Shukla, J. Skea, R. Slade, A. A. Khourdajie, R. van Diemen, D. McCollum, M. Pathak, S. Some, P. Vyas, R. Fradera, M. Belkacemi, A. Hasija, G. Lisboa, S. Luz, and J. Malley. Cambridge, UK and New York, NY, USA: Cambridge University Press, 2022. Chap. 3. DOI: [10.1017/9781009157926.005](https://doi.org/10.1017/9781009157926.005).
- [4] IPCC. “Summary for Policymakers”. In: *Climate Change 2022: Mitigation of Climate Change. Contribution of Working Group III to the Sixth Assessment Report of the Intergovernmental Panel on Climate Change*. Ed. by P. Shukla, J. Skea, R. Slade, A. A. Khourdajie, R. van Diemen, D. McCollum, M. Pathak, S. Some, P. Vyas, R. Fradera, M. Belkacemi, A. Hasija, G. Lisboa, S. Luz, and J. Malley. Cambridge, UK and New York, NY, USA: Cambridge University Press, 2022. DOI: [10.1017/9781009157926.001](https://doi.org/10.1017/9781009157926.001).
- [5] J. C. Minx, W. F. Lamb, M. W. Callaghan, S. Fuss, J. Hilaire, F. Creutzig, T. Amann, T. Beringer, W. de Oliveira Garcia, J. Hartmann, T. Khanna, D. Lenzi, G. Luderer, G. F. Nemet, J. Rogelj, P. Smith, J. L. Vicente Vicente, J. Wilcox, and M. del Mar Zamora Dominguez. “Negative emissions—Part 1: Research landscape and synthesis”. In: *Environ. Res. Lett.* 13 (6 2018), p. 063001. DOI: [10.1088/1748-9326/aabf9b](https://doi.org/10.1088/1748-9326/aabf9b).
- [6] M. Bui, C. S. Adjiman, A. Bardow, E. J. Anthony, A. Boston, S. Brown, P. S. Fennell, S. Fuss, A. Galindo, L. A. Hackett, J. P. Hallett, H. J. Herzog, G. Jackson, J. Kemper, S. Krevor, G. C. Maitland, M. Matuszewski, I. S. Metcalfe, C. Petit, G. Puxty, J. Reimer, D. M. Reiner, E. S. Rubin, S. A. Scott, N. Shah, B. Smit, J. P. M. Trusler, P. Webley, J. Wilcox, and N. Mac Dowell. “Carbon capture and storage (CCS): the way forward”. In: *Energy Environ. Sci.* 11 (5 2018), pp. 1062–1176. DOI: [10.1039/C7EE02342A](https://doi.org/10.1039/C7EE02342A).
- [7] R. B. Jackson, E. I. Solomon, J. G. Canadell, M. Cargnello, and C. B. Field. “Methane removal and atmospheric restoration”. In: *Nat Sustain* 2 (6 2019), pp. 436–438. DOI: [10.1038/s41893-019-0299-x](https://doi.org/10.1038/s41893-019-0299-x).
- [8] T. Ming, R. de_Richter, S. Shen, and S. Caillol. “Fighting global warming by greenhouse gas removal: destroying atmospheric nitrous oxide thanks to synergies between two breakthrough

- technologies”. In: *Environ Sci Pollut Res* 23 (7 2016), pp. 6119–6138. DOI: [10.1007/s11356-016-6103-9](https://doi.org/10.1007/s11356-016-6103-9).
- [9] Ministère de la Transition écologique et solidaire. *Stratégie Nationale Bas-Carbone*. 2020.
- [10] European Commission. *A Clean Planet for all. A European strategic long-term vision for a prosperous, modern, competitive and climate neutral economy*. 2018.
- [11] International Energy Agency. *Energy Technology Perspectives 2020 - Special Report on Carbon Capture Utilisation and Storage*. 2020. 174 pp. DOI: [10.1787/208b66f4-en](https://doi.org/10.1787/208b66f4-en).
- [12] J. Wilcox. *Carbon capture*. Springer New York, NY, 2012.
- [13] S. Budinis, S. Krevor, N. M. Dowell, N. Brandon, and A. Hawkes. “An assessment of CCS costs, barriers and potential”. In: *Energy Strategy Reviews* 22 (2018), pp. 61–81. DOI: [10.1016/j.esr.2018.08.003](https://doi.org/10.1016/j.esr.2018.08.003).
- [14] S. Chiquier, P. Patrizio, M. Bui, N. Sunny, and N. Mac Dowell. “The Efficiency, Timing and Permanence of CDR Pathways: A Comparative Analysis”. In: *Proceedings of the 16th Greenhouse Gas Control Technologies Conference*. 2022. DOI: [10.2139/ssrn.4298436](https://doi.org/10.2139/ssrn.4298436).
- [15] M. Erans, E. S. Sanz-Pérez, D. P. Hanak, Z. Clulow, D. M. Reiner, and G. A. Mutch. “Direct air capture: process technology, techno-economic and socio-political challenges”. In: *Energy Environ. Sci.* 15 (4 2022), pp. 1360–1405. DOI: [10.1039/D1EE03523A](https://doi.org/10.1039/D1EE03523A).
- [16] R. L. Siegelman, E. J. Kim, and J. R. Long. “Porous materials for carbon dioxide separations”. In: *Nat. Mater.* 20 (8 2021), pp. 1060–1072. DOI: [10.1038/s41563-021-01054-8](https://doi.org/10.1038/s41563-021-01054-8).
- [17] B. Smit, J. A. Reimer, C. M. Oldenburg, and I. C. Bourg. *Introduction to Carbon Capture and Sequestration*. Imperial College Press, 2014. DOI: [10.1142/p911](https://doi.org/10.1142/p911).
- [18] C. Azar, K. Lindgren, M. Obersteiner, K. Riahi, D. P. van Vuuren, K. M. G. J. den Elzen, K. Möllersten, and E. D. Larson. “The feasibility of low CO₂ concentration targets and the role of bio-energy with carbon capture and storage (BECCS)”. In: *Climatic Change* 100 (1 2010), pp. 195–202. DOI: [10.1007/s10584-010-9832-7](https://doi.org/10.1007/s10584-010-9832-7).
- [19] International Energy Agency. *World Energy Outlook 2022*. 2022. 524 pp. DOI: [10.1787/3a469970-en](https://doi.org/10.1787/3a469970-en).
- [20] C. Chung, J. Kim, B. K. Sovacool, S. Griffiths, M. Bazilian, and M. Yang. “Decarbonizing the chemical industry: A systematic review of sociotechnical systems, technological innovations, and policy options”. In: *Energy Research & Social Science* 96 (2023), p. 102955. DOI: [10.1016/j.erss.2023.102955](https://doi.org/10.1016/j.erss.2023.102955).
- [21] International Energy Agency. *Transforming Industry through CCUS*. 2019. 62 pp. DOI: [10.1787/09689323-en](https://doi.org/10.1787/09689323-en).
- [22] ADEME. *Le Captage et Stockage géologique du CO₂ (CSC) en France*. 2020.
- [23] International Energy Agency. *Global Hydrogen Review 2022*. 2022. 284 pp. DOI: [10.1787/a15b8442-en](https://doi.org/10.1787/a15b8442-en).
- [24] International Energy Agency. *Putting CO₂ to Use*. 2019. 86 pp. DOI: [10.1787/dfeabbf4-en](https://doi.org/10.1787/dfeabbf4-en).
- [25] B. Metz, O. Davidson, H. d. Coninck, M. Loos, and L. Meyer. “IPCC special report on carbon dioxide capture and storage”. In: (July 2005).
- [26] O. Bouc, H. Fabriol, E. Brosse, F. Kalaydjian, R. Farret, P. Gombert, P. Berest, V. Lagneau, J.-M. Pereira, and T. Fen-Chong. *Lignes de conduite pour la sécurité d’un site de stockage géologique de CO₂*. Tech. rep. 2011.
- [27] Global CCS Institute. *Global Status of CCS 2022*. 2022. 69 pp.
- [28] S. Smith, O. Geden, G. Nemet, M. Gidden, W. Lamb, C. Powis, R. Bellamy, M. Callaghan, A. Cowie, E. Cox, et al. *The State of Carbon Dioxide Removal*. 2023.
- [29] I. Czernichowski-Lauriol, V. Czop, F. Delprat-Jannaud, A. El Khamlichi, L. Jammes, S. Lafortune, D. Nevicato, and D. Savary. “The Gradual Integration of CCUS into National and Regional Strategies for Climate Change Mitigation, Energy Transition, Ecological Transition, Research and Innovation: An Overview for France”. In: *Proceedings of the 15th Greenhouse Gas Control Technologies Conference*. 2021, pp. 15–18.

- [30] International Energy Agency. *Exploring clean energy pathways*. 2019. 105 pp. DOI: [10.1787/c76b829e-en](https://doi.org/10.1787/c76b829e-en).
- [31] E. Dütschke, S. Alsheimer, R. Bohn Bertoldo, A. Delicado, V. Duscha, S. Germán, L. Gonçalves, L. Kappler, S. López-Asensio, C. Mays, C. Oltra, M. Poumadere, A. Prades, S. Preuß, J. Rowland, L. Schmidt, and F. M. L. Veloso. “Engaging the Public with CCUS: Reflection on a European Project Approach”. In: *Proceedings of the 16th Greenhouse Gas Control Technologies Conference*. 2022. DOI: [10.2139/ssrn.4284094](https://doi.org/10.2139/ssrn.4284094).
- [32] K. Sumida, D. L. Rogow, J. A. Mason, T. M. McDonald, E. D. Bloch, Z. R. Herm, T.-H. Bae, and J. R. Long. “Carbon Dioxide Capture in Metal–Organic Frameworks”. In: *Chem. Rev.* 112 (2 2012), pp. 724–781. DOI: [10.1021/cr2003272](https://doi.org/10.1021/cr2003272).
- [33] S. Vasudevan, S. Farooq, I. A. Karimi, M. Saeys, M. C. Quah, and R. Agrawal. “Energy penalty estimates for CO₂ capture: Comparison between fuel types and capture-combustion modes”. In: *Energy* 103 (2016), pp. 709–714. DOI: [10.1016/j.energy.2016.02.154](https://doi.org/10.1016/j.energy.2016.02.154).
- [34] S. Kitagawa. “Future Porous Materials”. In: *Acc. Chem. Res.* 50 (3 2017), pp. 514–516. DOI: [10.1021/acs.accounts.6b00500](https://doi.org/10.1021/acs.accounts.6b00500).
- [35] J. Rouquerol, D. Avnir, C. W. Fairbridge, D. H. Everett, J. M. Haynes, N. Pernicone, J. D. F. Ramsay, K. S. W. Sing, and K. K. Unger. “Recommendations for the characterization of porous solids (Technical Report)”. In: 66 (8 1994), pp. 1739–1758. DOI: [10.1351/pac199466081739](https://doi.org/10.1351/pac199466081739).
- [36] Z. Hu, Y. Wang, B. B. Shah, and D. Zhao. “CO₂ Capture in Metal–Organic Framework Adsorbents: An Engineering Perspective”. In: *Adv. Sustainable Syst.* 3 (1 2019), p. 1800080. DOI: [10.1002/adsu.201800080](https://doi.org/10.1002/adsu.201800080).
- [37] S. A. Rackley. *Carbon capture and storage*. Butterworth-Heinemann, 2017. DOI: [10.1016/C2015-0-01587-8](https://doi.org/10.1016/C2015-0-01587-8).
- [38] J. Zhang, P. A. Webley, and P. Xiao. “Effect of process parameters on power requirements of vacuum swing adsorption technology for CO₂ capture from flue gas”. In: *Energy Conversion and Management* 49 (2 2008), pp. 346–356. DOI: [10.1016/j.enconman.2007.06.007](https://doi.org/10.1016/j.enconman.2007.06.007).
- [39] National Academies of Sciences, Engineering, and Medicine. *Negative Emissions Technologies and Reliable Sequestration: A Research Agenda*. Washington, DC: The National Academies Press, 2019. ISBN: 978-0-309-48452-7. DOI: [10.17226/25259](https://doi.org/10.17226/25259).
- [40] L. Espinal, D. L. Poster, W. Wong-Ng, A. J. Allen, and M. L. Green. “Measurement, Standards, and Data Needs for CO₂ Capture Materials: A Critical Review”. In: *Environ. Sci. Technol.* 47 (21 2013), pp. 11960–11975. DOI: [10.1021/es402622q](https://doi.org/10.1021/es402622q).
- [41] Q. Qian, P. A. Asinger, M. J. Lee, G. Han, K. Mizrahi Rodriguez, S. Lin, F. M. Benedetti, A. X. Wu, W. S. Chi, and Z. P. Smith. “MOF-Based Membranes for Gas Separations”. In: *Chem. Rev.* 120 (16 2020), pp. 8161–8266. DOI: [10.1021/acs.chemrev.0c00119](https://doi.org/10.1021/acs.chemrev.0c00119).
- [42] W. Guan, Y. Dai, C. Dong, X. Yang, and Y. Xi. “Zeolite imidazolate framework (ZIF)-based mixed matrix membranes for CO₂ separation: A review”. In: *J Appl Polym Sci* 137 (33 2020), p. 48968. DOI: [10.1002/app.48968](https://doi.org/10.1002/app.48968).
- [43] U. W. Siagian, A. Raksajati, N. F. Himma, K. Khoiruddin, and I. Wenten. “Membrane-based carbon capture technologies: Membrane gas separation vs. membrane contactor”. In: *Journal of Natural Gas Science and Engineering* 67 (2019), pp. 172–195. DOI: [10.1016/j.jngse.2019.04.008](https://doi.org/10.1016/j.jngse.2019.04.008).
- [44] B. F. Hoskins and R. Robson. “Infinite polymeric frameworks consisting of three dimensionally linked rod-like segments”. In: *J. Am. Chem. Soc.* 111 (15 1989), pp. 5962–5964. DOI: [10.1021/ja00197a079](https://doi.org/10.1021/ja00197a079).
- [45] H. Li, M. Eddaoudi, M. O’Keeffe, and O. M. Yaghi. “Design and synthesis of an exceptionally stable and highly porous metal-organic framework”. In: *Nature* 402 (6759 1999), pp. 276–279. DOI: [10.1038/46248](https://doi.org/10.1038/46248).

- [46] C. R. Groom, I. J. Bruno, M. P. Lightfoot, and S. C. Ward. “The Cambridge Structural Database”. In: *Acta Crystallogr B Struct Sci Cryst Eng Mater* 72 (2 2016), pp. 171–179. DOI: [10.1107/S2052520616003954](https://doi.org/10.1107/S2052520616003954).
- [47] H. Furukawa, K. E. Cordova, M. O’Keeffe, and O. M. Yaghi. “The Chemistry and Applications of Metal-Organic Frameworks”. In: *Science* 341.6149 (Aug. 2013). DOI: [10.1126/science.1230444](https://doi.org/10.1126/science.1230444).
- [48] O. M. Yaghi, M. J. Kalmutzki, and C. S. Diercks. “Linkages in Covalent Organic Frameworks”. In: *Introduction to Reticular Chemistry*. John Wiley & Sons, Ltd, 2019. Chap. 8, pp. 197–223. ISBN: 9783527821099. DOI: [10.1002/9783527821099.ch8](https://doi.org/10.1002/9783527821099.ch8).
- [49] T. Tian, Z. Zeng, D. Vulpe, M. E. Casco, G. Divitini, P. A. Midgley, J. Silvestre-Albero, J.-C. Tan, P. Z. Moghadam, and D. Fairen-Jimenez. “A sol-gel monolithic metal-organic framework with enhanced methane uptake”. In: *Nat. Mater.* 17 (2 2018), pp. 174–179. DOI: [10.1038/nmat5050](https://doi.org/10.1038/nmat5050).
- [50] M. Witman, S. Ling, A. Gladysiak, K. C. Stylianou, B. Smit, B. Slater, and M. Haranczyk. “Rational Design of a Low-Cost, High-Performance Metal-Organic Framework for Hydrogen Storage and Carbon Capture”. In: *J. Phys. Chem. C* 121 (2 2017), pp. 1171–1181. DOI: [10.1021/acs.jpcc.6b10363](https://doi.org/10.1021/acs.jpcc.6b10363).
- [51] J. Liu. “Potential Industrial Applications of Metal-Organic Frameworks for Gas Separations”. In: *Gas Adsorption in Metal-Organic Frameworks*. CRC Press, 2018, pp. 481–510.
- [52] E. Ren and F.-X. Coudert. “Thermodynamic exploration of xenon/krypton separation based on a high-throughput screening”. In: *Faraday Discuss.* 231 (2021), pp. 201–223. DOI: [10.1039/D1FD00024A](https://doi.org/10.1039/D1FD00024A).
- [53] L. Yang and M. A. Carreon. “Green deoxygenation of fatty acids to transport fuels over metal-organic frameworks as catalysts and catalytic supports”. In: *Metal-Organic Frameworks (MOFs) for Environmental Applications*. Ed. by S. K. Ghosh. Elsevier, 2019, pp. 285–318. ISBN: 978-0-12-814633-0. DOI: [10.1016/B978-0-12-814633-0.00004-1](https://doi.org/10.1016/B978-0-12-814633-0.00004-1).
- [54] D. P. Broom and J. W. Burress. “Gas Storage in Metal-Organic Frameworks”. In: *Gas Adsorption in Metal-Organic Frameworks*. CRC Press, 2018, pp. 393–450.
- [55] R. Shah, S. Ali, F. Raziq, S. Ali, P. M. Ismail, S. Shah, R. Iqbal, X. Wu, W. He, X. Zu, A. Zada, Adnan, F. Mabood, A. Vinu, S. H. Jung, J. Yi, and L. Qiao. “Exploration of metal organic frameworks and covalent organic frameworks for energy-related applications”. In: *Coordination Chemistry Reviews* 477 (2023), p. 214968. DOI: [10.1016/j.ccr.2022.214968](https://doi.org/10.1016/j.ccr.2022.214968).
- [56] K. Dedecker, E. Dumas, B. Lavédrine, N. Steunou, and C. Serre. “Metal-organic frameworks for the capture of volatile organic compounds and toxic chemicals”. In: *Metal-Organic Frameworks (MOFs) for Environmental Applications*. Ed. by S. K. Ghosh. Elsevier, 2019, pp. 141–178. ISBN: 978-0-12-814633-0. DOI: [10.1016/B978-0-12-814633-0.00007-7](https://doi.org/10.1016/B978-0-12-814633-0.00007-7).
- [57] P. Zhang, Q. Wang, Y. Fang, W. Chen, A. A. Kirchon, M. Baci, M. Feng, V. K. Sharma, and H.-C. Zhou. “Metal-organic frameworks for capture and degradation of organic pollutants”. In: *Metal-Organic Frameworks (MOFs) for Environmental Applications*. Ed. by S. K. Ghosh. Elsevier, 2019, pp. 203–229. ISBN: 978-0-12-814633-0. DOI: [10.1016/B978-0-12-814633-0.00009-0](https://doi.org/10.1016/B978-0-12-814633-0.00009-0).
- [58] C. Xiao and S. Wang. “Radionuclide sequestration by metal-organic frameworks”. In: *Metal-Organic Frameworks (MOFs) for Environmental Applications*. Ed. by S. K. Ghosh. Elsevier, 2019, pp. 355–382. ISBN: 978-0-12-814633-0. DOI: [10.1016/B978-0-12-814633-0.00011-9](https://doi.org/10.1016/B978-0-12-814633-0.00011-9).
- [59] Q. He, F. Zhan, H. Wang, W. Xu, H. Wang, and L. Chen. “Recent progress of industrial preparation of metal-organic frameworks: synthesis strategies and outlook”. In: *Materials Today Sustainability* 17 (2022), p. 100104. DOI: [10.1016/j.mtsust.2021.100104](https://doi.org/10.1016/j.mtsust.2021.100104).
- [60] O. M. Yaghi, M. J. Kalmutzki, and C. S. Diercks. “CO₂ Capture and Sequestration”. In: *Introduction to Reticular Chemistry*. John Wiley & Sons, Ltd, 2019. Chap. 14, pp. 313–338. ISBN: 9783527821099. DOI: [10.1002/9783527821099.ch14](https://doi.org/10.1002/9783527821099.ch14).
- [61] S. Mukherjee, A. Kumar, and M. J. Zaworotko. “Metal-organic framework based carbon capture and purification technologies for clean environment”. In: *Metal-Organic Frameworks (MOFs) for*

- Environmental Applications*. Ed. by S. K. Ghosh. Elsevier, 2019, pp. 5–61. ISBN: 978-0-12-814633-0. DOI: 10.1016/B978-0-12-814633-0.00003-X.
- [62] United States Department of Energy. *Accelerating Breakthrough Innovation in Carbon Capture, Utilization, and Storage*. 2017. 291 pp.
- [63] J.-B. Lin, T. T. T. Nguyen, R. Vaidhyathan, J. Burner, J. M. Taylor, H. Durekova, F. Akhtar, R. K. Mah, O. Ghaffari-Nik, S. Marx, N. Fylstra, S. S. Iremonger, K. W. Dawson, P. Sarkar, P. Hovington, A. Rajendran, T. K. Woo, and G. K. H. Shimizu. “A scalable metal-organic framework as a durable physisorbent for carbon dioxide capture”. In: *Science* 374 (6574 2021), pp. 1464–1469. DOI: 10.1126/science.abi7281.
- [64] P. Hovington, O. Ghaffari-Nik, L. Mariac, A. Liu, B. Henkel, and S. Marx. “Rapid Cycle Temperature Swing Adsorption Process Using Solid Structured Sorbent for CO₂ capture from Cement Flue Gas”. In: *Proceedings of the 16th Greenhouse Gas Control Technologies Conference*. 2022. DOI: 10.2139/ssrn.3814414.
- [65] K. S. Park, Z. Ni, A. P. Côté, J. Y. Choi, R. Huang, F. J. Uribe-Romo, H. K. Chae, M. O’Keeffe, and O. M. Yaghi. “Exceptional chemical and thermal stability of zeolitic imidazolate frameworks”. In: *Proceedings of the National Academy of Sciences* 103.27 (July 2006), pp. 10186–10191. DOI: 10.1073/pnas.0602439103.
- [66] O. M. Yaghi, M. J. Kalmutzki, and C. S. Diercks. “Zeolitic Imidazolate Frameworks”. In: *Introduction to Reticular Chemistry*. John Wiley & Sons, Ltd, 2019. Chap. 20, pp. 463–479. ISBN: 9783527821099. DOI: 10.1002/9783527821099.ch20.
- [67] G. Fraux. “Molecular simulation of fluid adsorption in flexible nanoporous materials at multiple scales”. Theses. PSL Research University ; Chimie ParisTech, June 2019.
- [68] M. O’Keeffe, M. A. Peskov, S. J. Ramsden, and O. M. Yaghi. “The Reticular Chemistry Structure Resource (RCSR) Database of, and Symbols for, Crystal Nets”. In: *Acc. Chem. Res.* 41 (12 2008), pp. 1782–1789. DOI: 10.1021/ar800124u.
- [69] C. Baerlocher, L. B. McCusker, and D. H. Olson. *Atlas of Zeolite Framework Types (Sixth Edition)*. Amsterdam: Elsevier Science B.V., 2007. ISBN: 978-0-444-53064-6. DOI: 10.1016/b978-0-444-53064-6.x5186-x.
- [70] R. N. Widmer, G. I. Lampronti, S. Chibani, C. W. Wilson, S. Anzellini, S. Farsang, A. K. Kleppe, N. P. M. Casati, S. G. MacLeod, S. A. T. Redfern, F.-X. Coudert, and T. D. Bennett. “Rich Polymorphism of a Metal–Organic Framework in Pressure–Temperature Space”. In: *Journal of the American Chemical Society* 141.23 (May 2019), pp. 9330–9337. DOI: 10.1021/jacs.9b03234.
- [71] R. Banerjee, A. Phan, B. Wang, C. Knobler, H. Furukawa, M. O’Keeffe, and O. M. Yaghi. “High-Throughput Synthesis of Zeolitic Imidazolate Frameworks and Application to CO₂ Capture”. In: *Science* 319 (5865 2008), pp. 939–943. DOI: 10.1126/science.1152516.
- [72] Y. Liu, J. H. Pan, N. Wang, F. Steinbach, X. Liu, and J. Caro. “Remarkably Enhanced Gas Separation by Partial Self-Conversion of a Laminated Membrane to Metal-Organic Frameworks”. In: *Angew. Chem. Int. Ed.* 54 (10 2015), pp. 3028–3032. DOI: 10.1002/anie.201411550.
- [73] T. D. Bennett, F.-X. Coudert, S. L. James, and A. I. Cooper. “The changing state of porous materials”. In: *Nature Mater.* 20 (9 2021), pp. 1179–1187. DOI: 10.1038/s41563-021-00957-w.
- [74] J. J. Oppenheim, G. Skorupskii, and M. Dincă. “Aperiodic metal–organic frameworks”. In: *Chem. Sci.* 11 (41 2020), pp. 11094–11103. DOI: 10.1039/D0SC04798H.
- [75] S. R. Batten, N. R. Champness, X.-M. Chen, J. Garcia-Martinez, S. Kitagawa, L. Öhrström, M. O’Keeffe, M. Paik Suh, and J. Reedijk. “Terminology of metal–organic frameworks and coordination polymers (IUPAC Recommendations 2013)”. In: *Pure Appl. Chem.* 85 (8 2013), pp. 1715–1724. DOI: 10.1351/PAC-REC-12-11-20.
- [76] R. Thyagarajan and D. S. Sholl. “A Database of Porous Rigid Amorphous Materials”. In: *Chemistry of Materials* 32.18 (Aug. 2020), pp. 8020–8033. DOI: 10.1021/acs.chemmater.0c03057.

- [77] International Union of Crystallography. “Report of the Executive Committee for 1991”. In: *Acta Crystallogr A Found Crystallogr* 48 (6 1992), pp. 922–946. DOI: [10.1107/S0108767392008328](https://doi.org/10.1107/S0108767392008328).
- [78] E. G. Meekel, E. M. Schmidt, L. J. Cameron, A. D. Dharma, H. J. Windsor, S. G. Duyker, A. Minelli, T. Pope, G. O. Lepore, B. Slater, C. J. Kepert, and A. L. Goodwin. “Truchet-tile structure of a topologically aperiodic metal–organic framework”. In: *Science* 379 (6630 2023), pp. 357–361. DOI: [10.1126/science.ade5239](https://doi.org/10.1126/science.ade5239).
- [79] T. D. Bennett and S. Horike. “Liquid, glass and amorphous solid states of coordination polymers and metal–organic frameworks”. In: *Nature Rev. Mater.* 3 (11 2018), pp. 431–440. DOI: [10.1038/s41578-018-0054-3](https://doi.org/10.1038/s41578-018-0054-3).
- [80] S. R. Elliott. *Physics of amorphous materials*. London and New York: Longman, 1984. ISBN: 0-582-44636-8.
- [81] J. Fonseca, T. Gong, L. Jiao, and H.-L. Jiang. “Metal–organic frameworks (MOFs) beyond crystallinity: amorphous MOFs, MOF liquids and MOF glasses”. In: *J. Mater. Chem. A* 9 (17 2021), pp. 10562–10611. DOI: [10.1039/D1TA01043C](https://doi.org/10.1039/D1TA01043C).
- [82] A. F. Sapnik, I. Bechis, S. M. Collins, D. N. Johnstone, G. Divitini, A. J. Smith, P. A. Chater, M. A. Addicoat, T. Johnson, D. A. Keen, K. E. Jelfs, and T. D. Bennett. “Mixed hierarchical local structure in a disordered metal–organic framework”. In: *Nature Commun.* 12 (1 2021), p. 1213. DOI: [10.1038/s41467-021-22218-9](https://doi.org/10.1038/s41467-021-22218-9).
- [83] K. W. Chapman, G. J. Halder, and P. J. Chupas. “Pressure-Induced Amorphization and Porosity Modification in a Metal-Organic Framework”. In: *Journal of the American Chemical Society* 131.48 (Nov. 2009), pp. 17546–17547. DOI: [10.1021/ja908415z](https://doi.org/10.1021/ja908415z).
- [84] T. D. Bennett, A. L. Goodwin, M. T. Dove, D. A. Keen, M. G. Tucker, E. R. Barney, A. K. Soper, E. G. Bithell, J.-C. Tan, and A. K. Cheetham. “Structure and Properties of an Amorphous Metal-Organic Framework”. In: *Phys. Rev. Lett.* 104 (11 2010), p. 2272. DOI: [10.1103/PhysRevLett.104.115503](https://doi.org/10.1103/PhysRevLett.104.115503).
- [85] T. D. Bennett, P. Simoncic, S. A. Moggach, F. Gozzo, P. Macchi, D. A. Keen, J.-C. Tan, and A. K. Cheetham. “Reversible pressure-induced amorphization of a zeolitic imidazolate framework (ZIF-4)”. In: *Chem. Commun.* 47 (28 2011), p. 7983. DOI: [10.1039/c1cc11985k](https://doi.org/10.1039/c1cc11985k).
- [86] T. D. Bennett, Y. Yue, P. Li, A. Qiao, H. Tao, N. G. Greaves, T. Richards, G. I. Lampronti, S. A. T. Redfern, F. Blanc, O. K. Farha, J. T. Hupp, A. K. Cheetham, and D. A. Keen. “Melt-Quenched Glasses of Metal–Organic Frameworks”. In: *Journal of the American Chemical Society* 138.10 (Mar. 2016), pp. 3484–3492. DOI: [10.1021/jacs.5b13220](https://doi.org/10.1021/jacs.5b13220).
- [87] D. A. Keen and T. D. Bennett. “Structural investigations of amorphous metal–organic frameworks formed *via* different routes”. In: *Phys. Chem. Chem. Phys.* 20 (11 2018), pp. 7857–7861. DOI: [10.1039/C7CP08508G](https://doi.org/10.1039/C7CP08508G).
- [88] C. Orellana-Tavra, E. F. Baxter, T. Tian, T. D. Bennett, N. K. H. Slater, A. K. Cheetham, and D. Fairen-Jimenez. “Amorphous metal–organic frameworks for drug delivery”. In: *Chem. Commun.* 51 (73 2015), pp. 13878–13881. DOI: [10.1039/C5CC05237H](https://doi.org/10.1039/C5CC05237H).
- [89] T. D. Bennett, T. K. Todorova, E. F. Baxter, D. G. Reid, C. Gervais, B. Bueken, B. Van de Voorde, D. De Vos, D. A. Keen, and C. Mellot-Draznieks. “Connecting defects and amorphization in UiO-66 and MIL-140 metal–organic frameworks: a combined experimental and computational study”. In: *Phys. Chem. Chem. Phys.* 18 (3 2016), pp. 2192–2201. DOI: [10.1039/C5CP06798G](https://doi.org/10.1039/C5CP06798G).
- [90] T. D. Bennett, P. J. Saines, D. A. Keen, J.-C. Tan, and A. K. Cheetham. “Ball-Milling-Induced Amorphization of Zeolitic Imidazolate Frameworks (ZIFs) for the Irreversible Trapping of Iodine”. In: *Chem. Eur. J.* 19 (22 2013), pp. 7049–7055. DOI: [10.1002/chem.201300216](https://doi.org/10.1002/chem.201300216).
- [91] T. D. Bennett, D. A. Keen, J.-C. Tan, E. R. Barney, A. L. Goodwin, and A. K. Cheetham. “Thermal Amorphization of Zeolitic Imidazolate Frameworks”. In: *Angew. Chem. Int. Ed.* 50 (13 2011), pp. 3067–3071. DOI: [10.1002/anie.201007303](https://doi.org/10.1002/anie.201007303).

- [92] R. Gaillac, P. Pullumbi, K. A. Beyer, K. W. Chapman, D. A. Keen, T. D. Bennett, and F.-X. Coudert. “Liquid metal–organic frameworks”. In: *Nature Mater.* 16 (11 2017), pp. 1149–1154. DOI: [10.1038/nmat4998](https://doi.org/10.1038/nmat4998).
- [93] R. N. Widmer, G. I. Lampronti, S. Anzellini, R. Gaillac, S. Farsang, C. Zhou, A. M. Belenguer, C. W. Wilson, H. Palmer, A. K. Kleppe, M. T. Wharmby, X. Yu, S. M. Cohen, S. G. Telfer, S. A. T. Redfern, F.-X. Coudert, S. G. MacLeod, and T. D. Bennett. “Pressure promoted low-temperature melting of metal–organic frameworks”. In: *Nature Mater.* 18 (4 2019), pp. 370–376. DOI: [10.1038/s41563-019-0317-4](https://doi.org/10.1038/s41563-019-0317-4).
- [94] S.-X. Peng, Z. Yin, T. Zhang, Q. Yang, H.-B. Yu, and M.-H. Zeng. “Vibration assisted glass-formation in zeolitic imidazolate framework”. In: *J. Chem. Phys.* 157 (10 2022), p. 104501. DOI: [10.1063/5.0109885](https://doi.org/10.1063/5.0109885).
- [95] Z. Lin, J. J. Richardson, J. Zhou, and F. Caruso. “Direct synthesis of amorphous coordination polymers and metal–organic frameworks”. In: *Nat Rev Chem* 7 (4 2023), pp. 273–286. DOI: [10.1038/s41570-023-00474-1](https://doi.org/10.1038/s41570-023-00474-1).
- [96] S. Conrad, P. Kumar, F. Xue, L. Ren, S. Henning, C. Xiao, K. A. Mkhoyan, and M. Tsapatsis. “Controlling Dissolution and Transformation of Zeolitic Imidazolate Frameworks by using Electron-Beam-Induced Amorphization”. In: *Angew. Chem. Int. Ed.* 57 (41 2018), pp. 13592–13597. DOI: [10.1002/anie.201809921](https://doi.org/10.1002/anie.201809921).
- [97] C. Volkringer, C. Falaise, P. Devaux, R. Giovine, V. Stevenson, F. Pourpoint, O. Lafon, M. Osmond, C. Jeanjacques, B. Marcillaud, J. C. Sabroux, and T. Loiseau. “Stability of metal–organic frameworks under gamma irradiation”. In: *Chem. Commun.* 52 (84 2016), pp. 12502–12505. DOI: [10.1039/C6CC06878B](https://doi.org/10.1039/C6CC06878B).
- [98] T. D. Bennett, J.-C. Tan, Y. Yue, E. Baxter, C. Ducati, N. J. Terrill, H. H. -M. Yeung, Z. Zhou, W. Chen, S. Henke, A. K. Cheetham, and G. N. Greaves. “Hybrid glasses from strong and fragile metal–organic framework liquids”. In: *Nature Commun.* 6 (1 2015), p. 974. DOI: [10.1038/ncomms9079](https://doi.org/10.1038/ncomms9079).
- [99] L. Longley, S. M. Collins, C. Zhou, G. J. Smales, S. E. Norman, N. J. Brownbill, C. W. Ashling, P. A. Chater, R. Tovey, C.-B. Schönlieb, T. F. Headen, N. J. Terrill, Y. Yue, A. J. Smith, F. Blanc, D. A. Keen, P. A. Midgley, and T. D. Bennett. “Liquid phase blending of metal-organic frameworks”. In: *Nat Commun* 9 (1 2018), p. 882. DOI: [10.1038/s41467-018-04553-6](https://doi.org/10.1038/s41467-018-04553-6).
- [100] L. Longley, S. M. Collins, S. Li, G. J. Smales, I. Erucar, A. Qiao, J. Hou, C. M. Doherty, A. W. Thornton, A. J. Hill, X. Yu, N. J. Terrill, A. J. Smith, S. M. Cohen, P. A. Midgley, D. A. Keen, S. G. Telfer, and T. D. Bennett. “Flux melting of metal–organic frameworks”. In: *Chem. Sci.* 10 (12 2019), pp. 3592–3601. DOI: [10.1039/C8SC04044C](https://doi.org/10.1039/C8SC04044C).
- [101] J. Hou, C. W. Ashling, S. M. Collins, A. Krajnc, C. Zhou, L. Longley, D. N. Johnstone, P. A. Chater, S. Li, M.-V. Coulet, P. L. Llewellyn, F.-X. Coudert, D. A. Keen, P. A. Midgley, G. Mali, V. Chen, and T. D. Bennett. “Metal-organic framework crystal-glass composites”. In: *Nat Commun* 10 (1 2019), p. 15016. DOI: [10.1038/s41467-019-10470-z](https://doi.org/10.1038/s41467-019-10470-z).
- [102] L. Longley, C. Calahoo, R. Limbach, Y. Xia, J. M. Tuffnell, A. F. Sapnik, M. F. Thorne, D. S. Keeble, D. A. Keen, L. Wondraczek, and T. D. Bennett. “Metal-organic framework and inorganic glass composites”. In: *Nat Commun* 11 (1 2020), p. 974. DOI: [10.1038/s41467-020-19598-9](https://doi.org/10.1038/s41467-020-19598-9).
- [103] Y. Wang, H. Jin, Q. Ma, K. Mo, H. Mao, A. Feldhoff, X. Cao, Y. Li, F. Pan, and Z. Jiang. “A MOF Glass Membrane for Gas Separation”. In: *Angew. Chem. Int. Ed.* 59 (11 2020), pp. 4365–4369. DOI: [10.1002/anie.201915807](https://doi.org/10.1002/anie.201915807).
- [104] J. Hou, A. F. Sapnik, and T. D. Bennett. “Metal–organic framework gels and monoliths”. In: *Chem. Sci.* 11 (2 2020), pp. 310–323. DOI: [10.1039/C9SC04961D](https://doi.org/10.1039/C9SC04961D).
- [105] T. D. Bennett and A. K. Cheetham. “Amorphous Metal–Organic Frameworks”. In: *Acc. Chem. Res.* 47 (5 2014), pp. 1555–1562. DOI: [10.1021/ar5000314](https://doi.org/10.1021/ar5000314).

- [106] M. I. Nandasiri, S. R. Jambovane, B. P. McGrail, H. T. Schaefer, and S. K. Nune. "Adsorption, separation, and catalytic properties of densified metal-organic frameworks". In: *Coordination Chemistry Reviews* 311 (2016), pp. 38–52. doi: [10.1016/j.ccr.2015.12.004](https://doi.org/10.1016/j.ccr.2015.12.004).
- [107] W. Jeong, D.-W. Lim, S. Kim, A. Harale, M. Yoon, M. P. Suh, and J. Kim. "Modeling adsorption properties of structurally deformed metal-organic frameworks using structure-property map". In: *Proc. Natl. Acad. Sci. U.S.A.* 114 (30 2017), pp. 7923–7928. doi: [10.1073/pnas.1706330114](https://doi.org/10.1073/pnas.1706330114).
- [108] O. Smirnova, S. Hwang, R. Sajzew, A. Reupert, V. Nozari, S. Savani, C. Chmelik, L. Wondraczek, J. Kärger, and A. Knebel. "Precise control over gas transporting channels in zeolitic imidazolate framework glasses". In: *ChemRxiv* (2023). doi: [10.26434/chemrxiv-2023-b8nnx](https://doi.org/10.26434/chemrxiv-2023-b8nnx).
- [109] M. Pera-Titus. "Porous Inorganic Membranes for CO₂ Capture: Present and Prospects". In: *Chem. Rev.* 114 (2 2014), pp. 1413–1492. doi: [10.1021/cr400237k](https://doi.org/10.1021/cr400237k).
- [110] S. Horike, S. S. Nagarkar, T. Ogawa, and S. Kitagawa. "A New Dimension for Coordination Polymers and Metal-Organic Frameworks: Towards Functional Glasses and Liquids". In: *Angew. Chem. Int. Ed.* 59 (17 2020), pp. 6652–6664. doi: [10.1002/anie.201911384](https://doi.org/10.1002/anie.201911384).
- [111] A. Kertik, L. H. Wee, M. Pfannmöller, S. Bals, J. A. Martens, and I. F. J. Vankelecom. "Highly selective gas separation membrane using in situ amorphised metal-organic frameworks". In: *Energy Environ. Sci.* 10 (11 2017), pp. 2342–2351. doi: [10.1039/C7EE01872J](https://doi.org/10.1039/C7EE01872J).
- [112] B. Jin, S. Wang, D. Boglajenko, Z. Zhang, Q. Zhao, X. Ma, X. Zhang, and J. J. De Yoreo. "The role of amorphous ZIF in ZIF-8 crystallization kinetics and morphology". In: *Journal of Crystal Growth* 603 (2023), p. 126989. doi: [10.1016/j.jcrysgro.2022.126989](https://doi.org/10.1016/j.jcrysgro.2022.126989).
- [113] E. Massahud, H. Ahmed, R. Babarao, Y. Ehrnst, H. Alijani, C. Darmanin, B. J. Murdoch, A. R. Rezk, and L. Y. Yeo. "Acoustomicrofluidic Defect Engineering and Ligand Exchange in ZIF-8 Metal-Organic Frameworks". In: *Small Methods* (), p. 2201170. doi: <https://doi.org/10.1002/smt.202201170>.
- [114] Y. Fu, A. C. Forse, Z. Kang, M. J. Cliffe, W. Cao, J. Yin, L. Gao, Z. Pang, T. He, Q. Chen, Q. Wang, J. R. Long, J. A. Reimer, and X. Kong. "One-dimensional alignment of defects in a flexible metal-organic framework". In: *Science Advances* 9.6 (2023). doi: [10.1126/sciadv.ade6975](https://doi.org/10.1126/sciadv.ade6975).
- [115] T. D. Bennett, A. K. Cheetham, A. H. Fuchs, and F.-X. Coudert. "Interplay between defects, disorder and flexibility in metal-organic frameworks". In: *Nature Chem* 9 (1 2017), pp. 11–16. doi: [10.1038/nchem.2691](https://doi.org/10.1038/nchem.2691).
- [116] A. M. Bumstead, C. Castillo-Blas, I. Pakamorè, M. F. Thorne, A. F. Sapnik, A. M. Chester, G. Robertson, D. J. M. Irving, P. A. Chater, D. A. Keen, R. S. Forgan, and T. D. Bennett. "Formation of a meltable purinate metal-organic framework and its glass analogue". In: *Chem. Commun.* 59 (6 2023), pp. 732–735. doi: [10.1039/D2CC05314D](https://doi.org/10.1039/D2CC05314D).
- [117] K. W. Chapman, D. F. Sava, G. J. Halder, P. J. Chupas, and T. M. Nenoff. "Trapping Guests within a Nanoporous Metal-Organic Framework through Pressure-Induced Amorphization". In: *J. Am. Chem. Soc.* 133 (46 2011), pp. 18583–18585. doi: [10.1021/ja2085096](https://doi.org/10.1021/ja2085096).
- [118] N. Ma and S. Horike. "Metal-Organic Network-Forming Glasses". In: *Chem. Rev.* 122 (3 2022), pp. 4163–4203. doi: [10.1021/acs.chemrev.1c00826](https://doi.org/10.1021/acs.chemrev.1c00826).
- [119] L. Pan, Z. Ji, X. Yi, X. Zhu, X. Chen, J. Shang, G. Liu, and R.-W. Li. "Metal-Organic Framework Nanofilm for Mechanically Flexible Information Storage Applications". In: *Adv. Funct. Mater.* 25 (18 2015), pp. 2677–2685. doi: [10.1002/adfm.201500449](https://doi.org/10.1002/adfm.201500449).
- [120] S. Tominaka, H. Hamoudi, T. Suga, T. D. Bennett, A. B. Cairns, and A. K. Cheetham. "Topochemical conversion of a dense metal-organic framework from a crystalline insulator to an amorphous semiconductor". In: *Chem. Sci.* 6 (2 2015), pp. 1465–1473. doi: [10.1039/C4SC03295K](https://doi.org/10.1039/C4SC03295K).
- [121] C. Massobrio, J. Du, M. Bernasconi, and P. S. Salmon, eds. *Molecular Dynamics Simulations of Disordered Materials*. Cham: Springer International Publishing, 2015. doi: [10.1007/978-3-319-15675-0](https://doi.org/10.1007/978-3-319-15675-0).

- [122] X. Li, W. Song, K. Yang, N. M. A. Krishnan, B. Wang, M. M. Smedskjaer, J. C. Mauro, G. Sant, M. Balonis, and M. Bauchy. “Cooling rate effects in sodium silicate glasses: Bridging the gap between molecular dynamics simulations and experiments”. In: *The Journal of Chemical Physics* 147.7 (Aug. 2017), p. 074501. DOI: [10.1063/1.4998611](https://doi.org/10.1063/1.4998611).
- [123] R. Gaillac, P. Pullumbi, T. D. Bennett, and F.-X. Coudert. “Structure of Metal–Organic Framework Glasses by *Ab Initio* Molecular Dynamics”. In: *Chem. Mater.* 32 (18 2020), pp. 8004–8011. DOI: [10.1021/acs.chemmater.0c02950](https://doi.org/10.1021/acs.chemmater.0c02950).
- [124] A. M. Mroz, V. Posligua, A. Tarzia, E. H. Wolpert, and K. E. Jelfs. “Into the Unknown: How Computation Can Help Explore Uncharted Material Space”. In: *J. Am. Chem. Soc.* 144 (41 2022), pp. 18730–18743. DOI: [10.1021/jacs.2c06833](https://doi.org/10.1021/jacs.2c06833).
- [125] G. Maurin. “Role of Molecular Simulations in the Field of MOFs”. In: *The Chemistry of Metal–Organic Frameworks*. John Wiley & Sons, Ltd, 2016. Chap. 25, pp. 765–794. ISBN: 9783527693078. DOI: [10.1002/9783527693078.ch25](https://doi.org/10.1002/9783527693078.ch25).
- [126] C. Mellot-Draznieks, B. Slater, and R. Galvelis. “Computational Approaches to the Design, Crystal Structure Prediction, and Structure–Property Relationships of Metal–Organic Frameworks”. In: *Metal–Organic Frameworks: Materials Modeling towards Engineering Applications*. Jenny Stanford Publishing, 2015, pp. 19–70.
- [127] N. Castel and F.-X. Coudert. “Atomistic Models of Amorphous Metal–Organic Frameworks”. In: *The Journal of Physical Chemistry C* 126.16 (Apr. 2022), pp. 6905–6914. DOI: [10.1021/acs.jpcc.2c01091](https://doi.org/10.1021/acs.jpcc.2c01091).
- [128] R. L. McGreevy and L. Pusztai. “Reverse Monte Carlo Simulation: A New Technique for the Determination of Disordered Structures”. In: *Mol. Simulat.* 1 (6 1988), pp. 359–367. DOI: [10.1080/08927028808080958](https://doi.org/10.1080/08927028808080958).
- [129] R. L. McGreevy. “Reverse Monte Carlo modelling”. In: *J. Phys. Cond. Matter* 13.46 (Nov. 2001), R877–R913. DOI: [10.1088/0953-8984/13/46/201](https://doi.org/10.1088/0953-8984/13/46/201).
- [130] H. Y. Playford, L. R. Owen, I. Levin, and M. G. Tucker. “New Insights into Complex Materials Using Reverse Monte Carlo Modeling”. In: *Annu. Rev. Mater. Res.* 44 (1 2014), pp. 429–449. DOI: [10.1146/annurev-matsci-071312-121712](https://doi.org/10.1146/annurev-matsci-071312-121712).
- [131] E. O. R. Beake, M. T. Dove, A. E. Phillips, D. A. Keen, M. G. Tucker, A. L. Goodwin, T. D. Bennett, and A. K. Cheetham. “Flexibility of zeolitic imidazolate framework structures studied by neutron total scattering and the reverse Monte Carlo method”. In: *Journal of Physics: Condensed Matter* 25.39 (Sept. 2013), p. 395403. DOI: [10.1088/0953-8984/25/39/395403](https://doi.org/10.1088/0953-8984/25/39/395403).
- [132] S. Cao, T. D. Bennett, D. A. Keen, A. L. Goodwin, and A. K. Cheetham. “Amorphization of the prototypical zeolitic imidazolate framework ZIF-8 by ball-milling”. In: *Chem. Commun.* 48 (63 2012), p. 7805. DOI: [10.1039/c2cc33773h](https://doi.org/10.1039/c2cc33773h).
- [133] M. G. Tucker, D. A. Keen, M. T. Dove, and K. Trachenko. “Refinement of the Si–O–Si bond angle distribution in vitreous silica”. In: *J. Phys. Cond. Matter* 17.5 (Jan. 2005), S67–S75. DOI: [10.1088/0953-8984/17/5/008](https://doi.org/10.1088/0953-8984/17/5/008).
- [134] A. C. Wright and M. F. Thorpe. “Eighty years of random networks”. In: *Phys. Status Solidi B* 250.5 (Jan. 2013), pp. 931–936. DOI: [10.1002/pssb.201248500](https://doi.org/10.1002/pssb.201248500).
- [135] F. Wooten, K. Winer, and D. Weaire. “Computer Generation of Structural Models of Amorphous Si and Ge”. In: *Phys. Rev. Lett.* 54.13 (Apr. 1985), pp. 1392–1395. DOI: [10.1103/physrevlett.54.1392](https://doi.org/10.1103/physrevlett.54.1392).
- [136] F. Wooten and D. Weaire. “Modeling Tetrahedrally Bonded Random Networks by Computer”. In: *Solid State Physics*. Cambridge, MA: Elsevier, 1987, pp. 1–42. DOI: [10.1016/s0081-1947\(08\)60689-x](https://doi.org/10.1016/s0081-1947(08)60689-x).
- [137] W. Ching. “Periodic structural models and radial distribution functions of SiO_x: x=0. to 2.” In: *The Physics of MOS Insulators*. New York: Elsevier, 1980, pp. 63–67. DOI: [10.1016/b978-0-08-025969-7.50015-4](https://doi.org/10.1016/b978-0-08-025969-7.50015-4).

- [138] H. Wang, N. Li, Z. Hu, T. D. Bennett, X. Zhao, and W.-Y. Ching. “Structural, electronic, and dielectric properties of a large random network model of amorphous zeolitic imidazolate frameworks and its analogues”. In: *J. Am. Ceram. Soc.* 102 (8 2019), pp. 4602–4611. DOI: [10.1111/jace.16308](https://doi.org/10.1111/jace.16308).
- [139] P. Adhikari, M. Xiong, N. Li, X. Zhao, P. Rulis, and W.-Y. Ching. “Structure and Electronic Properties of a Continuous Random Network Model of an Amorphous Zeolitic Imidazolate Framework (a-ZIF)”. In: *J. Phys. Chem. C* 120 (28 2016), pp. 15362–15368. DOI: [10.1021/acs.jpcc.6b06337](https://doi.org/10.1021/acs.jpcc.6b06337).
- [140] L. Guttman. “Model of hydrogenated amorphous silicon”. In: *Phys. Rev. B* 23.4 (Feb. 1981), pp. 1866–1874. DOI: [10.1103/physrevb.23.1866](https://doi.org/10.1103/physrevb.23.1866).
- [141] P. Adhikari, N. Li, P. Rulis, and W.-Y. Ching. “Deformation behavior of an amorphous zeolitic imidazolate framework – from a supersoft material to a complex organometallic alloy”. In: *Phys. Chem. Chem. Phys.* 20 (46 2018), pp. 29001–29011. DOI: [10.1039/C8CP05610B](https://doi.org/10.1039/C8CP05610B).
- [142] M. Xiong, X. Zhao, G. Yin, W.-Y. Ching, and N. Li. “Unraveling the effects of linker substitution on structural, electronic and optical properties of amorphous zeolitic imidazolate frameworks-62 (a-ZIF-62) glasses: a DFT study”. In: *RSC Adv.* 10 (24 2020), pp. 14013–14024. DOI: [10.1039/C9RA09977H](https://doi.org/10.1039/C9RA09977H).
- [143] M. Xiong, N. Li, G. Yin, W.-Y. Ching, and X. Zhao. “Effects of the halogenated imidazolate linker on the fundamental properties of amorphous zeolitic imidazolate frameworks”. In: *J. Non-Cryst. Solids* 536 (2020), p. 120005. DOI: [10.1016/j.jnoncrysol.2020.120005](https://doi.org/10.1016/j.jnoncrysol.2020.120005).
- [144] D. E. Coupry, M. A. Addicoat, and T. Heine. “Extension of the Universal Force Field for Metal–Organic Frameworks”. In: *J. Chem. Theory Comput.* 12 (10 2016), pp. 5215–5225. DOI: [10.1021/acs.jctc.6b00664](https://doi.org/10.1021/acs.jctc.6b00664).
- [145] S. Bureekaew, S. Amirjalayer, M. Tafipolsky, C. Spickermann, T. K. Roy, and R. Schmid. “MOF-FF - A flexible first-principles derived force field for metal-organic frameworks”. In: *Phys. Status Solidi B* 250 (6 2013), pp. 1128–1141. DOI: [10.1002/pssb.201248460](https://doi.org/10.1002/pssb.201248460).
- [146] A. U. Ortiz, A. Boutin, A. H. Fuchs, and F.-X. Coudert. “Investigating the Pressure-Induced Amorphization of Zeolitic Imidazolate Framework ZIF-8: Mechanical Instability Due to Shear Mode Softening”. In: *J. Phys. Chem. Lett.* 4 (11 2013), pp. 1861–1865. DOI: [10.1021/jz400880p](https://doi.org/10.1021/jz400880p).
- [147] T. Weng and J. R. Schmidt. “Flexible and Transferable ab Initio Force Field for Zeolitic Imidazolate Frameworks: ZIF-FF”. In: *J. Phys. Chem. A* 123 (13 2019), pp. 3000–3012. DOI: [10.1021/acs.jpca.8b12311](https://doi.org/10.1021/acs.jpca.8b12311).
- [148] M. Bhogra and U. V. Waghmare. “Flat Phonon Band-Based Mechanism of Amorphization of MOF-5 at Ultra-low Pressures”. In: *J. Phys. Chem. C* 125.27 (July 2021), pp. 14924–14931. DOI: [10.1021/acs.jpcc.1c02598](https://doi.org/10.1021/acs.jpcc.1c02598).
- [149] R. Gaillac, P. Pullumbi, and F.-X. Coudert. “Melting of Zeolitic Imidazolate Frameworks with Different Topologies: Insight from First-Principles Molecular Dynamics”. In: *J. Phys. Chem. C* 122 (12 2018), pp. 6730–6736. DOI: [10.1021/acs.jpcc.8b00385](https://doi.org/10.1021/acs.jpcc.8b00385).
- [150] V. Haigis, Y. Belkhodja, F.-X. Coudert, R. Vuilleumier, and A. Boutin. “Challenges in first-principles NPT molecular dynamics of soft porous crystals: A case study on MIL-53(Ga)”. In: *J. Chem. Phys.* 141.6 (Aug. 2014), p. 064703. DOI: [10.1063/1.4891578](https://doi.org/10.1063/1.4891578).
- [151] M. Erkartal and M. Durandurdu. “Pressure-Induced Amorphization of MOF-5: A First Principles Study”. In: *ChemistrySelect* 3 (28 2018), pp. 8056–8063. DOI: [10.1002/slct.201801381](https://doi.org/10.1002/slct.201801381).
- [152] M. Erkartal and M. Durandurdu. “Pressure-induced amorphization, mechanical and electronic properties of zeolitic imidazolate framework (ZIF-8)”. In: *Mater. Chem. Phys.* 240 (2020), p. 122222. DOI: [10.1016/j.matchemphys.2019.122222](https://doi.org/10.1016/j.matchemphys.2019.122222).
- [153] T. P. Senftle, S. Hong, M. M. Islam, S. B. Kylasa, Y. Zheng, Y. K. Shin, C. Junkermeier, R. Engel-Herbert, M. J. Janik, H. M. Aktulga, T. Verstraelen, A. Grama, and A. C. T. van Duin. “The ReaxFF reactive force-field: development, applications and future directions”. In: *npj Comput. Mater.* 2.1 (Mar. 2016), p. 15011. DOI: [10.1038/npjcompumats.2015.11](https://doi.org/10.1038/npjcompumats.2015.11).

- [154] Y. K. Shin, C. M. Ashraf, and A. C. T. van Duin. “Development and Applications of the ReaxFF Reactive Force Field for Biological Systems”. In: *Computational Materials, Chemistry, and Biochemistry: From Bold Initiatives to the Last Mile*. Cham: Springer International Publishing, 2021, pp. 157–182. doi: 10.1007/978-3-030-18778-1_9.
- [155] Y. Yang, Y. K. Shin, S. Li, T. D. Bennett, A. C. T. van Duin, and J. C. Mauro. “Enabling Computational Design of ZIFs Using ReaxFF”. In: *J. Phys. Chem. B* 122 (41 2018), pp. 9616–9624. doi: 10.1021/acs.jpcc.8b08094.
- [156] T. To, S. S. Sørensen, M. Stepniewska, A. Qiao, L. R. Jensen, M. Bauchy, Y. Yue, and M. M. Smedskjaer. “Fracture toughness of a metal–organic framework glass”. In: *Nature Commun.* 11 (1 2020), p. 357. doi: 10.1038/s41467-020-16382-7.
- [157] T. To, S. S. Sørensen, Y. Yue, and M. M. Smedskjaer. “Bond switching is responsible for nanoductility in zeolitic imidazolate framework glasses”. In: *Dalton Trans.* 50 (18 2021), pp. 6126–6132. doi: 10.1039/D1DT00096A.
- [158] S. S. Sørensen, M. B. Østergaard, M. Stepniewska, H. Johra, Y. Yue, and M. M. Smedskjaer. “Metal–Organic Framework Glasses Possess Higher Thermal Conductivity than Their Crystalline Counterparts”. In: *ACS Appl. Mater. Interfaces* 12 (16 2020), pp. 18893–18903. doi: 10.1021/acsami.0c02310.
- [159] T. Du, S. S. Sørensen, Q. Zhou, M. Bauchy, and M. M. Smedskjaer. “Accessing a Forbidden Disordered State of a Zeolitic Imidazolate Framework with Higher Stiffness and Toughness through Irradiation”. In: *Chem. Mater.* 34 (19 2022), pp. 8749–8759. doi: 10.1021/acs.chemmater.2c01949.
- [160] Y. Yang, C. J. Wilkinson, K.-H. Lee, K. Doss, T. D. Bennett, Y. K. Shin, A. C. T. van Duin, and J. C. Mauro. “Prediction of the Glass Transition Temperatures of Zeolitic Imidazolate Glasses through Topological Constraint Theory”. In: *J. Phys. Chem. Lett.* 9 (24 2018), pp. 6985–6990. doi: 10.1021/acs.jpcllett.8b03348.
- [161] S. Monti, C. Li, and V. Carravetta. “Reactive Dynamics Simulation of Monolayer and Multilayer Adsorption of Glycine on Cu(110)”. In: *J. Phys. Chem. C* 117 (10 2013), pp. 5221–5228. doi: 10.1021/jp312828d.
- [162] S. A. Mohamed and J. Kim. “Gas Adsorption Enhancement in Partially Amorphized Metal–Organic Frameworks”. In: *The Journal of Physical Chemistry C* 125.8 (Feb. 2021), pp. 4509–4518. doi: 10.1021/acs.jpcc.0c10106.
- [163] L. J. Abbott, K. E. Hart, and C. M. Colina. “Polymatic: a generalized simulated polymerization algorithm for amorphous polymers”. In: *Theor. Chem. Acc.* 132.3 (Jan. 2013). doi: 10.1007/s00214-013-1334-z.
- [164] A. W. Thornton, K. E. Jelfs, K. Konstas, C. M. Doherty, A. J. Hill, A. K. Cheetham, and T. D. Bennett. “Porosity in metal–organic framework glasses”. In: *Chem. Commun.* 52 (19 2016), pp. 3750–3753. doi: 10.1039/C5CC10072K.
- [165] I. Bechis, A. F. Sapnik, A. Tarzia, E. H. Wolpert, M. A. Addicoat, D. A. Keen, T. D. Bennett, and K. E. Jelfs. “Modeling the Effect of Defects and Disorder in Amorphous Metal–Organic Frameworks”. In: *Chem. Mater.* 34 (20 2022), pp. 9042–9054. doi: 10.1021/acs.chemmater.2c01528.
- [166] R. S. K. Madsen, A. Qiao, J. Sen, I. Hung, K. Chen, Z. Gan, S. Sen, and Y. Yue. “Ultrahigh-field ⁶⁷Zn NMR reveals short-range disorder in zeolitic imidazolate framework glasses”. In: *Science* 367 (6485 2020), pp. 1473–1476. doi: 10.1126/science.aaz0251.
- [167] F.-X. Coudert and A. H. Fuchs. “Computational characterization and prediction of metal–organic framework properties”. In: *Coordination Chemistry Reviews* 307 (2016), pp. 211–236. doi: 10.1016/j.ccr.2015.08.001.
- [168] Q. Yang, D. Liu, and C. Zhong. “Molecular modeling of gas separation in metal–organic frameworks”. In: *Metal–Organic Frameworks: Materials Modeling Towards Engineering Applications* (2015), pp. 295–338.

- [169] S. Keskin. “Molecular Modeling of Metal–Organic Frameworks for Carbon Dioxide Separation Applications”. In: *Metal–Organic Frameworks: Materials Modeling towards Engineering Applications*. Jenny Stanford Publishing, 2015, pp. 357–398.
- [170] Y. G. Chung, E. Haldoupis, B. J. Bucior, M. Haranczyk, S. Lee, H. Zhang, K. D. Vogiatzis, M. Milisavljevic, S. Ling, J. S. Camp, B. Slater, J. I. Siepmann, D. S. Sholl, and R. Q. Snurr. “Advances, Updates, and Analytics for the Computation-Ready, Experimental Metal–Organic Framework Database: CoRE MOF 2019”. In: *J. Chem. Eng. Data* 64 (12 2019), pp. 5985–5998. DOI: [10.1021/acs.jced.9b00835](https://doi.org/10.1021/acs.jced.9b00835).
- [171] E. Ren, P. Guilbaud, and F.-X. Coudert. “High-throughput computational screening of nanoporous materials in targeted applications”. In: *Digital Discovery* 1 (4 2022), pp. 355–374. DOI: [10.1039/D2DD00018K](https://doi.org/10.1039/D2DD00018K).
- [172] Z. Yao, B. Sánchez-Lengeling, N. S. Bobbitt, B. J. Bucior, S. G. H. Kumar, S. P. Collins, T. Burns, T. K. Woo, O. K. Farha, R. Q. Snurr, and A. Aspuru-Guzik. “Inverse design of nanoporous crystalline reticular materials with deep generative models”. In: *Nat Mach Intell* 3 (1 2021), pp. 76–86. DOI: [10.1038/s42256-020-00271-1](https://doi.org/10.1038/s42256-020-00271-1).
- [173] S. M. Moosavi, B. Á. Novotny, D. Ongari, E. Moubarak, M. Asgari, Ö. Kadioglu, C. Charalambous, A. Ortega-Guerrero, A. H. Farmahini, L. Sarkisov, S. Garcia, F. Noé, and B. Smit. “A data-science approach to predict the heat capacity of nanoporous materials”. In: *Nat. Mater.* 21 (12 2022), pp. 1419–1425. DOI: [10.1038/s41563-022-01374-3](https://doi.org/10.1038/s41563-022-01374-3).
- [174] Z. Yao, Y. Lum, A. Johnston, L. M. Mejia-Mendoza, X. Zhou, Y. Wen, A. Aspuru-Guzik, E. H. Sargent, and Z. W. Seh. “Machine learning for a sustainable energy future”. In: *Nature Reviews Materials* (2022), pp. 1–14.
- [175] S. G. Louie, Y.-H. Chan, F. H. da Jornada, Z. Li, and D. Y. Qiu. “Discovering and understanding materials through computation”. In: *Nat. Mater.* 20 (6 2021), pp. 728–735. DOI: [10.1038/s41563-021-01015-1](https://doi.org/10.1038/s41563-021-01015-1).
- [176] M. P. Allen and D. J. Tildesley. *Computer Simulation of Liquids*. Oxford University Press, June 2017. ISBN: 9780198803195. DOI: [10.1093/oso/9780198803195.001.0001](https://doi.org/10.1093/oso/9780198803195.001.0001).
- [177] R. Gaillac. “Modélisation moléculaire des propriétés physico-chimiques de matériaux microporeux”. Theses. Université Paris sciences et lettres, June 2018.
- [178] D. Frenkel and B. Smit. *Understanding Molecular Simulation: From Algorithms to Applications*. Elsevier, 2002. DOI: [10.1016/b978-0-12-267351-1.x5000-7](https://doi.org/10.1016/b978-0-12-267351-1.x5000-7).
- [179] L. Verlet. “Computer Experiments on Classical Fluids. I. Thermodynamical Properties of Lennard-Jones Molecules”. In: *Physical Review* 159.1 (July 1967), pp. 98–103. DOI: [10.1103/physrev.159.98](https://doi.org/10.1103/physrev.159.98).
- [180] M. Ducamp. “Étude théorique des matériaux adaptatifs”. Theses. Université Paris sciences et lettres, July 2022.
- [181] M. E. Tuckerman. *Statistical Mechanics: Theory and Molecular Simulation*. Oxford University Press, 2010. ISBN: 978-0-198-52526-4.
- [182] S. Rogge, L. Vanduyfhuys, A. Ghysels, M. Waroquier, T. Verstraelen, G. Maurin, and V. Van Speybroeck. “A Comparison of Barostats for the Mechanical Characterization of Metal–Organic Frameworks”. In: *J. Chem. Theory Comput.* 11 (12 2015), pp. 5583–5597. DOI: [10.1021/acs.jctc.5b00748](https://doi.org/10.1021/acs.jctc.5b00748).
- [183] S. Nosé. “A unified formulation of the constant temperature molecular dynamics methods”. In: *The Journal of Chemical Physics* 81.1 (July 1984), pp. 511–519. DOI: [10.1063/1.447334](https://doi.org/10.1063/1.447334).
- [184] W. G. Hoover. “Canonical dynamics: Equilibrium phase-space distributions”. In: *Physical Review A* 31.3 (Mar. 1985), pp. 1695–1697. DOI: [10.1103/physreva.31.1695](https://doi.org/10.1103/physreva.31.1695).
- [185] G. Bussi, D. Donadio, and M. Parrinello. “Canonical sampling through velocity rescaling”. In: *The Journal of Chemical Physics* 126 (1 2007), p. 014101. DOI: [10.1063/1.2408420](https://doi.org/10.1063/1.2408420).
- [186] G. J. Martyna, D. J. Tobias, and M. L. Klein. “Constant pressure molecular dynamics algorithms”. In: *The Journal of Chemical Physics* 101 (5 1994), pp. 4177–4189. DOI: [10.1063/1.467468](https://doi.org/10.1063/1.467468).

- [187] R. M. Martin. *Electronic Structure Basic Theory and Practical Methods*. Cambridge: Cambridge University Press, 2004. ISBN: 9780511805769. DOI: [10.1017/CB09780511805769](https://doi.org/10.1017/CB09780511805769).
- [188] D. Marx and J. Hutter. *Ab Initio Molecular Dynamics*. Vol. 63. 3. Cambridge: Cambridge University Press, Mar. 2009, pp. 54–56. ISBN: 9780511609633. DOI: [10.1017/CB09780511609633](https://doi.org/10.1017/CB09780511609633).
- [189] P. Hohenberg and W. Kohn. “Inhomogeneous Electron Gas”. In: *Physical Review* 136.3B (Nov. 1964), B864–B871. DOI: [10.1103/physrev.136.b864](https://doi.org/10.1103/physrev.136.b864).
- [190] W. Kohn and L. J. Sham. “Self-Consistent Equations Including Exchange and Correlation Effects”. In: *Physical Review* 140.4A (Nov. 1965), A1133–A1138. DOI: [10.1103/physrev.140.a1133](https://doi.org/10.1103/physrev.140.a1133).
- [191] R. Stowasser and R. Hoffmann. “What Do the Kohn–Sham Orbitals and Eigenvalues Mean?” In: *J. Am. Chem. Soc.* 121 (14 1999), pp. 3414–3420. DOI: [10.1021/ja9826892](https://doi.org/10.1021/ja9826892).
- [192] P. E. Blöchl. “Projector augmented-wave method”. In: *Phys. Rev. B* 50 (24 1994), pp. 17953–17979. DOI: [10.1103/PhysRevB.50.17953](https://doi.org/10.1103/PhysRevB.50.17953).
- [193] N. Marzari, A. Ferretti, and C. Wolverton. “Electronic-structure methods for materials design”. In: *Nat. Mater.* 20 (6 2021), pp. 736–749. DOI: [10.1038/s41563-021-01013-3](https://doi.org/10.1038/s41563-021-01013-3).
- [194] J. P. Perdew. “Jacob’s ladder of density functional approximations for the exchange-correlation energy”. In: *AIP Conference Proceedings*. AIP, 2001. DOI: [10.1063/1.1390175](https://doi.org/10.1063/1.1390175).
- [195] J. P. Perdew, A. Ruzsinszky, G. I. Csonka, O. A. Vydrov, G. E. Scuseria, L. A. Constantin, X. Zhou, and K. Burke. “Restoring the Density-Gradient Expansion for Exchange in Solids and Surfaces”. In: *Physical Review Letters* 100.13 (Apr. 2008). DOI: [10.1103/physrevlett.100.136406](https://doi.org/10.1103/physrevlett.100.136406).
- [196] S. Grimme. “Semiempirical GGA-type density functional constructed with a long-range dispersion correction”. In: *Journal of Computational Chemistry* 27.15 (2006), pp. 1787–1799. DOI: [10.1002/jcc.20495](https://doi.org/10.1002/jcc.20495).
- [197] S. Grimme, J. Antony, S. Ehrlich, and H. Krieg. “A consistent and accurate *ab initio* parametrization of density functional dispersion correction (DFT-D) for the 94 elements H–Pu”. In: *The Journal of Chemical Physics* 132 (15 2010), p. 154104. DOI: [10.1063/1.3382344](https://doi.org/10.1063/1.3382344).
- [198] J. VandeVondele, M. Krack, F. Mohamed, M. Parrinello, T. Chassaing, and J. Hutter. “Quickstep: Fast and accurate density functional calculations using a mixed Gaussian and plane waves approach”. In: *Computer Physics Communications* 167 (2 2005), pp. 103–128. DOI: [10.1016/j.cpc.2004.12.014](https://doi.org/10.1016/j.cpc.2004.12.014).
- [199] J. D. Evans, G. Fraux, R. Gaillac, D. Kohen, F. Trouselet, J.-M. Vanson, and F.-X. Coudert. “Computational Chemistry Methods for Nanoporous Materials”. In: *Chem. Mater.* 29 (1 2017), pp. 199–212. DOI: [10.1021/acs.chemmater.6b02994](https://doi.org/10.1021/acs.chemmater.6b02994).
- [200] A. K. Rappe, C. J. Casewit, K. S. Colwell, W. A. Goddard, and W. M. Skiff. “UFF, a full periodic table force field for molecular mechanics and molecular dynamics simulations”. In: *Journal of the American Chemical Society* 114.25 (Dec. 1992), pp. 10024–10035. DOI: [10.1021/ja00051a040](https://doi.org/10.1021/ja00051a040).
- [201] W. Smith and T. Forester. “DL_POLY_2.0: A general-purpose parallel molecular dynamics simulation package”. In: *Journal of Molecular Graphics* 14.3 (1996), pp. 136–141. ISSN: 0263-7855. DOI: [https://doi.org/10.1016/S0263-7855\(96\)00043-4](https://doi.org/10.1016/S0263-7855(96)00043-4).
- [202] N. L. Allinger, Y. H. Yuh, and J. H. Lii. “Molecular mechanics. The MM3 force field for hydrocarbons. 1”. In: *Journal of the American Chemical Society* 111.23 (Nov. 1989), pp. 8551–8566. DOI: [10.1021/ja00205a001](https://doi.org/10.1021/ja00205a001).
- [203] J. P. Dürholt, G. Fraux, F.-X. Coudert, and R. Schmid. “Ab Initio Derived Force Fields for Zeolitic Imidazolate Frameworks: MOF-FF for ZIFs”. In: *Journal of Chemical Theory and Computation* 15.4 (Mar. 2019), pp. 2420–2432. DOI: [10.1021/acs.jctc.8b01041](https://doi.org/10.1021/acs.jctc.8b01041).
- [204] E. Acuna-Yeomans, J. Gutierrez-Sevillano, S. Calero, and D. Dubbeldam. “Evaluation of ZIF-8 flexible force fields for structural and mechanical properties”. In: *Microporous and Mesoporous Materials* 348 (2023), p. 112406. DOI: [10.1016/j.micromeso.2022.112406](https://doi.org/10.1016/j.micromeso.2022.112406).
- [205] R. Schmid, G. Schmitz, J. P. Dürholt, J. Keupp, and R. Amabile. *cmc-tools*. <https://github.com/MOFplus/cmc-tools>. 2021.

- [206] T. Liang, Y. K. Shin, Y.-T. Cheng, D. E. Yilmaz, K. G. Vishnu, O. Vernalis, C. Zou, S. R. Phillpot, S. B. Sinnott, and A. C. van Duin. “Reactive Potentials for Advanced Atomistic Simulations”. In: *Annu. Rev. Mater. Res.* 43 (1 2013), pp. 109–129. DOI: [10.1146/annurev-matsci-071312-121610](https://doi.org/10.1146/annurev-matsci-071312-121610).
- [207] D. Brenner. “The Art and Science of an Analytic Potential”. In: *physica status solidi (b)* 217.1 (2000), pp. 23–40. DOI: [https://doi.org/10.1002/\(SICI\)1521-3951\(200001\)217:1<23::AID-PSSB23>3.0.CO;2-N](https://doi.org/10.1002/(SICI)1521-3951(200001)217:1<23::AID-PSSB23>3.0.CO;2-N).
- [208] M. Buehler. *Introduction to Modeling and Simulation*. MIT OpenCourseWare, 2012.
- [209] A. C. T. van Duin, S. Dasgupta, F. Lorant, and W. A. Goddard. “ReaxFF: A Reactive Force Field for Hydrocarbons”. In: *J. Phys. Chem. A* 105 (41 2001), pp. 9396–9409. DOI: [10.1021/jp004368u](https://doi.org/10.1021/jp004368u).
- [210] M. F. Russo and A. C. van Duin. “Atomistic-scale simulations of chemical reactions: Bridging from quantum chemistry to engineering”. In: *Nuclear Instruments and Methods in Physics Research Section B: Beam Interactions with Materials and Atoms* 269 (14 2011), pp. 1549–1554. DOI: [10.1016/j.nimb.2010.12.053](https://doi.org/10.1016/j.nimb.2010.12.053).
- [211] A. P. Thompson, H. M. Aktulga, R. Berger, D. S. Bolintineanu, W. M. Brown, P. S. Crozier, P. J. in ’t Veld, A. Kohlmeyer, S. G. Moore, T. D. Nguyen, R. Shan, M. J. Stevens, J. Tranchida, C. Trott, and S. J. Plimpton. “LAMMPS - a flexible simulation tool for particle-based materials modeling at the atomic, meso, and continuum scales”. In: *Computer Physics Communications* 271 (Feb. 2022), p. 108171. DOI: [10.1016/j.cpc.2021.108171](https://doi.org/10.1016/j.cpc.2021.108171).
- [212] S. Batzner, A. Musaelian, L. Sun, M. Geiger, J. P. Mailoa, M. Kornbluth, N. Molinari, T. E. Smidt, and B. Kozinsky. “E(3)-equivariant graph neural networks for data-efficient and accurate interatomic potentials”. In: *Nat Commun* 13 (1 2022), p. 1. DOI: [10.1038/s41467-022-29939-5](https://doi.org/10.1038/s41467-022-29939-5).
- [213] J. Behler. “First Principles Neural Network Potentials for Reactive Simulations of Large Molecular and Condensed Systems”. In: *Angew. Chem. Int. Ed.* 56.42 (Aug. 2017), pp. 12828–12840. DOI: [10.1002/anie.201703114](https://doi.org/10.1002/anie.201703114).
- [214] V. L. Deringer, M. A. Caro, and G. Csányi. “Machine Learning Interatomic Potentials as Emerging Tools for Materials Science”. In: *Adv. Mater.* 31 (46 2019), p. 1902765. DOI: [10.1002/adma.201902765](https://doi.org/10.1002/adma.201902765).
- [215] P. Friederich, F. Häse, J. Proppe, and A. Aspuru-Guzik. “Machine-learned potentials for next-generation matter simulations”. In: *Nat. Mater.* 20 (6 2021), pp. 750–761. DOI: [10.1038/s41563-020-0777-6](https://doi.org/10.1038/s41563-020-0777-6).
- [216] H. B. Demuth, M. H. Beale, O. De Jess, and M. T. Hagan. *Neural Network Design*. 2nd. Stillwater, OK, USA: Martin Hagan, 2014. ISBN: 0971732116.
- [217] E. Kocer, T. W. Ko, and J. Behler. “Neural Network Potentials: A Concise Overview of Methods”. In: *Annu. Rev. Phys. Chem.* 73 (1 2022), pp. 163–186. DOI: [10.1146/annurev-physchem-082720-034254](https://doi.org/10.1146/annurev-physchem-082720-034254).
- [218] T. B. Blank, S. D. Brown, A. W. Calhoun, and D. J. Doren. “Neural network models of potential energy surfaces”. In: *The Journal of Chemical Physics* 103 (10 1995), pp. 4129–4137. DOI: [10.1063/1.469597](https://doi.org/10.1063/1.469597).
- [219] J. Behler. “Four Generations of High-Dimensional Neural Network Potentials”. In: *Chem. Rev.* 121 (16 2021), pp. 10037–10072. DOI: [10.1021/acs.chemrev.0c00868](https://doi.org/10.1021/acs.chemrev.0c00868).
- [220] Y. Li, H. Li, F. C. Pickard, B. Narayanan, F. G. Sen, M. K. Y. Chan, S. K. R. S. Sankaranarayanan, B. R. Brooks, and B. Roux. “Machine Learning Force Field Parameters from Ab Initio Data”. In: *J. Chem. Theory Comput.* 13 (9 2017), pp. 4492–4503. DOI: [10.1021/acs.jctc.7b00521](https://doi.org/10.1021/acs.jctc.7b00521).
- [221] S. Vandenhaute, M. Cools-Ceuppens, S. DeKeyser, T. Verstraelen, and V. Van Speybroeck. “Machine learning potentials for metal-organic frameworks using an incremental learning approach”. In: *npj Comput Mater* 9 (1 2023), p. 10575. DOI: [10.1038/s41524-023-00969-x](https://doi.org/10.1038/s41524-023-00969-x).
- [222] J. D. Morrow, J. L. A. Gardner, and V. L. Deringer. “How to validate machine-learned interatomic potentials”. In: *J. Chem. Phys.* 158 (12 2023), p. 121501. DOI: [10.1063/5.0139611](https://doi.org/10.1063/5.0139611).
- [223] O. T. Unke, S. Chmiela, H. E. Sauceda, M. Gastegger, I. Poltavsky, K. T. Schütt, A. Tkatchenko, and K.-R. Müller. “Machine Learning Force Fields”. In: *Chem. Rev.* 121 (16 2021), pp. 10142–10186. DOI: [10.1021/acs.chemrev.0c01111](https://doi.org/10.1021/acs.chemrev.0c01111).

- [224] I. Batatia, S. Batzner, D. P. Kovács, A. Musaelian, G. N. C. Simm, R. Drautz, C. Ortner, B. Kozinsky, and G. Csányi. *The Design Space of $E(3)$ -Equivariant Atom-Centered Interatomic Potentials*. 2022. DOI: [10.48550/ARXIV.2205.06643](https://doi.org/10.48550/ARXIV.2205.06643).
- [225] P. Reiser, M. Neubert, A. Eberhard, L. Torresi, C. Zhou, C. Shao, H. Metni, C. van Hoesel, H. Schopmans, T. Sommer, and P. Friederich. “Graph neural networks for materials science and chemistry”. In: *Commun Mater* 3 (1 2022), p. 010201. DOI: [10.1038/s43246-022-00315-6](https://doi.org/10.1038/s43246-022-00315-6).
- [226] M. Geiger and T. Smidt. *e3nn: Euclidean Neural Networks*. 2022. DOI: [10.48550/ARXIV.2207.09453](https://doi.org/10.48550/ARXIV.2207.09453).
- [227] K. T. Schütt, P. Kessel, M. Gastegger, K. A. Nicoli, A. Tkatchenko, and K.-R. Müller. “SchNetPack: A Deep Learning Toolbox For Atomistic Systems”. In: *J. Chem. Theory Comput.* 15 (1 2019), pp. 448–455. DOI: [10.1021/acs.jctc.8b00908](https://doi.org/10.1021/acs.jctc.8b00908).
- [228] H. Wang, L. Zhang, J. Han, and W. E. “DeePMD-kit: A deep learning package for many-body potential energy representation and molecular dynamics”. In: *Computer Physics Communications* 228 (2018), pp. 178–184. DOI: [10.1016/j.cpc.2018.03.016](https://doi.org/10.1016/j.cpc.2018.03.016).
- [229] D. A. Keen. “A comparison of various commonly used correlation functions for describing total scattering”. In: *J Appl Crystallogr* 34 (2 2001), pp. 172–177. DOI: [10.1107/S0021889800019993](https://doi.org/10.1107/S0021889800019993).
- [230] U. Balucani and R. Vallauri. “Evolution of bond-angle distribution from liquid to glassy states”. In: *Chemical Physics Letters* 166.1 (1990), pp. 77–81. ISSN: 0009-2614. DOI: [10.1016/0009-2614\(90\)87053-T](https://doi.org/10.1016/0009-2614(90)87053-T).
- [231] D. Chandler. *Introduction to Modern Statistical Mechanics*. Oxford University Press, 1987.
- [232] Mu, D. S. Kosov, and G. Stock. “Conformational Dynamics of Trialanine in Water. 2. Comparison of AMBER, CHARMM, GROMOS, and OPLS Force Fields to NMR and Infrared Experiments”. In: *J. Phys. Chem. B* 107 (21 2003), pp. 5064–5073. DOI: [10.1021/jp022445a](https://doi.org/10.1021/jp022445a).
- [233] L. Frentzel-Beyme, P. Kolodzeiski, J.-B. Weiß, A. Schneemann, and S. Henke. “Quantification of gas-accessible microporosity in metal-organic framework glasses”. In: *Nat Commun* 13 (1 2022), p. 705. DOI: [10.1038/s41467-022-35372-5](https://doi.org/10.1038/s41467-022-35372-5).
- [234] T. F. Willems, C. H. Rycroft, M. Kazi, J. C. Meza, and M. Haranczyk. “Algorithms and tools for high-throughput geometry-based analysis of crystalline porous materials”. In: *Microporous and Mesoporous Materials* 149 (1 2012), pp. 134–141. DOI: [10.1016/j.micromeso.2011.08.020](https://doi.org/10.1016/j.micromeso.2011.08.020).
- [235] M. Pinheiro, R. L. Martin, C. H. Rycroft, A. Jones, E. Iglesia, and M. Haranczyk. “Characterization and comparison of pore landscapes in crystalline porous materials”. In: *Journal of Molecular Graphics and Modelling* 44 (2013), pp. 208–219. DOI: [10.1016/j.jmkgm.2013.05.007](https://doi.org/10.1016/j.jmkgm.2013.05.007).
- [236] M. Pinheiro, R. L. Martin, C. H. Rycroft, and M. Haranczyk. “High accuracy geometric analysis of crystalline porous materials”. In: *CrystEngComm* 15 (37 2013), p. 7531. DOI: [10.1039/c3ce41057a](https://doi.org/10.1039/c3ce41057a).
- [237] O. M. Yaghi, M. J. Kalmutzki, and C. S. Diercks. “Topology”. In: *Introduction to Reticular Chemistry*. John Wiley & Sons, Ltd, 2019. Chap. 18, pp. 429–452. ISBN: 9783527821099. DOI: [10.1002/9783527821099.ch18](https://doi.org/10.1002/9783527821099.ch18).
- [238] J. T. Crum, J. R. Crum, C. Taylor, and W. F. Schneider. “Characterization and analysis of ring topology of zeolite frameworks”. In: *Microporous and Mesoporous Materials* (2023), p. 112466. DOI: [10.1016/j.micromeso.2023.112466](https://doi.org/10.1016/j.micromeso.2023.112466).
- [239] S. L. Roux and P. Jund. “Ring statistics analysis of topological networks: New approach and application to amorphous GeS₂ and SiO₂ systems”. In: *Computational Materials Science* 49.1 (June 2010), pp. 70–83. DOI: [10.1016/j.commatsci.2010.04.023](https://doi.org/10.1016/j.commatsci.2010.04.023).
- [240] C. S. Marians and L. W. Hobbs. “Network properties of crystalline polymorphs of silica”. In: *Journal of Non-Crystalline Solids* 124.2-3 (Oct. 1990), pp. 242–253. DOI: [10.1016/0022-3093\(90\)90269-r](https://doi.org/10.1016/0022-3093(90)90269-r).
- [241] D. S. Franzblau. “Computation of ring statistics for network models of solids”. In: *Physical Review B* 44.10 (Sept. 1991), pp. 4925–4930. DOI: [10.1103/physrevb.44.4925](https://doi.org/10.1103/physrevb.44.4925).
- [242] L. Guttman. “Ring structure of the crystalline and amorphous forms of silicon dioxide”. In: *Journal of Non-Crystalline Solids* 116.2-3 (Feb. 1990), pp. 145–147. DOI: [10.1016/0022-3093\(90\)90686-g](https://doi.org/10.1016/0022-3093(90)90686-g).

- [243] F. Wooten. “Structure, odd lines and topological entropy of disorder of amorphous silicon”. In: *Acta Crystallographica Section A Foundations of Crystallography* 58.4 (June 2002), pp. 346–351. DOI: [10.1107/s0108767302006669](https://doi.org/10.1107/s0108767302006669).
- [244] K. Goetzke and H.-J. Klein. “Properties and efficient algorithmic determination of different classes of rings in finite and infinite polyhedral networks”. In: *Journal of Non-Crystalline Solids* 127.2 (Feb. 1991), pp. 215–220. DOI: [10.1016/0022-3093\(91\)90145-v](https://doi.org/10.1016/0022-3093(91)90145-v).
- [245] V. A. Blatov, A. P. Shevchenko, and D. M. Proserpio. “Applied Topological Analysis of Crystal Structures with the Program Package ToposPro”. In: *Crystal Growth & Design* 14 (7 2014), pp. 3576–3586. DOI: [10.1021/cg500498k](https://doi.org/10.1021/cg500498k).
- [246] L. Zoubritzky and F.-X. Coudert. “CrystalNets.jl: Identification of Crystal Topologies”. In: *SciPost Chem.* 1 (2022), p. 005. DOI: [10.21468/SciPostChem.1.2.005](https://doi.org/10.21468/SciPostChem.1.2.005).
- [247] B. J. Bucior, A. S. Rosen, M. Haranczyk, Z. Yao, M. E. Ziebel, O. K. Farha, J. T. Hupp, J. I. Siepmann, A. Aspuru-Guzik, and R. Q. Snurr. “Identification Schemes for Metal–Organic Frameworks To Enable Rapid Search and Cheminformatics Analysis”. In: *Crystal Growth & Design* 19 (11 2019), pp. 6682–6697. DOI: [10.1021/acs.cgd.9b01050](https://doi.org/10.1021/acs.cgd.9b01050).
- [248] V. Calandrini, E. Pellegrini, P. Calligari, K. Hinsén, and G. Kneller. “nMoldyn - Interfacing spectroscopic experiments, molecular dynamics simulations and models for time correlation functions”. In: *JDN* 12 (2011), pp. 201–232. DOI: [10.1051/sfn/201112010](https://doi.org/10.1051/sfn/201112010).
- [249] C. Chakravarty, P. G. Debenedetti, and F. H. Stillinger. “Lindemann measures for the solid-liquid phase transition”. In: *The Journal of Chemical Physics* 126.20 (May 2007), p. 204508. DOI: [10.1063/1.2737054](https://doi.org/10.1063/1.2737054).
- [250] P. Virtanen, R. Gommers, T. E. Oliphant, M. Haberland, T. Reddy, D. Cournapeau, E. Burovski, P. Peterson, W. Weckesser, J. Bright, S. J. van der Walt, M. Brett, J. Wilson, K. J. Millman, N. Mayorov, A. R. J. Nelson, E. Jones, R. Kern, E. Larson, C. J. Carey, Í. Polat, Y. Feng, E. W. Moore, J. VanderPlas, D. Laxalde, J. Perktold, R. Cimrman, I. Henriksen, E. A. Quintero, C. R. Harris, A. M. Archibald, A. H. Ribeiro, F. Pedregosa, P. van Mulbregt, and SciPy 1.0 Contributors. “SciPy 1.0: Fundamental Algorithms for Scientific Computing in Python”. In: *Nature Methods* 17 (2020), pp. 261–272. DOI: [10.1038/s41592-019-0686-2](https://doi.org/10.1038/s41592-019-0686-2).
- [251] A. Hjorth Larsen, J. Jørgen Mortensen, J. Blomqvist, I. E. Castelli, R. Christensen, M. Dułak, J. Friis, M. N. Groves, B. Hammer, C. Hargus, E. D. Hermes, P. C. Jennings, P. Bjerre Jensen, J. Kermode, J. R. Kitchin, E. Leonhard Kolsbjerg, J. Kubal, K. Kaasbjerg, S. Lysgaard, J. Bergmann Maronsson, T. Maxson, T. Olsen, L. Pastewka, A. Peterson, C. Rostgaard, J. Schiøtz, O. Schütt, M. Strange, K. S. Thygesen, T. Vegge, L. Vilhelmsen, M. Walter, Z. Zeng, and K. W. Jacobsen. “The atomic simulation environment—a Python library for working with atoms”. In: *J. Phys.: Condens. Matter* 29 (27 2017), p. 273002. DOI: [10.1088/1361-648X/aa680e](https://doi.org/10.1088/1361-648X/aa680e).
- [252] R. Gaillac, P. Pullumbi, and F.-X. Coudert. “ELATE: an open-source online application for analysis and visualization of elastic tensors”. In: *J. Phys.: Condens. Matter* 28 (27 2016), p. 275201. DOI: [10.1088/0953-8984/28/27/275201](https://doi.org/10.1088/0953-8984/28/27/275201).
- [253] M. E. Fortunato and C. M. Colina. “pysimm: A python package for simulation of molecular systems”. In: *SoftwareX* 6 (2017), pp. 7–12. DOI: [10.1016/j.softx.2016.12.002](https://doi.org/10.1016/j.softx.2016.12.002).
- [254] N. Castel and F.-X. Coudert. “Challenges in Molecular Dynamics of Amorphous ZIFs Using Reactive Force Fields”. In: *J. Phys. Chem. C* 126 (45 2022), pp. 19532–19541. DOI: [10.1021/acs.jpcc.2c06305](https://doi.org/10.1021/acs.jpcc.2c06305).
- [255] M. Benoit, S. Ispas, and M. E. Tuckerman. “Structural properties of molten silicates from ab initio molecular-dynamics simulations: Comparison between CaO – Al₂O₃ – SiO₂ and SiO₂”. In: *Phys. Rev. B* 64 (22 2001), p. 1044. DOI: [10.1103/PhysRevB.64.224205](https://doi.org/10.1103/PhysRevB.64.224205).
- [256] H. Aktulga, J. Fogarty, S. Pandit, and A. Grama. “Parallel reactive molecular dynamics: Numerical methods and algorithmic techniques”. In: *Parallel Computing* 38.4-5 (Apr. 2012), pp. 245–259. DOI: [10.1016/j.parco.2011.08.005](https://doi.org/10.1016/j.parco.2011.08.005).

- [257] L. B. du Bourg, A. U. Ortiz, A. Boutin, and F.-X. Coudert. “Thermal and mechanical stability of zeolitic imidazolate frameworks polymorphs”. In: *APL Materials* 2.12 (Dec. 2014), p. 124110. DOI: [10.1063/1.4904818](https://doi.org/10.1063/1.4904818).
- [258] M. Parrinello and A. Rahman. “Strain fluctuations and elastic constants”. In: *The Journal of Chemical Physics* 76.5 (Mar. 1982), pp. 2662–2666. DOI: [10.1063/1.443248](https://doi.org/10.1063/1.443248).
- [259] S. Dwivedi, M. Kowalik, N. Rosenbach, D. S. Alqarni, Y. K. Shin, Y. Yang, J. C. Mauro, A. Tanksale, A. L. Chaffee, and A. C. van Duin. “Atomistic Mechanisms of Thermal Transformation in a Zr-Metal Organic Framework, MIL-140C”. In: *The Journal of Physical Chemistry Letters* 12.1 (Dec. 2020), pp. 177–184. DOI: [10.1021/acs.jpcllett.0c02930](https://doi.org/10.1021/acs.jpcllett.0c02930).
- [260] M. Eckhoff and J. Behler. “From Molecular Fragments to the Bulk: Development of a Neural Network Potential for MOF-5”. In: *J. Chem. Theory Comput.* 15.6 (May 2019), pp. 3793–3809. DOI: [10.1021/acs.jctc.8b01288](https://doi.org/10.1021/acs.jctc.8b01288).
- [261] V. L. Deringer, N. Bernstein, G. Csányi, C. Ben Mahmoud, M. Ceriotti, M. Wilson, D. A. Drabold, and S. R. Elliott. “Origins of structural and electronic transitions in disordered silicon”. In: *Nature* 589 (7840 2021), pp. 59–64. DOI: [10.1038/s41586-020-03072-z](https://doi.org/10.1038/s41586-020-03072-z).
- [262] J. Wang, H. Shen, R. Yang, K. Xie, C. Zhang, L. Chen, K.-M. Ho, C.-Z. Wang, and S. Wang. “A deep learning interatomic potential developed for atomistic simulation of carbon materials”. In: *Carbon* 186 (2022), pp. 1–8. DOI: [10.1016/j.carbon.2021.09.062](https://doi.org/10.1016/j.carbon.2021.09.062).
- [263] S. K. Achar, J. J. Wardzala, L. Bernasconi, L. Zhang, and J. K. Johnson. “Combined Deep Learning and Classical Potential Approach for Modeling Diffusion in UiO-66”. In: *J. Chem. Theory Comput.* 18 (6 2022), pp. 3593–3606. DOI: [10.1021/acs.jctc.2c00010](https://doi.org/10.1021/acs.jctc.2c00010).
- [264] J. Behler et al. “RuNNer-A neural network code for high-dimensional potential-energy surfaces”. In: *Universität Göttingen* (2018).
- [265] M. Herbold and J. Behler. “Machine learning transferable atomic forces for large systems from underconverged molecular fragments”. In: *Phys. Chem. Chem. Phys.* (2023). DOI: [10.1039/D2CP05976B](https://doi.org/10.1039/D2CP05976B).
- [266] Y. Yu, W. Zhang, and D. Mei. “Artificial Neural Network Potential for Encapsulated Platinum Clusters in MOF-808”. In: *J. Phys. Chem. C* 126 (2 2022), pp. 1204–1214. DOI: [10.1021/acs.jpcc.1c09178](https://doi.org/10.1021/acs.jpcc.1c09178).
- [267] P.-L. Kang, C. Shang, and Z.-P. Liu. “Large-Scale Atomic Simulation via Machine Learning Potentials Constructed by Global Potential Energy Surface Exploration”. In: *Acc. Chem. Res.* 53 (10 2020), pp. 2119–2129. DOI: [10.1021/acs.accounts.0c00472](https://doi.org/10.1021/acs.accounts.0c00472).
- [268] O. Tayfuroglu, A. Kocak, and Y. Zorlu. “A neural network potential for the IRMOF series and its application for thermal and mechanical behaviors”. In: *Phys. Chem. Chem. Phys.* 24 (19 2022), pp. 11882–11897. DOI: [10.1039/D1CP05973D](https://doi.org/10.1039/D1CP05973D).
- [269] H. Furukawa, F. Gándara, Y.-B. Zhang, J. Jiang, W. L. Queen, M. R. Hudson, and O. M. Yaghi. “Water Adsorption in Porous Metal–Organic Frameworks and Related Materials”. In: *J. Am. Chem. Soc.* 136 (11 2014), pp. 4369–4381. DOI: [10.1021/ja500330a](https://doi.org/10.1021/ja500330a).
- [270] A. Pedone, M. Bertani, L. Brugnoli, and A. Pallini. “Interatomic potentials for oxide glasses: Past, present, and future”. In: *Journal of Non-Crystalline Solids: X* 15 (2022), p. 100115. DOI: [10.1016/j.nocx.2022.100115](https://doi.org/10.1016/j.nocx.2022.100115).
- [271] F. C. Mocanu, K. Konstantinou, T. H. Lee, N. Bernstein, V. L. Deringer, G. Csányi, and S. R. Elliott. “Modeling the Phase-Change Memory Material, Ge₂Sb₂Te₅, with a Machine-Learned Interatomic Potential”. In: *J. Phys. Chem. B* 122 (38 2018), pp. 8998–9006. DOI: [10.1021/acs.jpccb.8b06476](https://doi.org/10.1021/acs.jpccb.8b06476).
- [272] L. Bonati and M. Parrinello. “Silicon Liquid Structure and Crystal Nucleation from Ab Initio Deep Metadynamics”. In: *Phys. Rev. Lett.* 121 (26 2018), p. 629. DOI: [10.1103/PhysRevLett.121.265701](https://doi.org/10.1103/PhysRevLett.121.265701).
- [273] T. D. Kühne, M. Iannuzzi, M. Del Ben, V. V. Rybkin, P. Seewald, F. Stein, T. Laino, R. Z. Khaliullin, O. Schütt, F. Schiffrmann, D. Golze, J. Wilhelm, S. Chulkov, M. H. Bani-Hashemian, V. Weber, U. Borštnik, M. TAILLEFUMIER, A. S. Jakobovits, A. Lazzaro, H. Pabst, T. Müller, R. Schade, M. Guidon, S. Andermatt, N. Holmberg, G. K. Schenter, A. Hehn, A. Bussy, F. Belleflamme, G. Tabacchi,

- A. Glöß, M. Lass, I. Bethune, C. J. Mundy, C. Plessl, M. Watkins, J. VandeVondele, M. Krack, and J. Hutter. "CP2K: An electronic structure and molecular dynamics software package - Quickstep: Efficient and accurate electronic structure calculations". In: *J. Chem. Phys.* 152 (19 2020), p. 194103. DOI: 10.1063/5.0007045.
- [274] J. P. Perdew, K. Burke, and M. Ernzerhof. "Generalized Gradient Approximation Made Simple". In: *Phys. Rev. Lett.* 77 (18 1996), pp. 3865–3868. DOI: 10.1103/PhysRevLett.77.3865.
- [275] S. Goedecker, M. Teter, and J. Hutter. "Separable dual-space Gaussian pseudopotentials". In: *Phys. Rev. B* 54 (3 1996), pp. 1703–1710. DOI: 10.1103/PhysRevB.54.1703.
- [276] D. P. Kingma and J. Ba. *Adam: A Method for Stochastic Optimization*. 2017. arXiv: 1412.6980 [cs.LG].
- [277] A. Musaelian, S. Batzner, A. Johansson, L. Sun, C. J. Owen, M. Kornbluth, and B. Kozinsky. "Learning local equivariant representations for large-scale atomistic dynamics". In: *Nat Commun* 14 (1 2023), p. 1. DOI: 10.1038/s41467-023-36329-y.
- [278] K. Yang, G. Zhou, and Q. Xu. "The elasticity of MOFs under mechanical pressure". In: *RSC Adv* 6 (44 2016), pp. 37506–37514. DOI: 10.1039/C5RA23149C.
- [279] L. R. Redfern and O. K. Farha. "Mechanical properties of metal–organic frameworks". In: *Chem. Sci.* 10 (46 2019), pp. 10666–10679. DOI: 10.1039/C9SC04249K.
- [280] N. Castel and F.-X. Coudert. "Computation of Finite Temperature Mechanical Properties of Zeolitic Imidazolate Framework Glasses by Molecular Dynamics". In: *Chemistry of Materials* (2023). DOI: 10.1021/acs.chemmater.3c00392.
- [281] A. Katrusiak. "High-pressure crystallography". In: *Acta Crystallogr A Found Crystallogr* 64 (1 2008), pp. 135–148. DOI: 10.1107/S0108767307061181.
- [282] A. K. Varshneya and J. C. Mauro. "Chapter 8 - Elastic properties and hardness of glass". In: *Fundamentals of Inorganic Glasses (Third Edition)*. Ed. by A. K. Varshneya and J. C. Mauro. Third Edition. Elsevier, 2019, pp. 187–214. ISBN: 978-0-12-816225-5. DOI: 10.1016/B978-0-12-816225-5.00008-0.
- [283] M. de Jong, W. Chen, T. Angsten, A. Jain, R. Notestine, A. Gamst, M. Sluiter, C. Krishna Ande, S. van der Zwaag, J. J. Plata, C. Toher, S. Curtarolo, G. Ceder, K. A. Persson, and M. Asta. "Charting the complete elastic properties of inorganic crystalline compounds". In: *Sci Data* 2 (1 2015), p. 345. DOI: 10.1038/sdata.2015.9.
- [284] S. Chibani and F.-X. Coudert. "Systematic exploration of the mechanical properties of 13 621 inorganic compounds". In: *Chem. Sci.* 10 (37 2019), pp. 8589–8599. DOI: 10.1039/C9SC01682A.
- [285] M. Matsui. "Molecular dynamics simulation of structures, bulk moduli, and volume thermal expansivities of silicate liquids in the system CaO-MgO-Al₂O₃-SiO₂". In: *Geophys. Res. Lett.* 23 (4 1996), pp. 395–398. DOI: 10.1029/96GL00260.
- [286] S. Ono, J. P. Brodholt, and G. David Price. "Elastic, thermal and structural properties of platinum". In: *Journal of Physics and Chemistry of Solids* 72 (3 2011), pp. 169–175. DOI: 10.1016/j.jpcs.2010.12.004.
- [287] D. Andersson and B. Beeler. "Ab initio molecular dynamics (AIMD) simulations of NaCl, UCl₃ and NaCl-UCl₃ molten salts". In: *Journal of Nuclear Materials* 568 (2022), p. 153836. DOI: 10.1016/j.jnucmat.2022.153836.
- [288] W. Perger, J. Criswell, B. Civalleri, and R. Dovesi. "Ab-initio calculation of elastic constants of crystalline systems with the CRYSTAL code". In: *Computer Physics Communications* 180 (10 2009), pp. 1753–1759. DOI: 10.1016/j.cpc.2009.04.022.
- [289] Y. Wang, J. J. Wang, H. Zhang, V. R. Manga, S. L. Shang, L.-Q. Chen, and Z.-K. Liu. "A first-principles approach to finite temperature elastic constants". In: *J. Phys.: Condens. Matter* 22 (22 2010), p. 225404. DOI: 10.1088/0953-8984/22/22/225404.

- [290] S. Henke, M. T. Wharmby, G. Kieslich, I. Hante, A. Schneemann, Y. Wu, D. Daisenberger, and A. K. Cheetham. "Pore closure in zeolitic imidazolate frameworks under mechanical pressure". In: *Chem. Sci.* 9 (6 2018), pp. 1654–1660. doi: 10.1039/C7SC04952H.
- [291] R. J. Angel. "Equations of State". In: *Reviews in Mineralogy and Geochemistry* 41 (1 2000), pp. 35–59. doi: 10.2138/rmg.2000.41.2.
- [292] P. Vervoorts, J. Stebani, A. S. J. Méndez, and G. Kieslich. "Structural Chemistry of Metal–Organic Frameworks under Hydrostatic Pressures". In: *ACS Materials Lett.* 3 (12 2021), pp. 1635–1651. doi: 10.1021/acsmaterialslett.1c00250.
- [293] P. Vervoorts, C. L. Hobday, M. G. Ehrenreich, D. Daisenberger, and G. Kieslich. "The Zeolitic Imidazolate Framework ZIF-4 under Low Hydrostatic Pressures". In: *Z. Anorg. Allg. Chem.* 645 (15 2019), pp. 970–974. doi: 10.1002/zaac.201900046.
- [294] H. Nam, A. Bengtson, K. Vörtler, S. Saha, R. Sakidja, and D. Morgan. "First-principles molecular dynamics modeling of the molten fluoride salt with Cr solute". In: *Journal of Nuclear Materials* 449 (1-3 2014), pp. 148–157. doi: 10.1016/j.jnucmat.2014.03.014.
- [295] A. Ortiz, J. Sánchez-González, L. González-Méndez, and F. Cumbreira. "Determination of the thermal stability and isothermal bulk modulus of the ZrO₂ polymorphs at room temperature by molecular dynamics with a semi-empirical quantum-chemical model". In: *Ceramics International* 33 (5 2007), pp. 705–709. doi: 10.1016/j.ceramint.2005.12.006.
- [296] I. M. Padilla Espinosa, N. Barua, and R. V. Mohan. "Hydrostatic compression and pressure phase transition of major Portland cement constituents – Insights via molecular dynamics modeling". In: *Cement* 7 (2022), p. 100017. doi: 10.1016/j.cement.2021.100017.
- [297] F. Birch. "Finite Elastic Strain of Cubic Crystals". In: *Phys. Rev.* 71 (11 1947), pp. 809–824. doi: 10.1103/PhysRev.71.809.
- [298] J. R. Ray. "Elastic constants and statistical ensembles in molecular dynamics". In: *Computer Physics Reports* 8.3 (Aug. 1988). Publisher: North-Holland, pp. 109–151. ISSN: 01677977. doi: 10.1016/0167-7977(88)90009-3.
- [299] R. Hill. "The Elastic Behaviour of a Crystalline Aggregate". In: *Proc. Phys. Soc. A* 65 (5 1952), pp. 349–354. doi: 10.1088/0370-1298/65/5/307.
- [300] Z. Shi, S. Hartati, A. Arramel, and N. Li. "Unraveling the bond structure, porosity, and mechanical properties amorphous ZIF-4 and its topological equivalents: Large scale ab initio calculations". In: *APL Mater.* 11 (2 2023), p. 021103. doi: 10.1063/5.0139208.
- [301] I. E. Collings and A. L. Goodwin. "Metal–organic frameworks under pressure". In: *Journal of Applied Physics* 126 (18 2019), p. 181101. doi: 10.1063/1.5126911.
- [302] J.-C. Tan, B. Civalleri, A. Erba, and E. Albanese. "Quantum mechanical predictions to elucidate the anisotropic elastic properties of zeolitic imidazolate frameworks: ZIF-4 vs. ZIF-zni". In: *CrystEngComm* 17 (2 2015), pp. 375–382. doi: 10.1039/C4CE01564A.
- [303] M. R. Ryder and J.-C. Tan. "Explaining the mechanical mechanisms of zeolitic metal–organic frameworks: revealing auxeticity and anomalous elasticity". In: *Dalton Trans.* 45 (10 2016), pp. 4154–4161. doi: 10.1039/C5DT03514G.
- [304] Z. Shi, K. Weng, and N. Li. "The Atomic Structure and Mechanical Properties of ZIF-4 under High Pressure: Ab Initio Calculations". In: *Molecules* 28 (1 2023), p. 22. doi: 10.3390/molecules28010022.
- [305] L. Zhang, Z. Hu, and J. Jiang. "Sorption-Induced Structural Transition of Zeolitic Imidazolate Framework-8: A Hybrid Molecular Simulation Study". In: *J. Am. Chem. Soc.* 135 (9 2013), pp. 3722–3728. doi: 10.1021/ja401129h.
- [306] S. Horike, N. Ma, Z. Fan, S. Kosasang, and M. M. Smedskjaer. "Mechanics, Ionics, and Optics of Metal–Organic Framework and Coordination Polymer Glasses". In: *Nano Lett.* 21 (15 2021), pp. 6382–6390. doi: 10.1021/acs.nanolett.1c01594.
- [307] C. A. Schröder, I. A. Baburin, L. van Wüllen, M. Wiebcke, and S. Leoni. "Subtle polymorphism of zinc imidazolate frameworks: temperature-dependent ground states in the energy landscape

BIBLIOGRAPHY

- revealed by experiment and theory”. In: *CrystEngComm* 15 (20 2013), pp. 4036–4040. DOI: [10.1039/C2CE26045J](https://doi.org/10.1039/C2CE26045J).
- [308] E. C. Spencer, R. J. Angel, N. L. Ross, B. E. Hanson, and J. A. K. Howard. “Pressure-Induced Cooperative Bond Rearrangement in a Zinc Imidazolate Framework: A High-Pressure Single-Crystal X-Ray Diffraction Study”. In: *J. Am. Chem. Soc.* 131 (11 2009), pp. 4022–4026. DOI: [10.1021/ja808531m](https://doi.org/10.1021/ja808531m).

RÉSUMÉ EN FRANÇAIS

1	Des MOF amorphes pour la séparation de CO ₂	174
2	Étude des <i>a</i> MOF par simulation moléculaire.	177
3	Défis de la simulation d' <i>a</i> ZIF par champs de force réactifs	178
4	Potentiels ML pour la production de modèles d' <i>a</i> ZIF.	180
5	Propriétés mécaniques à température finie des <i>a</i> ZIF	181
	Conclusions	183



Les réseaux métallo-organiques (MOF) sont des matériaux hybrides composés d'ions métalliques reliés par des ligands organiques qui forment des réseaux tridimensionnels. Du fait de leur porosité et de leur grande versatilité structurale et chimique, ils constituent des candidats prometteurs pour de nombreuses applications industrielles, notamment pour la séparation du CO₂. Même si la majorité de la littérature se concentre sur des structures cristallines, un nombre croissant de MOF amorphes (*a*MOF) ont été synthétisés, qui conservent à la fois les avantages intrinsèques des cristaux tout en possédant des propriétés physiques et chimiques distinctes.

Cependant, la détermination expérimentale de la structure microscopique de ces phases amorphes est complexe, avec des expériences de diffraction qui n'offrent que des informations indirectes. Un ensemble de méthodes numériques coexistent pour résoudre leurs structures et modéliser ces matériaux désordonnés, qui souffrent cependant d'un manque de comparaison directe et systématique. Durant ma thèse, j'ai utilisé plusieurs méthodes de simulation moléculaire aux buts, échelles et coûts de calcul différents – dynamique moléculaire *ab initio*, champs de force classiques et réactifs, et potentiels ML – afin de générer des modèles microscopiques d'*a*MOF et d'étudier leurs propriétés.

1 DES MOF AMORPHES POUR LA SÉPARATION DE CO₂

OBJECTIFS CLIMATIQUES ET ÉMISSIONS NÉGATIVES

L'Accord de Paris de 2015 vise à « contenir l'élévation de la température moyenne de la planète nettement en dessous de 2 °C par rapport aux niveaux préindustriels et en poursuivant l'action menée pour limiter l'élévation de la température à 1,5 °C par rapport aux niveaux préindustriels, étant entendu que cela réduirait sensiblement les risques et les effets des changements climatiques ». L'élévation de température étant principalement causée par l'augmentation de la concentration des gaz à effet de serre (GES) dans l'atmosphère [1], la limiter suppose a minima de stabiliser cette concentration. Au premier ordre cela signifie que le flux de GES anthropogéniques vers l'atmosphère devra s'annuler (voire devenir négatif) : on parle alors d'émissions nettes nulles (ou négatives) ou de *neutralité carbone*.

Si l'on suppose qu'il restera toujours des émissions positives causées par l'activité humaine dans certains secteurs (transport, alimentation, etc.) alors cela signifie qu'il faudra simultanément retirer des GES de l'atmosphère, autrement dit produire des *émissions négatives*. Plusieurs catégories d'émissions négatives existent avec des niveaux de maturité et volumes permis très hétérogènes [5], dont l'augmentation du puits naturel lié à un changement d'usage des sols (LUC - *land-use change*) et le captage et stockage du carbone (CCS - *carbon capture and storage*). Jugés plus matures et crédibles, ils sont présents dans la majorité des scénarios reproduits par le dernier rapport du GIEC comme illustré figure R1.

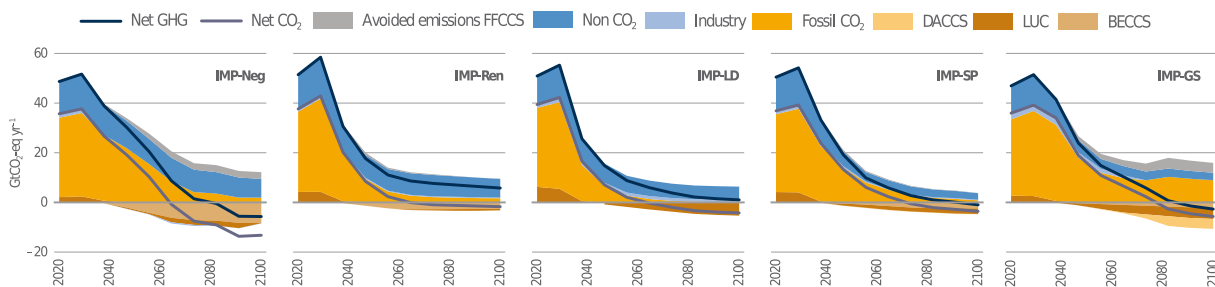


FIGURE R1: Émissions négatives (LUC, DACCS, BECCS) et émissions résiduelles pour cinq scénarios d'atténuation (IMP - *illustrative mitigation pathways*). Figure adaptée de Ref. [3].

Cet objectif de neutralité carbone est repris par la France et l'Union européenne qui ont inscrit dans la loi l'atteinte de cet objectif en 2050. Bien que la réduction drastique des émissions de GES reste la priorité, les documents stratégiques proposent un effort simultané d'augmentation des émissions négatives, en particulier en s'appuyant sur le CCS. Ainsi dans le scénario sous-tendant la dernière Stratégie Nationale Bas-Carbone (SNBC) [9], le puits de GES en 2050, égal aux émissions, est composé à 20% de CCS. La vision stratégique à long terme de la Commission européenne précise quant à elle une répartition des émissions négatives avec une part du CCS allant de 10 à 45% selon les scénarios [10].

LE CAPTAGE, LE STOCKAGE ET LA VALORISATION DE CO₂

Derrière les termes captage, stockage et valorisation de CO₂ (CCUS - *carbon capture utilization and storage*) on trouve un ensemble de technologies et d'applications industrielles qui ont comme point commun de piéger des molécules de CO₂ pour ensuite valoriser ce gaz ou le stocker [11]. En raison de la faible densité du CO₂ dans l'air (de l'ordre de 400 ppm), il est technologiquement plus facile, énergétiquement plus efficace, et économiquement plus rentable de capter du CO₂ dans des gaz où il est présent en forte densité, typiquement en sortie d'usines ou de centrales électriques, que directement dans l'atmosphère (DACCS - *direct air capture*).

Un premier usage du CCUS consiste à capter le CO₂ en sortie des centrales électriques thermiques à biomasse (BECCS - *bioenergy with CCS*), permettant de réaliser des émissions négatives en séquestrant le CO₂ capté par la biomasse lors de sa croissance [18]. L'industrie est un autre domaine d'application majeur pour capter soit les émissions directes de CO₂ inévitablement produites par les réactions chimiques

des procédés (ciment et sidérurgie notamment), soit celles liées à une consommation d'énergie (par exemple le chauffage à haute température) produite par des sources fossiles [21]. Finalement, le CCUS peut servir pour la production d'hydrogène bas-carbone, vecteur présent dans de nombreux scénarios de décarbonation [23]. Dans l'ensemble, la contribution du CCUS à la réduction des émissions mondiales est chiffrée entre 10 et 20% selon les différents scénarios de l'Agence Internationale de l'Énergie [11].

VOIES TECHNOLOGIQUES ACTUELLES ET APPORTS DES MATÉRIAUX POREUX

Le procédé aujourd'hui le plus commun, déployé à l'échelle industrielle sur plusieurs sites, est la capture par un solvant présentant une affinité pour les molécules de CO₂ [6]. La capture se fait en deux temps : les gaz de combustion sont d'abord mis en contact avec le solvant, qui se charge en molécules de CO₂, puis le solvant est « régénéré » dans un autre compartiment en élevant sa température pour libérer les molécules de CO₂ qui s'y étaient fixées [17]. Plusieurs limitations laissent envisager l'apparition de meilleurs procédés : les solvants sont relativement instables à haute température ce qui restreint la qualité de la régénération, la durée de vie est limitée par la décomposition des amines et surtout la capacité calorifique élevée de ces solvants (liée à celle de l'eau) est la cause de la principale dépense d'énergie lors de la régénération [32].

Comme on ne s'attend qu'à des améliorations incrémentales de l'efficacité globale des procédés à base de solvants [16], plusieurs autres technologies de capture ont été proposées pour surmonter ces limitations. Un certain nombre d'approches prometteuses reposent sur des matériaux poreux, c'est-à-dire présentant dans leur structure des vides ou des cavités appelés *pores*, à commencer par l'adsorption de gaz. Contrairement à l'absorption où les molécules de CO₂ pénètrent dans la phase liquide, l'adsorption est un phénomène où les molécules se fixent à la surface d'une phase solide. L'utilisation d'adsorbants solides poreux permet de réduire la pénalité énergétique de la capture notamment en vertu de leur plus faible capacité calorifique [16, 32]. Se passer de solvants liquides permet aussi de réduire le besoin en eau et de limiter les risques environnementaux liés aux composés toxiques contenus dans ces solvants [17]. Les technologies reposant sur l'adsorption ont aujourd'hui passé l'échelle du démonstrateur avec succès [38].

En dehors des procédés d'adsorption, les matériaux poreux ont aussi un rôle à jouer en tant que nouveaux matériaux pour des technologies de séparation membranaire du CO₂ [17]. Ne nécessitant pas de régénération thermique du sorbant liquide ou solide, les technologies membranaires constituent une option énergétiquement intéressante [41].

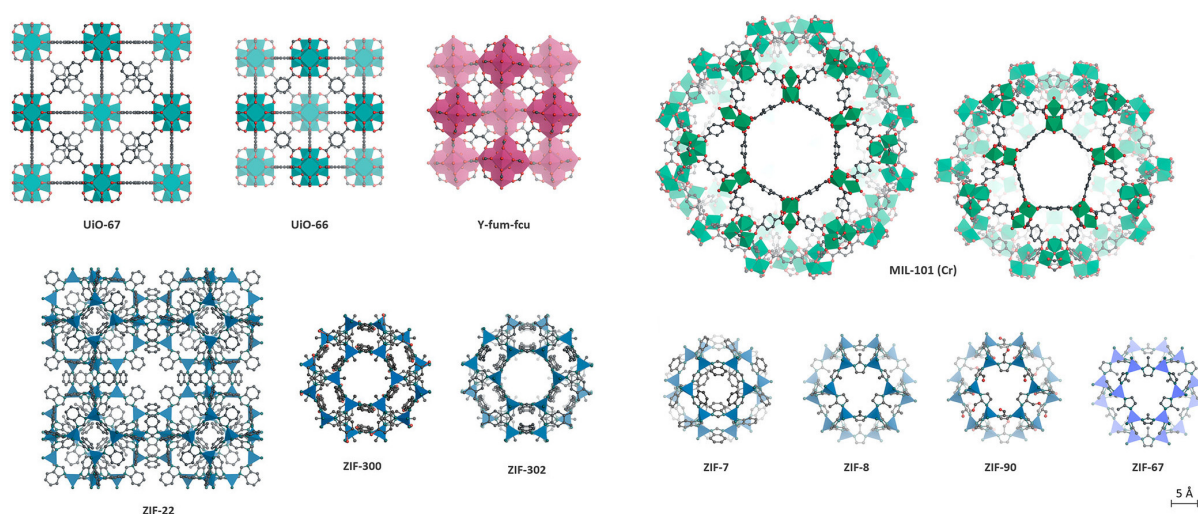


FIGURE R2: Exemples de structures de réseaux métallo-organiques (MOF). Figure adaptée de Ref. [41].

LES RÉSEAUX MÉTALLO-ORGANIQUES

Les réseaux métallo-organiques ou MOF (pour *metal-organic frameworks*) constituent une nouvelle famille de matériaux découverte au début des années 2000 [45] combinant éléments organiques et inorganiques, assemblés à l'échelle microscopique pour former des millions de structures potentielles dont quelques-unes sont présentées à titre d'exemple en figure R2. Les MOF sont composés de deux types de briques élémentaires, assemblées différemment selon les besoins : des briques inorganiques, contenant un ion métallique et des briques (« ligands ») organiques. Cela permet de synthétiser des matériaux « sur mesure » présentant des jeux de caractéristiques que les matériaux nanoporeux traditionnels ne peuvent atteindre [49, 50].

Les MOF sont particulièrement prometteurs pour le captage du CO₂ par adsorption ou par membranes grâce à leur grande surface par unité de volume, des tailles de pores et des affinités chimiques hautement personnalisables grâce au choix des briques moléculaires, et leur potentiel d'être produits à l'échelle industrielle [32]. Ce large choix de compositions possibles permet d'optimiser les MOF pour différentes configurations industrielles [36, 61].

MOF AMORPHES : UNE NOUVELLE CLASSE DE MATÉRIAUX À EXPLORER

Jusqu'à très récemment, les MOF ont été appréhendés essentiellement en tant que matériaux cristallins. Pourtant leur production (illustrée figure R3) par amorphisation, par augmentation de température, de pression ou encore par broyage mécanique, présente un grand intérêt tant sur le plan des mécanismes de changement de phase à l'œuvre – susceptibles d'apparaître dans les procédés industriels lors des cycles d'adsorption - que des applications potentielles des phases amorphes obtenues. Un ensemble de MOF amorphes (*aMOF*) ont été produits, dont des liquides, gels et verres de MOF [79].

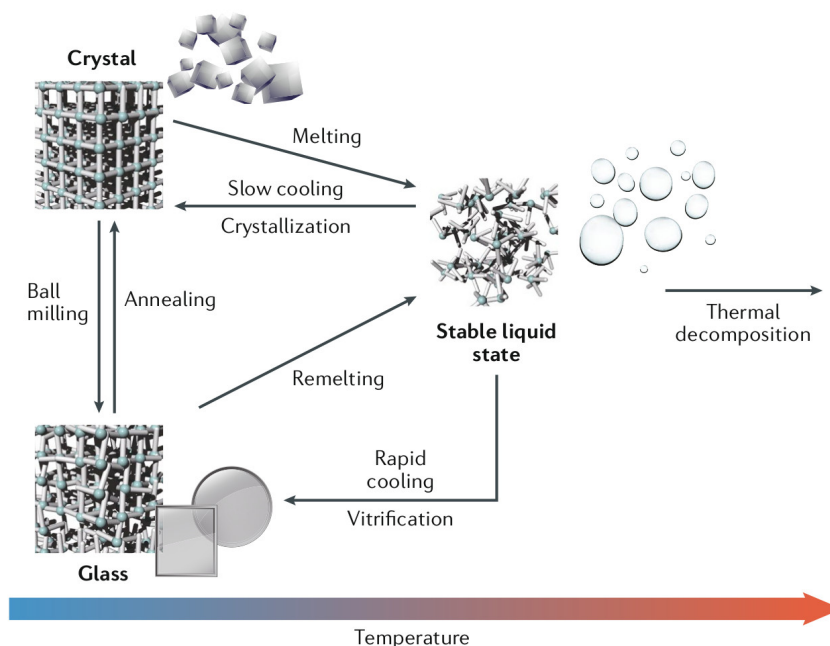


FIGURE R3: Différentes voies de fabrication des verres de MOF. Figure tirée de Ref. [79].

Les phases amorphes des MOF possèdent des propriétés physiques et chimiques utiles, non accessibles aux phases cristallines (isotropie, absence de joints de grains, grande transparence, etc.), tout en conservant les avantages intrinsèques des MOF cristallins (surfaces élevées, porosité, personnalisation, etc.) [81]. Ces phases désordonnées peuvent ainsi offrir de nouvelles combinaisons de propriétés distinctes de celles des structures cristallines connues [73].

En outre l'intégration des phases amorphes dans les procédés industriels est facilitée du fait de leur grande robustesse mécanique et de la possibilité d'éviter la transformation des poudres de MOF cristallins

(par compression, ajout de liant) qui induit une perte de capacité d'adsorption [105, 106]. En plus de ces utilisations pour l'adsorption les aMOF sont un matériau de choix pour les technologies membranaires, notamment car ils ne possèdent pas les nombreux effets de bords des cristaux [109, 110].

2 ÉTUDE DES aMOF PAR SIMULATION MOLÉCULAIRE

MODÈLES MICROSCOPIQUES D'aMOF

Cependant, malgré leurs propriétés prometteuses les états amorphes sont particulièrement difficiles à caractériser, tout comme leurs structures à l'échelle microscopique sont complexes à déterminer. Bien que des informations structurales indirectes puissent être obtenues par diffraction, elles ne peuvent pas, contrairement aux cristaux, mener facilement à la résolution des structures atomiques [74]. En outre, la description numérique des matériaux désordonnés est plus complexe que celle des cristaux, avec un ensemble de méthodes numériques qui coexistent et relativement peu de modèles microscopiques de MOF amorphes présents dans la littérature.

Dans cette thèse, j'ai listé et comparé les méthodologies existantes pour les aMOF, basées à la fois sur des données expérimentales et des simulations numériques : *Reverse Monte Carlo* (RMC) [84], *Continuous Random Networks* (CRN) [139], dynamique moléculaire classique [146] et *ab initio* [92], champs de force réactifs [155] et algorithmes de polymérisation [164].

Après examen, il ressort clairement que dans la plupart des cas le problème de la modélisation est mathématiquement sous-déterminé et qu'il est difficile d'arbitrer entre différents modèles. En outre, les comparaisons directes et approfondies des modèles sont rares dans la littérature existante, et les propriétés géométriques, physiques et chimiques des modèles n'ont pas été systématiquement comparées entre elles.

MÉTHODES DE SIMULATION MOLÉCULAIRE

Les simulations numériques utilisées pour l'étude de systèmes chimiques et physiques constituent aujourd'hui un champ de recherche à part entière. Parfois appelées expériences *in silico*, elles sont complémentaires des expériences et des théories analytiques. Elles permettent tout d'abord d'éclairer les mécanismes microscopiques à l'œuvre quand les mesures expérimentales ne donnent qu'une vue globale du phénomène, d'accéder à des échelles de temps très courtes et autrement inobservables et d'étudier des conditions inaccessibles expérimentalement [167]. Une meilleure compréhension des mécanismes et leur caractérisation permettent notamment d'interpréter et de guider les travaux expérimentaux visant à améliorer les procédés existants et synthétiser de nouveaux matériaux [125]. En outre, le développement

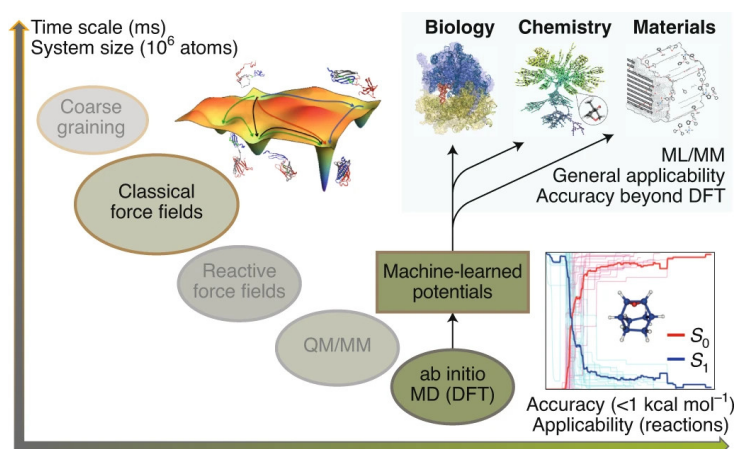


FIGURE R4: Illustration de multiples méthodes de simulations moléculaires qui donnent accès à différentes échelles avec une précision variable. Figure tirée de Ref. [215].

d'importantes bases de données de structures de MOF, avec un nombre de structures et combinaisons considérable, rend le criblage à haute fréquence possible et désirable. Cette approche repose sur les progrès des sciences d'exploitations des données (apprentissage automatique, etc.) et tire bénéfice des modèles numériques spécifiques aux MOF [172, 173]. Elle permet d'explorer à très faible coût les millions de structures possibles afin de détecter les plus prometteuses avant de les synthétiser, ou encore de fournir des informations sur des grandeurs qui n'ont pas été mesurées expérimentalement sur des MOF déjà synthétisés et répertoriés [126, 171].

Au cours de mon doctorat, j'ai eu recours à une stratégie possible de production de modèles d'*a*MOF consistant à simuler la transition de phase de l'état cristallin vers la phase amorphe par dynamique moléculaire (MD) afin d'imiter *in silico* les voies de formation expérimentales. Les dynamiques moléculaires permettent de suivre l'évolution d'un système de particules au cours du temps, formant un échantillon du matériau, sur des échelles allant typiquement de la picoseconde à la nanoseconde, et ainsi d'observer des mécanismes inaccessibles directement par l'expérience [176]. Il y a autant de dynamiques moléculaires qu'il y a de façon de décrire les forces s'exerçant entre les atomes, avec des portées, échelles et coûts de calcul différents, comme représenté figure R4. Parmi elles, j'ai utilisé des dynamiques moléculaires *ab initio* [187], avec des champs de force classiques [145] et réactifs [206], ou encore des potentiels ML [213], pour générer des modèles atomistiques d'*a*MOF et étudier leurs propriétés.

LES ZEOLITIC IMIDAZOLATE FRAMEWORKS COMME OBJETS D'ÉTUDE

Durant ma thèse j'ai étudié les *zeolitic imidazolate frameworks* (ZIF), une classe de MOF construits autour de nœuds tétraédriques composés de métaux de transition, liés entre eux par des ligands imidazolates, formant des topologies tétraédriques [66]. Les ZIF concentrent la majorité des études dédiées aux MOF amorphes en raison de leur remarquable stabilité thermique [65, 82].

En particulier, je me suis essentiellement focalisé sur ZIF-4, le premier *a*MOF bien caractérisé [84] qui sert depuis d'exemple prototypique de MOF amorphe. Construit à partir de nœuds métalliques Zn^{2+} et d'imidazolates (Im), il est représenté figure R5.

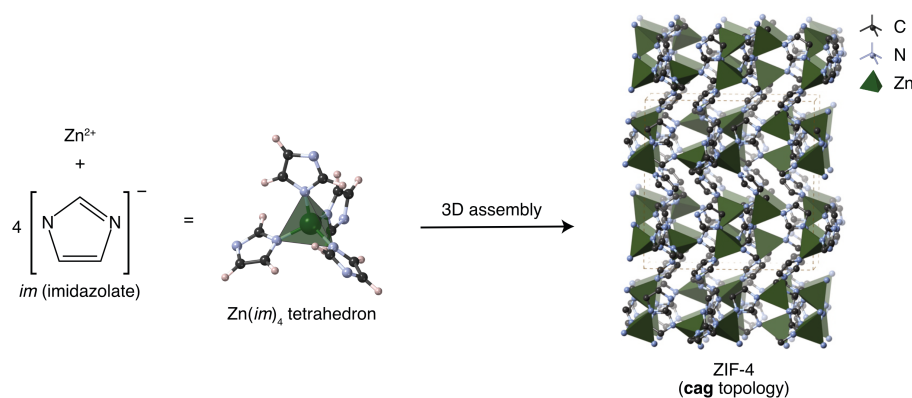


FIGURE R5: Représentation de l'assemblage de ZIF-4 sous la forme d'un réseau tridimensionnel de tétraèdres $Zn(Im)_4$.

3 DÉFIS DE LA SIMULATION D'*a*ZIF PAR CHAMPS DE FORCE RÉACTIFS

CHAMPS DE FORCE RÉACTIFS

Dans des travaux antérieurs, la dynamique moléculaire *ab initio* (AIMD) a été utilisée avec succès pour modéliser des MOF liquides par fusion de la phase cristalline [92, 93, 149], et ensuite générer des configurations de verres [123]. Cependant, cette approche est très coûteuse en temps de calcul, ce qui limite son utilisation à de petites échelles temporelles et spatiales. Les dynamiques classiques, couramment utilisées pour les MOF cristallins, ne constituent pas une alternative efficace, car elles sont

incapables de simuler la rupture ou la reformation des liaisons, deux processus pourtant inhérents à la formation de la plupart des MOF amorphes [146].

Des champs de force réactifs ont ainsi été proposés comme compromis entre la précision chimique et le coût de calcul, permettant de simuler la rupture et la reformation de liaisons [153]. À partir des travaux de Yang et al. [155], plusieurs études se sont appuyées sur des champs de force réactifs (ReaxFF) pour générer des modèles de verres de ZIF par trempe [156, 158], c'est-à-dire en simulant la fonte d'un cristal suivi d'un rapide refroidissement.

PRODUCTION DE VERRES PAR TREMPÉ

Cette procédure de trempe, qui reproduit la réalité expérimentale (à des échelles spatiales en temporelles beaucoup plus réduites), est utilisée depuis longtemps pour modéliser la structure de multiples matériaux vitreux tels que les silicates [121, 255]. Dans ce travail, j'ai adapté la procédure de trempe des travaux précédents, pour obtenir celle représentée figure R6. Une structure cristalline est d'abord préparée puis chauffée à 300 K, avant d'être fondue en la chauffant au-dessus du point de fusion. Le liquide produit est ensuite refroidi à température ambiante, donnant un verre. Ce dernier est enfin équilibré afin de calculer ses propriétés structurales et dynamiques.

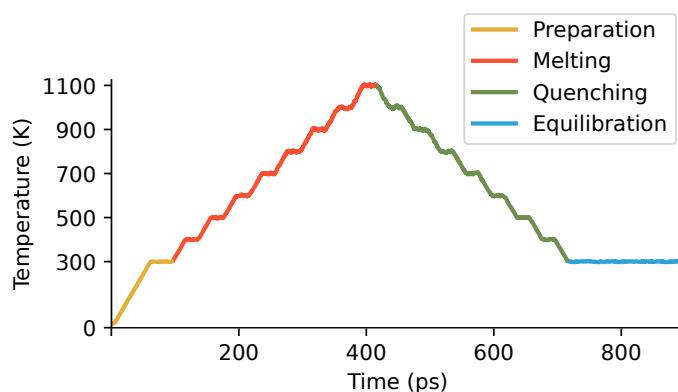


FIGURE R6: Température en fonction du temps pendant la procédure de formation du verre avec ReaxFF, comprenant la préparation (orange), la fusion (rouge), la trempe (vert) et l'équilibrage (bleu).

Les modèles générés avec ReaxFF n'avaient jusqu'alors dans la littérature pas été soumis à une comparaison directe et approfondie avec ceux obtenus par des approches alternatives. J'ai démontré que les simulations réalisées étaient pourtant extrêmement sensibles au choix de la méthodologie et des paramètres de simulation. Cela m'a conduit à recommander de toujours soigneusement vérifier la cohérence physique du système, à chaque instant de la dynamique moléculaire.

COMPARAISON DES PROPRIÉTÉS STRUCTURALES

Afin d'évaluer quantitativement la validité du modèle de verre trempé produit avec ReaxFF, j'ai comparé ses caractéristiques structurales avec celles de modèles de verre générés à un niveau théorique plus élevé, à savoir les modèles *ab initio* du travail de Gaillac et al. [123].

J'ai montré que les modèles de verre générés avec ReaxFF sont nettement différents de leurs homologues *ab initio*, avec des différences structurales considérables à la fois dans l'ordre à courte et moyenne distances, ainsi que dans leurs propriétés macroscopiques. Le contraste le plus saisissant se trouve dans la distribution des angles N–Zn–N, reproduite figure R7. Alors que la structure tétraédrique Zn(Im)₄ fait que l'on s'attend à des distributions unimodales autour de 109°, la distribution du verre ReaxFF est très différente avec une large distribution d'angles dans le spectre 70–170°. Cela est dû en grande partie à une représentation sous-contrainte des interactions Zn–N par ReaxFF, qui ne reproduit pas fidèlement l'une des caractéristiques clés de la chimie des ZIF qu'est la nature directionnelle de la liaison Zn–N.

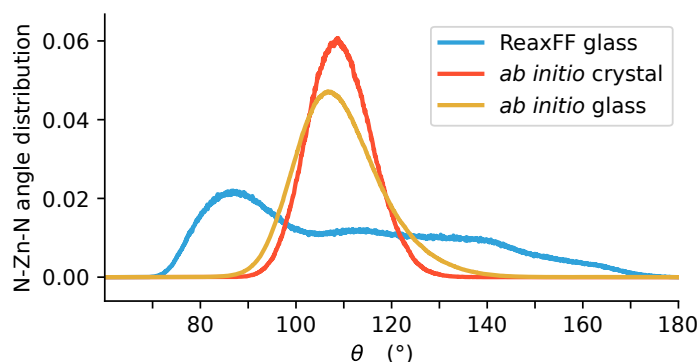


FIGURE R7: Distribution de l'angle N–Zn–N pour le verre ReaxFF (bleu), le verre *ab initio* (orange) et le cristal *ab initio* (rouge).

Toutes ces observations suggèrent que les propriétés structurales des ZIF obtenues à partir de ReaxFF doivent être interprétées avec prudence, et incitent soit à recourir à d'autres méthodologies, soit à attendre un nouveau développement de ReaxFF pour les ZIF (qui pourrait s'inspirer de ce travail).

4 POTENTIELS ML POUR LA PRODUCTION DE MODÈLES D'*a*ZIF

UNE NOUVELLE GÉNÉRATION DE POTENTIELS RÉACTIFS

Devant les difficultés rencontrées avec ReaxFF, le développement de nouveaux potentiels interatomiques s'impose, qui doivent être capables de décrire la rupture et à la formation des liaisons métal–ligand pendant l'amorphisation, tout en étant plus économes en temps de calcul que les dynamiques *ab initio*.

Une solution particulièrement prometteuse est le développement de potentiels interatomiques par apprentissage automatique, ou potentiel *machine-learned* (ML) [213]. L'idée de base des potentiels ML (MLP) est d'utiliser des données obtenues à un plus haut niveau de théorie (typiquement *ab initio*) pour ajuster des potentiels interatomiques, sans s'appuyer sur les formes fonctionnelles analytiques des champs de force classiques ou réactifs [219]. Plusieurs MLP ont été développés avec succès pour des MOF [221, 260] comme pour la génération de systèmes amorphes [261, 262], mais encore jamais pour modéliser des MOF amorphes,

La construction d'un MLP se fait en plusieurs étapes et commence par la construction d'un ensemble de données de référence, sur lesquelles le MLP est ensuite entraîné pour les reproduire avec précision. Puis une validation minutieuse est finalement nécessaire avant de pouvoir utiliser le MLP. La collecte d'une grande quantité de données d'entraînement à partir de calculs *ab initio* étant l'un des facteurs limitant le développement de MLP, j'ai utilisé dans ce travail NequIP (*Neural Equivariant Interatomic Potential*) [212], une architecture très efficace en termes de données et qui a fait ses preuves sur une grande variété de systèmes, dont des MOF [221].

MLP POUR ZIF-4

L'ambition de ce travail est de développer le premier MLP utilisé pour générer des MOF amorphes, en se concentrant sur les *a*ZIF et en commençant par ZIF-4. À partir d'un ensemble limité de données d'entraînement constitué d'une trajectoire de ZIF-4 liquide, j'ai obtenu des MLP reproduisant avec une précision exceptionnelle de multiples propriétés structurales de plusieurs phases (cristal, liquide, verres). Ce travail a été réalisé en collaboration avec Jack D. Evans de l'Université d'Adélaïde.

J'ai ensuite réitéré le travail effectué avec ReaxFF en générant de nouveaux modèles de verres trempés avec les MLP, que j'ai ensuite comparé aux données *ab initio*. Dans l'ensemble on observe une excellente

reproduction des propriétés structurales, à l’instar de la distribution angulaire N–Zn–N reproduite figure R8 à titre d’exemple.

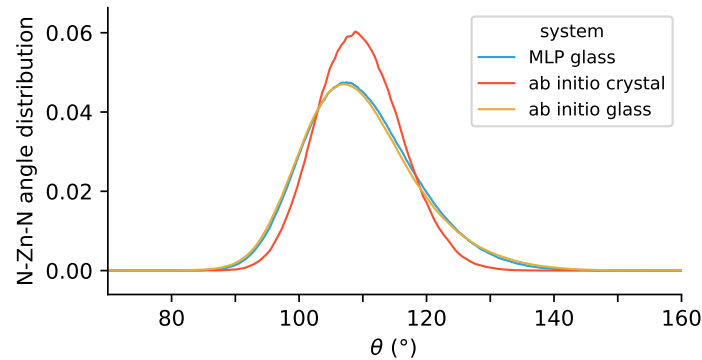


FIGURE R8: Distribution de l’angle N–Zn–N pour le verre MLP (bleu), le verre *ab initio* (orange) et le cristal *ab initio* (rouge).

VERS UN MLP UNIVERSEL POUR LES ZIF

Après le succès rencontré avec ZIF-4, le travail actuel vise à aller au-delà de ce système en cherchant à développer un MLP universel pour de multiples structures de ZIF. Pour ce faire, j’ai généré des données d’entraînement *ab initio* sur différentes structures, volumes et phases dans le but de construire des trajectoires de liquides. J’ai d’abord sélectionné plusieurs structures de ZIF à base de Zn avec différentes topologies et ligands, puis j’ai simulé quatre trajectoires à 300 K avec différentes déformations pour chaque cristal. Une fois tous les modèles de cristaux préparés, ils ont été chauffés à haute température (1200-1750 K) afin d’obtenir des trajectoires, idéalement liquides, pour l’entraînement des MLP.

5 PROPRIÉTÉS MÉCANIQUES À TEMPÉRATURE FINIE DES *a*ZIF

L’ÉTUDE DES PROPRIÉTÉS MÉCANIQUES

Bien que la stabilité mécanique des MOF soit essentielle pour les processus à l’échelle industrielle, la réponse de ces matériaux aux contraintes mécaniques constitue un domaine d’étude encore relativement émergent [278, 279]. Alors que de multiples techniques expérimentales ont été employées avec succès pour déterminer les propriétés mécaniques des MOF cristallins, il y a un manque d’études sur les phases amorphes [81]. Certaines méthodes, notamment reposant sur la diffraction des rayons X à haute pression [281], ne sont pas directement applicables aux matériaux désordonnés, et beaucoup d’autres nécessitent de grands échantillons de verre qui sont difficiles à préparer [81, 282]. Heureusement, les mêmes propriétés mécaniques peuvent être étudiées par des simulations numériques [167].

Parmi les nombreuses propriétés mécaniques à température finie, je me suis concentré sur le module d’élasticité isostatique (K) qui caractérise la variation du volume (V) d’un solide soumis à une pression hydrostatique uniforme (P) et est défini par $K = -V(\partial P/\partial V)_T$. Il fournit des informations clés pour les applications, notamment sur la stabilité du MOF lors des processus de préparation [292] ou des cycles d’adsorption par inversion de pression [278]. J’ai utilisé de multiples formes de dynamiques moléculaires et méthodes de calcul des propriétés mécaniques à température finie, que j’ai évaluées sur un ensemble de modèles de cristaux et verres de ZIF-4.

VALEURS DE RÉFÉRENCE PAR DYNAMIQUE *AB INITIO*

Utilisant pour la première fois la méthode de la différence finie couplée à des dynamiques moléculaires *ab initio* pour un MOF (illustré figure R9), j’ai proposé la première valeur fiable du K d’un ZIF amorphe dans la littérature. J’ai ainsi obtenu un module d’élasticité isostatique pour le ZIF-4 cristallin de $K_{\text{cristal}} = 1.39$ GPa, en accord avec les précédents travaux expérimentaux [290, 293] et numériques [302, 303]. En

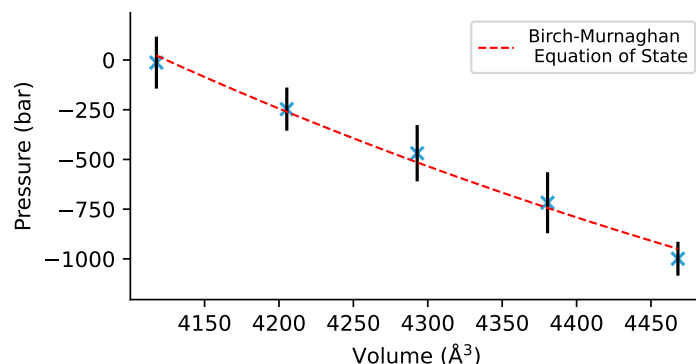


FIGURE R9: Pression en fonction du volume pour le cristal. Chaque volume correspond à une dynamique moléculaire *ab initio* à volume fixé.

outre, j'ai montré que les verres de ZIF-4 ont un module d'élasticité isostatique plus important que le cristal avec $K_{\text{verre}} = 2.43 \pm 0.09$ GPa, tout en confirmant des précédents résultats qui trouvaient que ZIF-4 possédait une densité plus importante dans sa phase vitreuse [233].

ÉVALUATION DE DYNAMIQUES MOLÉCULAIRES PLUS ÉCONOMES

J'ai ensuite pu utiliser ces valeurs de référence pour valider des méthodes de dynamiques moléculaires moins coûteuses en temps de calcul : champs de force réactifs, classiques et potentiels ML. Pour chacun des types de dynamique moléculaire, j'ai comparé différentes méthodes de calcul sur un ensemble de modèles de cristaux et de verres de ZIF-4.

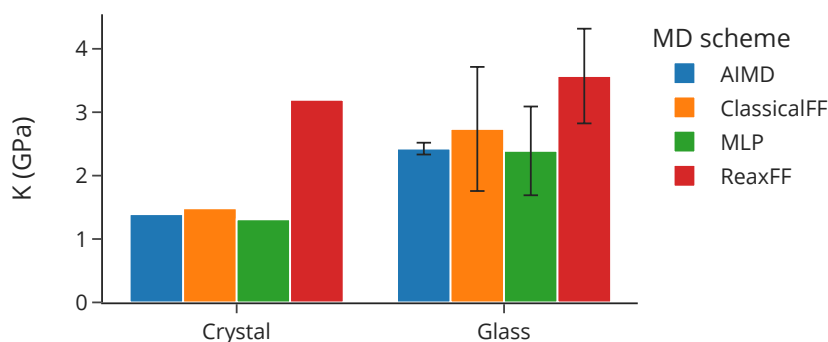


FIGURE R10: Module d'élasticité isostatique K pour le cristal et les verres *ab initio* du ZIF-4, obtenu par différences finies pour plusieurs formes de dynamiques moléculaires.

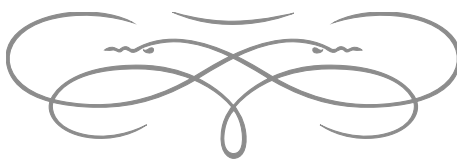
Comme présenté figure R10, les valeurs de K des champs de force classiques et potentiels ML sont en accord raisonnable avec les calculs *ab initio*, là où ReaxFF n'a pas réussi à différencier le cristal des verres. Les densités pour ces deux premières méthodes sont également cohérentes avec les dynamiques *ab initio* et les expériences [233]. Cela montre que les champs de force classiques comme les potentiels ML sont prêts à être déployés pour une évaluation plus large et systématique des propriétés mécaniques de multiples ZIF.

CONCLUSIONS

Durant ma thèse, j'ai utilisé plusieurs méthodes de simulation moléculaire pour générer des modèles microscopiques d'*a*MOF et étudier leurs propriétés. Utilisant ZIF-4 comme prototype d'*a*MOF, j'ai étudié l'utilisation de champs de force réactifs pour générer des modèles de verre par trempe, et mis en évidence leur incapacité à reproduire fidèlement des caractéristiques clés de la chimie des ZIF. Afin d'offrir une alternative numériquement efficace permettant la génération de modèles de verres de ZIF, j'ai construit des potentiels ML qui reproduisent très précisément les propriétés structurales des modèles *ab initio*. Finalement, j'ai étudié en détail le calcul des propriétés mécaniques à température finie de cristaux et verres de ZIF-4, en appliquant une série de méthodes et de formes de dynamique moléculaire. Dans l'ensemble cette thèse a permis de mettre en évidence l'absence trop fréquente de comparaison directe et approfondie des modèles dans la littérature existante, et a souligné les propriétés géométriques, physiques et chimiques très différentes des multiples modèles proposés.

Ce travail ouvre des perspectives pour le développement et l'utilisation de modèles d'*a*MOF, en s'appuyant sur l'expertise acquise avec ZIF-4. Tout d'abord, le développement en cours d'un MLP plus universel pour les ZIF devrait permettre la génération de multiples verres de ZIF, leur caractérisation structurale, et l'examen de leurs propriétés mécaniques à température finie. Si les MLP ne tiennent pas toutes leurs promesses, les propriétés mécaniques pourraient alternativement être calculées avec le développement d'une paramétrisation de champs de force classiques adaptés aux ZIF amorphes.

Plus généralement et afin d'améliorer la qualité des modèles amorphes à l'avenir, des études plus larges seraient nécessaires, intégrant de nombreuses techniques expérimentales différentes (infrarouge et Raman, RMN, etc.), pour fournir des données *in situ*. En plus de fournir un aperçu direct de la nature des phases amorphes des MOF, ces données pourraient être utilisées comme référence pour tester différents modèles microscopiques. Des bases de données de matériaux poreux amorphes pourraient alors être développées, à l'instar de celles pour les phases cristallines, et contribuer à accélérer les efforts de modélisation de ces systèmes. Finalement, le développement de stratégies de modélisation multi-échelles pourrait s'avérer fructueux en permettant de combiner les atouts des différentes méthodes déjà disponibles.



RÉSUMÉ

Les réseaux métallo-organiques (MOF) sont des matériaux hybrides composés d'ions métalliques reliés par des ligands organiques qui forment des réseaux tridimensionnels. Du fait de leur porosité et de leur grande versatilité structurale et chimique, ils forment des candidats prometteurs pour de multiples applications industrielles, notamment pour la séparation du CO₂. Même si la majorité de la littérature se concentre sur des structures cristallines, un nombre croissant de MOF amorphes (*a*MOF) ont été synthétisés, qui conservent à la fois les avantages intrinsèques des cristaux tout en possédant des propriétés physiques et chimiques distinctes. Cependant, la détermination expérimentale de la structure microscopique de ces phases amorphes est complexe, avec les expériences de diffraction qui n'offrent que des informations indirectes. Afin de résoudre leurs structures et modéliser ces matériaux désordonnés, un ensemble de méthodes numériques coexistent, qui souffrent cependant d'un manque de comparaison directe et systématique entre modèles.

Durant ma thèse, j'ai utilisé plusieurs méthodes de simulation moléculaire aux buts, échelles et coûts de calcul différents – dynamique moléculaire *ab initio*, champs de force classiques et réactifs, et potentiels ML – pour générer des modèles microscopiques d'*a*MOFs et étudier leurs propriétés. Utilisant ZIF-4 en tant que prototype d'*a*MOF, j'ai étudié l'utilisation de champs de force réactifs pour générer des modèles de verre par trempe, et mis en évidence leur incapacité à reproduire fidèlement des caractéristiques clés de la chimie des ZIFs. Afin d'offrir une alternative numériquement efficace pour la génération de modèles de verres de ZIF, j'ai construit des potentiels interatomiques par apprentissage automatique (ML) qui reproduisent très précisément les propriétés structurales des modèles *ab initio*. Finalement, j'ai étudié en détail le calcul des propriétés mécaniques à température finie de cristaux et verres de ZIF-4, en appliquant une série de méthodes et de formes de dynamique moléculaire.

MOTS CLÉS

simulation moléculaire, matériaux poreux, réseaux métallo-organiques, phases désordonnées, CO₂

ABSTRACT

Metal-organic frameworks (MOFs) are hybrid materials composed of inorganic nodes bridged by organic linkers to form three-dimensional architectures. Taking advantage of their porosity and structural and chemical tunability, they have been proposed for applications in various industrial-scale processes, notably for CO₂ separation. While the majority of studies in the literature are focused on crystalline structures, a growing number of amorphous MOFs (*a*MOFs) have been reported, which retain intrinsic advantages of crystals and powders but possess distinct physical and chemical properties. However, the determination of the framework structure of these *a*MOFs at the microscopic scale is experimentally difficult, with diffraction experiments only providing indirect structural information. In order to work around or alleviate this challenge, an array of computational methods coexist to model these disordered materials, with a lack of direct and in-depth comparison of the models.

During my PhD, I used various simulation methods with different scopes, scales and computational costs – *ab initio* molecular dynamics, classical and reactive force fields, and machine-learned potentials – to generate atomistic models of *a*MOFs and study their properties. With the prototypical *a*MOF structure ZIF-4 as a test case, I investigated the use of reactive force fields to generate glass models by melt-quenching, and found that it failed to faithfully reproduce key characteristics of the chemistry of ZIFs. To provide another tractable alternative to the generation of ZIF glasses, I developed machine-learned potentials and found that they lead to an excellent reproduction of the structural properties of *ab initio* data. Finally, I have extensively investigated the computation of finite temperature mechanical properties of ZIF-4 crystals and glasses, by applying a range of methods and molecular dynamics schemes.

KEYWORDS

molecular simulation, porous materials, metal-organic frameworks, amorphous materials, CO₂ separation